A Two-Scale Approach to Elastohydrodynamic Lubrication

by

Gregory Nicholas de Boer

Submitted in accordance with the requirements for the degree of

Doctor of Philosophy

The University of Leeds

School of Mechanical Engineering

March 2015

Intellectual Property and Publication Statement

The candidate confirms that the work submitted is his own, except where work which has formed part of jointly authored publications has been included. The contribution of the candidate and the other authors to this work has been explicitly indicated below. The candidate confirms that appropriate credit has been given within the thesis where reference has been made to the work of others.

Chapters 4 and 5 of this thesis contain theory and results presented by the author at the 5th World Tribology Congress in Turin, Italy (de Boer, et al. [1]) and also by Dr Leiming Gao at the Advances in Structural Engineering and Mechanics (ASEM) 2013 conference in Jeju, South Korea (Gao, et al. [2]). The work produced by Dr Gao in [2] does not form part of this thesis. The author later published his contributions to these conferences as a journal article in Tribology International (de Boer, et al. [3]) in which the role of three-dimensional topography in elastohydrodynamic lubrication was investigated via a two-scale method.

The theory and results in chapters 4 and 6 of this thesis were presented by the author at the Lubrication, Maintenance, and Tribotechology 2014 conference in Manchester, UK (de Boer, et al. [4]) and at the 10th ISSMO/ASMO-UK Conference on Engineering Design Optimisation Product and Process Improvement in Delft, the Netherlands (de Boer, et al. [5]). The latter had proceedings in which work investigating metamodelling and optimisation of topography by the two-scale method for elastohydrodynamic lubrication was explored.

Acknowledgements

I would like to thank my supervisor Dr Rob Hewson who has been an outstanding mentor throughout this project. I must also thank Prof Harvey Thompson whose continued advice has significantly improved my research. Other academics have also helped me significantly, including Dr Leiming Gao, Prof Vassili Toropov, and Dr Jon Summers.

I acknowledge the University of Leeds and the Engineering and Physical Sciences Research Council (EPSRC) Grant Number EP/I013733/1 for funding this project. I would like to extend by thanks to those members of administrative, technical and IT staff within the School of Mechanical Engineering who have helped me during this work. Ted Allwood and Dr Graham Blyth deserve special mentions for their years of support and untouchable running of the computer network across the faculty.

Special mentions go to my parents Nicholas de Boer and Veronica de Boer, and my also to my brother Oliver de Boer. Their continued support throughout my time as a postgraduate research student has provided me with the very best chance of being able to complete this thesis.

I would not have been capable of producing this work without the ongoing support of my peers. Specific thanks goes to Nicholas Raske, Ben Rothwell, Adam Johns, Adam Thompson, Laura Sanders, Kieran Hood, and Dan Rollins and Hazel Rollins to name a few. They have all made my time as a PhD student worthwhile and well spent.

Abstract

Derived from the Heterogeneous Multiscale Methods (HMM), a two-scale method is developed in this thesis for the analysis of Elastohydrodynamic Lubrication (EHL) and micro-EHL in tilted-pad bearings with three-dimensional topography. A relationship linking the pressure gradient to mass flow rate is derived and represented in the bearing domain through homogenisation of near-periodic simulations which describe the Fluid Structure Interaction (FSI) of topographical features. This relationship is approximated using Response Surface Methodology (RSM) which allows the scales to be coupled by a Moving Least Squares (MLS) metamodel at a reduced computational effort.

For the parameters investigated the influence of compressibility and piezoviscosity was found to be more significant than that of non-Newtonian (shear-thinning) behaviour on textured bearing performance. As the size of topography increased two-scale solutions demonstrated that at constant load the coefficient of friction increased and the minimum film thickness decreased over a range of pad lengths and tilt angles. Through the two-scale method the micro-EHL effect on film thickness was quantified and shown to be at least an order of magnitude or less than that of the total EHL effect.

Parameterisation of topography led to an optimisation procedure which aimed to reduce the coefficient of friction in textured bearings as to improve their performance under load. It was shown through this procedure that a transverse topography benefits the performance over a longitudinal one. The best performing topography was found to have a mix of both longitudinal and transverse components, and it was also shown that very different topographies can exhibit similar characteristics. Through the metamodelling process deviation from the smooth surface model was quantified by the constants associated with the MLS approximations.

Table of Contents

List of Figures

List of Tables

Abbreviations

ALE	Arbitrary Lagrangian-Eulerian
ANN	Artificial Neural Networks
BBD	Box-Behnken Design
BVP	Boundary Value Problem
CCD	Central Composite Design
CCC	Centre Composite Circumscribed
CCF	Centre Composite Faced
CCI	Centre Composite Inscribed
CCS	Centre Composite Scaled
CFD	Computational Fluid Dynamics
CV	Cross Validation
DoE	Design of Experiments
EHL	Elastohydrodynamic Lubrication
EPSRC	Engineering and Physical Sciences Research Council
FE	Finite Element
FFT	Fast Fourier Transform
FSI	Fluid Structure Interaction
GA	Genetic Algorithm
HMM	Heterogeneous Multiscale Methods
IVP	Initial Value Problem
LHC	Latin Hypercube
LOOCV	Leave One Out Cross Validation
LS	Least Squares
MARS	Multivariate Adaptive Regression Splines

MLS	Moving Least Squares
OLHC	Optimum Latin Hypercube
PTFE	Polytetrafluoroethylene
RAAE	Relative Average Absolute Error
RAM	Random Access Memory
RBF	Radial Basis Function
RMAE	Relative Maximum Absolute Error
RMSE	Root Mean Squared Error
RSM	Response Surface Methodology
SVR	Support Vector Regression

Nomenclature

$A, \Delta A$	Area, area deformation (m^2)
$C_1 - C_{10}$	MLS constants
D_0, D_1	Dowson-Higginson compressibility
E, E'	Young's modulus, equivalent modulus (Pa)
$\mathbf{F}$	Vector of forces per unit volume (N/m^3)
g	Film gap (μm)
h	Undeformed film thickness (μm)
$\mathbf{K}, \mathbf{K}_G$	Stiffness matrix, global stiffness matrix (μm/MPa)
k_1	Local stiffness (μm/MPa)
k	Number of folds
L	Cell length (μm)
L_p	Pad length (mm)
$p, \Delta p$	Pressure, pressure jump (MPa)
p_r	Viscous reference pressure (GPa)
p^*	Load-per-unit-area (N/mm^2)
q	Mass flow rate (kg/s)
r	Micro-EHL effect on minimum film thickness (%)
s	Small scale film thickness (μm)
Δs	Deformation of small scale film thickness (μm)
s_{min}	Small scale minimum film thickness (μm)
t, t'	Pad thickness, equivalent thickness (mm)
U	Wall velocity (m/s)
$\mathbf{u}$	Fluid velocity (m/s)
V	Volume (m^3)

W	Load capacity (kN)
x, y, z	Cartesian coordinates (m)
Z	Piezo-viscous index
α	Topography amplitude (μm)
$\dot{\gamma}$	Shear rate (1/s)
δ	Deformation (μm)
δ_t	Topography function (μm)
ξ	Pressure error at outlet (Pa)
η, η_0	Viscosity, ambient viscosity (Pa.s)
η_p	Piezoviscosity (Pa.s)
η_r	Roelands reference viscosity (μPa.s)
μ	Coefficient of friction
ν	Poisson's ratio
ρ, ρ_0	Density, ambient density (kg/m^3)
σ	Stress (N/m^2)
θ	Under relaxation factor
τ, τ_0	Shear stress, Eyring stress (N/mm^2)
φ	Tilt angle (°)
ψ	Longitudinal/transverse ratio
s	Small scale variable

Chapter 1 – Introduction

Elastohydrodynamic lubrication (EHL) is a field of study concerned with tribology and describes the formation of a lubricant film between two non-conformal machine elements which are under load and in relative motion to each other. EHL exists in mechanical systems with a high elastic modulus such as roller bearings, cam-tappets, and gear teeth. Systems with a lower elastic modulus also experience this kind of lubrication and are often referred to as soft-EHL. Examples of soft-EHL include polymer-layered pad bearings, rubber seals, and car tyres on a wet road [14]. EHL has been the focus of many engineers since the publication of the Jost Report on tribology in 1966 [15] which quantified the financial importance of understanding the friction, lubrication and wear of mechanical systems and subsequently to improve engineering design and efficiency.

In an EHL contact the pressures can reach upward of 4 GPa, in soft-EHL pressures of 10 MPa can be readily achieved [16]. Under EHL conditions the properties of lubricating oils tend to be non-Newtonian. Both viscosity and density become heavily dependent on pressure and shear-thinning occurs if the sliding between surfaces is sufficient and the lubricant is a generalised Newtonian fluid. Viscous heating of the lubricant can also impact on the viscosity.

Conventionally the flow of lubricant in an EHL contact is modelled by the Reynolds equation [16], which is a version of the Navier-Stokes equations integrated across the film thickness. Elastic deformation in a highly-loaded EHL contact is calculated using Hertzian contact theory, or in soft-EHL other elastic contact theories can be used [17]. This approach has been applied with great success, comparing well with experiments under realistic operating conditions [18]. However the assumptions on which the Reynolds equation is based apply only to smooth surfaces and do not include the effects of surface roughness, which plays a major role in determining the fluid film lubrication [16]. Under these assumptions pressure is assumed constant across the film and the gradients of fluid properties across the film are assumed to be negligible or are greatly simplified, such that they are never truly resolved.

The application of Computational Fluid Dynamics (CFD) to EHL problems has facilitated the solution of the Navier-Stokes equations for the entire fluid system,

allowing the solution for all gradients across the fluid film. CFD also allows for more sophisticated modelling of fluid flow phenomena than can be achieved through the Reynolds approach such as cavitation, rheology, and thermal transport. Dependencies of pressure, temperature, and shear rate on any other variable (viscosity, density, etc.) can be implemented and the corresponding effects studied. This makes the CFD approach favourable for researchers and a number of studies have been conducted which employ these methods to model an entire EHL contact, e.g. Hartinger [19], and Almqvist [20], [7].

The resolution required by the CFD approach to model the influence of surface roughness requires a fine mesh, leading to a large computational expense. Although the CFD approach may be capable of modelling the entire EHL system, it should be used in conjunction with other methods which either simplify surface roughness or allow the scales associated with topography and the bearing domain to be modelled independently and later coupled together.

Surface roughness plays a major role in influencing the formation of lubricant films in an EHL contact, often the size of the topography is of the order of magnitude of the film thickness leading to a breakdown of the assumptions of the Reynolds approach [16]. Much of the past and current research into EHL has been focused on analysing the role of surface roughness in determining the performance of bearings. Through the analysis of both experiments and simulations, it is not clear whether certain topographical features can lead to a reduction in friction coefficient or minimum film thickness for a given load capacity [21], [22]. Quantifying the effect of surface roughness is a complex issue because parameterising and modelling real surfaces is a challenge which authors have tackled either by deriving analytical, stochastic, or homogenisation based approaches to modelling surface roughness.

However various techniques have been developed by a number of researchers to analyse surface roughness in EHL. Some of these methods use CFD to model the scale of topography independently and then apply the results to the bearing domain by a modified Reynolds equation (usually of the form of Patir and Cheng [23]), which is inclusive of flow factors that account for perturbations introduced by the surface roughness. For example see de Kraker, et al. [24], [25] and Sahlin, et al. [26], [27]. More recently these homogenisation type approaches, which this group of methods are referred to, have become more applicable to EHL as the processing power of

computational facilities improves and modelling the scale of surface roughness develops as a more realistic aim.

One such homogenisation approach is to employ the Heterogeneous Multiscale Methods (HMM) [28] to the EHL problem. The HMM are a general set of modelling techniques that can be used wherever there is a significant separation in scales, such as the difference in scale between surface roughness and the bearing domain. The HMM have been employed to a range of thin film problems including direct gravure roll coating [29] and EHL [30]. In application to EHL the HMM replaces the Reynolds equation with a numerical function that does not have an analytical form, this function describes the pressure gradient – mass flow rate relationship inclusive of topography and is populated by homogenised near-periodic simulations undertaken at the small scale. Because the function is not analytical Response Surface Methodology (RSM) is used to approximate the discrete data over the range of variables, allowing non-linearity introduced by the topography at the small scale to be captured and modelled effectively in a large scale simulation.

The aim of this research is to:

- Develop a two-scale method based on the HMM for modelling the effects of three-dimensional topography in an EHL contact.
- Include compressibility, piezoviscosity, and non-Newtonian (shear-thinning) behaviour in the simulations.
- Use response surface methods to couple the scales modelled.
- Compare results with and without topography to the Reynolds approach.
- Perform optimisation of topography in order to minimise the coefficient of friction generated by textured bearings under load.

1.1 Thesis Layout

Chapter 2 forms a literature review of EHL which outlines the Reynolds approach, the application of CFD, and the current research into modelling surface roughness. In chapter 3 an overview of RSM is provided, indicating the current methods used for model building and validation. Chapter 4 details the two-scale EHL method based on the HMM for including the effects of three-dimensional topography in

textured bearings. In chapter 5 results for the two-scale EHL method outlined in chapter 4 are presented using a tilted-pad bearing as an example. The influence of fluid properties and the size of topography are provided and compared against results of the Reynolds approach. Chapter 6 provides results of the two-scale method concerned with performing optimisation of topography. Results in chapter 6 are concentrated more with the aspects of RSM employed rather than the tribological implications explored in chapter 5. Chapter 7 summarises and concludes the results observed from the two-scale EHL method and goes on to make recommendations for future research.

Chapter 2 – Review of Elastohydrodynamic Lubrication

2.1 Introduction

This chapter introduces the relevant literature and current research into the modelling of elastohydrodynamically lubricated contacts. A description of the formulation of the problem is given along with details of the governing equations and fluid properties. Also included is a discussion of the techniques used for modelling fluids and solids in elastohydrodynamic lubrication (EHL).

2.1.1 Definition of EHL

The Stribeck curve (see fig. 2.1) is used to categorise the tribological and frictional properties between two surfaces, the curve stems from many carefully reproduced and wide-ranging experiments conducted on journal bearings [31]. Three main categories are identified: (1) – boundary lubrication where the surfaces asperities are in contact and rubbing or scuffing exists; (2) – mixed lubrication where some surface asperities contact and a lubricant film forms between; (3) – hydrodynamic lubrication where a full film of lubricant is formed between the two surfaces [32].

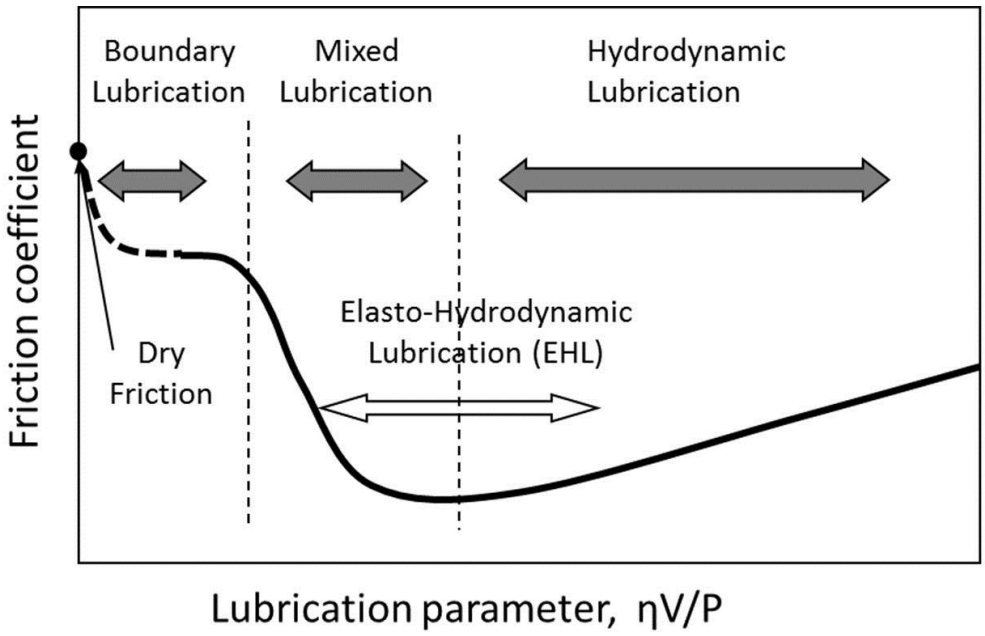

Fig. 2.1 - Schematic of the Stribeck curve (Kondo, et al. [6]), where η is the lubricant viscosity, V is the speed of the surface motion, and P is the load applied to the surface

EHL exists between mixed and hydrodynamic lubrication corresponding to small film thicknesses, high pressures and a minimum coefficient of friction for the contact [33]. EHL is the regime of lubrication which occurs in contacts where elastic deformation of the bounding surfaces has a significant influence on the thickness of the fluid film. The elastic deformation is generated as a result of high pressures in contact, which generally also leads to a substantial increase in lubricant viscosity. Both these effects positively influence the film thickness [16]. Examples of where EHL contacts can be found include tilted-pad bearings, rolling bearings, cam-tappet systems, gear teeth, flexible seals, and synovial joints [14]. Often in these types of contacts the size of surface topography is comparable with the film thickness, causing a breakdown in smooth surface approximations and assumptions [34].

2.2 EHL Modelling

The origins of the analysis of EHL can be traced back to 1886 when Osborne Reynolds published his seminal article deriving the partial differential equation describing the pressure distribution and load-carrying capacity of lubricating films in journal bearings [35]. Both Martin [36] and Gümbel [37] applied the Reynolds equation to the lubrication of gear teeth in 1916 and found film thicknesses that were too small to explain the lubrication observed. Meldahl [38] in 1941 included elastic deformation due to contact pressures but was still unable to observe the correct film thicknesses. In 1945, Ertel [39] (published under the name of Grubin in 1949 [40]) used a semi-analytical method to solve Reynolds equation and added a pressure-viscosity effect on the film thickness such that he was finally able to predict the correct order of magnitude of the full film. Since then this regime of lubrication has been known as elastohydrodynamic lubrication.

The first numerical calculations for line contact problems were provided by Petrusevich [41] and Dowson and Higginson [42], [43]. By 1976/1977 Hamrock and Dowson [44], [45], [46] had derived and solved the EHL for circular oil lubrication. The curve fit to their numerical solutions is still the most widely used predictor for film thickness in EHL. Lubrecht, et al. [47], [48] introduced multilevel techniques which improved the efficiency of numerical calculations, this led to a significant increase in the accuracy of the solution. Venner [49] introduced performing transient calculations by further improving the multilevel technique. The multilevel method for solving EHL

problems is detailed in full by Venner and Lubrecht [50]. In 1994 Nijenbanning, et al. [51] produced a new film thickness formula based on a curve fit to the multilevel solutions, after this date there was no need to further improve the accuracy of smooth surface EHL.

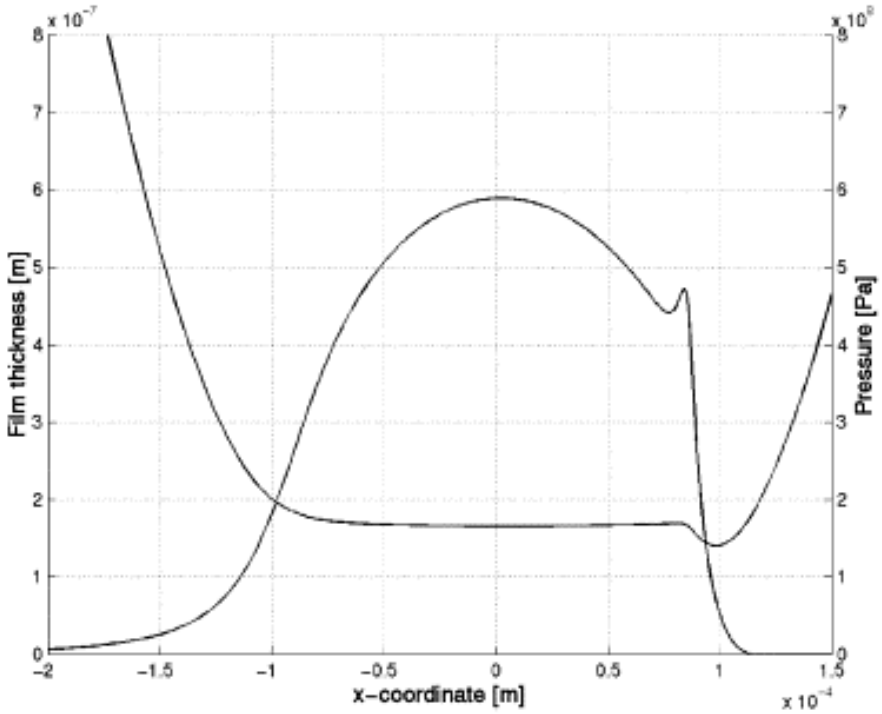

Fig. 2.2 – Pressure and film thickness distributions in an EHL line contact under sliding conditions (Almqvist and Larsson [7])

Tzeng and Saibel [34], [52] showed that surface roughness impacted the EHL performance of mechanical bearings and in 1978 Patir and Cheng [23] developed an average flow model which allowed the scales of surface topography and the bearing domain to be treated separately. This method demonstrated that a transverse roughness would benefit the performance of the bearing by reducing the coefficient of friction over a longitudinal one, a result which was confirmed by many experiments and calculations over the next few years (Jeng [53], Akamatsu, et al. [54], Greenwood and Johnson [55], Greenwood and Morales-Espejel [56], Venner and ten Napel [57]). The full EHL equations had also been solved at the scales of roughness and the bearing domain (Zhu and Hu [58]) but it was not until the concept of amplitude reduction was introduced by Venner and Lubrecht [59] that real surfaces could be investigated. Morales-Espejel [60] and Masen [61] used this methodology by employing Fast Fourier Transformations

(FFTs) of real surfaces and applying the results to the EHL model. Although these articles allude to the influence of topography on bearing performance there is still no definitive general methodology which can describe the influence of surface topography on EHL contact performance.

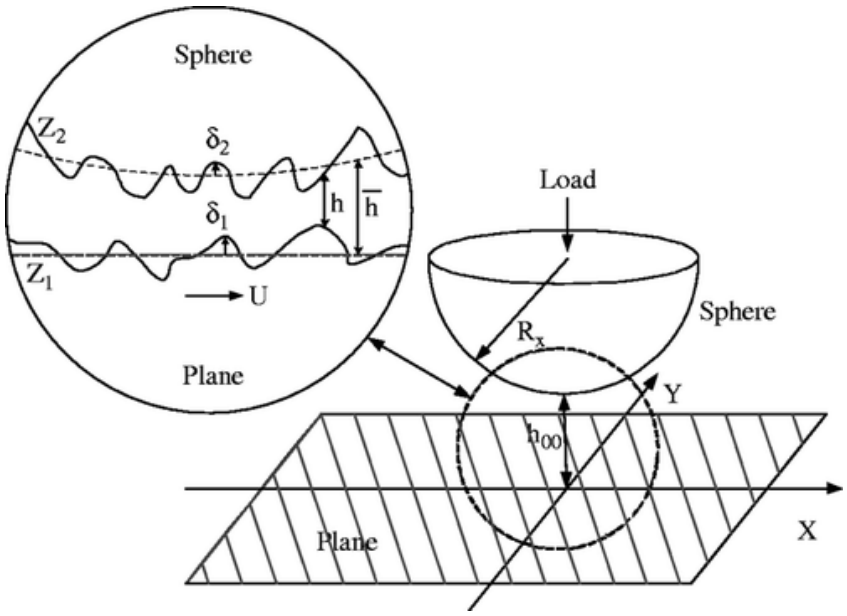

Fig. 2.3 – Illustration of the separation in scales between surface roughness and the bearing domain (Chu, et al. [8])

Much of the current and recent research is concerned with modelling surface roughness in EHL contacts, a more detailed discussion of this research topic relevant to the research presented in this thesis is given in section 2.3. For further details on the origins of EHL see Dowson [14], Dowson and Ehret [62], and Spikes [63]. And for further details on other current research topics in EHL such as greased or starved lubrication see Lugt and Morales-Espejel [64].

2.3 Surface Roughness Modelling

The Reynolds equation (Reynolds [35]) is well established as an accurate means of describing fluid flow in the elastohydrodynamic lubrication of smooth surface geometries (Dowson and Higginson [42]). More recently the focus of lubrication engineers has been directed toward analysis of surface topography and the influence that this has on bearing load capacity and friction coefficients (Tzeng and Saibel [34]). The potential of topographical features to improve bearing performance has increased the

importance of surface roughness and texturing within bearing design (Etsion, et al. [21]). A number of authors have obtained solutions to the Reynolds equation which fully resolve lubrication flow at both the scale of topography and that of the bearing contact region (Venner and Lubrecht [59], Morales-Espejel, et al. [60], Hooke, et al. [65], Krupka and Hartl [66]). As topographical features become more important flow analyses based on solutions of the Stokes or Navier-Stokes equations have been shown to be more accurate than those based on the conventional Reynolds equation (Szeri [22]).

Studies which compare solutions to Reynolds, Stokes and Navier-Stokes equations for textured surfaces have been conducted by a number of researchers (Almqvist, et al. [67], [68], van Odyck and Venner [69], Tichy and Bou Said [70], Arghir, et al. [71], Sahlin, et al. [72], Dobrica and Fillon [9], Cupillard, at al. [73]). Significant differences in load capacity between Reynolds and Stokes solutions were found in the presence of topographical features. The inclusion of inertial effects via the generalised Reynolds equation (Wilson and Duffy [74]) or Navier-Stokes equations illustrated the influence of inertia on load capacity and the consequent benefit of using Computational Fluid Dynamics (CFD) to model the fluid film flow within a textured bearing. CFD has also been used on smooth geometries to enable the modelling of a range of phenomena which occur in EHL such as thermal transport, rheology, cavitation (Hartinger, et al. [19]), wall slip (Aurelian, et al. [75]) and structural models (Bruyere, et al. [76]).

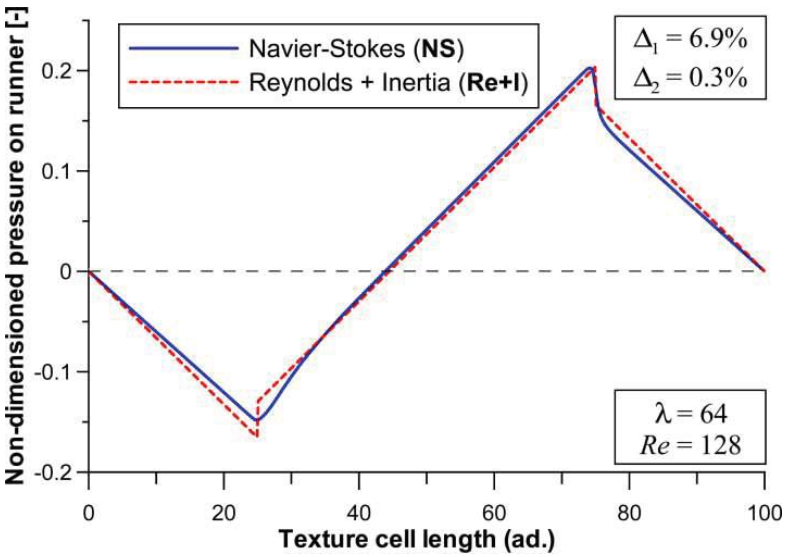

Fig. 2.4 – Effect of the Reynolds equations and the Navier-Stokes equations on the pressure reached in a textured runner bearing (Dobrica and Fillon [9])

Both single-scale deterministic (where the surface topographical features are fully described and resolved over the global domain) and two-scale homogenisation (where the flow about surface topographical features are solved independently and the results are applied to the global domain) models have been used by researchers to analyse bearings with surface texturing. Although CFD has the potential to comprehensively describe lubrication phenomena most research in this field to date remains focused on the use of the Reynolds equation, whether that is by single-scale deterministic (Mourier, et al. [77], Zhu, et al. [78], Gao, et al. [79], Felix-Quinonez, et al. [80]) or two-scale homogenisation (Tichy and Bou Said [70], Jai and Bou Said [81], Sahlin, et al. [82], [26], Martin [83]) models. Few single-scale deterministic models have been developed which employ the Navier-Stokes equations (Tichy and Bou Said [70], Almqvist [20], [84], [7], Li and Chen [85]) because of the large separation in scales between each local feature and the entire domain. The grid resolution required to model such a difference is beyond most computational facilities, making an analytical or two-scale homogenisation based approach more realistic.

Stochastic approaches to modelling roughness were introduced by Cheng and Dyson [86], their method derived an analytical approach for a simple roughness to be incorporated into EHL simulations. Greenwood and Johnson [55] noticed that a sinusoidal roughness produces pressure ripples in the presence of sliding and that roughness is largely flattened, from this observation they were able to develop analytical relationships to describe pressure and deformed roughness. Venner [49] observed that at the centre of a wavy EHL contact, the viscosity is so high that the Poiseuille term in the Reynolds equation can be disregarded, reducing the flow to a linear transport equation. Greenwood and Morales-Espejel [56] used this important result to develop an analytical method for calculating the pressures of any sinusoidal roughness. Using the amplitude reduction results of Venner and Lubrecht [59], Morales-Espejel [60] and Masen [61] exploited the similarities in transverse and longitudinal amplitude reduction curves to expand this analytical approach to any 3D roughness by expressing it in Fourier terms. Hooke, et al. [65], [87] applied perturbation methods and developed a fully analytical model for sinusoidal waviness (which is extended to a real roughness) that does not depend on the amplitude reduction curves of Venner and Lubrecht [59].

Patir and Cheng [23] introduced the average flow model where the Reynolds equation is modified with flow factors that allow the scale of topography and that of the

domain to be treated separately. These flow factors were calculated from simulations describing the local surface texture with periodic boundary conditions which are subsequently coupled into a global-scale simulation. Using this average flow model Sahlin, et al. [82] developed a method of homogenisation for hydrodynamic bearings with periodic roughness, the flow factors were calculated from homogenised results of the compressible Reynolds equation. This concept was then extended by Sahlin, et al. [26] to a mixed lubrication regime with prescribed sinusoidal roughness. Still using the Reynolds equation to describe the small scale fluid flow, a contact mechanics model was used to determine both elastic and plastic asperity deformation. Solid-solid contact was implemented to derive the bearing surface and as such Fluid Structure Interaction (FSI) was not considered at either scale.

Studies have been conducted where the Navier-Stokes equations are used to describe the small scale problem. de Kraker, et al. [24], [25] applied the incompressible Navier-Stokes equations to describe small scale fluid flow and an averaged Reynolds equation (similar to that of Patir and Cheng [23]) with elastic deformation were implemented at the large scale. Flow factors were introduced to account for the small scale simulations but micro-EHL effects were not considered. A similar model developed for discrete cell gravure roll coating by Hewson, et al. [29]. A relationship was derived linking homogenised results of Stokes flow simulations at the small scale to a pressure gradient – mass flow rate relationship at the large scale. The linearity of Stokes flow allowed for simple incorporation of the small scale simulations into the large scale simulation.

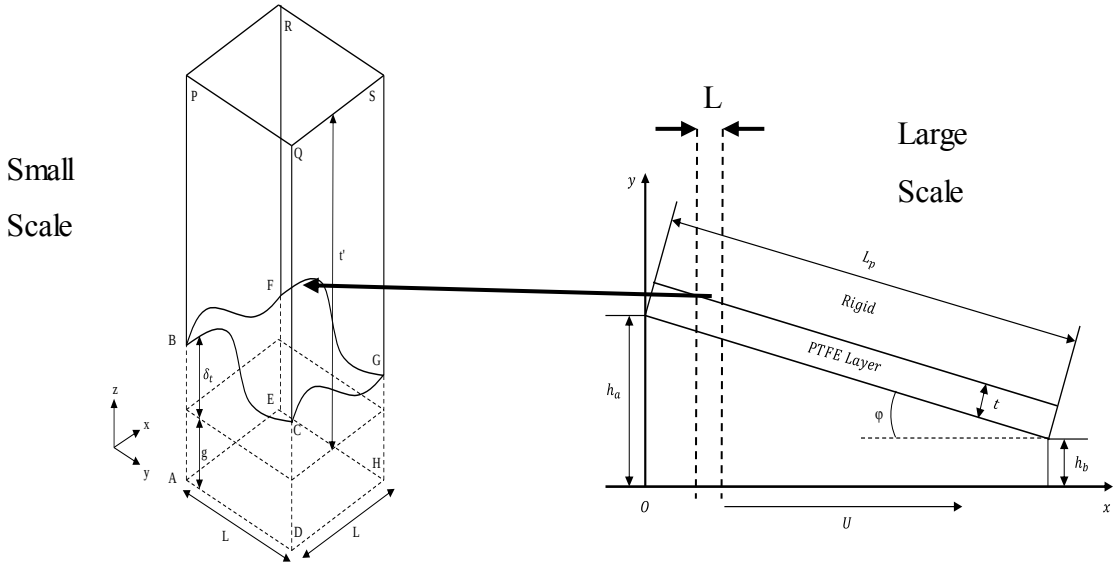

Fig. 2.5 – The two-scale homogenisation based approach to EHL (de Boer, et al. [3])

Based on the Heterogeneous Multiscale Method (HMM) developed by E and Engquist [88], and E, et al. [89] a framework for the analysis of EHL and micro-EHL in two-dimensions was outlined by Gao and Hewson [30]. Both local and global EHL effects were described. The incompressible Navier-Stokes equations were used to define fluid flow at the small scale. Results of near-periodic small scale simulations were homogenised and applied to the global solution via a pressure gradient – mass flow rate relationship. Periodicity was vital to the coupling mechanism, allowing small scale simulations to be treated as a point at the large scale. The resulting relationship binding these two scales was shown to be non-linear due to deformation of the bearing surface and small scale flow effects. Interpolation was used at the large scale to inspect between previously obtained small scale results. These results were represented via a full factorial Design of Experiments (DoE). Deformation at both scales was treated through the separation of the stiffness matrix into local and non-local influences. Results of smooth surface simulations at the small scale were presented and compared well with the smooth surface model when applied to a tilted-pad bearing problem. Results including topography demonstrated the influence of micro-EHL and the robustness of this method in capturing these effects.

In de Boer, et al. [3] the multiscale framework outlined by Gao and Hewson [30] was extended to three-dimensional small scale simulations and more representative lubricant behaviour was considered. The two-scale method derived was valid where the bearing has no cross-flow or side-leakage implemented at the large scale. However, additional comments were made as to how the general solution could be achieved. The steady-state, isothermal, laminar and compressible Navier-Stokes equations governed fluid flow at the small scale, where piezoviscosity and non-Newtonian (shear-thinning) behaviour were also modelled. A method for the homogenisation of small scale simulations in three-dimensions was introduced. This data was similarly coupled to the large scale via a pressure gradient – mass flow rate relationship. The small scale data was represented by a Moving Least Squares (MLS) approximation, a metamodel describing this relationship was built and validated using k-fold Cross Validation (CV) in a method similar to that used by the author in Loweth, et al. [90] and also by Narayanan, et al. [91]. This method employed an Optimum Latin Hypercube (OLHC) to populate the DoE used for small scale simulations, in order to span the entire design space as effectively as possible with the fewest number of designs (Bates, et al. [92], Toropov, et al. [93]). Numerical simulations of this multiscale approach were presented

for a range of topography amplitudes and compared to the smooth surface model over a range of operating conditions and degrees of freedom.

The work of de Boer, et al. [3] was further expanded in de Boer, et al. [5] to perform optimisation of surface topography in order to minimise the coefficient of friction in textured bearings. It was shown using the two-scale method that a transverse topography produces lower coefficients of friction than a longitudinal one and that through the use of metamodelling a range of different surface topographies can be investigated.

2.4 Governing Equations

2.4.1 The Reynolds Equation

In general, fluid flow is described by the Navier-Stokes and continuity equations. Listed below are the assumptions which lead to the derivation of the Reynolds equation from the Navier-Stokes equations and form the basis of the smooth surface model [16].

1. No body forces are present.
2. Pressure is considered constant across the lubricant film.
3. No slip of the fluid at the bounding walls.
4. The flow of lubricant is laminar.
5. Both inertial and surface tension forces are negligible in comparison to viscous forces.
6. Shear stress and velocity gradients are only significant across the film thickness.
7. Viscosity of the lubricant is Newtonian.
8. Viscosity is constant over the film thickness.
9. The boundary surfaces are parallel or at very small angles to each other.

With these assumptions the Reynolds equation in two-dimensions is expressed by Eq. (2.1) [35]. Where x is the coordinate direction concurrent with the direction of flow, y is the coordinate direction perpendicular to x and the film thickness h, ρ is the lubricant density, η is the lubricant viscosity, p the pressure in the film, and t is time.

The bounding surface velocities u_1, u_2, v_1, and v_2 correspond to the lower and upper surfaces of the geometry in the x and y directions respectively.

$$\frac{\partial}{\partial x}\left[\frac{\rho h^3}{\eta}\frac{\partial p}{\partial x}\right] + \frac{\partial}{\partial y}\left[\frac{\rho h^3}{\eta}\frac{\partial p}{\partial y}\right] = 6\left\{\frac{\partial}{\partial x}[\rho h(u_1 + u_2)] + \frac{\partial}{\partial y}[\rho h(v_1 + v_2)] + 2\frac{\partial}{\partial t}[\rho h]\right\} \tag{2.1}$$

By considering only steady flow (negating time derivatives) in one-dimension and using the identity $u = (u_1 + u_2)/2$ to set the entrainment velocity u, Eq. (2.2) is derived.

$$\frac{d}{dx}\left[\frac{\rho h^3}{\eta}\frac{dp}{dx}\right] = 12\frac{d}{dx}[\rho h u] \tag{2.2}$$

The Reynolds equation has been adapted by authors to incorporate non-Newtonian behaviour including the dependency of viscosity on pressure, temperature, and shear rate and of density on pressure and temperature (Contry, et al. [94], Johnson and Tevaarwerk [95], Roelands [96], Dowson and Higginson [97], Hewson, et al. [98]). Dowson [99] introduced a generalised Reynolds equation which allowed fluid properties to vary over the film thickness and he also solved an energy equation for thermal transport in the lubricant. Spikes [100] derived and solved an extended Reynolds equation which allowed for effects of slip at the boundary surfaces to be included.

Boundary conditions applied to the Reynolds equation dictate that ambient pressure is met at both inlet and outlet. However toward the outlet of the bearing cavitation occurs as pressure drops below the vapour pressure of the lubricant, this is commonly modelled using the Swift-Steiber boundary condition or Reynolds exit condition (Eq. (2.3)) which sets the pressure to zero (ambient pressure) at the location where cavitation begins [33].

$$\frac{dp}{dx} = p = 0 \tag{2.3}$$

2.4.2 Elastic Deformation and Film Thickness

The Hertzian theory of elastic contact is commonly used to calculate deformation in highly-loaded EHL simulations, this method was originally formulated by Hertz [101] in 1881 for the contact of two bodies. Hertz considered two smooth, ellipsoidal contacting solids and by making the following assumptions was able to derive Eq. (2.4) for the elastic deformation in an elastic contact δ[18].

1. The contacting bodies are homogenous and the stresses experienced are inside the yield stresses of the materials.
2. Tangential forces are not induced between the solids.
3. The dimensions of the contacting region are negligible in comparison to the radii of the contact.
4. The solids are at rest and equilibrium.
5. The solids are semi-infinite (plane-strain dominates).

$$\delta = \frac{1}{E_r} \iint_S \frac{p\, dx'dy'}{\sqrt{(x-x')^2 + (y-y')^2}} \tag{2.4}$$

In Eq. (2.4) p represents the pressure acting on the elemental area of $dx'dy'$ and E_r is the reduced elastic modulus for the contacting solids. The reduced elastic modulus allows the system to be modelled such that one surface is rigid and the other includes the total deformation of the system. Where $E_{1,2}$ and $\nu_{1,2}$ are the Young's moduli and Poisson's ratios of the contacting bodies the reduced elastic modulus is expressed by Eq. (2.5).

$$\frac{1}{E_r} = \frac{1}{\pi}\left(\frac{1-\nu_1^2}{E_1} + \frac{1-\nu_2^2}{E_2}\right) \tag{2.5}$$

For more information on the Hertz theory of elastic contact the reader is referred to Johnson [17].

In EHL the geometry considered is commonly a converging-diverging bearing, including deformation the film thickness equation is expressed by Eq. (2.6). In general the film thickness equation is the sum of undeformed film thickness and elastic deformation of the bounding surfaces.

$$h = h_0 + \frac{x^2}{2R_x} + \frac{y^2}{2R_y} + \delta \tag{2.6}$$

Where $R_{x,y}$ are the contact radii in the x and y coordinate direction respectively and h_0 is the central undeformed film thickness. The solution for elastic deformation requires a constant of integration which is included through h_0 such that the undeformed film thickness can be negative but with deformation gives a positive overall film thickness. h_0 is subsequently adjusted to solve for the load carrying capacity (integral of pressure over x and y) of the bearing since load will monotonically increase with decreasing h_0.

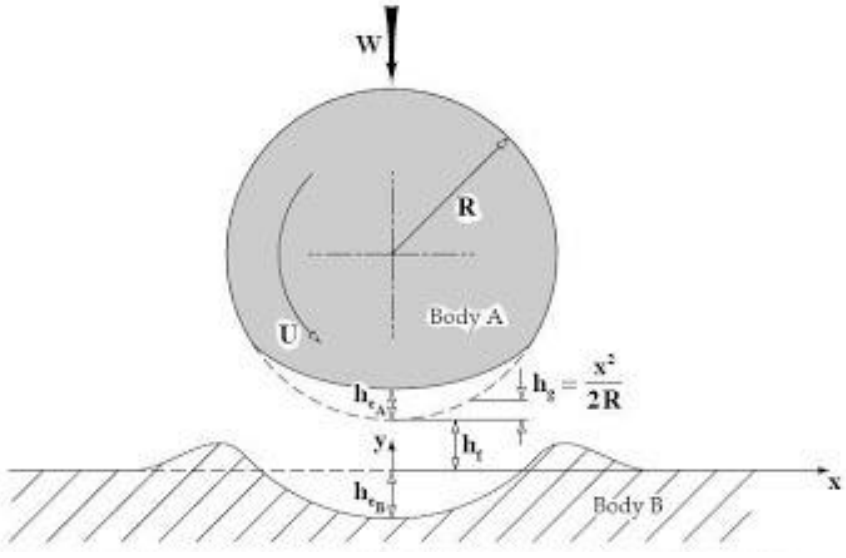

Fig. 2.6 – Effect of elastic deformation on the lubricant profile (Stachowiak and Batchelor [10])

In soft-EHL the contact mechanics considered are similar to Hertzian contact where the influence on deformation due to pressure diminishes with distance from the point of application. Using structural mechanics stiffness properties for the system can be derived, leading to a matrix operation which relates deformation to pressure, see Eq. (2.7). The stiffness matrix **K** describes the influence of pressure at any given point of application to the magnitude of deformation at a specific location, such that as they are superimposed the entire deformation profile due to a pressure distribution over the domain is described [102]. Film thickness becomes the sum of the undeformed geometry and deformation, the minimum undeformed film thickness can be subsequently adjusted to solve for a load carrying capacity.

$$\delta = \mathbf{K} \times \mathrm{p} \tag{2.7}$$

2.4.3 Thermal Effects

Thermal effects in EHL can be an important factor to consider, Dowson [99] was the first to solve an energy transport equation for the fluid flow for an EHL contact. Eq. (2.8) is derived by employing the following assumptions [16].

1. Velocity and temperature gradients are only significant across the thickness of the film and are negligible in the direction of flow.
2. Velocity across the film is negligible.
3. Thermal conductivity is constant across the film.

$$\beta \mathrm{u} \mathrm{T} \frac{\partial \mathrm{p}}{\partial \mathrm{x}} + \eta \left(\frac{\partial \mathrm{u}}{\partial \mathrm{z}} \right)^2 = \rho \mathrm{u} \mathrm{C}_\mathrm{p} \frac{\partial \mathrm{T}}{\partial \mathrm{x}} - \mathrm{k} \frac{\partial^2 \mathrm{T}}{\partial \mathrm{z}^2} \tag{2.8}$$

Here z is the coordinate direction over the film, T is the lubricant temperature, β the coefficient of thermal expansion, $\mathrm{C_p}$ the lubricant specific heat capacity at constant pressure, and k the thermal conductivity. From left to right the terms of Eq. (2.8) represent compressive heating, viscous heating, convection and conduction. Jaeger

[103] and later Carslaw and Jaeger [104] provided the most commonly used boundary conditions for assessing the temperature at the solid surfaces.

2.4.4 Viscosity-Pressure-Temperature Relations

The viscosity of lubricants varies significantly with pressure and temperature. Barus [105] proposed Eq. (2.9) for the pressure dependency of viscosity.

$$\eta_{\mathrm{Barus}} = \eta_0 \exp(\alpha p) \tag{2.9}$$

Where η_0 is the viscosity at ambient pressure and α the pressure viscosity coefficient. The Barus relation over predicts viscosity at pressures approaching 1 GPa, a more representative relation was formulated by Roelands [96] which can be written in the form of Eq. (2.10) [106].

$$\eta_{\mathrm{Roelands}} = \eta_r \exp\left(\ln\left(\frac{\eta_0}{\eta_r}\right)\left(1+\frac{p}{p_r}\right)^z\right) \tag{2.10}$$

In Eq. (2.10) η_r is the Roelands reference viscosity, p_r is the Roelands reference pressure, and Z the piezoviscous index. Houpert [107] extended this to include temperature dependency on the lubricant viscosity in EHL. Bair [108] demonstrated that the Roelands relation under predicts viscosity at high pressure and instead suggested an equation based on free volume theory and glass transition temperatures [109].

2.4.5 Non-Newtonian Behaviour

Johnson and Tevaarwerk [95] demonstrated that lubricants in elastohydrodynamic contacts do not exhibit Newtonian behaviour and that the shear stress in over predicted by the Newtonian model. The Ree-Eyring model (Eq. (2.11)) was instead proposed and includes a non-linear stress-strain relationship for shear-

thinning behaviour, with $\dot{\gamma}$ the shear rate, τ the shear stress, τ_0 the Eyring stress, $\dot{\tau}$ the rate of shear stress, and η_{Eyring} the non-Newtonian viscosity.

$$\dot{\gamma} = \frac{\dot{\tau}}{G} + \frac{\tau_0}{\eta_{\mathrm{Eyring}}} \sinh\left(\frac{\tau}{\tau_0}\right) \tag{2.11}$$

Contry [94] used these findings to develop a Reynolds equation that replaced the viscosity with an effective viscosity which was calculated by averaging over the film thickness. In Eq. (2.11) the shear rate is written as the sum of elastic shear strain rate and viscous shear strain rate, however Bair, et al. [110] showed that time-dependency in the viscous response in an EHL contact is unlikely and the term is therefore dropped. The non-Newtonian (shear-thinning) viscosity for an EHL contact is then expressed by Eq. (2.12).

$$\eta_{\mathrm{Eyring}} = \frac{\tau_0}{\dot{\gamma}} \sinh^{-1}\left(\frac{\eta_0 \dot{\gamma}}{\tau_0}\right) \tag{2.12}$$

To compound the non-Newtonian behaviour with the pressure dependency of lubricant viscosity, the viscosity can be written as a function of pressure and shear-rate by Eq. (2.13) [19].

$$\eta(p, \dot{\gamma}) = \frac{\tau_0}{\dot{\gamma}} \sinh^{-1}\left(\frac{\eta_{\mathrm{Roelands}} \dot{\gamma}}{\tau_0}\right) \tag{2.13}$$

2.4.6 Compressibility

Compressibility in lubricants is considered barotropic whereby the temperature effect on density is neglected in favour of the strong pressure dependency. A commonly used equation used to describe the variation of density with pressure was formulated by Dowson and Higginson [43] (Eq. (2.14)), where ρ_0 is the density at ambient pressure.

$$\rho = \rho_0 \frac{0.59 \times 10^9 + 1.34p}{0.59 \times 10^9 + p} \tag{2.14}$$

2.5 Numerical Methods

The first numerical solutions to the elastohydrodynamic problem were presented by Hamrock and Dowson [44], [45], [46] using an inverse method based on a Gauss-Seidel iteration scheme. The results of these simulations were used to create their renowned minimum and central film thickness equations which are still widely used as bearing design tools to date. A number of authors developed this method to extend the range of operating conditions and load carrying capacity (Chittenden, et al. [111], [112], Evans and Snidle [113], [114]) and Okamura [115] used the Newton-Raphson method to improve the computing speed and rate of convergence.

Lubrecht [47], [48], [116] introduced multigrid techniques which accelerated the computational process. Venner [49], [117], [118], [119] developed a distributive relaxation scheme and distributive line-relaxation scheme allowing the EHL problem to be solved for high loads. Venner also adapted the multigrid EHL solvers to include the multi-integration method developed by Brandt and Lubrecht [120]. Evans and Hughes [121] and Holmes, et al. [122], [123], [124] used the differential deflection method to perform calculation of the elastic deformation based on a half-space approach, this led to a significant increase in efficiency and stability allowing the solution of heavy loads, transient problems, 3D roughness, and mixed lubrication problems.

More recently Habchi, et al. [125], [126] replaced the half-space approach for calculating elastic deformation in the film thickness equation with a full-body elasticity and derived the entire EHL formulation into a single system that is solved by an iterative loop. This is known as the full system approach and has indicated efficiency in dealing with high loads, thermal transport, and complex rheology (Habchi, et al. [127], [128], [129]). Recently work is ongoing to include the Navier-Stokes equations using this method, the current architecture only facilitates for the application of Reynolds equation.

CFD methods have been used by a number of authors to solve the EHL problem using the Navier-Stokes equations (Hartinger, et al. [19], Almqvist, et al. [20]). So far only relatively low load cases have been investigated and the large separation in scales

between topography and the bearing domain limits these methods to smooth surfaces. Homogenisation approaches such as Sahlin, et al. [82], [26] and de Kraker, et al. [24], [25] have been used in favour of the deterministic CFD approach. Gao and Hewson [30] and de Boer, et al. [3], [5] used CFD via a homogenisation approach to include the effect of roughness in the global bearing domain, for more details on the modelling of surface roughness in EHL see section 2.3.

2.6 Summary

In this chapter a history of EHL was presented along with a literature review of the past and present research into the effect of surface roughness in EHL contacts. An outline of the governing equations of the smooth surface model was given highlighting the Reynolds equation, Hertzian contact mechanics, thermal transport and lubricant rheology. A description of the literature relating to the numerical methods used in modelling EHL was presented.

Chapter 3 – Review of Response Surface Methodology

3.1 Introduction

This chapter explores Response Surface Methodology (RSM) by introducing the fundamental aspects and research into these methods. RSM is used to represent a set of data through an approximation, in the context of this work it is used to describe a relationship which couples the two scales investigated in an EHL simulation. A discussion of the various approximation techniques is given and subsequently how these models are validated. The importance of a Design of Experiments (DoE) for effective metamodel building is highlighted and the methods used to formulate this are expanded.

3.1.1 Definition of RSM

RSM refers to the process of model building and evaluation which leads to an approximation that predicts an unknown response using data obtained from previous experiments. This is also known as metamodelling or surrogate modelling (Box and Draper [130]), but will be referred to as RSM throughout the remainder of this work. RSM is a well-established means of reducing the effort required to predict responses over many variables and wide ranges, as well as smoothing numerical noise.

3.2 Design of Experiments

Design of Experiments (DoE) is the name given to the choice of techniques used for selecting experiments within a certain design space. The choice of DoE is fundamental to the accuracy of the response surface over the range of the input variables, where the aim is to efficiently fill the entire design space. Efficient space-filling is necessary to reduce the expense of performing each experiment (Keane and Nair [131]). The experiments refer to a series of tests for which input variables are changed according to a given rule over a known range in order to investigate changes in the output response.

In order to create a DoE it is necessary to select design variables, these are also referred to as factors or parameters. The range of variability for each design variable is determined and this defines the design space, or region of interest, for the response. The

term levels refers to the number of different values a parameter can hold according its discretisation. The objective function and set of experiments are known as the response variable and sample space respectively (Cavazzuti [11]).

3.2.1 Full Factorial Design

The most common and intuitive strategy for creating a DoE is the full factorial design, where the samples are given by every possible combination of the factor values on each level. Letting k denote the number of factors and L the number of levels per factor the total sample size N for the general full factorial case is given by Eq. (3.1).

$$N = \prod_{i=1}^{i=k} L_i \tag{3.1}$$

Full factorial designs make efficient use of the sample data and enable the main and interaction effects of the factors to be identified. However as the number of design variables increases the sample size grows exponentially making them less applicable for large problems and other methods have been proposed (Box, et al. [132]).

An n^k full factorial design has n levels for each of the k design variables. Fig 3.1 illustrates the full factorial designs of $2^2, 2^3$, and 3^3. When implementing each of these DoEs the number of experiments matches the sum of polynomial terms in a two-dimensional quadratic, three-dimensional quadratic, and three-dimensional cubic function respectively. This demonstrates the use of full-factorial designs for performing polynomial regression.

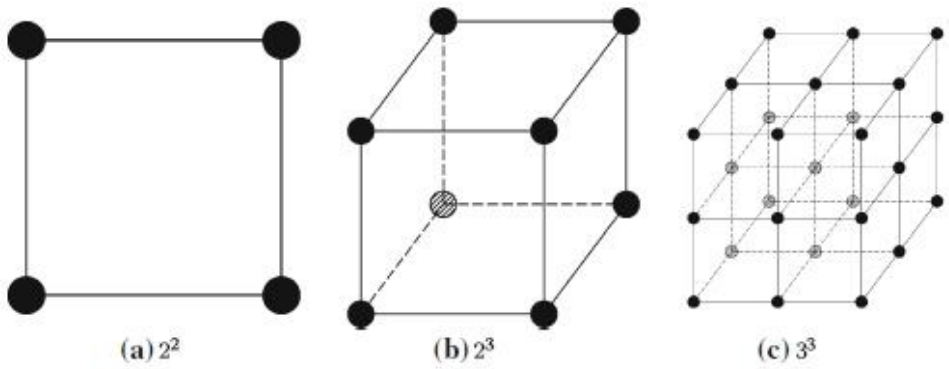

Fig 3.1 – Simple full factorial designs (Cavazzuti [11])

3.2.2 Fractional Factorial Design

The idea of a fractional factorial design is to only run a subset of the full factorial experiments such that the main and interaction effects of the response can still be identified. The size of the fractional design can be one-half, one-quarter, etc. of the full factorial one. The fractional samples must be selected particularly such that they are both balanced and orthogonal, in this sense balanced means that the sample space is created such that the factors have the same number of samples in each level. A wide list of the most common fractional designs can be found in the literature (see Montgomery [133]), it is of note that some fractional factorial designs are equivalent to Latin Square designs described later.

An example of fractional factorial design is given in fig. 3.2 below.

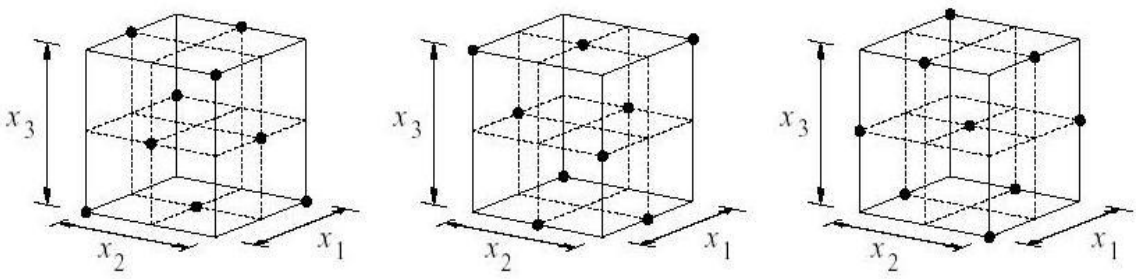

Fig. 3.2 – Three one-third fractions of the 3^3 factorial design (Box and Draper [12])

3.2.3 Central Composite Design

A Central Composite Design (CCD) is a 2^k full factorial design upon which central and star points are added. Star points refer to sample points in which all parameters but one are set to the mean level, and the remaining parameter is given in terms of the distance from the central point. The distance from the central point to the star points can be chosen in different ways (Koch, et al. [134]):

- Centre Composite Circumscribed (CCC), all the samples are placed on a hypersphere centred at the central point.
- Centre Composite Faced (CCF), the value of the parameter remains on the same levels as the 2^k full factorial design.

- Central Composite Inscribed (CCI), same as CCC but the specific limits of each level cannot be violated, a CCC design scaled so that all points have the same distance from the central point.
- Centre Composite Scaled (CCS), applied different distances depending on whether the point is inside the design space or hypersphere.

With k parameters, 2k star points and one central point are added to the 2^k full factorial design such that the total sample size is $2^k + 2k + 1$.

Fig. 3.3 illustrates some graphical examples of central composite designs of experiments.

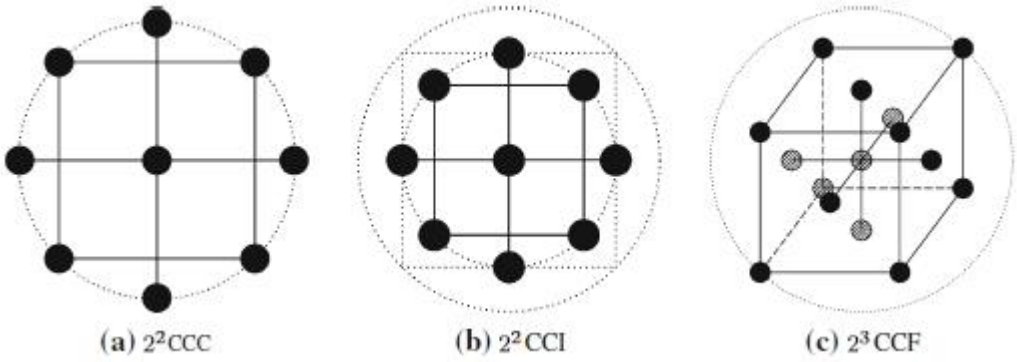

Fig. 3.3 – Examples of central composite design (Cavazzuti [11])

3.2.4 Box-Behnken Design

Box and Behnken [135] developed incomplete three-level factorial designs which are built by combining two-level factorial designs with incomplete block designs in a particular manner. Box-Behnken Designs (BBDs) were introduced in order to limit the sample size as the number of parameters increases (Massart [136]). The sample size is limited to a value which permits the evaluation of second order least squares polynomial coefficients. In this method a block of samples corresponding to a two-level factorial design is repeated over different sets of the parameters, parameters not included in the two-level design remain at the mean level throughout the block. The type and size of factorial design, and the number of blocks evaluated depend on the number of parameters investigated and are chosen so that the design meets the criterion of rotatability. An experimental design has rotatbility if the variance in the predicted response at any point is a function of the distance from the central point alone [135].

No general rule exists for defining BBD and so the reader is refered to Box and Behnken [135] for tables listing the various possibilities. BBD are similar to the CCC and CCI designs as all samples have the same distance from the central point. And as such the vertices of the design space lie far from the Box-Benken samples and any response surface built from this type of design may be inaccurate near these regions. The same property also exists for CCI designs. An example of a BBD for 3 design variables is given in fig. 3.4 below.

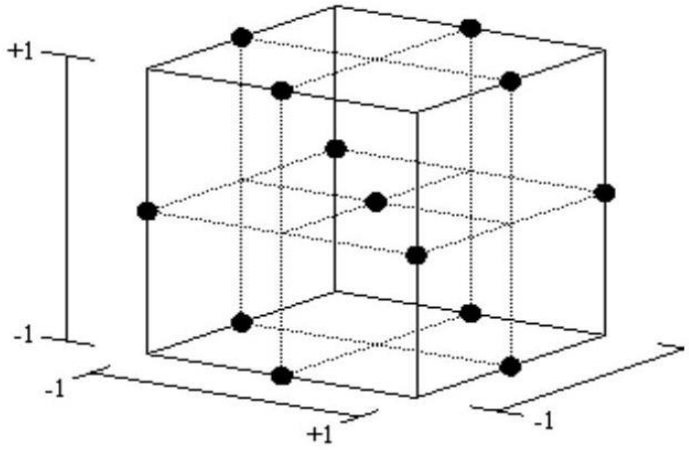

Fig. 3.4 – Box-Behnken design for 3 design variables (Box and Draper [12])

3.2.5 Other Level-Based Designs

Plackett and Burman [137] created a factorial based design in which the sample size must be multiples of 4 up to 36 and the number of factors k can be up to $N - 1$ (the number of samples minus one). Placket-Burman designs are mainly useful for screening the interaction effects of the response over the design space.

Taguchi design [138] is a method developed for quality control which seeks the best values possible for controllable factors whilst reducing the sensitivity to uncontrollable factors. Taguchi design is a mix of fractional factorial and orthogonal designs, control variables are distinguished from noise variables the former of which can be varied. The two sets of variables form outer (control) and inner (noise) orthogonal designs. These are combined such that for each sample of the inner array the full set of experiments of the outer array is performed. This forms the crossed array which allows the interaction between control and noise variables to be deduced.

3.2.6 Space-Filling Designs

So far the designs discussed have their derivations from statistics and rely upon level-based discretisation to uniformly fill the design space. Space-filling designs do not need discretised parameters and the sample size is chosen by the user rather than given by the number of parameters in the problem. Space-filling designs are favoured when creating response surfaces since the likelihood of a region within the design space being far from a sample is significantly reduced (McKay, et al. [139]). However, space-filling designs do not allow the main and interaction effects between parameters to be as easily investigated as with level-based factorial designs (Sacks, et al. [140]).

The most inherent space-filling design is the random one by which the design space is filled with uniformly distributed random samples. The random DoE is however flawed since there is no guarantee that large clusters of samples will be close together, leaving gaps in other regions and overall failing to fill the entire design space.

3.2.7 Latin Hypercube

A Latin Hypercube (LHC) DoE divides the design space into an orthogonal grid with N elements per k parameters. Within the multi-dimensional grid N sub-volumes are created such that along each row and column only one is chosen. It is imperative that the sub-volumes are chosen such that there are no spurious relations between dimensions and that the samples are spread over the design space, if this condition of correlation reduction is not met then the LHC would leave most of the design space unexplored (Olsson, et al [141]). An example of correlation reduction of an LHC for $k = 2, N = 10$ is given in fig. 3.5.

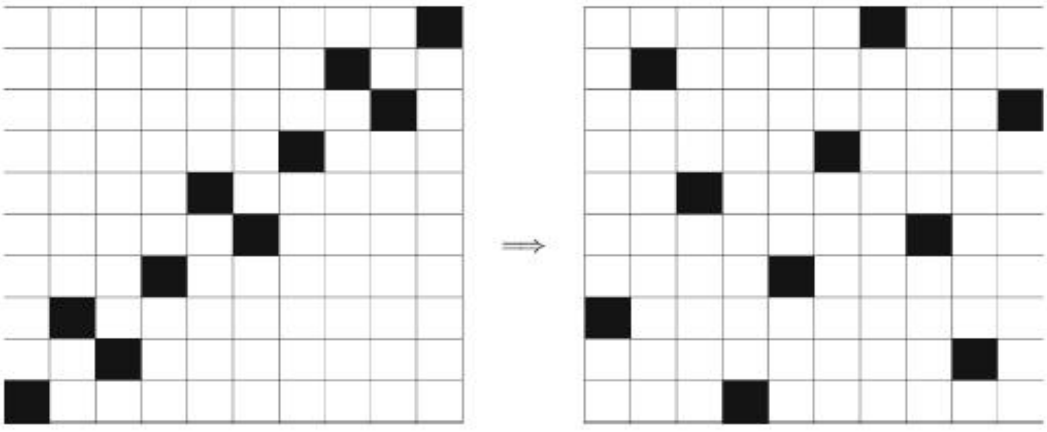

Fig. 3.5 – Correlation reduction of an LHC for $k = 2, N = 10$ (Cavazzuti [11])

3.2.8 Optimum Latin Hypercube

Optimal Latin Hypercube (OLHC) design attempts to fill the design space with the fewest number of designs possible this is very useful if the experiment evaluations are expensive. Two methods which have been derived to produce an optimised LHC are the Morris-Mitchell and Audze-Eglais optimality criterions.

Morris and Mitchell [142] used a series of randomly formed LHC to create an OLHC based on a criterion that maximises the minimum distances between the points $r_{p,q}$, mathematically this is written using Eq. (3.2).

$$\max\left(\min\left(r_{p,q}: 1 \leq p \neq q \leq N\right)\right) \tag{3.2}$$

Alternatively, the Audze-Eglais optimality criterion distributes the points $r_{p,q}$ by minimising the reciprocal of the squared distances between all points. The physical analogy for this is that by letting the points be considered unit masses then they will exert repulsive forces upon each other, meaning that the system of points has potential energy. The system of points will reach equilibrium when the potential energy of the repulsive forces is at a minimum. The repulsive forces are inversely proportional to the squared distance between points, leading to Eq. (3.3).

$$\min\left(\sum_{p=1}^{p=N}\sum_{q=p+1}^{q=N}\frac{1}{r_{p,q}^2}\right) \tag{3.3}$$

Bates, et al. [92] and Toropov, et al. [93] achieved OLHC design using the Audze-Eglais optimality criterion by implementing a permutation genetic algorithm. The genetic algorithm solves for the best design by generational design, with the best designs inherited and the worst neglected. Mutation of random designs ensures that a global optimum is achieved.

Fig. 3.6 shows DoE's created for various sample sizes using the two optimality criterions with $k = 2$.

N	Morris-Mitchell	Audze-Eglais
20	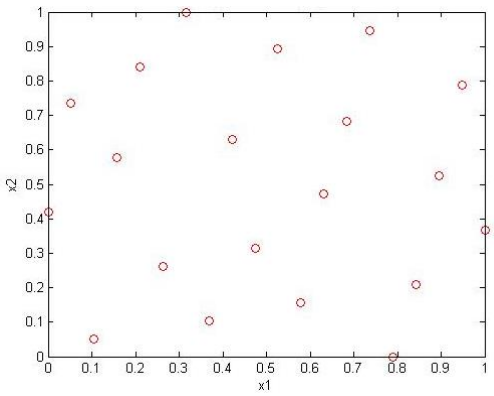	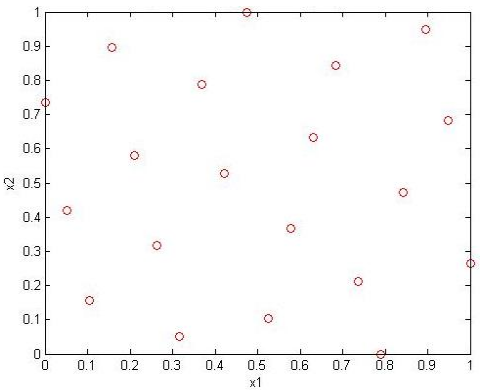
50	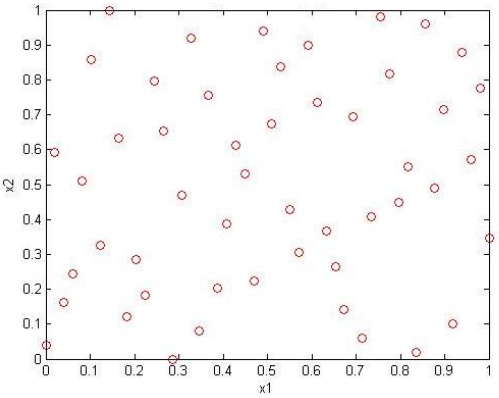	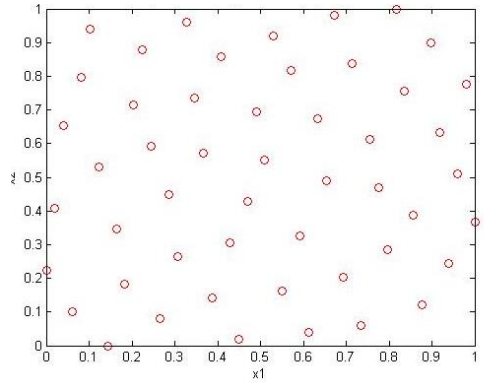
100	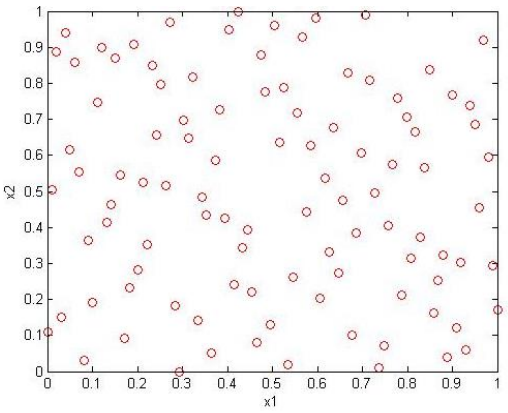	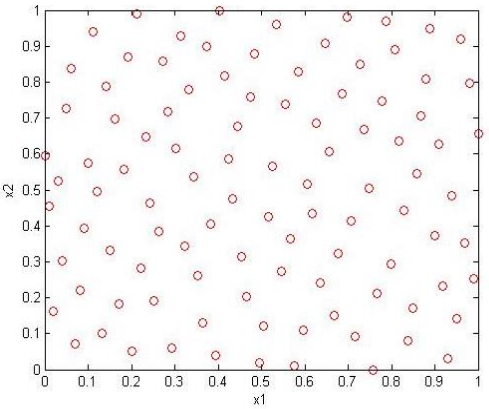

Fig. 3.6 – Morris-Mitchell and Audze-Eglais OLHCs for k = 2

3.2.9 Other Space-Filling Designs

Hammersley sampling is a statistical means of producing a space-filling DoE using low-discrepancy sequences (Simpson, et al. [143]). A LHC allows uniformity along one direction and has random placement up to the k^{th} dimension, whereas Hammersley sampling allows uniformity for all N points in a k-dimesnional hypercube

(Kalagnanam and Diwekar [144]). Low-discrepancy implies a uniform distribution of points in space.

Low-discrepancy sequences such as the van der Corput sequence [145] which appear in Hammersley sampling have also been utilised by other authors to produce space-filling DoEs. These methods are based on pseudo-random number generators, whereby checks are performed on the quality of the random number generation. Examples include the Halton sequence [146], Faure sequence [147], [148], and the Sobol sequence [149].

Uniform designs were introduced by Fang [150] and later refined by Fang and Wang [151], these provide uniformly spaced scatter designs of points and are a derivative of fractional factorial designs with the added property of uniformity. They are similar to LHC for one-dimensional DoEs but vary significantly for higher-dimensions, a review of uniform design theory can be found in Fang, et al. [152].

3.3 Model Building

The aim of the RSM is to approximate a response variable with respect to the corresponding design variables over the entire design space which it encompasses. RSM is directly related to the DoE such that the experiments selected will determine the response generated. The use of response surfaces is advantageous because it is inexpensive to compute in comparison to running the corresponding experiments. And in general RSM techniques assist with the smoothing of numerical noise.

Mathematically any response variable y can be written as a function of the design variables $\mathbf{x}$ such that $y = f(\mathbf{x})$. The RSM approximation $\hat{y}$ can be interpolated to any position in the design space $\hat{\mathbf{x}}$ through the response surface equivalent function $\tilde{f}$ using the DoE data. The response surface may also require tuning parameters θ to be selected to reduce the error in the approximation, leading to Eq. (3.4) as the general equation of an RSM predictor.

$$y = f(\mathbf{x}) \Rightarrow \hat{y} = \tilde{f}(\hat{\mathbf{x}}, \mathbf{x}, y, \theta) \tag{3.4}$$

The concept of RSM was introduced by Box and Wilson [153] who were the first to suggest using a first-order polynomial model for approximating response variables. Since this date many RSM techniques have been developed and the most prominent are outlined in this section.

3.3.1 Least Squares Method

The Least Squares (LS) method is a solution process for solving an over-determined system of equations and can be interpreted as a method for data fitting. Gauss developed the method in 1795 but the work was not published until a few years later (Gauss [154]).

LS involves fitting a polynomial to a data set obtained from a DoE such that the coefficients are tuned to the data set. For example a linear regression would take the form of Eq. (3.5).

$$\tilde{f}_i = \beta_0 + \sum_{j=1}^{j=k} x_{i,j}\beta_j \quad , \quad i = 1, \dots, N \tag{3.5}$$

Where β are the polynomial coefficients which the system of equation must be solved for, k is the number of parameters, and N the number of DoE points. The LS method solves for the best fit of the data set by minimising the sum of squared residuals S at the DoE points. The residual errors are the difference between the experimental responses and the value predicted by the LS regression at the same positions in the design space, leading to Eq. (3.6)

$$S = \sum_{i=1}^{i=N} \left(f_i - \beta_0 - \sum_{j=1}^{j=k} x_{i,j}\beta_j \right)^2 \tag{3.6}$$

In order to minimise S, Eq. (3.6) is differentiated with respect to each of its components and set equal to zero giving Eqs. (3.7) and (3.8).

$$\frac{\partial S}{\partial \beta_0} = -2 \sum_{i=1}^{i=N} \left(f_i - \beta_0 - \sum_{j=1}^{j=k} x_{i,j} \beta_j \right) = 0 \tag{3.7}$$

$$\frac{\partial S}{\partial \beta_l} = -2 \sum_{i=1}^{i=N} \left(f_i - \beta_0 - \sum_{j=1}^{j=k} x_{i,j} \beta_j \right) x_{i,l} = 0 \quad , \quad l = 1, \dots, k \tag{3.8}$$

Letting $\mathbf{X}$ be the matrix of DoE points, $\mathbf{y}$ the vector of response variables and $\boldsymbol{\beta}$ the vector of polynomial coefficients, Eqs. (3.7) and (3.8) can be rewritten to form Eq. (3.9).

$$\frac{\partial S}{\partial \boldsymbol{\beta}} = -2(\mathbf{X}^{\mathrm{T}} \times \mathbf{y}) + 2(\mathbf{X}^{\mathrm{T}} \times \mathbf{X}) \times \boldsymbol{\beta} = 0 \tag{3.9}$$

Which solving for $\boldsymbol{\beta}$ yields Eq. (3.10).

$$\boldsymbol{\beta} = (\mathbf{X}^{\mathrm{T}} \times \mathbf{X})^{-1} \times (\mathbf{X}^{\mathrm{T}} \times \mathbf{y}) \tag{3.10}$$

The approximation function then reads as Eq. (3.11) for the vector of response surface approximations $\hat{\mathbf{y}}$ at the interpolation locations $\hat{\mathbf{X}}$.

$$\hat{\mathbf{y}} = \hat{\mathbf{X}} \times \boldsymbol{\beta} \tag{3.11}$$

The LS method forms a closed solution and is advantageous because of the fast computing speed, the matrix inversion operation only has to be performed once and the coefficients are then known throughout the design space. However the models tend not to be very accurate and are best for interpreting the main trends in the response variable, weighted versions of the LS method have been derived to tune the response to closer fit the DoE data.

3.3.2 Moving Least Squares Method

Moving Least Squares (MLS) is a form of weighted LS where the weights are functions of the Euclidian distance between the sample points and where the response surface is assessed. The weight associated with each sample location decays as the evaluation location moves away from it, according to a decay type response. The method was developed by a number of authors including McLain [155], Gordon and Wixom [156], Barnhill [157], and Lancaster [158] using the weighted metric of Shepard [159]. However the formulation presented by Lancaster and Salkauskas [160] is commonly noted as the first full derivation of the method now referred to MLS.

The first step of the MLS method is to define an estimate $\hat{y}$ at an arbitrary location in the design space based on the values at a series of sample locations f_i.

$$\hat{y} = \sum_{i=1}^{i=N} w_i(r_i) f_i \tag{3.12}$$

In Eq. (3.12) the weights w_i are functions of the Euclidian norm $r_i = \|x - x_i\|$ between the sample locations x_i and the assessment location x.

It is possible to control the closeness of fit of the MLS approximation by altering a parameter in the weight decay function. The closeness of fit parameter θ (see Eqs. (3.13) – (3.17)) enables the control of the rate of decay which the weight function produces, or in another sense the radius beyond which a sample point has no influence on the resulting approximation. This feature allows MLS approximations to handle numerical noise in the response variable and produce a smooth function over the design space. A popular choice for the weight function is Gaussian decay as described by Eq. (3.13).

$$w_i = \exp(-\theta r_i^2) \tag{3.13}$$

The closeness of fit can vary between zero (LS regression) and any value until over-fitting occurs (where the response fits so closely to the sample data that no

interpolation takes place between the sample locations (Myers, et al. [161])). Other weight decay functions include cubic, fourth, fifth, and seventh order polynomials as described by Eqs. (3.14), (3.15), (3.16), and (3.17) respectively.

$$w_i = 1 - 3\rho_i^2 + 2\rho_i^3 \tag{3.14}$$

$$w_i = 1 - 6\rho_i^2 + 8\rho_i^3 - 3\rho_i^4 \tag{3.15}$$

$$w_i = 1 - 10\rho_i^3 + 15\rho_i^4 - 6\rho_i^5 \tag{3.16}$$

$$w_i = 1 - 35\rho_i^4 + 84\rho_i^5 - 70\rho_i^6 + 20\rho_i^7 \tag{3.17}$$

Where $\rho_i = r_i/R_{max}$, R_{max} is the normalised radius of the sphere of influence and ρ_i is limited to an upper bound of unity. R_{max} inversely relates to the closeness of fit parameter θ where a lower value indicates a closer fit. The effect of tuning the closeness of fit parameter to the data set can be seen in fig. 3.7 where the image on the right-hand-side is a more accurate representation of the surface.

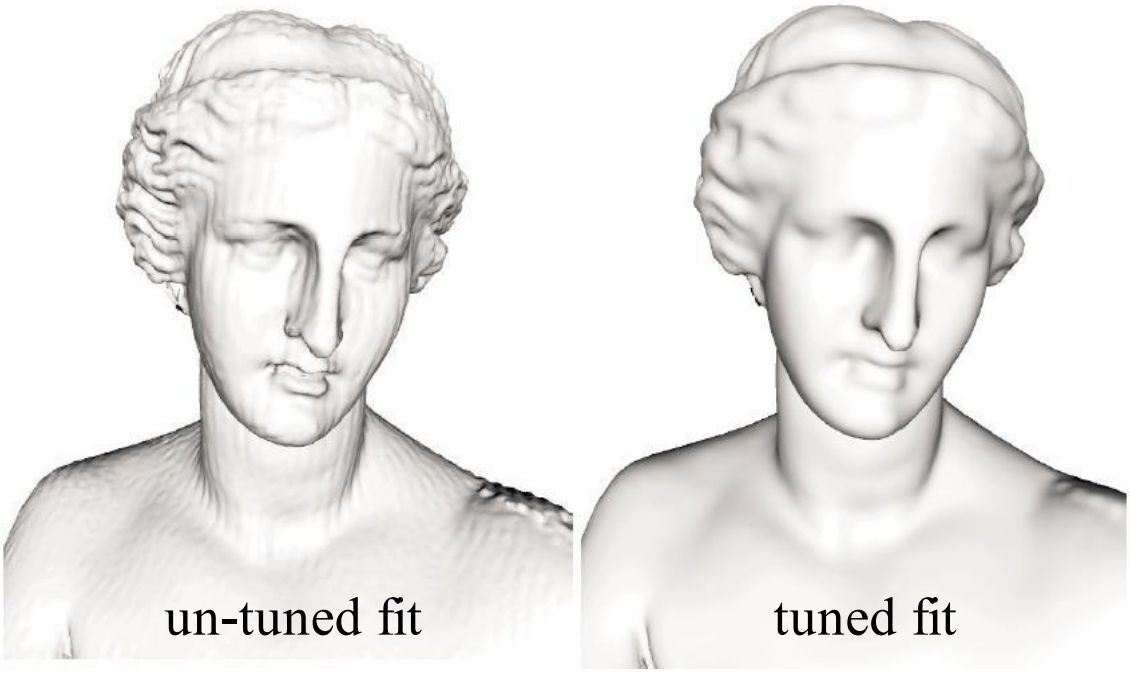

Fig. 3.7 – Visualisation of the effect of tuning a MLS metamodel (Alexa, et al. [13])

The MLS method is conducted by selecting a basis function, for example using the linear regression fit of Eq. (3.5) the sum of squared residuals becomes Eq. (3.18) which is inclusive of the weights associated with each sample location.

$$S = \sum_{i=1}^{i=N} w_i \left(f_i - \beta_0 - \sum_{j=1}^{j=k} x_{i,j} \beta_j \right)^2 \tag{3.18}$$

Differentiating Eq. (3.18) with respect to each of the design variables and setting equal to zero solves for the minimum squared error between the approximation and sample values, this yields Eqs. (3.19) and (3.20).

$$\frac{\partial S}{\partial \beta_0} = -2 \sum_{i=1}^{i=N} w_i \left(f_i - \beta_0 - \sum_{j=1}^{j=k} x_{i,j} \beta_j \right) = 0 \tag{3.19}$$

$$\frac{\partial S}{\partial \beta_l} = -2 \sum_{i=1}^{i=N} w_i \left(f_i - \beta_0 - \sum_{j=1}^{j=k} x_{i,j} \beta_j \right) x_{i,l} = 0 \quad , \quad l = 1, \dots, k \tag{3.20}$$

Using the same rationale as applied to the derivation of Eq. (3.9), Eqs. (3.19) and (3.20) can be written as Eq. (3.21), where $\mathbf{W}$ is the matrix of weights between the assessment and sample locations.

$$\frac{\partial S}{\partial \boldsymbol{\beta}} = -2\left(\mathbf{X}^T \times (\mathbf{W} \times \mathbf{y})\right) + 2\left(\mathbf{X}^T \times (\mathbf{W} \times \mathbf{X})\right) \times \boldsymbol{\beta} = 0 \tag{3.21}$$

Solving for the location specific coefficients $\boldsymbol{\beta}$ gives Eq. (3.22).

$$\boldsymbol{\beta} = \left(\mathbf{X}^T \times (\mathbf{W} \times \mathbf{X})\right)^{-1} \left(\mathbf{X}^T \times (\mathbf{W} \times \mathbf{y})\right) \tag{3.22}$$

Once the weights are computed from Eq. (3.22) the operation of (3.11) can be used to assess the MLS approximation $\hat{\mathbf{y}}$ at the interpolation points $\hat{\mathbf{X}}$. The difference between the LS operation and this is that the weights used to determine $\boldsymbol{\beta}$ change with the interpolation points and so no analytic form of the approximation exists. Fig. 3.8 illustrates the difference in interpolation between the LS and MLS methods for a one-dimensional numerical function.

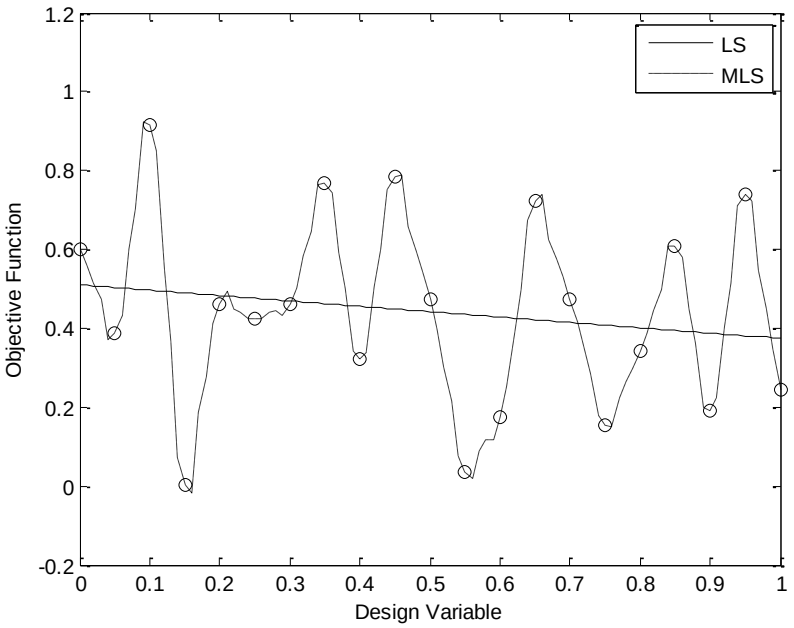

Fig 3.8 – LS and MLS data fitting of a numerical function in one-dimension

Currently there is much research involving the MLS method for various applications including investigating the dependency of variables in a given response (Coelho [162]), developing meshless methods (Salehi and Dehghan [163], [164]), using derivative information to analyse the sensitivity of the response (Mirzaei, et al. [165]), and for solving optimisation problems (Loweth, et al. [90], Song and Lee [166], [167], Choi, et al. [168]).

de Boer, et al. [3] used MLS response surfaces to couple two scales of a simulation where the information provided at one scale was modelled independently at the other. Later in de Boer, et al. [5] this method was extended to perform optimisation of the features at one scale based on the information provided at the other. The use of MLS ensured accuracy in capturing the non-linear response generated and how the response function varied from the trend without the separation of scales associated with the problem.

3.3.3 Radial Basis Functions

Radial Basis Functions (RBFs) were introduced by Hardy [169] in 1971, the RBF uses a linear combination of radially symmetric functions based on the Euclidian distance between data points to build an approximation. An RBF takes the form of Eq. (3.23), where ψ are the basis functions and w the corresponding weights.

$$\hat{f} = \sum_{i=1}^{i=N} w_i \psi(r_i) \tag{3.23}$$

The solution to the RBF function is obtained by estimating the w_i, this is achieved by letting the basis function centres coincide with the actual data points forming a square matrix from which the inverse can be found. The beauty of the RBF function is that Eq. (3.23) is linear with respect to the function weights but the estimator $\hat{f}$ can express highly non-linear responses.

The choice of basis function will have an important effect on the accuracy of the RBF, common choices of basis functions include linear, cubic, thin plate spline, Gaussian, multiquadratic, and inverse multiquadratic which are expressed by Eqs. (3.24) – (3.29) respectively. Where σ^2 is the variance in the observed values.

$$\psi(r_i) = r_i \tag{3.24}$$

$$\psi(r_i) = r_i^3 \tag{3.25}$$

$$\psi(r_i) = r_i^2 \ln(r_i) \tag{3.26}$$

$$\psi(r_i) = \exp(-r_i^2/2\sigma^2) \tag{3.27}$$

$$\psi(r_i) = (r_i^2 + \sigma^2)^{\frac{1}{2}} \tag{3.28}$$

$$\psi(r_i) = (r_i^2 + \sigma^2)^{-\frac{1}{2}} \tag{3.29}$$

RBFs have been shown to produce good approximations for both smooth and noisy data (Forrester, et al. [170]) and also an array of deterministic and stochastic response functions (Powell [171]). Gaussian and inverse multiquadratic basis functions are favoured because they tend to produce a symmetric positive matrix (Vapnik [172]), ensuring this and a well-spread distribution of function centres will lead to accurate computation of the weights (Michelli [173]).

3.3.4 Kriging

Krige [174] developed a method for approximating response variables in application to mathematical statistics on ore mining, this method was later referred to as Kriging (Matheron [175]) and first applied to computer experiments by Sacks, et al [140]. Kriging is similar to an RBF where the basis function takes the form of Eq. (3.30).

$$\psi^{(i)} = \exp\left(-\sum_{j=1}^{j=k} \theta_j \left| x_j^{(i)} - x_j \right|^{p_j} \right) \tag{3.30}$$

Eq. (3.30) is similar to the Gaussian type basis function (Eq. (3.27)) where instead of varying with $1/\sigma^2$ the Kriging basis has a vector $\boldsymbol{\theta}$ where the elements θ_j can vary allowing the width of the function to vary from variable to variable. The Gaussian basis vector has an exponent exclusively of 2 whereas in the Kriging basis the exponents $\mathbf{p}$ are allowed to vary for each dimension of $\mathbf{x}$. Typically $\theta_j \in [10^{-3}, 10^2]$ and $p_j \in [1,2]$.

In order to build the Kriging model we must view the observed responses as if they are obtained from a stochastic process by denoting a set of random vectors $\mathbf{Y}$. The random field has a mean of $\mathbf{1}\mu$ and the random variables are correlated with each other using the basis function expression (Eq. (3.31)).

$$\mathrm{cor}\left[\mathrm{Y}\left(\mathbf{x}^{(i)}\right),\mathrm{Y}\left(\mathbf{x}^{(l)}\right)\right]=\exp\left(-\sum_{j=1}^{j=k}\theta_j\left|x_j^{(i)}-x_j^{(l)}\right|^{p_j}\right) \tag{3.31}$$

The values of $\boldsymbol{\theta}$ and $\mathbf{p}$ are estimated by maximizing the ln-likelihood of $\mathbf{y}$, the ln-likelihood $\ln(\mathrm{L})$ of the sample data is expressed by Eq. (3.32).

$$\ln(\mathrm{L})=-\frac{\mathrm{N}}{2}\ln(2\pi)-\frac{\mathrm{N}}{2}\ln(\sigma^2)-\frac{1}{2}\ln|\boldsymbol{\psi}|-\frac{(\mathbf{y}-\mathbf{1}\mu)^{\mathrm{T}}\boldsymbol{\psi}^{-1}(\mathbf{y}-\mathbf{1}\mu)}{2\sigma^2} \tag{3.32}$$

Where $\boldsymbol{\psi}$ is the correlation matrix of observed data, obtained through Eq. (3.31). The maximum ln-likelihood is subsequently found by taking derivatives of Eq. (3.32) and setting equal to zero, giving Eqs. (3.33) and (3.34) for the maximum likelihood estimates of the mean $\hat{\mu}$ and variance $\hat{\sigma}^2$.

$$\hat{\mu}=\frac{\mathbf{1}^{\mathrm{T}}\boldsymbol{\psi}^{-1}\mathbf{y}}{\mathbf{1}^{\mathrm{T}}\boldsymbol{\psi}^{-1}\mathbf{1}} \tag{3.33}$$

$$\hat{\sigma}^2=\frac{(\mathbf{y}-\mathbf{1}\mu)^{\mathrm{T}}\boldsymbol{\psi}^{-1}(\mathbf{y}-\mathbf{1}\mu)}{\mathrm{N}} \tag{3.34}$$

Substituting $\hat{\mu}$ and $\hat{\sigma}^2$ back into Eq. (3.32) and removing constant terms gives the concentrated ln-likelihood function Eq. (3.35).

$$\ln(\mathrm{L})\approx-\frac{\mathrm{N}}{2}\ln(\hat{\sigma}^2)-\frac{1}{2}\ln|\boldsymbol{\psi}| \tag{3.35}$$

The value of Eq. (3.35) depends upon the values of the unknown parameters $\boldsymbol{\theta}$ and $\mathbf{p}$ which need to be chosen to maximise the function. It is not possible to differentiate the function and so the function is optimised instead. The evaluation of the concentrated ln-likelihood is inexpensive and so a global search optimisation using a genetic algorithm or simulated annealing are proposed (Forrester, et al. [170]). The

complexity of using a Kriging model lies with the model building because optimisation is needed to setup the values of $\boldsymbol{\theta}$ and $\mathbf{p}$, while the implementation and numerical assessment after these parameters are known is computationally inexpensive (Jia and Taflanidis [176]).

3.3.5 Support Vector Regression

Support Vector Regression (SVR) is an application of statistical learning theory for support vector machines developed by Vapnik and Lerner [177] and Vapnik and Chervonenkis [178] in Russia during the 1960's. The theory generalises the properties of learning machines which enables them to be applied to unseen data. The method was further developed and became applicable outside of learning machines, specifically to regression analysis (Vapnik [179], Schölkopf and Smola [180]).

The SVR method allows calculation of an error margin of the sample set ε which the user is willing to accept without affecting the SVR prediction. This can be of great use if the data is derived from a physical experiment or if numerical noise is expected in the response. The error margin forms what is referred to as the ε-tube about the predictor, sample points which lie inside the ε-tube are ignored and the predictor is defined purely by those which lie outside or on this region (the support vectors).

In general the SVR prediction is an extension of an RBF where the sum of basis functions $\psi^{(i)}$ and corresponding weights $w^{(i)}$ are added to a base term μ to form Eq. (3.36). However in SVR the calculation of the predictor is different to an RBF where the concern is with minimising the vector norm $|\mathbf{w}|^2$. This becomes a trade-off between the model complexity and margin of tolerable error, for more details see Smola and Schölkopf [181].

$$\hat{f} = \mu + \sum_{i=1}^{i=N} w^{(i)} \psi\left(\mathbf{x}, \mathbf{x}^{(i)}\right) \tag{3.36}$$

3.3.6 Multivariate Adaptive Regression Splines

Multivariate Adaptive Regression Splines (MARS) were introduced by Friedman [182] in 1991, in this method the basis functions are selected through a

forwards and backwards iterative approach. MARS can be seen as an extension of linear regression models which automatically captures non-linearity and interactions between variables. The major advantages to a MARS model are that they produce accurate results and there is a major reduction in computational cost associated with constructing the model. The MARS model can be written using Eq. (3.37) and solved by the algorithm of Chen [183].

$$\hat{f} = \sum_{m=1}^{m=M} a_m B_m(\mathbf{x}) \tag{3.37}$$

Where a_m are the coefficients of expansion, and B_m are the basis functions which are represented by Eq. (3.38).

$$B_m(\mathbf{x}) = \prod_{k=1}^{K_m} \left[s_{k,m}\left(x_{v(k,m)} - t_{k,m}\right) \right]_+^q \tag{3.38}$$

Where K_m are the number of factors in the m^{th} basis function, $s_{k,m} = \pm 1$, $x_{v(k,m)}$ is the v^{th} variable, $1 \leq v(k,m) \leq N$, and $t_{k,m}$ is a knot location on each of the corresponding variables. The subscript $+$ means that the function is a truncated power function of the form of Eq. (3.39).

$$\left[s_{k,m}\left(x_{v(k,m)} - t_{k,m}\right) \right]_+^q = \begin{cases} \left[s_{k,m}\left(x_{v(k,m)} - t_{k,m}\right) \right]^q & s_{k,m}\left(x_{v(k,m)} - t_{k,m}\right) > 0 \\ 0 & s_{k,m}\left(x_{v(k,m)} - t_{k,m}\right) \leq 0 \end{cases} \tag{3.39}$$

3.3.7 Artificial Neural Networks

Artificial Neural networks (ANN) have also been used to create response surfaces, this is because they have been shown to accurately reproduce a wide range of non-linear functions in a range of applications from metal-cutting to cancer diagnosis (Gosavi [184]). In an ANN the function is represented by a series of neurons at which

data processing is performed. Each neuron has k connected neurons with an associated weight w and a basis b, the sum of input signals gives the output v according to Eq. (3.40). See Desai, et al. [185] for more details.

$$v_k = \sum_{j=1}^{j=m} w_{k,j} x_j + b_k \tag{3.40}$$

3.4 Model Validation

In order to create an accurate response surface the approximation must be tuned or trained to the DoE data, and specifically with respect to Gaussian MLS metamodels the closeness of fit parameter must be chosen which best represent the observed values. The best value of the closeness of fit parameter can be found by assessing and subsequently minimising the error between the response surface prediction and the response variable at each of the observed locations. Two sets of training data are identified: (1) the building set which is used to build the approximation over a range of closeness of fits; (2) the validation set where the known observations can be compared with the response surface approximation created from (1). The choice of error assessment criteria and the method of selecting the building and validation sets are important factors to consider when performing a Cross Validation (CV) procedure, which is the name given to this type of process.

3.4.1 Error Assessment Criteria

There are various criteria which can be used in CV to assess the error between the response surface prediction and the observed values. These include: (1) the Root Mean Squared Error (RMSE); (2) the R^2 value; (3) the Relative Average Absolute Error (RAAE); and (4) the Relative Maximum Absolute Error (RMAE). As RMSE, RAAE, and RMAE tend toward zero the accuracy of the response surface increases, and for R^2 the value tends toward unity (Jin, et al. [186]).

The RMSE is calculated using Eq. (3.41), where n is the number of validation measurements being assessed, $\hat{y}_i$ are the response surface predicted values, and y_i the observed values.

$$\mathrm{RMSE} = \sqrt{\frac{1}{n}\sum_{i=1}^{i=n}(\hat{y}_i - y_i)^2} \tag{3.41}$$

The R^2 value is given by Eq. (3.42), where $\bar{y}$ is the mean of the observed values.

$$R^2 = 1 - \sum_{i=1}^{i=n}(\hat{y}_i - y_i)^2 \Big/ \sum_{i=1}^{i=n}(\hat{y}_i - \bar{y})^2 \tag{3.42}$$

Letting σ denote the standard deviation of the observed values, the RAAE is determined by Eq. (3.43).

$$\mathrm{RAAE} = \sum_{i=1}^{i=n}|\hat{y}_i - y_i| / n\sigma \tag{3.43}$$

The RMAE is described by Eq. (3.44), where $\mathbb{Z}_n^+$ is the set of positive integers up to and including n.

$$\mathrm{RMAE} = \max_{i\in\mathbb{Z}_n^+}|\hat{y}_i - y_i| / \sigma \tag{3.44}$$

The work by the author in Loweth, et al. [90] and also by Narayanan, et al. [91] demonstrated that using the different error assessment criteria can lead to very different choices of the closeness of fit parameters for any given data set. They also go on to select the RMSE as the most consistent choice of error measurement, a criteria which other authors have gone on to use as a result of their recommendations (Taflanidis, et al. [187], de Boer, et al. [3], [5]).

3.4.2 k-fold Cross Validation

k-fold CV is a method for tuning the closeness of fit parameter to a given data set by minimising the error between observed and predicted values. The method selects a random subset (fold) of size k from the DoE and calls this the validation set, the remaining points are deemed the building set and from which the approximation is subsequently generated. The error between the response surface predicted values and observed values are recorded and averaged over many randomly selected folds. The closeness of fit is varied and the value which produces the minimum averaged error is chosen as the optimal closeness of fit for the data set.

By removing points from the DoE and building the response surface without them bias is placed toward points which are used more often as measurements of the response surface error. Therefore the process of selecting the validation set, the size of the validation set, and the number of repeat validations are important factors to consider in order to reduce noise in the validation response. The method of random selection must ensure that over the number of repeat validations an even distribution of times each point is used to build and to validate is upheld. This implies that some tests to the random selection method should be conducted and that the number of repeat validations should be just enough to cover the use of each point in both the building and validation phases. The size of the fold can drastically change the performance of the response surface because if large regions of the design space are sparsely populated once the validation points are removed then the response surface prediction will be poor in these regions. The error between the response surface and observed value is likely to be smaller when most of the points are used for building, leading to the Leave-One-Out CV method be favoured as discussed in section 3.4.3. de Boer, et al. [3], [5] suggested using a validation set up to 30% of the total DoE size whereas Loweth, et al. [90] used folds of size 3, 5, and 7 (6%, 10%, and 14% of the DoE size respectively), both found good and consistent validation curves and were able to identify the optimal closeness of fit parameter.

3.4.2 Leave-One-Out Cross Validation

In Leave-One-Out Cross Validation (LOOCV) the size of the validation set (fold) is $k = 1$, the process therefore becomes an iterative one where each point in the DoE is removed in turn and the error between the response surface prediction and

observed value calculated and averaged over the number of DoE points. In a similar fashion to k-fold CV the closeness of fit is varied and the value which produces the minimum averaged error is selected as the optimum closeness of fit for the data set.

The LOOCV was shown by de Boer, et al. [5] to have a smooth response over a reasonable range of the closeness of fit parameter, this can be attributed to the lack of bias in the way that building and validation points are selected using the method. Each point in the DoE is used to validate the approximation once and used to build the approximation $N-1$ times. This implies that the validation response surfaces are likely to be stable as most of the DoE points are used to build them, reducing the number of regions in the design space where there are few experiments. Also the systematic way of choosing the validation points reduces the need for a random selection, subsequently leading to a noise-free validation curve and determination of the optimal closeness of fit (Goel and Stander [188]).

3.4.2 Nested Design of Experiments

A nested DoE creates two separate designs which independently form a space-filling DoEs over the design space and combined together still form a space-filling design. The validation set is chosen to be approximately $\frac{1}{3}$ of the size of the combined DoE, using the remaining $\frac{2}{3}$ to be used as building points. Because the building set forms a DoE on its own the resulting response surface should be a good representation of the observed values over the entire design space, meaning that the error assessment always produces a good judgement of the total approximation (Qian, et al. [189]). This avoids the issues associated with the k-fold and Leave-One-Out CV methods where the validating response surfaces are created from designs that do not represent the entire design space. However creating a nested DoE is not a simple process, due to the optimality conditions for space-filling as discussed in sections 3.2.6 to 3.2.9.

3.5 Summary

In this chapter a literature review of RSM was presented and included descriptions of the relevant material associated with DoEs, model building and model validation. A range of different concepts for selecting the experiments (DoE) required to

subsequently create accurate response surfaces was given. Various types of RSM concepts were presented along with the methods used to validate their accuracy.

Chapter 4 – Two-Scale Elastohydrodynamic Lubrication: Theoretical Formulation and Numerical Solution Procedure

4.1 Introduction

In this chapter the theoretical formulation and numerical solution procedure for two-scale Elastohydrodynamic Lubrication (EHL) are outlined. The two scales are those of the bearing domain and surface topography respectively. The large scale EHL simulation considered is a one-dimensional tilted-pad bearing, this is coupled using the Heterogeneous Multiscale Method (HMM) to three-dimensional small scale simulations which describe the micro-EHL of surface topography. A description of the Fluid Structure Interaction (FSI) problem at both scales is given and subsequently an outline of how the two scales are coupled via periodicity and homogenisation. Metamodelling techniques are used to represent small scale simulations in the large scale simulation and reduce the total number of simulations needed to accurately perform the analysis. A numerical procedure for computationally solving the two-scale EHL problem is described.

4.2 Heterogeneous Multiscale Method

The Heterogeneous Multiscale Method (HMM) is a general modelling technique based on the analysis of problems with two distinct scales (E and Engquist [88]). As a starting point a solver is chosen for a known large scale model, in which some terms are explicitly unknown. The HMM replaces these unknown quantities with the results of numerical simulations at the small scale. The key to the application of HMM proposed by Gao and Hewson [30] was how the two scales were coupled and the application of near-periodicity in the small scale simulation. By using the same rationale a similar, though more general, formulation is described here. Homogenised small scale results describe the pressure gradient – mass flow rate relationship, and the large scale subsequently applies this to a global pressure distribution and conservation of mass. This approach is limited because only small scale inertial effects can be included, however by neglecting large scale inertial effects the resulting simulation is consistent with the assumptions which define the smooth surface model. Large scale variables are determined via the homogenised relationship through interpolation of the small scale

solutions. In this method a response surface approximation is used in place of the small scale data as a route to interpolation.

4.3 Large Scale Simulation

The large scale simulation describes EHL in the global bearing domain. In a manner similar to that of conventional EHL analyses, hydrodynamic lubricant pressure is coupled with elastic deformation of the bearing surface. A Cartesian coordinate system (x, h) is defined for the large scale simulations.

4.3.1 Bearing Domain

Fig. 4.1 illustrates the linear-converging tilted-pad bearing which is analysed in this study at the large scale. Such geometry minimises cavitation in the outlet region as the pressure will remain above the ambient value (although this may not necessarily hold at the small scale where micro-cavitation could conceivably occur). This geometry is chosen as an example of the how the two-scale method can be utilised.

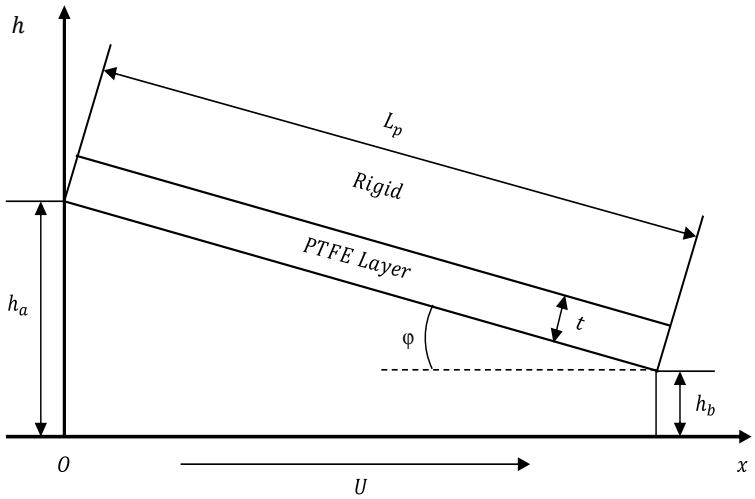

Fig. 4.1 – Large scale bearing geometry

The pad length (L_p) is representative of the contact region for the bearing. The deformable polytetrafluoroethylene (PTFE) layer of the pad has a thickness (t) and incorporates elastic deformation from the resulting simulation. The backing to the pad is assumed to be rigid. A minimum undeformed film thickness for the tilted-pad bearing

(h_b) at outlet is adjusted for a given tilt angle (φ) such that the undeformed film thickness distribution (h) is determined by Eq. (4.1).

$$h = h_b + \left(L_p \cos\varphi - x\right)\tan\varphi \tag{4.1}$$

The lower surface of the bearing contact moves with speed U in the x-coordinate direction and the upper PTFE layer remains stationary. Topography is defined at the small scale (outlined in section 4.4.1) and can be parameterised such that the effects of different topographies can be studied at large scale (see section 4.9). These topographical features are periodically distributed across the length of the pad on the PTFE layer. The function describing topography does not change along the bearing length.

4.3.2 Fluid Flow Model

One-dimensional flow is considered at the large scale in this study. This is governed by equations defining the pressure gradient and mass conservation:

$$\frac{dp}{dx} = f(p, q, g) \tag{4.2}$$

$$\frac{dq}{dx} = 0 \tag{4.3}$$

The pressure gradient ($\frac{dp}{dx}$) is a homogenised function of the pressure (p), mass flow rate per unit width (q) and film gap (g). The three parameters on the right hand side of Eq. (4.2) are the only large scale parameters which influence the small scale flow. This relationship is obtained from the small scale simulations, the details of which can be found in the following subsection. Dirichlet boundary conditions apply to Eqs. (4.2) and (4.3) such that pressure at the global inlet (p_a) and outlet (p_b) is zero (ambient pressure):

$$p_a = p_b = 0 \tag{4.4}$$

The one-dimensional large scale problem could be extended to two-dimensions to account for cross-flow or side-leakage by deriving a similar expression to that given by Eq. (4.2), whereby the relationship between the flow rate in both the x and y directions can be expressed as functions of the pressure gradients in these directions, the pressure, and local large scale geometry. Conservation of mass in the x and y directions can then be applied to close the two-dimensional problem.

4.3.3 Elastic Deformation

Elastic deformation of the bearing surface is calculated in a similar way to classic EHL analyses. Deformation is found via a matrix operation, where the influence of pressure on displacement decreases with the distance from the point at which it is applied [33]. The total deformation influence matrix (**K**), also known as the deformation coefficient matrix, is calculated using elasticity theory [190]. More details on how the stiffness matrix is obtained can be found in section 4.8.2. The relationship describing how pressure (load per unit area (p^*)) relates to surface deformation is given by Eq. (4.5):

$$\delta = \mathbf{K} \times p^* \tag{4.5}$$

4.3.4 Separation of the Deformation Matrix

Eq. (4.5) can be rewritten such that total deformation is the sum of local and non-local influences:

$$\delta = k_1(\mathbf{I} \times p^*) + \mathbf{K}_G \times p^* \tag{4.6}$$

In Eq. (4.6), k_1 is the local stiffness which comprises only the diagonal matrix terms and is subsequently modelled at the small scale. The term $k_1(\mathbf{I} \times p^*)$ accounts for local deformation and $\mathbf{K}_G \times p^*$ non-local deformation. Where $\mathbf{K}_G$ is the global deformation influence matrix, this can be solved for given the relationship with the total deformation matrix in Eq. (4.7):

$$\mathbf{K}_G = \mathbf{K} - k_1\mathbf{I} \tag{4.7}$$

Separating deformation of the pad into these two terms highlights how deformation at local and global scales can be treated independently. By implementing this mechanism both micro-EHL and global EHL effects are described by the two-scale method.

4.3.5 Pressure - Deformation Coupling

By separating the deformation influence matrix into the large scale problem described the effect of local deformation (characterised by the local stiffness (k_1)) on the pressure gradient – mass flow rate relationship is given by Eq. (4.2). The film gap (g) becomes the sum of the undeformed film thickness (h) and non-local deformation:

$$g = h + \mathbf{K}_G \times p^* \tag{4.8}$$

Eqs. (4.2), (4.3) and (4.8) are coupled and solved iteratively until convergence in the pressure field is reached. Due to the presence of topography at the small-scale Eq. (4.2) will also describes small scale fluid flow and structural effects which are not defined by the large scale mechanics, as described in the following subsection.

4.3.6 Bearing Performance

Two important bearing performance criteria are derived from the large scale simulation: the load capacity (W) and coefficient of friction (μ). These are calculated from Eqs. (4.9) and (4.10):

$$W = \int_0^{L_p \cos\varphi} p^* \, dx \tag{4.9}$$

$$\mu = \frac{1}{W} \int_0^{L_p \cos\varphi} \tau \, dx \tag{4.10}$$

τ is the shear force per unit area (shear stress) in the fluid. In the two-scale method this and the load per unit area (p^*) are derived from the small scale simulations along with the pressure gradient – mass flow rate relationship. As such both τ and p^* are also homogenised functions of the pressure (p), mass flow rate per unit width (q) and film gap (g).

4.4 Small Scale Simulations

The small scale simulations are defined by steady-state, isothermal, compressible, laminar flow as described by the Navier-Stokes equations and elastic deformation of the small scale features. Coupling is achieved through an Arbitrary Lagrangian-Eulerian (ALE) approach in a Finite Element (FE) simulation. For the small scale simulation a Cartesian coordinate system (x_s, y_s, z_s) is defined, and where appropriate a subscript s is used to distinguish the small scale variables and operators.

4.4.1 Fluid Domain

Fig. 4.2 illustrates the small scale fluid domain used in this study. The domain is described by the undeformed film gap (g) and the cell size (L) in both the x and y dimensions respectively. For the purpose of simplicity the cell size in both dimensions are equal, however this is not a requirement for the multiscale approach described. The cell film thickness (s) is the sum of film gap (g) and the periodic function describing topography (δ_t).

$$s = g + \delta_t \tag{4.11}$$

Periodicity must be maintained in the cell film thickness (pre-deformation) at the boundaries in order to satisfy the underlying multiscale theory assumptions. Therefore the function describing topography must also be periodic, Eq. (4.12) has been chosen for the purpose of this study. α is the topography amplitude where a value of $\alpha = 0$ corresponds to a smooth surface, the solution for which can be directly described by Reynolds equation. The different topography amplitudes investigated are represented through multiple metamodels.

$$\delta_t = \frac{\alpha}{4}\left[\sin\left(2\pi\frac{x_s}{L} - \pi\right) + \sin\left(2\pi\frac{y_s}{L} - \pi\right) + 2\right] \tag{4.12}$$

Parameterisation of topography is possible using this two-scale method, the parameters describing δ_t become additional variables in the pressure gradient – mass flow rate relationship (Eq. (4.2)). A single topographical feature has been chosen for the first part of this study however in section 4.9 parameterisation of the small scale simulations is discussed in more detail.

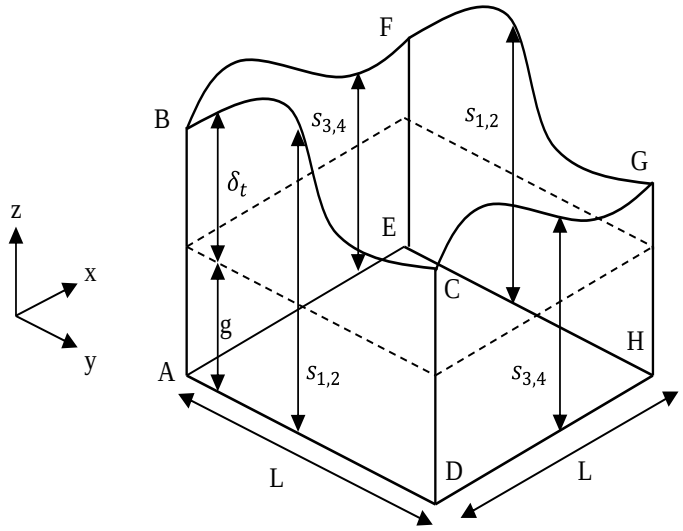

Fig. 4.2 – Small scale fluid domain

4.4.2 Fluid Flow Model

The small scale flow is considered steady, laminar, compressible and isothermal as described by the Navier-Stokes equations in the following form [191]:

$$\nabla_s \cdot (\rho_s \mathbf{u}_s) = 0 \tag{4.13}$$

$$\rho_s(\mathbf{u}_s \cdot \nabla_s)\mathbf{u}_s = \nabla_s \cdot \left[-p_s\mathbf{I} + \eta_s(\nabla_s\mathbf{u}_s + (\nabla_s\mathbf{u}_s)^T) - \frac{2}{3}\eta_s(\nabla_s \cdot \mathbf{u}_s)\mathbf{I}\right] \tag{4.14}$$

Where ρ_s denotes the fluid density, η_s is the fluid viscosity, p_s is the fluid pressure, $\mathbf{u}_s$ is the velocity vector and $\mathbf{I}$ the unit tensor. Eq. (4.13) is the continuity equation which describes the conservation of mass in the fluid domain and Eq. (4.14) is the partial differential equation describing the conservation of momentum for laminar flow of a compressible fluid. Applying the assumptions of the smooth surface model which includes neglecting inertial terms (left hand side of Eq. (4.14)) and derivatives across the film thickness, allows Eqs. (4.13) and (4.14) to be reduced to the Reynolds equation.

4.4.3 Fluid Properties

Compressibility is modelled via the Dowson-Higginson equation (Eq. 4.15) where fluid density is barotropic [43]. ρ_0 is the ambient density, and D_0, $D_1$are constants.

$$\rho_s = \rho_0 \frac{D_0 + D_1 p_s}{D_0 + p_s} \tag{4.15}$$

Viscosity is both piezoviscous and non-Newtonian (shear-thinning). The piezoviscous response is governed by Eq. (4.16) as defined by the Roelands equation [96]. η_p is the piezoviscous viscosity, η_0 is the viscosity at ambient conditions, η_r the Roelands reference viscosity, p_r the Roelands reference pressure, and Z the pressure-viscosity index [106].

$$\eta_p = \eta_r \exp\left(\ln\left(\frac{\eta_0}{\eta_r}\right)\left(1+\frac{p_s}{p_r}\right)^z\right) \tag{4.16}$$

Shear-thinning behaviour is modelled using the Ree-Eyring model (Eq. (4.17)) as originally developed by Johnson and Tevaarwerk [95] and further refined by Bair, et al. [110], where τ_0 is the Eyring stress and $\dot{\gamma}_s$ the shear rate.

$$\eta_s = \frac{\tau_0}{\dot{\gamma}_s}\sinh^{-1}\left(\frac{\eta_p \dot{\gamma}_s}{\tau_0}\right) \tag{4.17}$$

4.4.4 Fluid Boundary Conditions

In reference to fig. 4.2 the fluid flow boundary conditions are described. The lower surface ADHE is a moving wall with velocity U in the x-coordinate direction. BCGF is a no-slip boundary which forms the fluid/solid interface. The remaining faces form two sets of near-periodic (scaled to account for deformation and compressibility) boundaries, ABCD/EFGH and ABFE/DCGH. The boundaries which are normal to the direction of motion of the moving wall (ABCD/EFGH) experience a jump in pressure, generating a pressure gradient in x over the domain. The other set (ABFE/DCGH) remains fully periodic with pressure as there is no gradient defined in this direction for the large scale solution. If the large scale model requires such gradients then these can be generated by another jump condition imposed on these boundaries, however this adds an extra dimension to the design space.

The pressure jump condition is modelled by Eq. (4.18) where the pressure profile is shifted by Δp_s. Subscripts 1 and 2 denote downstream and upstream boundaries respectively.

$$p_{s,2} = p_{s,1} + \Delta p_s \tag{4.18}$$

Deformation of the upper surface creates challenges when implementing a boundary condition for velocity because the resulting outward facing area (A_s) of each pair face are no longer equal, as portrayed in fig. 4.3.

Mass flow rate must be equal across the boundaries in order to satisfy mass conservation at both scales and the underlying assumptions of the HMM analysis. This leads to the application of a near-periodic boundary condition for velocity Eq. (4.19) and corresponding equations (4.20) and (4.21) for density and area ratios.

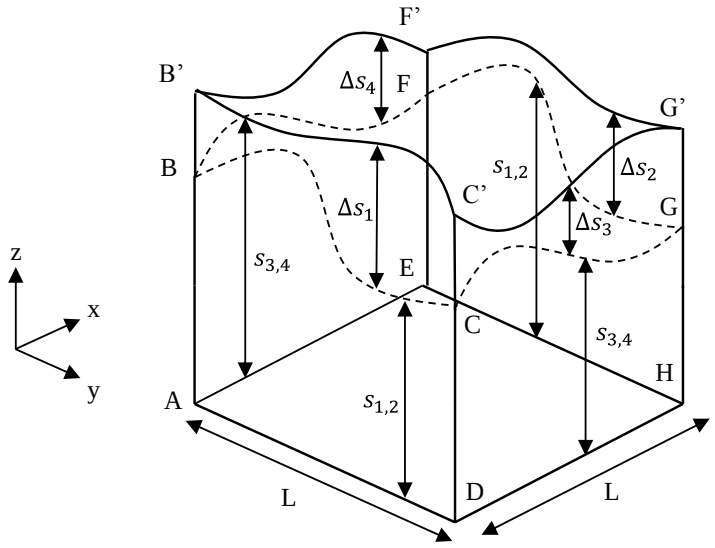

Fig. 4.3 – Deformed small scale fluid domain

$$\mathbf{u}_{s,2} = \mathbf{u}_{s,1} \cdot \frac{\rho_{s,1}}{\rho_{s,2}} \cdot \frac{A_{s,1}}{A_{s,2}} \tag{4.19}$$

$$\frac{\rho_{s,1}}{\rho_{s,2}} = \frac{\left(D_0 + D_1 p_{s,1}\right)\left(D_0 + p_{s,1} + \Delta p_s\right)}{\left(D_0 + p_{s,1}\right)\left(D_0 + D_1\left(p_{s,1} + \Delta p_s\right)\right)} \tag{4.20}$$

$$\frac{A_{s,1}}{A_{s,2}} = \frac{1 + \frac{\Delta A_{s,1}}{A_{s,0}}}{1 + \frac{\Delta A_{s,2}}{A_{s,0}}} \tag{4.21}$$

Eq. (4.20) accounts for compressibility at the boundaries. Eq. (4.21) describes how the ratio of areas relates to the strain in area over the boundary. $A_{s,0}$ is the boundary outward facing area pre-deformation and ΔA is the area deformation of the

boundary. This boundary condition is consistent with the HMM, where near-periodicity is maintained over a small scale feature. As the scale separation increases this becomes an increasingly valid assumption. As the length of the small scale feature tends toward zero the small scale feature vanishes (the Reynolds equation is obtained) and the problem can be solved analytically.

4.4.5 Spring Column Representation

The small scale EHL model is based on the fluid flow due to topography and the local stiffness properties. Deformation at the small scale uses an equivalent thickness (t') of the solid domain to ensure that the resulting deformation due to fluid pressure is equal to the column deformation achieved from the local stiffness (k_1) at the large scale. This is described by Eq. (4.22).

$$t' = k_1 E' \tag{4.22}$$

The equivalent elastic modulus (E') is derived to represent the mechanical properties of the large scale problem to a fully constrained column of bearing material in three-dimensions at the small scale [190].

$$E' = \frac{(1-\nu)E}{(1+\nu)(1-2\nu)} \tag{4.23}$$

Where E and ν are the Young's Modulus and Poisson's Ratio of the bearing material respectively. Eq. (4.23) is not valid for incompressible materials $(\nu = 0.5)$ since t' will tend to infinity, invalidating the column of material approach. By applying an equivalent thickness to the problem the small scale FSI is accurately described as the material properties and required stiffness properties are maintained. It is important to note that this approach is only valid where the size of the equivalent thickness is an order of magnitude greater than the size and deformation of the topographical feature. Because discretisation at the large scale determines the magnitude of the local stiffness

k_1, ensuring this separation in scales raises some challenges, as discussed in section 4.8.2.

4.4.6 Solid Domain

The solid column is located above the fluid domain as illustrated by fig. 4.4. FSI occurs at the interface connecting the two domains using an ALE approach as described in section 4.4.9. The thickness (t') is derived as previously outlined from the material and stiffness properties required at the large scale. Topography (δ_t) is removed from the solid column. The size and subsequent deformation of topography must be an order of magnitude smaller than the solid column thickness such that the local topography dependent stress field is not affected.

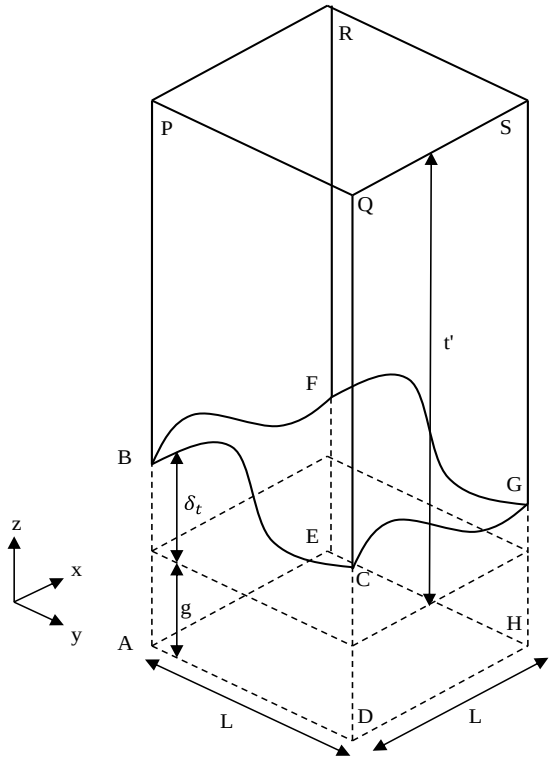

Fig. 4.4 – Small scale solid domain

4.4.7 Solid Deformation Model

Structural mechanics is considered at the small scale using a conventional three-dimensional FE analysis in order to represent the local stiffness (k_1) required at the large scale. The force balance is characterised by Eq. (4.24) where the solid material is

assumed homogeneous, isotropic and linearly elastic [192]. In Eq. (4.24), σ_s is the stress tensor, $\mathbf{F}_s$ the vector of load per unit volume, and V_s the volume.

$$-\nabla_s \cdot \sigma_s = \mathbf{F}_s V_s \tag{4.24}$$

4.4.8 Solid Boundary Conditions

With reference to fig. 4.4 the small scale solid boundary conditions are described. The upper boundary PQSR is fully constrained. The sides of the spring column BPQC, BPRF, FRSG and CQSG are constrained normal to the surface. The fluid/solid interface BCGF is loaded by the pressure p_s generated from the fluid flow simulations, i.e. the stress normal to the boundary is equal to the pressure.

4.4.9 Pressure – Deformation Coupling

An Arbitrary Lagrangian-Eulerian (ALE) approach is used to fully-couple the pressure and deformation in the small scale simulations by moving the elements of the meshed domains. The ALE incorporates features of both Lagrangian and Eulerian approaches where elements can either be moved systematically, arbitrarily, or not at all such that distortion of the mesh is reduced and large deformations can be modelled [193]. The FSI problem is solved iteratively, where pressures cause deformation and deformation alters the pressure field, until convergence in both the pressure and deformation fields is achieved.

Here the FSI interface BCGF dictates deformation of the mesh (Δz_s) where the elements on this surface are moved by the exact amount calculated due to the pressure loading (Δs). Elements within the fluid and solid domains are deformed by the amount given at BCGF as a function of x_s and y_s and subsequently scaled using Laplace smoothing such that there is no deformation of the mesh elements at the moving wall ADHE and fully constrained solid boundary PQSR respectively. Fig. 4.5 provides a schematic of the ALE approach used in this study.

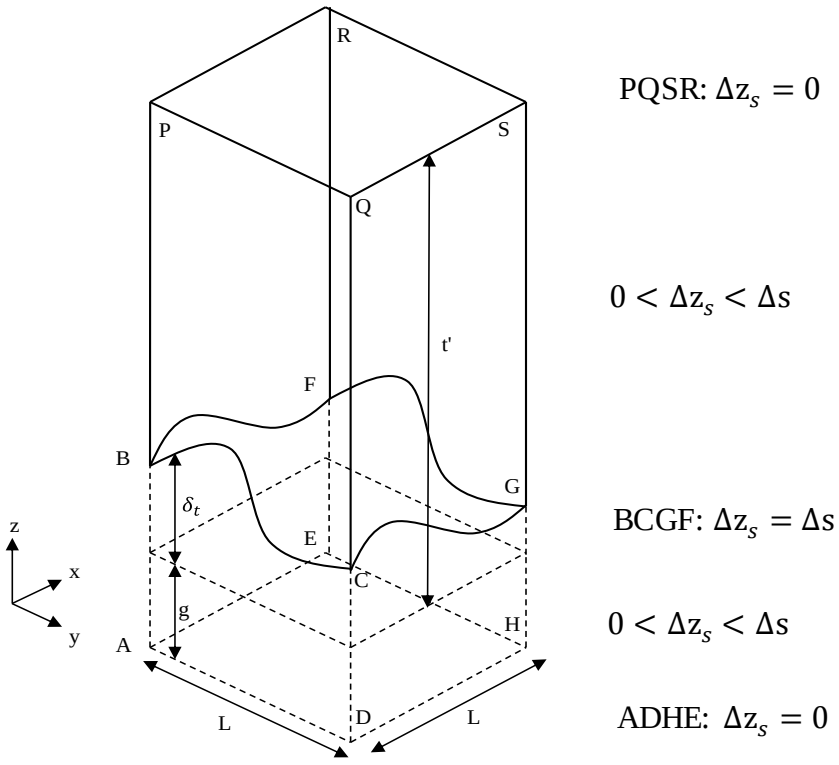

Fig. 4.5 – Schematic of the ALE approach used in the small scale simulations

4.5 Homogenisation

Given a pressure constraint (placed directly in the centre of ADHE of fig.2, denoted by p) and the initial gap (g, which includes the undeformed film thickness plus deformation of non-diagonal terms of the stiffness matrix, excluding the diagonal terms), the solution fields for pressure and velocity can be obtained by solving for small scale model. The homogenised pressure gradient $\left(\frac{dp}{dx}\right)$ over a unit cell is calculated using Eq. (4.25).

$$\frac{dp}{dx} = \frac{\Delta p_s}{L} \tag{4.25}$$

The mass flow rate per unit width (q) at the large scale is determined from the mass flow rate which characterises the small scale flow and the magnitude of the extra dimension considered at this scale. Eq. (4.26) is calculated on the deformed boundary AB'C'D of fig. 4.3.

$$q = \frac{1}{L}\int_{0}^{s+\Delta s}\int_{0}^{L} \rho_s u_s \, dy_s dz_s \tag{4.26}$$

Where Δs is the deformation of the fluid domain thickness. The pressure constraint (p), pressure gradient $\left(\frac{dp}{dx}\right)$, initial gap (g), and the mass flow rate per unit width (q) are required for interpolation of the small scale results for use in a large scale simulation.

As pressure is not linearly distributed with the x-direction in the small scale domain due to effects which occur in the presence of topography as well as that due to deformation, compressibility, piezoviscosity, etc., an average cell pressure (p^*) is derived which describes the load per unit area in the large scale simulation and from which the load capacity and elastic deformation of the bearing is determined.

$$p^* = \frac{1}{L^2}\int_{0}^{L}\int_{0}^{L} p_s \, dx_s dy_s \tag{4.27}$$

This average cell pressure is used to determine the deformation at the large scale. The shear force per unit area (τ) is calculated from Eq. (4.28) at the small scale, this is equivalent to shear stress in the large scale model. The integration of Eqs. (4.27) and (4.28) is over the moving wall boundary ADHE of Fig. 4.2.

$$\tau = \frac{1}{L^2}\int_{0}^{L}\int_{0}^{L} \eta_s \frac{du_s}{dz_s} \, dx_s dy_s \tag{4.28}$$

The small scale minimum film thickness (s_{min}) can be reported using Eq. (4.29). This film thickness is representative of the EHL and micro-EHL effect and is thus a measure of the deformation of the small scale features. Eq. (4.29) is performed on the deformed fluid/solid interface B'C'G'F'.

$$s_{min} = \min_{x_s, y_s}(s + \Delta s) \tag{4.29}$$

The role of additional flow phenomenon such as viscosity and density cannot be shown at the large scale because they vary significantly in the small scale solutions, meaning that homogenisation does not reflect the true magnitude of the variable in the small scale domain.

4.6 Analogy with the Smooth Surface Model

When considering fluid flow, the smooth surface case (where the size of the topography is zero, $\alpha = 0$) can be compared with Reynolds equation to provide a benchmark for the multiscale approach. This is because without topography the small scale problem can be accurately described by the lubrication approximation. Eq. (4.30) is the corresponding incompressible, isoviscous Reynolds equation in one-dimension using the separation of the stiffness matrix assuming a Newtonian viscosity. Note that in the smooth surface case the load-per-unit-area and pressure are equivalent.

$$\frac{dp}{dx} = \frac{12\eta_0}{\rho_0(g + k_1 p)^3}\left(\frac{\rho_0 U}{2}(g + k_1 p) - q\right) \tag{4.30}$$

4.7 Response Surface Methodology (RSM)

RSM refers to the process of building, validating and implementing the approximation based on the previously obtained experiments, this is also known as surrogate or metamodelling [130]. Representation of the small scale data at the large scale is achieved through the use of a Moving Least Squares (MLS) approximation. The approximation describes the small scale solutions over the entire design space. The design space encompasses the complete range of values required by the large scale solver. Creating a model of this nature requires a Design of Experiments (DoE) which ensures the most efficient spread of simulations in the design space. An Optimum Latin Hypercube (OLHC) was used to span as much of the design space with as few designs as possible [92]. Eq. (4.2) is replaced by Eq. (4.31) where the tilde notation represents

known values corresponding to small scale simulations of the evaluated function and θ is a metamodel tuning parameter. Similar representations are defined for the load per unit area (p^*), shear force per unit area (τ), and small scale minimum film thickness (s_{min}).

$$\frac{dp}{dx} \cong \tilde{f}\left(\tilde{p}, \tilde{g}, \tilde{q}, \widetilde{\frac{dp}{dx}}, p, g, q, \theta\right) \tag{4.31}$$

4.7.1 Moving Least Squares (MLS) Approximation

MLS is derived from conventional weighted least squares model building, however the weights describing the influence of a point in the approximation do not remain constant but are functions of the normalised Euclidian distances from sampling points to the point where the metamodel is evaluated. The weight associated with a particular sampling point decays as an evaluation point moves away from the sampling point. It is not possible to obtain an analytical form of the MLS function representing the metamodel but its evaluation is computationally inexpensive and therefore used in this work. Eqs. (4.32), (4.33), (4.34), and (4.35) illustrate polynomial basis functions used to model the multiscale relationships for the pressure gradient, load per unit area, shear force per unit area, and small scale minimum film thickness respectively. Each of these is based upon the corresponding equations obtained from the smooth surface model but inclusive of extra constants which are determined through the MLS operation. These constants $(C_1 - C_{10})$ are functions of the position within the design space at which the metamodel is being assessed. The dimensions of C_3 are MPa/mm, C_5 and C_8 are N/mm^2, C_{10} is μm, and the remaining constants are dimensionless.

$$\frac{dp}{dx} = \frac{12\eta_0}{\rho_0(g + k_1 p)^3}\left(\frac{C_1\rho_0 U}{2}(g + k_1 p) - C_2 q\right) + C_3 - 1 \tag{4.32}$$

$$p^* = C_4 p + C_5 - 1 \tag{4.33}$$

$$\tau = \frac{6\eta_0}{\rho_0(g + k_1 p)^2}\left(\frac{2C_6\rho_0 U}{3}(g + k_1 p) - C_7 q\right) + C_8 - 1 \tag{4.34}$$

$$s_{min} = C_9(g + k_1 p) + C_{10} - 1 \tag{4.35}$$

Deviations from the smooth surface model introduced by the small scale model are captured by these constants. In the incompressible, isoviscous, smooth surface case the set of constants will be unity throughout the design space as the computational results are the same as the smooth surface model.

MLS metamodels can be tuned to the DoE data by varying the closeness of fit parameter θ. Changing θ controls the rate at which the weight decays with distance from a sampling point or in another perspective the sphere of influence surrounding an evaluation point beyond which a sample point will have no effect on the resulting metamodel approximation. This parameter allows MLS approximations to efficiently deal with numerical noise, where the user has choice over how 'close' or 'loose' the fit is [131]. Several strategies have been derived in order to automatically predict the closeness of fit parameter for a given data set [170]. Following from the work of Loweth, et al. [90] θ is best determined using the either the k-fold or Leave-One-Out Cross Validation (CV) methods.

4.7.2 k-fold Cross Validation (CV)

In k-fold CV a random set of size k is removed from the DoE and the MLS approximation is built from the remaining sample points (building set) using a given closeness of fit parameter (θ). The approximation is then compared against the known function value at the removed locations (validation set) by calculating the Root Mean Squared Error (RMSE).

$$\mathrm{RMSE} = \sqrt{\frac{1}{k}\sum_{i=1}^{i=k}\left(f_i - \tilde{f}_i\right)^2} \tag{4.36}$$

In Eq. (4.36), k is the number of validation points, $\tilde{f}_i$ belong to the set of known function evaluations and f_i to the set of corresponding MLS approximations. This

process of error checking is repeated over many k-sized folds of the validation set as to include all points in both the building and validation phases. An average of the RMSE is then used to provide the error for the approximation at the current closeness of fit parameter (θ). A range of θ values is specified and the above process is carried out across this range. The smallest average RMSE calculated gives the value of the closeness of fit which produces the most accurate MLS approximation for the data provided. The average RMSE versus closeness of fit parameter response is subject to a significant amount of numerical noise making the search for a minimum RMSE difficult. Practical experience [90] suggests that the following must all be specified in order to reduce this noise: the number of repeat folds (1000 is chosen to limit numerical cost), the size of each fold used (~30% of the DoE size), the method of randomisation by which folds are chosen, and the range of the closeness of fit parameter chosen for investigation (this can vary between zero (least squares regression) and any value until over-fitting occurs [161], the range of 0-100 was found to be suitable in this case).

4.7.3 Leave-One-Out CV

Leave-One-Out CV differs from k-fold CV in that the size of the validation set $k = 1$. Each point in the entire data set is removed in turn and the metamodel built from the remaining points (building set). The error at the validation point is then assessed and averaged for a given closeness of fit over the total number of points held. The closeness of fit is varied and the value which produces the minimum error over all values is selected. The RMSE is again employed as a metamodel assessment criteria, however since $k = 1$ this is equivalent to the absolute error between the metamodel approximation and the known observed value. Leave-One-Out CV produces a smoother error response than k-fold CV because the folds are not randomly selected but systematically chosen in turn. This implies that each point is assessed only once as part of the error criteria giving equal weighting to the error at each location, whereas the k-fold method will bring bias to the error criteria at locations where the error assessment has been made numerous times. Leave-One-Out CV is also much faster since each time there is a call to the MLS function only one matrix inversion operation is required, in k-fold CV each call to the MLS function requires k independent matrix operations.

4.8 Numerical Method

4.8.1 Geometry and Materials

The lubricant modelled is an idealised compressible, piezoviscous and non-Newtonian (shear-thinning) fluid, the solid considered is a linearly elastic PTFE as described earlier. Details of the constants related to these fluid and solid properties and those used as operating conditions and geometrical identities are listed in Table 4.1.

Parameter	**Value/Range**	**Unit**
D_0, D_1	0.59×10^9, 1.34	-
E	0.5	GPa
k_1	0.4667	µm/MPa
L	10	µm
L_p	[20, 25]	mm
p_r	0.196	GPa
t	0.5	mm
U	1	m/s
W	75, 100	kN
Z	0.4486	-
α	[0, 7.5]	µm
η_0	1	Pa.s
η_r	6.31×10^{-5}	Pa.s
ν	0.4	-
ρ_0	870	kg/m^3
τ_0	5	N/mm^2
φ	[0.05, 0.06]	°

Table 4.1 - Parameters values and ranges

4.8.2 Stiffness Properties

In this study only elastic deformation of the pad is modelled and bending is not considered. The stiffness matrix (**K**) is calculated using the method described by Rodkiewicz and Yang [102]. The FE method is used to model solid deformation of the

pad. By implementing the principle of virtual work mechanical characteristics for the pad are formulated. The pad is discretised evenly and unit loads applied to each of the pad face elements in turn. The resulting deformation distributions become a row in the total deformation matrix. As these distributions are superimposed they provide the pad deformation due to pressure acting on all elements. This can be scaled directly to account for any load within the elastic limit of the material. A graphical illustration of this method is outlined in fig. 4.6.

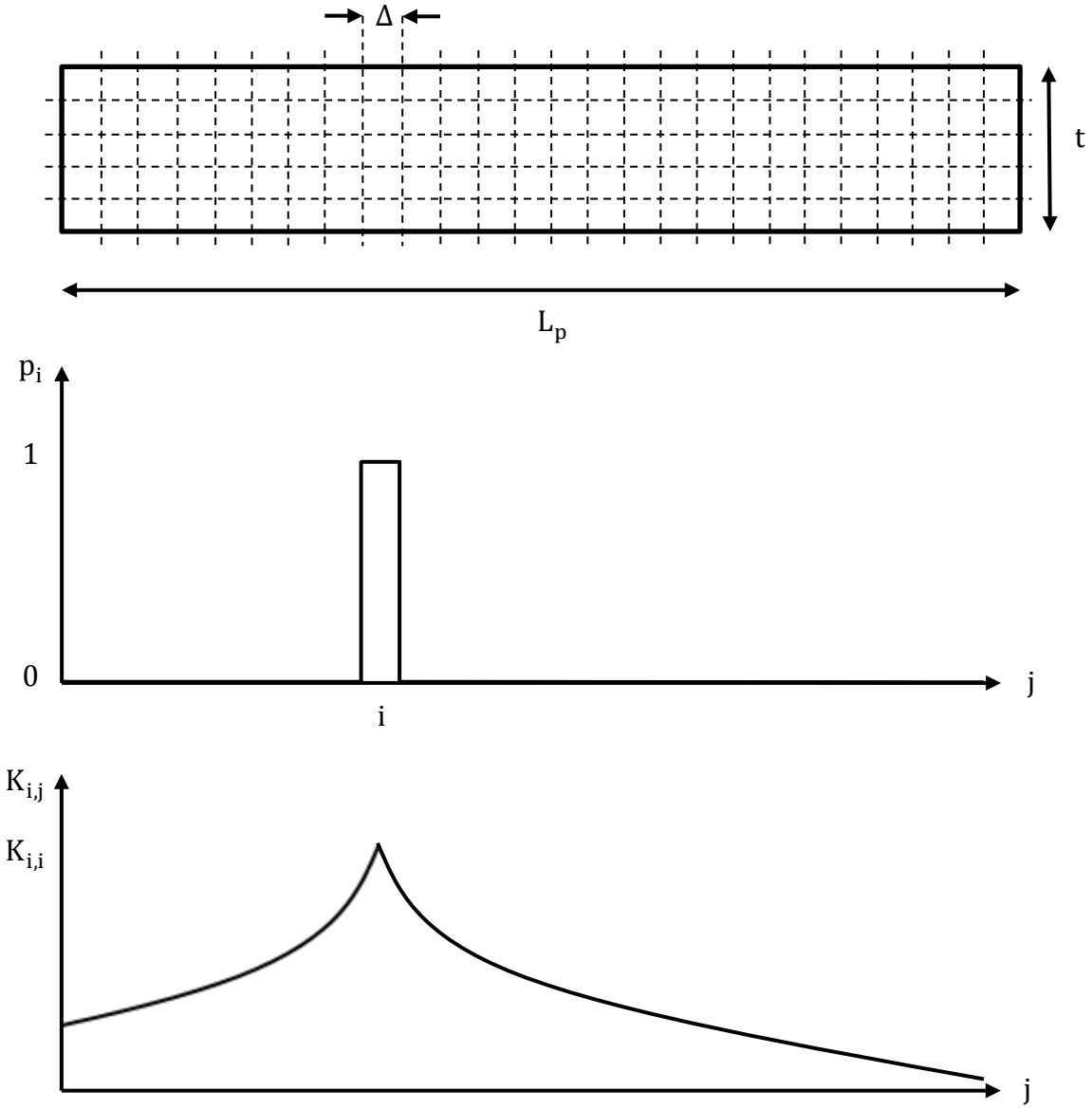

$$\delta_j = \sum_{i=1}^{i=N} K_{i,j} p_i \qquad (4.37)$$

Fig. 4.6 – Graphical illustration of the derivation of the stiffness matrix

The value of the diagonal terms of the matrix ($K_{i,i}$) which govern the large scale local stiffness are affected by the size of elements chosen to represent the bearing surface. This leads to a potential breakdown of the multiscale theory required at the small scale. In order for the spring column approach to remain valid, the magnitude and deformation of topography at the small scale ($\delta_t + \Delta s$) must be at least an order of magnitude smaller than the equivalent thickness (t') derived from the local stiffness properties (k_1). If there are too many discrete elements the resulting thickness ($K_{i,i}E'$) becomes too small for this assumption to hold, as illustrated in fig. 4.7.

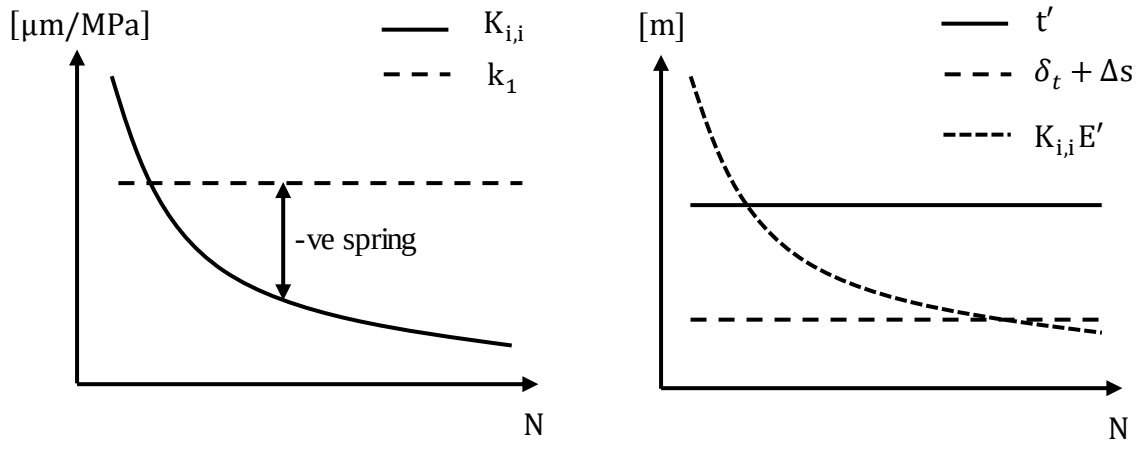

Fig. 4.7 – Effect of the number of pad surface elements on the diagonal stiffness matrix term and the separation of scales in the two-scale method

To solve this issue the stiffness at the small scale is set to a value which will always provide a large enough thickness, the local stiffness (k_1). The small scale simulations provide a solution corresponding to this stiffness. Because deformation is linearly elastic the result can be scaled directly to match the required large scale local stiffness, which leads to the inverse spring model represented in Eq. (4.8). In this study the local stiffness is constant and thus the same small scale data can be used for any large scale definition of the stiffness matrix. The formulation outlined here is therefore more general than the method developed by Gao and Hewson [30].

4.8.3 Solution Procedure

The first stage of the solution procedure is to determine suitable ranges for the gap, pressure and pressure gradient which will result in flow rates of the order required to compute the large scale pressure field. These limits were found by running simulations with Reynolds equation (Eq. (4.30)) in place of the pressure gradient – mass flow rate relationship using the method as outlined below. The resulting limits are tabulated in Table 4.2. The OLHC DoE was specified using a permutation Genetic Algorithm (GA) code [92] and the small scale simulations setup and run sequentially using the FE method as implemented by COMSOL Multiphysics (USA). k-fold CV was subsequently performed on the resulting data sets to find the closeness of fit parameters needed for the MLS approximations, ready for large scale implementation.

For a given large scale undeformed geometry (h), the solution procedure begins with an initial guess of the pressure distribution (p_{old}) and load-per-unit-area (p^*_{old}). This was chosen as the corresponding smooth surface solution to the Reynolds equation $f_{Re}(h)$ (Eq. (4.30)). The film gap (g) was then updated according to Eq. (4.8) to include non-diagonal deformation terms. The pressure (p), load-per-unit-area (p^*_{new}), shear stress (τ), and mass flow rare (q) were then solved from this updated geometry and the pressure gradient – mass flow rate relationship (Eq. (4.2)), which is inclusive of the local elastic deformation obtained for the small scale simulations. The actual representation of this is governed by the MLS approximations (Eqs. (4.32) – (4.34)) derived after the small data is acquired. This process was subsequently repeated until convergence in the pressure field was obtained, the tolerance chosen for this was 10^{-3}. For each iteration the large scale load per unit area (p^*) was relaxed by a factor of, $\theta = 0.5$ due to instabilities in the numerical solution method. A flow chart of this process is given in fig. 4.8.

The solution of Eqs. (4.2) and (4.3) are obtained using a shooting method for the mass flow rate (q) to satisfy the pressure boundary conditions. The mass flow rate was initially selected by intersecting pre-determined upper (q_U) and lower bounds (q_L). The mass flow rate was adjusted each iteration depending on whether the error in the pressure boundary condition at outlet (ξ) is either under (ξ_U) or over predicted (ξ_L). The mass flow rate was determined each iteration by using a linear bisector approach to predict the value which gives a pressure error at outlet $\xi = 0$. The bounds were then adjusted according to whether the current mass flow rate over or under predicts the

pressure at outlet. A flow chart describing this solution procedure is given in fig. 4.9. This is an Initial Value Problem (IVP) which was solved using the MATLAB (The Maths Works Inc., USA) solver ode45 to perform $4^{th}/5^{th}$ order Runge-Kutta integration of the pressure gradient equation. Once this process converged the pressure, pressure gradient, load per unit area, shear force per unit area and mass flow rate were returned.

In order to generate comparable results across varying operating conditions and degrees of freedom a fixed load was required for all large scale simulations. In order to implement this the minimum film thickness of the bearing (h_b) was adjusted subject to Eq. (4.1), where a reduction in h_b increases the bearing load capacity (W). From the processes outlined in figs. 4.8 and 4.9 the load capacity of the bearing was determined as a function of the undeformed geometry and small scale simulations. By implementing a method of bisectors the minimum deformed gap (g_b) and coefficient of friction (μ) for a given load was obtained. Upper (h_U) and lower (h_L) bounds for the minimum undeformed film thickness were selected and the corresponding load capacities determined (W_U and W_L respectively). The value of h_b for the next iteration (h_I) was selected by determining the value which gives a load capacity of W_R according to the linear relationship provided by the bounding cases. The bounds were then updated according to whether the calculated load capacity (W_I) was over or under predicted at the current undeformed film thickness. Convergence was reached when the difference in the calculated load capacity and required load capacity (W_R) were within 10^{-3} of each other. A flow chart of this process is outlined in fig. 4.10.

Parameter	**Range**	**Unit**
$\frac{dp}{dx}$	[-40, 10]	MPa/mm
p	[0, 10]	MPa
g	[5, 50]	µm

Table 4.2 – Ranges applied to the DoE used for the small scale simulations

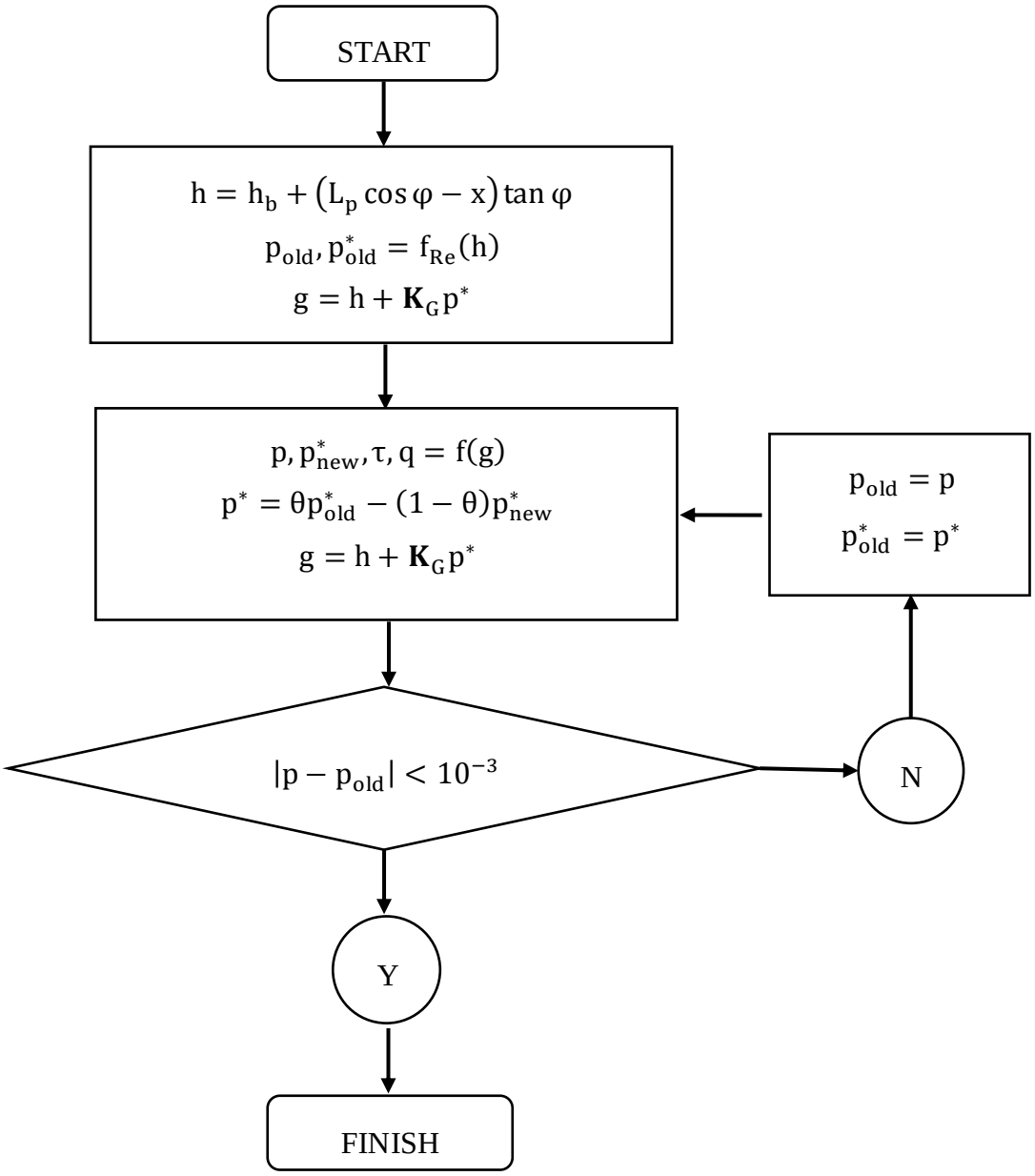

Fig. 4.8 – Flow chart of the large scale pressure-deformation solver

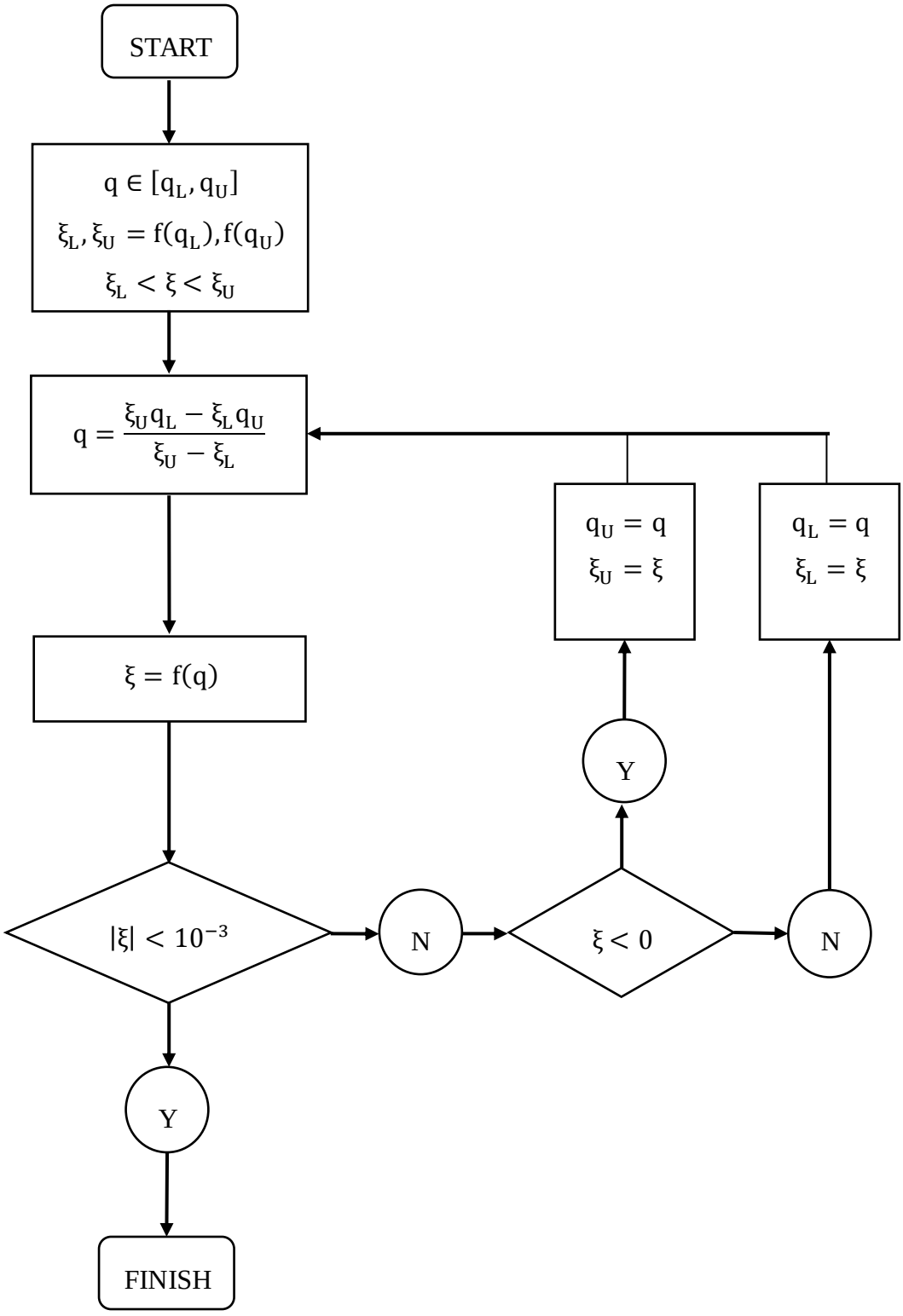

Fig. 4.9 – Flow chart of the shooting method for pressure solving

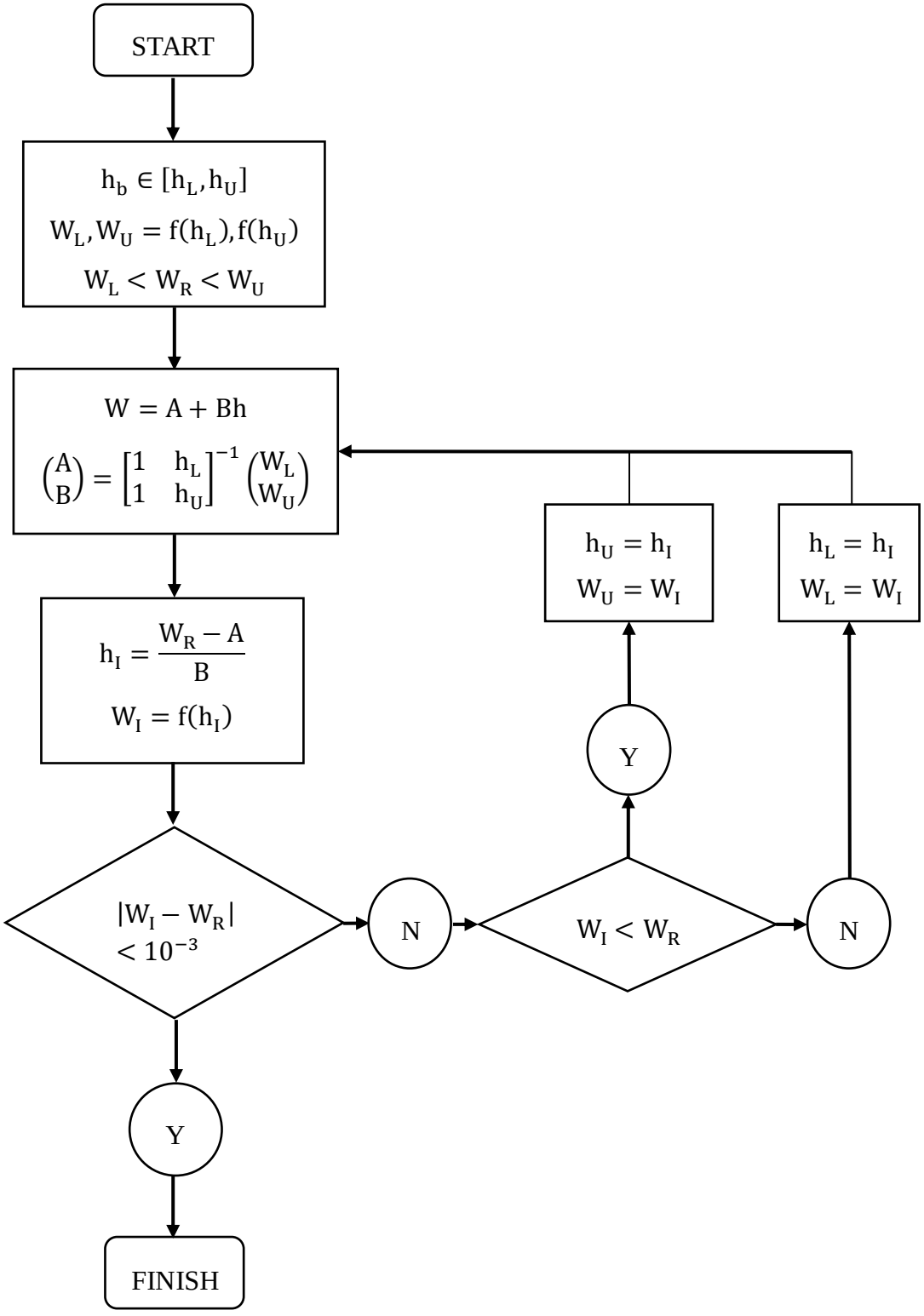

Fig. 4.10 – Flow chart of the bisector approach for fixed load simulations

4.9 Optimisation of Topography

Optimisation of topography was achieved using the two-scale method, the function describing topography was parameterised at the small scale and one extra dimension added to the pressure gradient – mass flow rate relationship to describe the effect of varying the geometry. Using the same methods and metamodels as outlined previously the topography can be varied for the textured bearing and the performance assessed over a range of the design variables at the large scale. The lowest coefficient of friction was identified for the range of topographies by a bracketing type optimisation procedure.

4.9.1 Theoretical Formulation

The function describing topography (δ_t) was parameterised with the variable ψ which is referred to as the longitudinal/transverse ratio. By varying ψ the shape of the topography can be controlled and the effect of different topographies on the pressure gradient – mass flow rate relationship investigated. The topography function is given in Eq. (4.37).

$$\delta_t = \frac{\alpha}{2}\left[\psi\left(\sin\left(2\pi\frac{x_s}{L}\right)+1\right)+(1-\psi)\left(\sin\left(2\pi\frac{y_s}{L}\right)+1\right)\right] \tag{4.37}$$

When $\psi = 0$ topography is longitudinal to the flow direction and conversely when $\psi = 1$ topography is transverse to the flow direction. Between these limits the topography described is a linear combination of longitudinal and transverse waviness, such that at $\psi = 0.5$ both components are of equal measure. The optimisation process will indicate the value of the longitudinal/transverse ratio (ψ) which produces the lowest coefficient of friction (μ) for the textured bearing.

Contour plots of the different topographies which are achieved using Eq. (4.37) are presented in figs. 4.11 – 4.15 for $\psi = 0, 0.25, 0.5, 0.75,$ and 1 respectively. For the optimisation procedure, the topography amplitude is set to $\alpha = 7.5$ μm, the pad length and tilt angle are $L_p = 25$ mm and $\varphi = 0.05°$, the load capacity is set to $W = 100$ kN, and all other parameters are specified in Table 4.1.

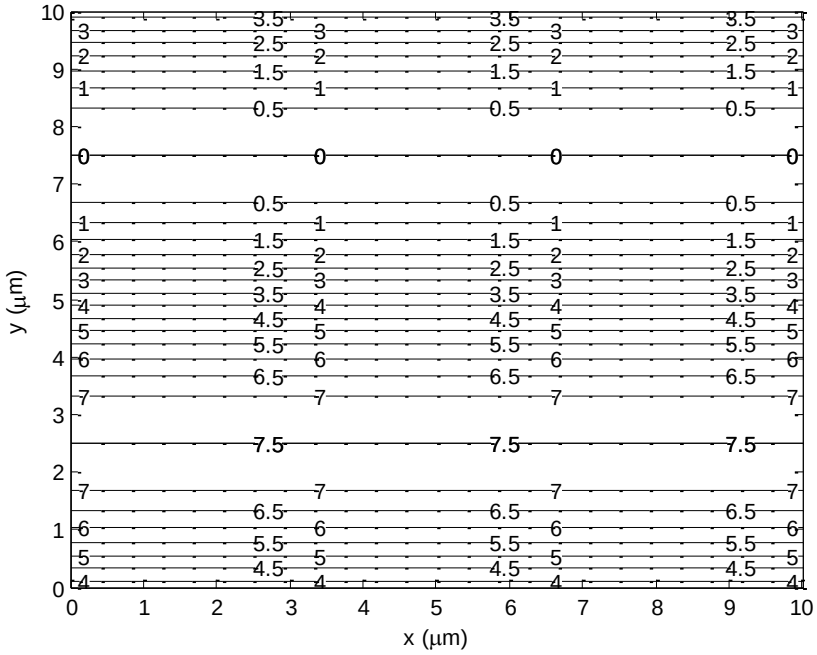

Fig. 4.11 – Topography in μm at $\psi = 0$ (100% longitudinal)

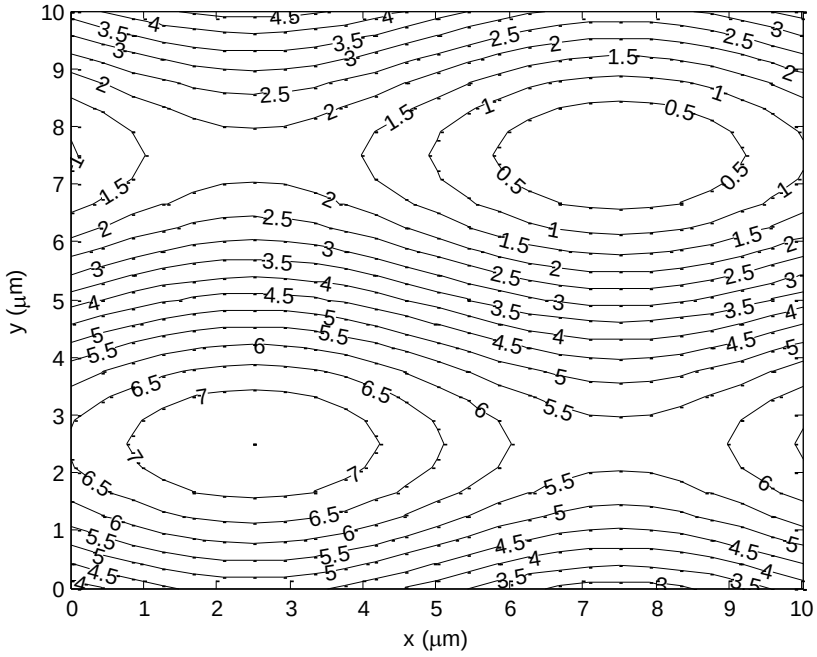

Fig. 4.12 – Topography in μm at $\psi = 0.25$ (75% longitudinal, 25% transverse)

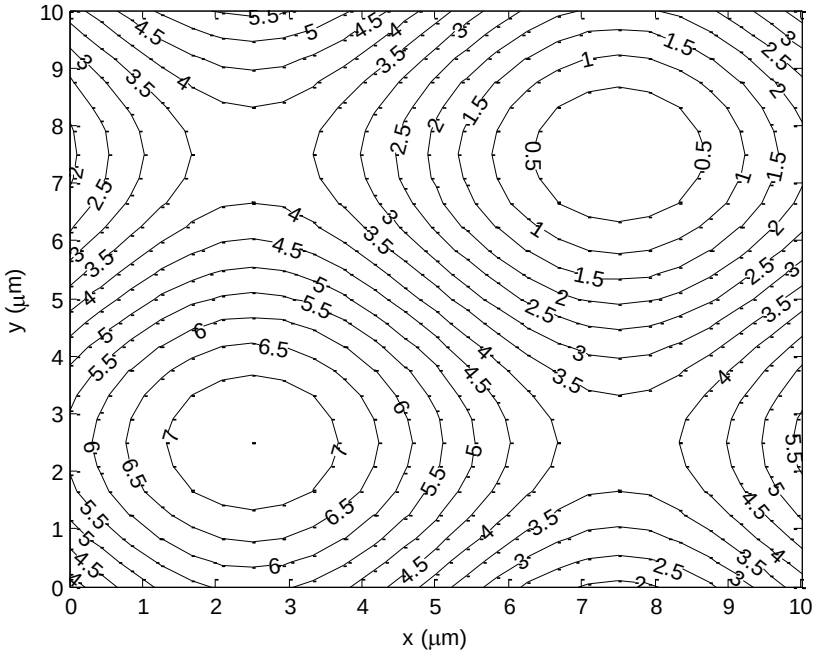

Fig. 4.13 – Topography in μm at $\psi = 0.5$ (50% longitudinal, 50% transverse)

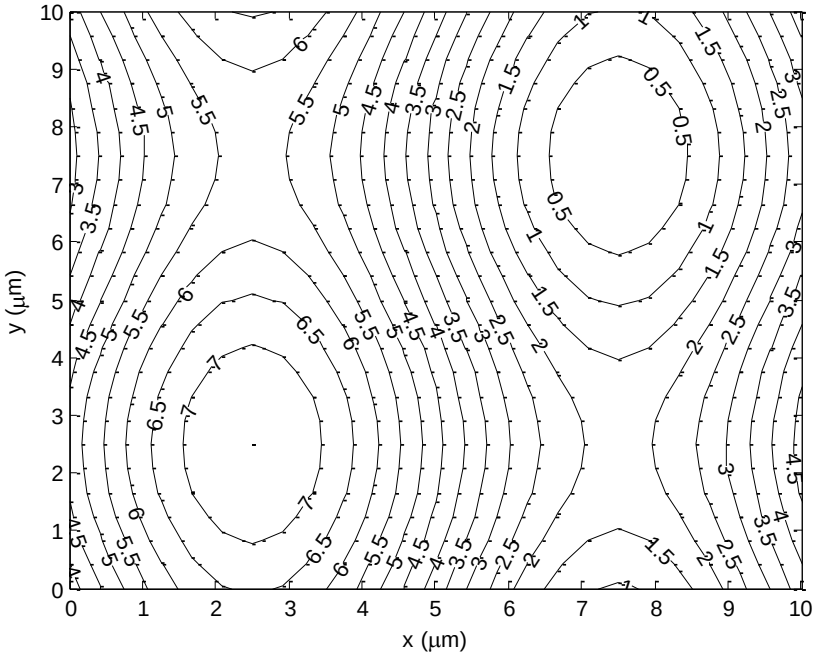

Fig. 4.14 – Topography in μm at $\psi = 0.75$ (25% longitudinal, 75% transverse)

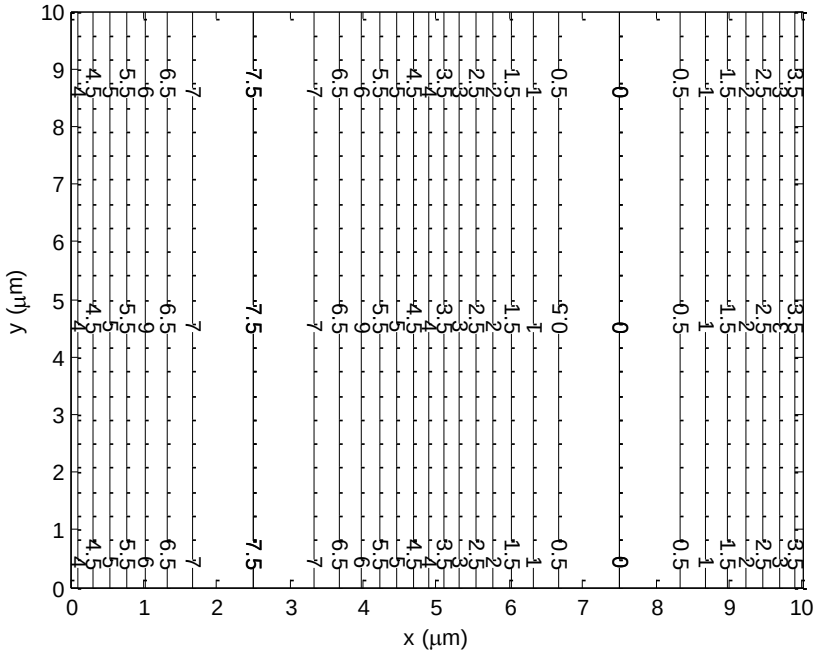

Fig. 4.15 – Topography in μm at $\psi = 1$ (100% transverse)

The two-scale method can be conducted in the same manner described when parameterising the topography was not considered, except that the pressure gradient – mass flow rate, load per unit area – mass flow rate, shear stress – mass flow rate relationships must now include the extra dimension introduced by varying the small scale geometry. Eq. (4.38) is used in place of Eq. (4.2) and subsequently for the metamodel Eq. (4.39) in place of Eq. (4.31). The same MLS basis functions as described by Eqs. (4.32) – (4.35) are used for the four-dimensional metamodels.

$$\frac{dp}{dx} = f(p, q, g, \psi) \tag{4.38}$$

$$\frac{dp}{dx} \cong \tilde{f}\left(\tilde{p}, \tilde{g}, \tilde{q}, \tilde{\psi}, \widetilde{\frac{dp}{dx}}, p, g, q, \psi, \theta\right) \tag{4.39}$$

4.9.2 Solution Procedure

A four-dimensional OLHC DoE is needed to specify the required small scale simulations, this was generated using the same permutation GA code [92]. The ranges used for this are the same as Table 4.2 and the longitudinal/transverse ratio (ψ) is

bounded by [0,1]. The remainder of the solution procedure follows the same processes as outlined in section 4.8.3 where the function describing topography does not change over the length of the bearing, however the method for pressure solving at the large scale is conducted via an alternative method to the IVP outlined.

A Boundary Value Problem (BVP) is setup using the MATLAB solver bvp4c to solve Eqs. (4.2) and (4.3). This method guarantees the boundary conditions for pressure are met and requires a close initial guesses of p and q to perform the operation. The initial guesses are initially specified as the corresponding Reynolds solution but are updated at convergence of the BVP to the values obtained from the latest iteration of the deformation loop. The pressure gradient – mass flow rate relationship and continuity equation must be written in Cauchy form to use this method. The number of calls to the metamodel function is not controlled by the user and as such the range of values which the BVP solver uses may fall outside the range covered by the small scale simulations. Because the metamodels are based on the corresponding smooth surface model equations, if the metamodel is assessed far away from the design space the function will become the smooth surface model and is therefore well-conditioned. Assessment of values which fall outside the range of the DoE do not influence the final solutions, all of which are inside the design space.

One further process is needed to perform the optimisation. ψ is varied parametrically over the entire range and the coefficient of friction (μ) recorded for the textured bearings under load. The value of ψ which produces the minimum μ is recorded and the range of ψ refined around this value, this is repeated until the location of the minimum μ converges. The minimum μ is determined by inspecting that the first derivative of μ with ψ is zero, the second derivative is greater than zero and that the value of μ is lowest over the entire set. The gradients required are assessed numerically using finite differencing. This type of process for finding the global minimum is known as an unconstrained heuristic-based bracketing optimisation [194]. A flow chart of this process is given in fig. 4.16.

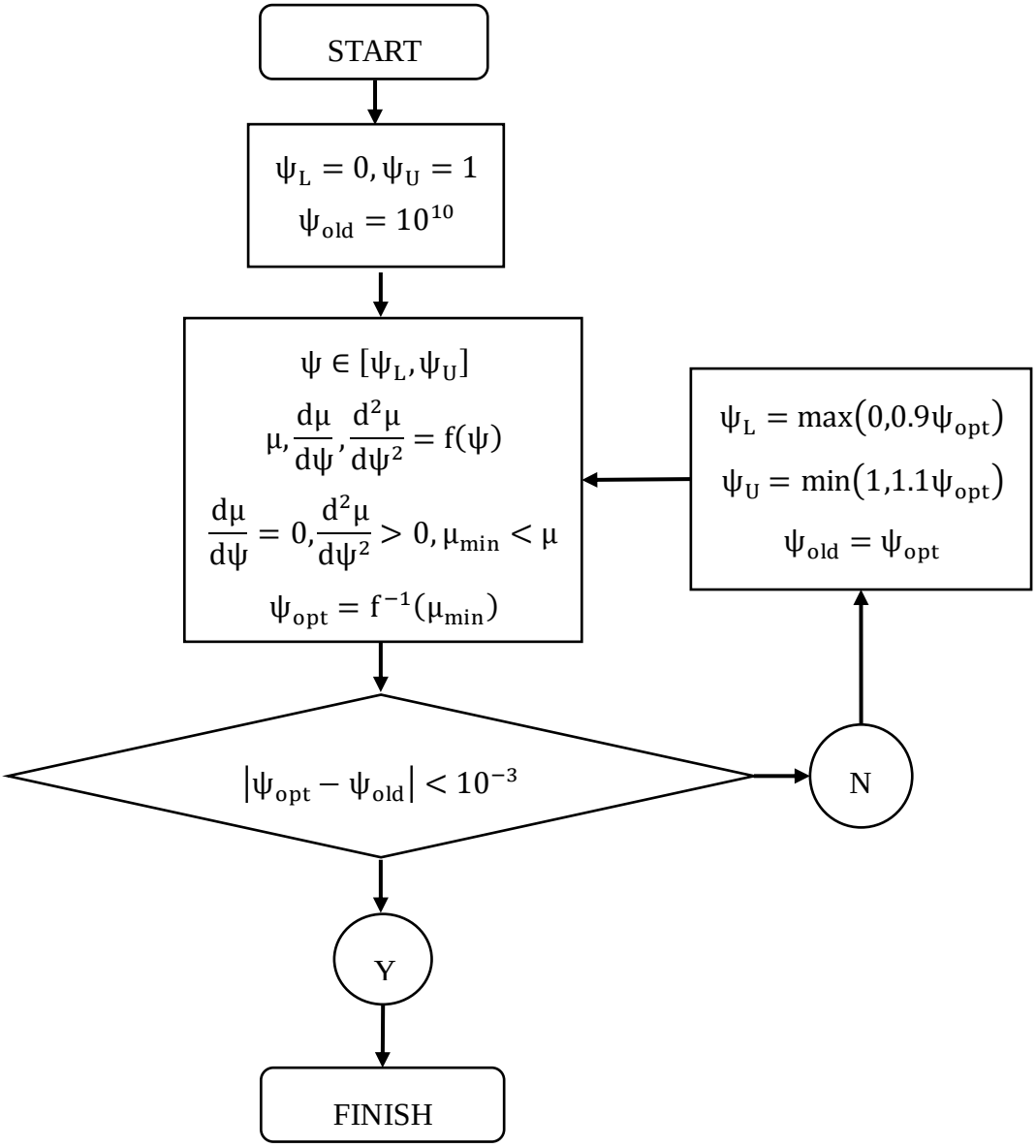

Fig. 4.16 – Flow chart of the bracketing optimisation method

4.10 Summary

In this chapter the theoretical formulation and numerical solution procedure for the two-scale EHL method were presented for a one-dimensional converging tilted-pad bearing geometry, additional comments were made as to how the method can be expanded to two-dimensional problems. Details of the simulations at both scales are described along with the RSM used to couple them. Further to this an explanation of how optimisation of topography can be performed is given along with the solution procedure used to achieve this.

Chapter 5 – Two-Scale Elastohydrodynamic Lubrication: Effect of Three-Dimensional Topography in Tilted-Pad Bearings

5.1 Introduction

This chapter describes solutions generated from the two-scale method for a tilted-pad bearing with a single three-dimensional topography. Results presented and discussed here are divided into three subsections. The first establishes the numerical accuracy of the two-scale method, the second subsection analyses the small scale simulations, and the third analyses contains results relating to smooth and textured surfaces at the large scale.

5.2 Numerical Accuracy

The numerical accuracy for the two-scale method is assessed through grid independence of simulations at both scales and validation of the RSM used to couple these scales.

5.2.1 Grid Independence

Small scale grid independence was determined by varying the total number of elements for each case and comparing the resulting mass flow rate. The absolute percentage error in mass flow rate against the mass flow rate with the largest number of elements (31,250) is plotted in fig. 5.1 for a topography amplitude α = 7.5 μm. In this simulation compressibility, piezoviscosity, and non-Newtonian (shear-thinning) behaviour were included, the cell pressure p = 5 MPa, the pressure gradient $\frac{dp}{dx}$ = -10 MPa/mm, and the gap g = 25 μm.

From fig. 5.1 it was seen that the change in percentage error is reduced as the number of nodes increases illustrating convergence. 16,000 elements were chosen for this study as this allowed the small scale phenomena to be accurately captured at a moderate computational cost. Each small scale simulation at this resolution took between 15 and 20 minutes to compute on a 2.7 GHz 6 core processor, whereas at 31,250 elements this was more in the region of 40 minutes. 8 GB of RAM (Random

Access Memory) was required for the selected resolution, with the 31,250 elements simulations requiring upwards of 20 GB of RAM.

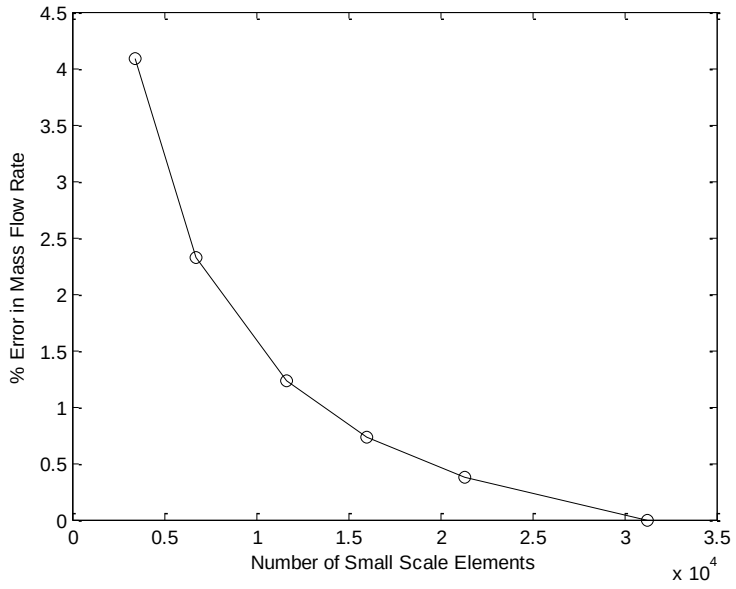

Fig. 5.1 – Small scale grid independence

Grid independence at the large scale is considered by comparison of the mass flow rate predicted by the solver for a set case and geometry over a range of the number of nodes. Using the metamodel generated from small scale data where the topography amplitude α = 5 μm and the flow phenomena are included the absolute percentage error in mass flow rate against the mass flow rate with the largest number of nodes (4,000) was compared. The pad length, tilt angle, and load capacity were set to L_p = 22.5 mm, φ = 0.05°, and W = 100 kN respectively and the result shown in fig. 5.2. All large scale simulations in this chapter use the IVP shooting method outlined in section 4.8.3 for large scale pressure solving.

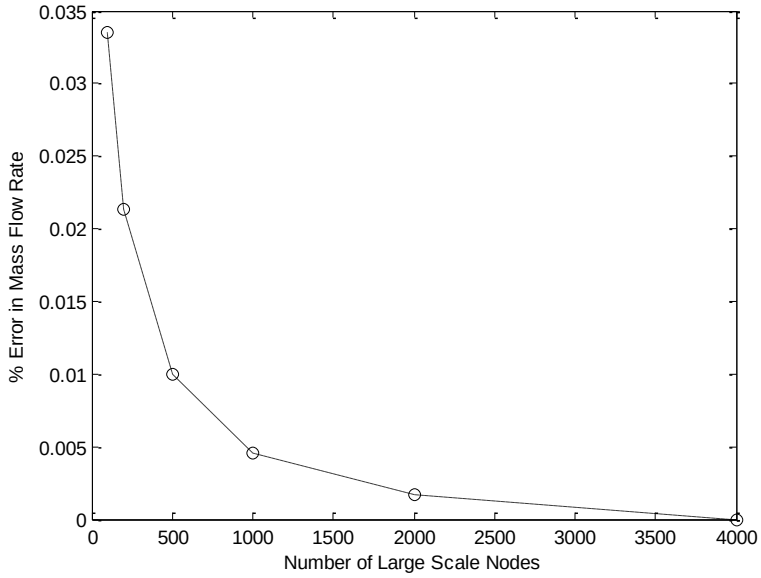

Fig. 5.2 – Large scale grid independence

Convergence is achieved as the error in the resulting mass flow rate tends toward zero with increasing discretisation. In light of the findings presented in fig. 5.2 a conservative 1,000 nodes was chosen as an appropriate compromise between accuracy and computational expense. The 1,000 node simulation took ~5 minutes to compute at 1.5GB of RAM and the 4,000 node simulation took ~20 minutes at 3.5 GB of RAM.

5.2.2 RSM Accuracy

The response surface approach used to couple the large and small scale simulations was validated by assessing the accuracy in predicting Reynolds equation for incompressible, isoviscous flow against the smooth surface case and from homogenised small scale simulations where topography, compressibility, piezoviscosity, and non-Newtonian behaviour are present. To achieve this a 200 point DoE for each set of the small scale simulations was specified using the permutation GA of Bates, et al. [92]. These DoEs were subsequently populated and the corresponding metamodels validated using k-fold CV with $k = 60$. These metamodels were then applied to a large scale simulation under typical operating conditions for which the load carrying capacity of the bearing was set to W = 100 kN, the pad length and tilt angle were L_p = 22.5 mm and φ = 0.05° respectively and the topography amplitudes investigated were α = 0 and 7.5 μm.

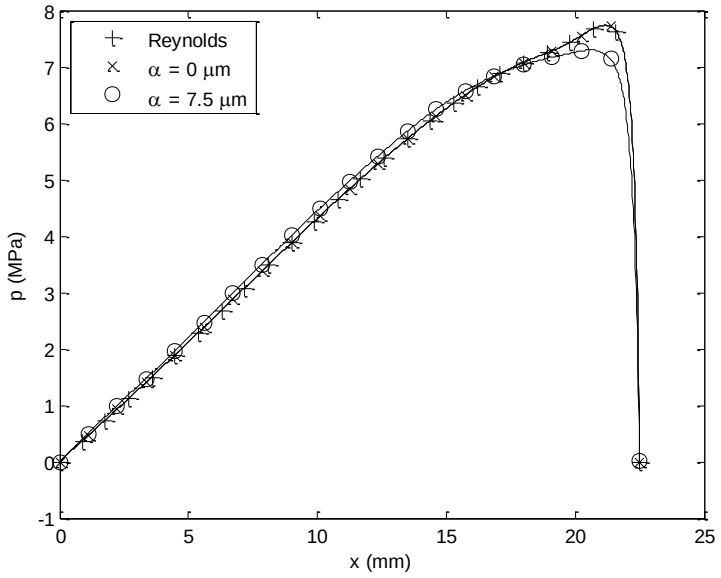

Fig. 5.3 – Pressure distributions with and without topography

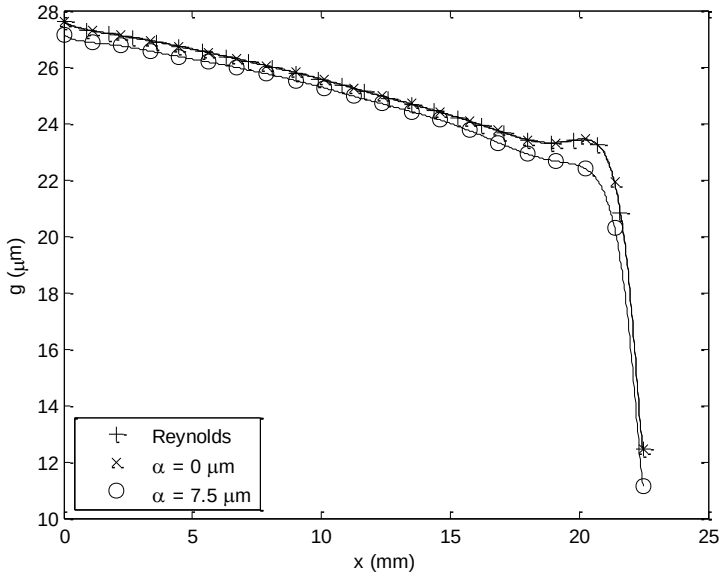

Fig. 5.4 – Film thickness distributions with and without topography

From figs. 5.3 and 5.4 it can be seen that the difference between the solution of the Reynolds equation and smooth surface pressure and film thickness solutions is negligible, demonstrating the accuracy of the multiscale method in modelling the smooth surface lubrication problem. In comparison to the smooth surface case it can be seen from fig. 5.3 that due to the presence of topography and flow phenomena the resulting maximum pressure reached in the bearing is lower and occurs closer toward the inlet. This has an impact on the distribution of deformation and as such the shape of

the film thickness seen in fig. 5.4. The film thickness is significantly decreased in magnitude across the length of the bearing.

In order to validate the trends presented in figs. 5.3 and 5.4 results generated at the large scale through the metamodel are compared against the exact corresponding small scale simulations. The mass flow rate as predicted by the large scale solver is compared to the corresponding mass flow rate determined by separate simulations at the small scale. Three locations along the distributions of pressure gradient, pressure and gap: maximum gap (0 mm), maximum pressure (19.75 mm), and minimum gap (22.5 mm) are selected and the results of this test are tabulated in Table 5.1.

	Large Scale x-Coordinate		
Parameter	0 mm	19.75 mm	22.5 mm
Pressure gradient, $\frac{dp}{dx}$	0.4596 MPa/mm	0 MPa/mm	-31.74 MPa/mm
Pressure, p	0 MPa	7.297 MPa	0 MPa
Gap, g	27.14 μm	22.08 μm	11.14 μm
% error in mass flow rate	-0.261 %	-0.099 %	0.833 %

Table 5.1 – Percentage error in mass flow rate inclusive of topography and flow phenomena

The absolute percentage error in mass flow rate predicted between the metamodel and exact small scale simulations is < 1% for all cases considered. This indicates that the metamodel is accurately capturing the effects of topography and flow phenomena upon bearing performance. This also validates the choice in size and spread of the DoE used.

5.3 Small Scale Solutions

Contours of pressure at the FSI interface and sliding wall are shown for a representative example small scale simulation in figs. 5.5 and 5.6 respectively. Fig. 5.7 shows, for the same conditions, pressure contours in the film obtained from the smooth surface model. The corresponding contours of film thickness for this example simulation are given in Fig. 5.8. In this simulation the cell pressure p = 5 MPa, the

pressure gradient $\frac{dp}{dx}$ = -20 MPa/mm, the gap g = 10 μm, the topography amplitude α = 7.5 μm.

From figs. 5.5 and 5.6 it is shown that pressure in the small scale domain is not constant through the film due to the presence of topography and use of the Navier-Stokes equations to describe fluid flow. This is in contrast to that predicted by the smooth surface model at this scale under the same conditions (fig. 5.7). The mass flow rate predicted by the Navier-Stokes solution was found to be 31.23 % greater than that obtained from the smooth surface model. The numerical cost of the Navier-Stokes solution was 193.0 % of the smooth surface solution. It is also shown in figs. 5.5 and 5.6 that the jump in pressure over the domain which leads to the homogenised pressure gradient is not uniformly distributed. As such the cell pressure and load-per-unit-area at this scale differ and subsequently need to be defined separately. The distribution of film thickness shown in fig. 5.8 is similar to that of the topography modelled such that as the solid spring column moves the shape of topography is maintained, although local deformation of topography does occur and is at least an order of magnitude or more smaller than average change in film thickness over the domain. The difference in film thickness between the upstream and downstream boundaries, which generates the difference in area that leads to the near-periodic boundary condition for velocity, is small but not negligible. With the result that the velocity field varies slowly from one cell to the next remaining consistent with the HMM used to derive the method.

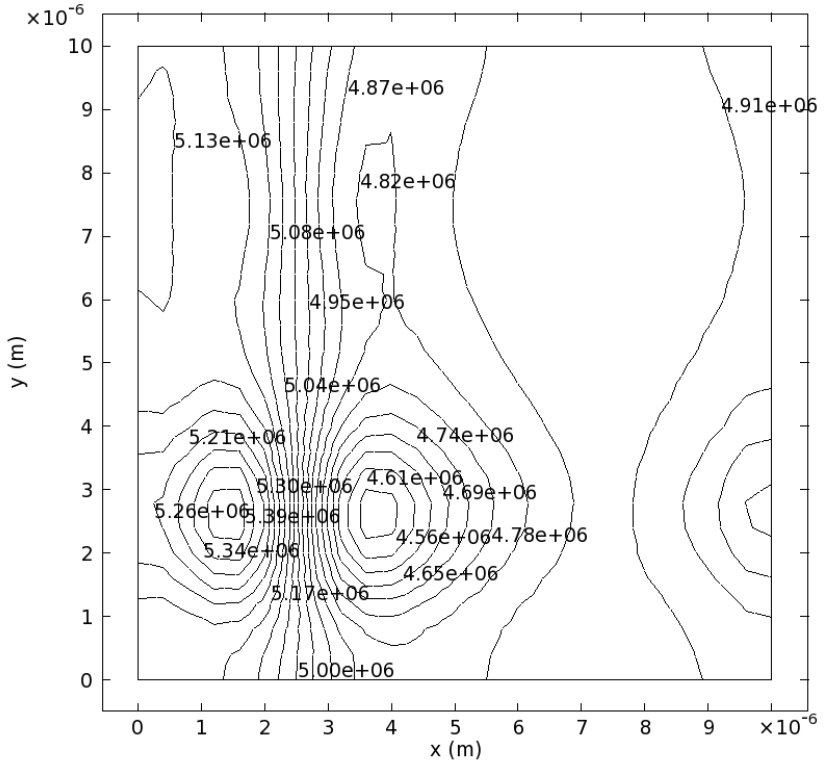

Fig. 5.5 – Contours of pressure at the FSI interface in Pa, $\frac{dp}{dx}$ = -20 MPa/mm, p = 5 MPa, g = 10 μm

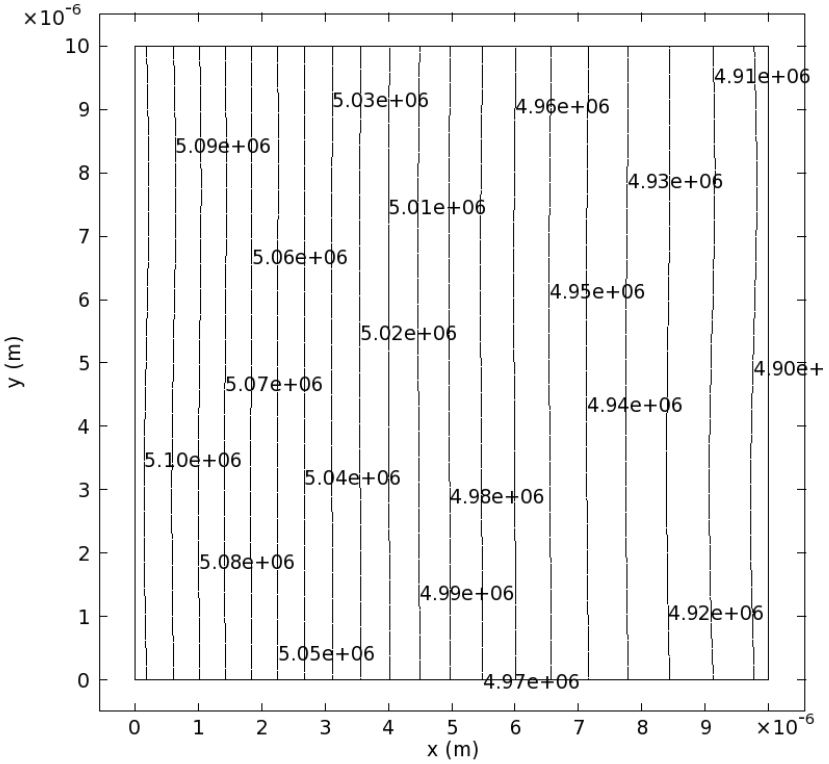

Fig. 5.6 – Contours of pressure at the sliding wall in Pa, $\frac{dp}{dx}$ = -20 MPa/mm, p = 5 MPa, g = 10 μm

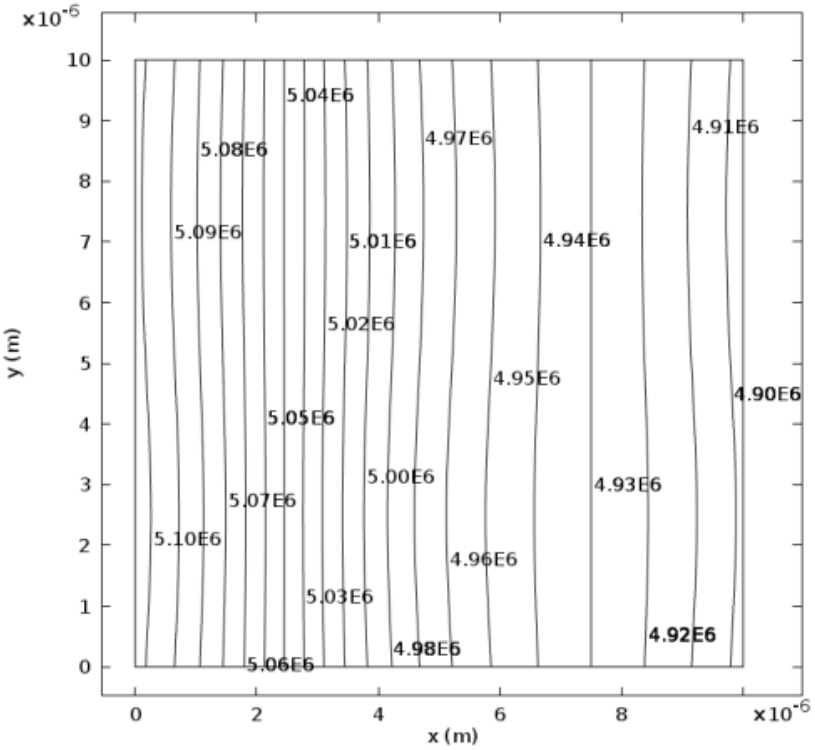

Fig. 5.7 – Contours of pressure in the film obtained from the smooth surface model in Pa,

$\frac{dp}{dx}$ = -20 MPa/mm, p = 5 MPa, g = 10 μm

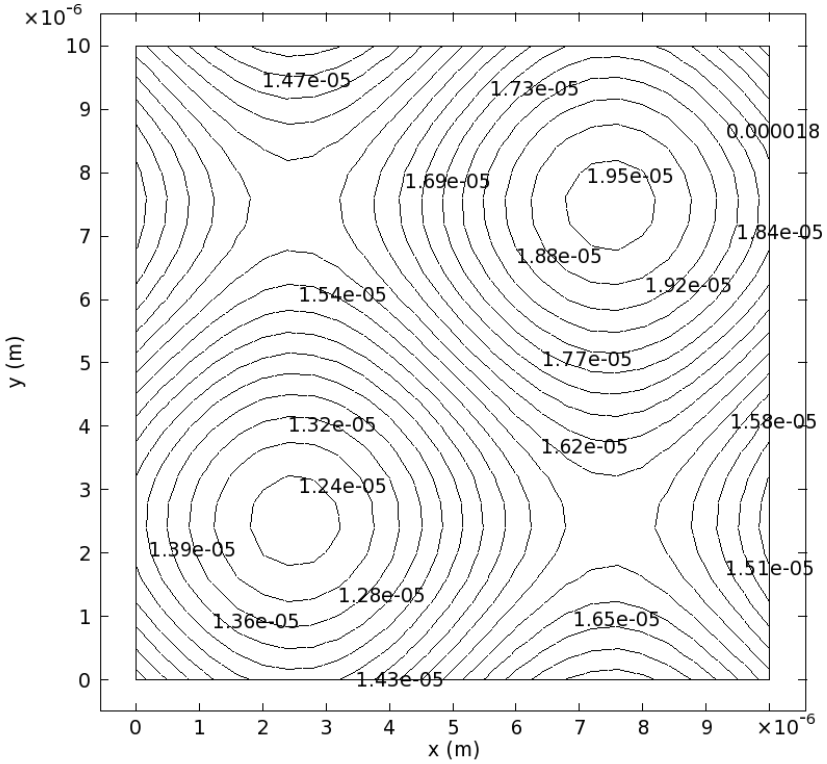

Fig. 5.8 – Contours of film thickness in m,

$\frac{dp}{dx}$ = -20 MPa/mm, p = 5 MPa, g = 10 μm

Contours of small scale velocity components (u, v, w) from the same example small scale simulation as figs. 5.7 and 5.8 are presented in fig. 5.9 for two planes cut through the domain at $x = L/4$ and $x = 3L/4$ and in fig. 5.10 for two planes cut through the domain at $y = L/4$ and $y = 3L/4$. From figs. 5.9 and 5.10 the near-periodic boundary condition for velocity can be visualised where the flow entering and exiting the fluid domain is almost identical at the boundaries, slight differences in the contours can be attributed to deformation of the FSI interface and compressibility of the lubricant.

Fluid is driven through the domain by entrainment from the moving wall and the pressure jump leading to a majority of flow travelling in the x-coordinate direction as shown in figs. 5.9.1a, 5.9.2a, 5.10.1a, and 5.10.2a. The flow in the x-direction is slightly faster than the speed of the moving wall before reducing to the no-slip condition at the FSI interface. Slight perturbation of the x-component velocity field from that which would be given by the smooth surface model is exhibited and the magnitude of this is linked to the inclusion of y and z velocity components.

Figs. 5.9.1b, 5.9.2b, 5.9.1c, and 5.9.2c indicate that in the presence of topography flow across the thickness of the film, cross-flow, and recirculation are observed. The patterns seen in these are non-symmetrical and can be attributed to the inclusion of inertial terms in the Navier-Stokes equations (Eqs. (4.13) and (4.14)) used to govern flow at this scale. A single local minimum is observed for the y-component of velocity in both slices which lies directly within the domain. The centre of this local minimum moves from one slice to the next indicating that this flow feature exists entirely along the x-direction of the domain. The z-component of velocity indicates a region containing a local maximum which exists between the near-periodic boundaries of the fluid domain and similarly extends along the x-direction of the domain.

The y-component of velocity in the x-z plane seen in figs. 5.10.1b and 5.10.2b indicates a local minimum which exists across the near-periodic boundaries and another within a central region of the domain. However fig. 5.10.2b indicates that two minima exist across the boundary whereas fig. 5.10.1b only shows one. Figs. 5.10.1c and 5.10.2c demonstrate the growth of a maximum and a minimum for the z-component of velocity along the y-direction of the fluid domain, the maximum is located within the domain and the minimum exists between the near-periodic boundaries.

	x = L/4	x = 3L/4
u	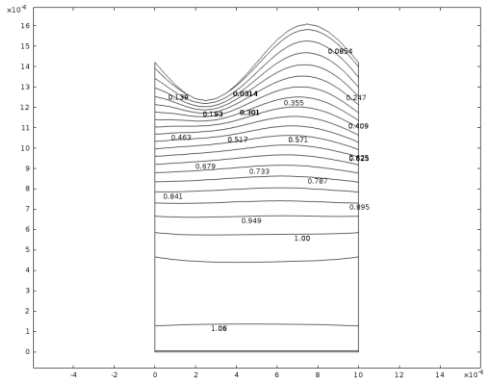	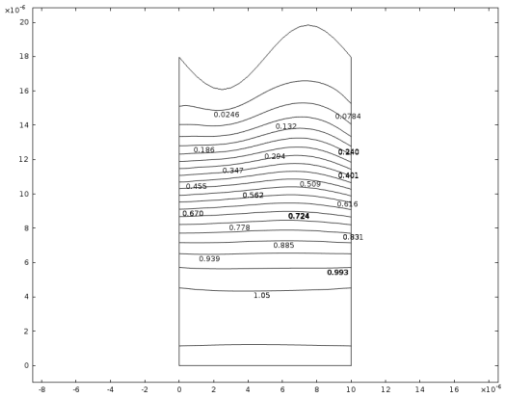
	Fig 5.9.1a – u vs. y and z at x = L/4	Fig 5.9.2a - u vs. y and z at x = 3L/4
v	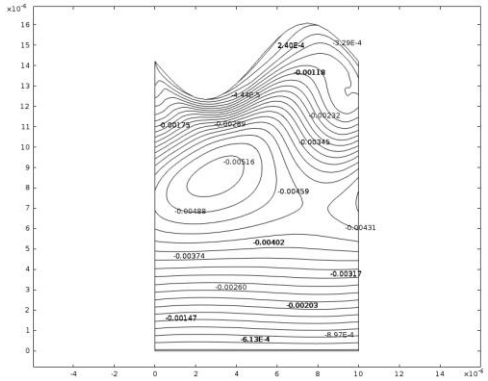	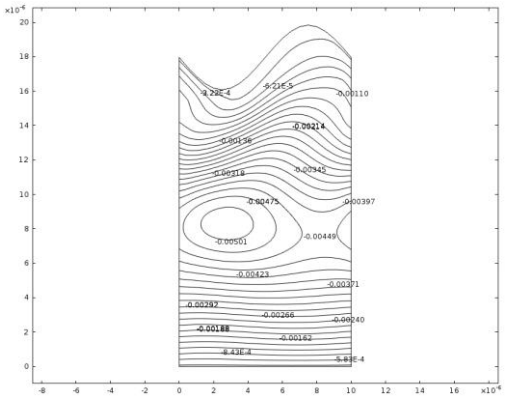
	Fig 5.9.1b - v vs. y and z at x = L/4	Fig 5.9.2b - v vs. y and z at x = 3L/4
w	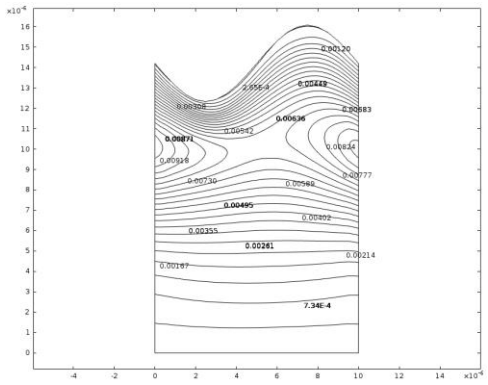	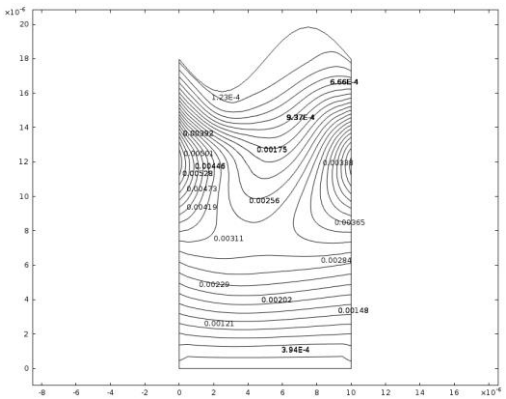
	Fig 5.9.1c - w vs. y and z at x = L/4	Fig 5.9.2c - w vs. y and z at x = 3L/4

Fig. 5.9 – Contours of small scale velocity components in m/s in the y-z plane, $\frac{dp}{dx}$ = -20 MPa/mm, p = 5 MPa, g = 10 μm

	y = L/4	y = 3L/4
u	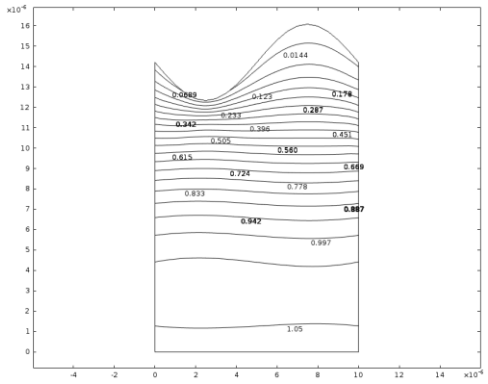	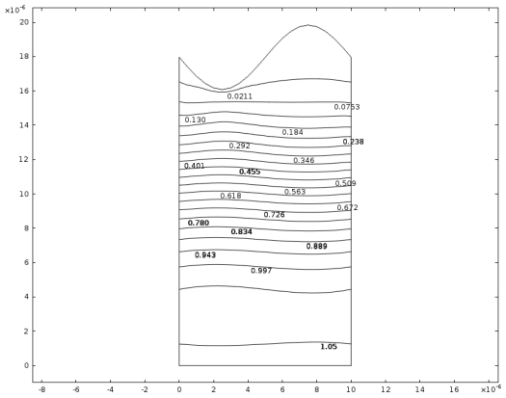
	Fig 5.10.1a – u vs. x and z at y = L/4	Fig 5.10.2a - u vs. x and z at y = 3L/4
v	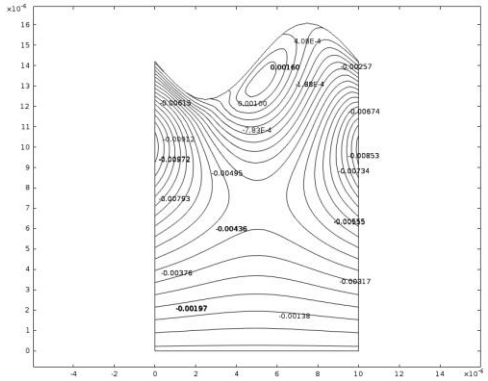	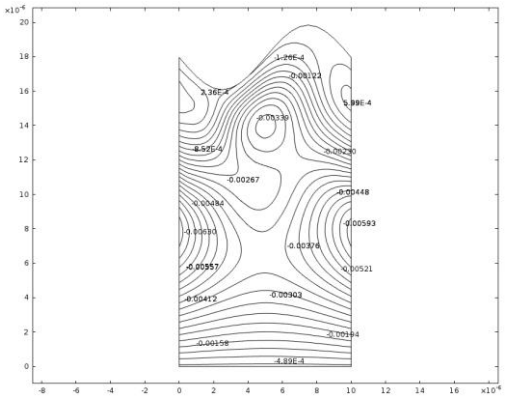
	Fig 5.10.1b - v vs. x and z at y = L/4	Fig 5.10.2b - v vs. x and z at y = 3L/4
w	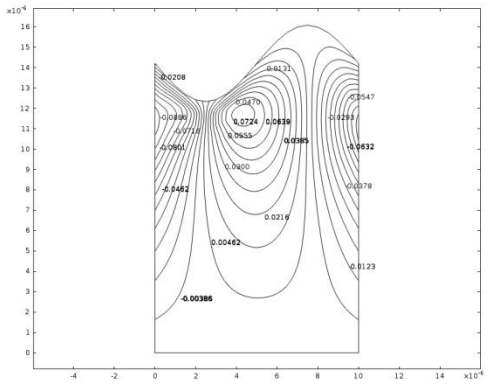	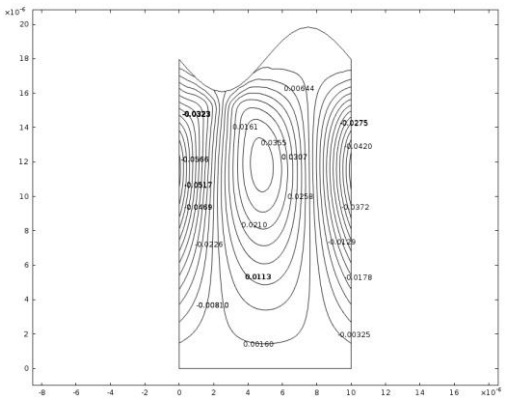
	Fig 5.10.1c - w vs. x and z at y = L/4	Fig 5.10.2c - w vs. x and z at y = 3L/4

Fig. 5.10 – Contours in m/s of small scale velocity components in m/s in the x-z plane, $\frac{dp}{dx}$ = -20 MPa/mm, p = 5 MPa, g = 10 μm

Figs. 5.11 and 5.12 show contours of pressure at the FSI interface and film thickness for an example simulation where $\frac{dp}{dx}$ = 10 MPa/mm, p = 5 MPa, and g = 10 μm. Comparison of these figures with figs. 5.7 and 5.8 allows the influence of pressure gradient on flow features to be inspected when pressure and film gap are kept constant.

Fig. 5.11 shows how pressure is increased over the length of the domain due to the positive pressure jump, whereas in fig. 5.7 pressure is reduced from one side of the domain to the other. Fig. 5.7 exhibits a sharp increase and decrease in pressure near the region which corresponds to the minimum film thickness. The maximum pressure is spread over the length of the domain perpendicular to the direction of flow in both figures. The maximum pressure is reached by a much steeper gradient in fig. 5.7 than fig. 5.11, and in fig. 5.11 there is no sudden drop to a minimum pressure after the maximum. This indicates that a positive pressure gradient has the effect of smoothing the pressure distribution over the domain. Both figures also represent a plateau of pressure near the region of maximum film thickness where the contour lines are sparse in these regions. The film thickness distributions presented in figs. 5.8 and 5.12 are almost identical, this indicates that the magnitude of the pressure gradient has a negligible effect on the deformation of the small scale simulations.

Velocity contours are presented for the same conditions as investigated above in figs. 5.13 and 5.14 and from which clear differences in the flow structure can be seen to that observed in figs. 5.9 and 5.10. Figs. 5.13.1a, 5.13.2a, 5.14.1a, and 5.14.2a all demonstrate that the x-component of velocity is dominated by entrainment from the moving wall and that it does not increase beyond this speed, contrasting the observations made from figs. 5.9 and 5.10. In these figures negative flow velocities travelling in the opposing direction to the moving wall motion is observed, this was not seen when a negative pressure gradient was applied.

Figs. 5.13.1b, 5.13.2b, 5.13.1c, and 5.13.2c illustrate that local maxima and minima of the y and z velocity components move significantly along the x-direction of the domain, which is in direct contrast to that shown in fig. 5.9. However figs. 5.14.1b, 5.14.2b, 5.14.1c, and 5.14.2c show that these flow features do not move far along the y-direction of the domain, which is consistent with that presented in fig. 5.10. In general, for the conditions investigated the magnitude of local maxima and minima for the y and z velocity components are smaller when a positive pressure gradient is applied over the domain than when a negative gradient is applied.

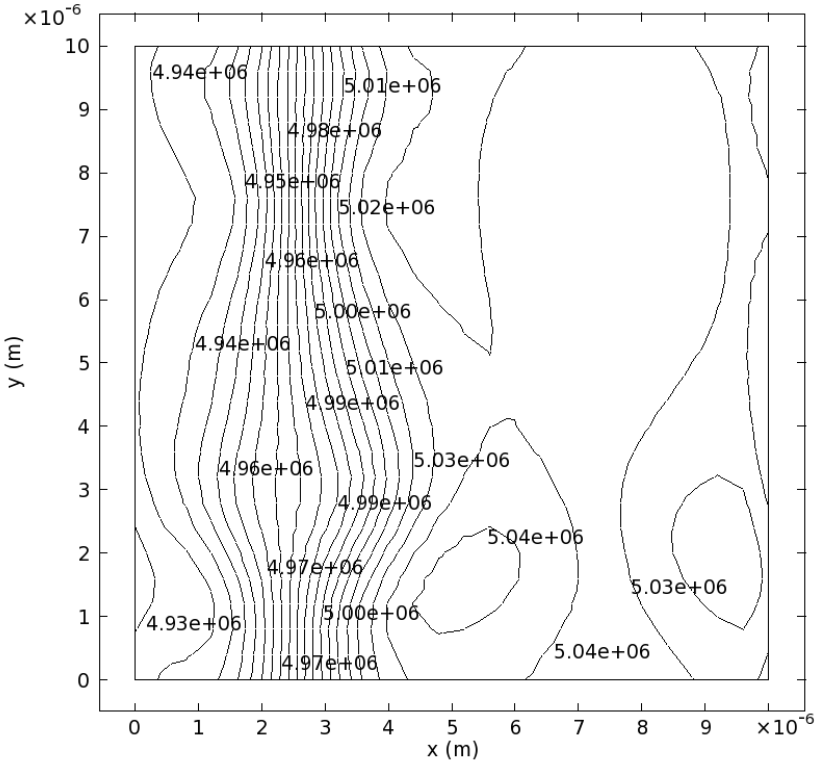

Fig. 5.11 – Contours of pressure at the FSI interface in Pa, $\frac{dp}{dx}$ = 10 MPa/mm, p = 5 MPa, g = 10 μm

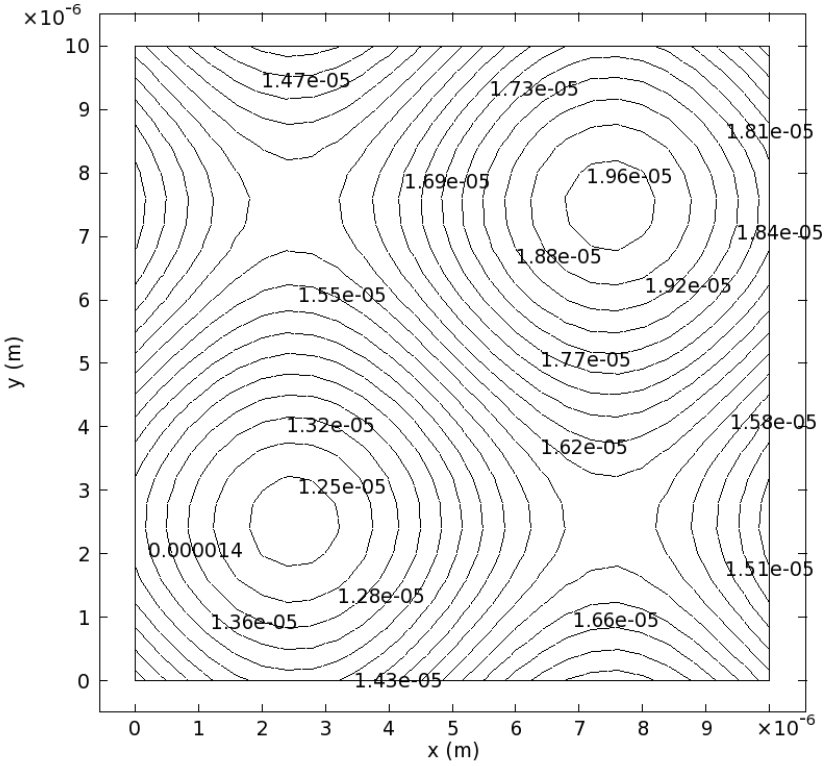

Fig. 5.12 – Contours of film thickness in m, $\frac{dp}{dx}$ = 10 MPa/mm, p = 5 MPa, g = 10 μm

	x = L/4	x = 3L/4
u	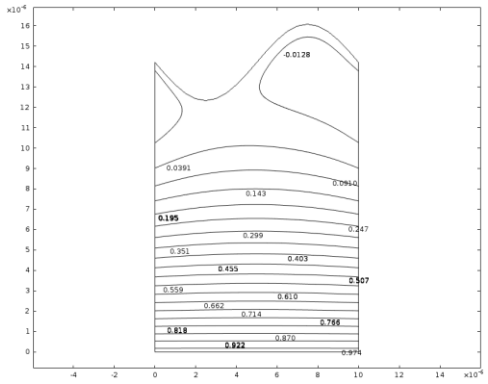	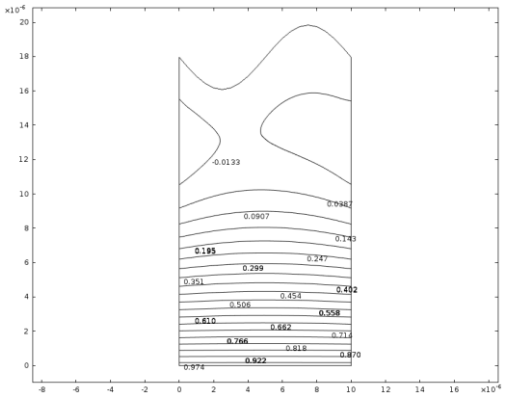
	Fig 5.13.1a – u vs. y and z at x = L/4	Fig 5.13.2a - u vs. y and z at x = 3L/4
v	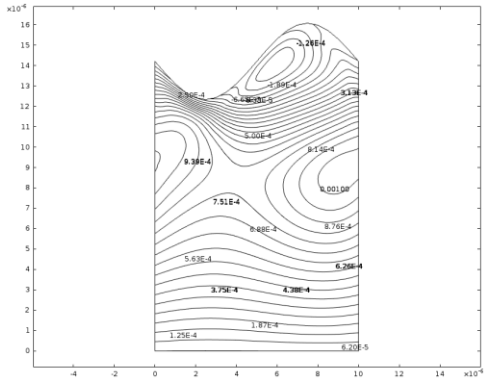	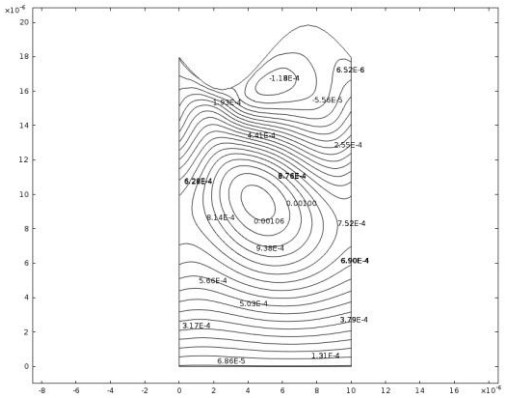
	Fig 5.13.1b - v vs. y and z at x = L/4	Fig 5.13.2b - v vs. y and z at x = 3L/4
w	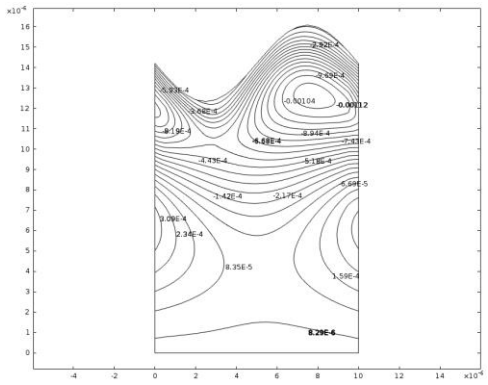	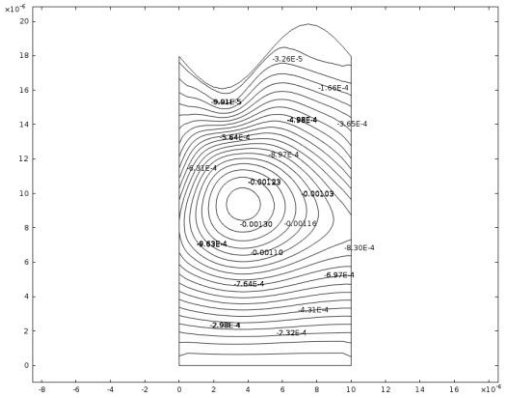
	Fig 5.13.1c - w vs. y and z at x = L/4	Fig 5.13.2c - w vs. y and z at x = 3L/4

Fig. 5.13 – Contours of small scale velocity components in m/s in the y-z plane, $\frac{dp}{dx}$ = 10 MPa/mm, p = 5 MPa, g = 10 μm

	y = L/4	y = 3L/4
u	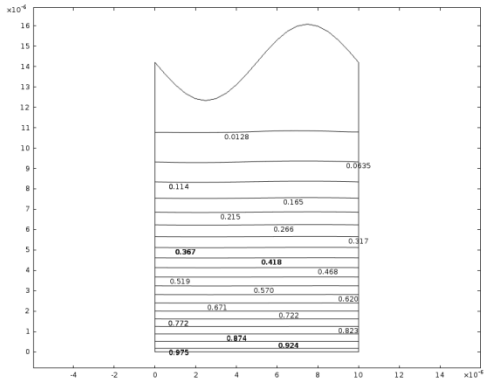	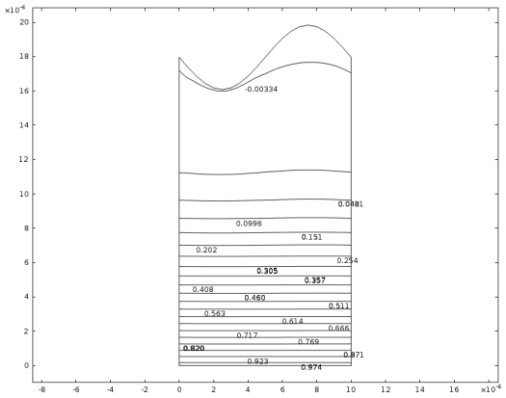
	Fig 5.14.1a – u vs. x and z at y = L/4	Fig 5.14.2a - u vs. x and z at y = 3L/4
v	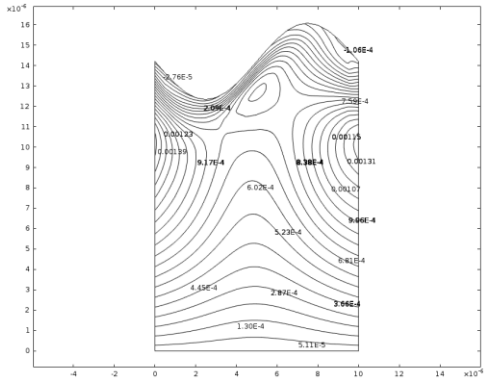	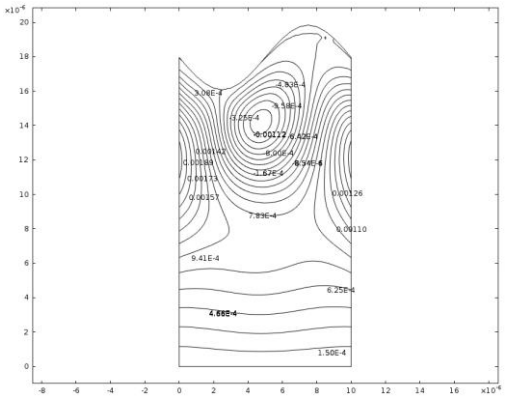
	Fig 5.14.1b - v vs. x and z at y = L/4	Fig 5.14.2b - v vs. x and z at y = 3L/4
w	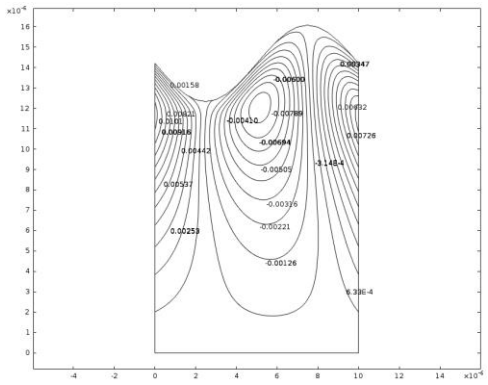	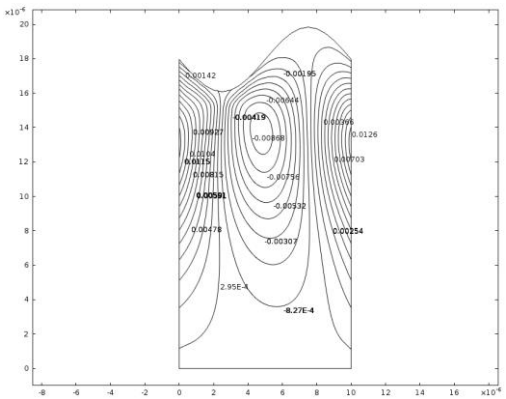
	Fig 5.14.1c - w vs. x and z at y = L/4	Fig 5.14.2c - w vs. x and z at y = 3L/4

Fig. 5.14 – Contours of small scale velocity components in m/s in the x-z plane, $\frac{dp}{dx}$ = 10 MPa/mm, p = 5 MPa, g = 10 μm

Figs. 5.15 – 5.18 show pressure, film thickness and velocity contours of a simulation where $\frac{dp}{dx}$ = 0 MPa/mm, p = 0 MPa, g = 10 μm and figs. 5.19 – 5.22 show the same but for a different simulation where $\frac{dp}{dx}$ = 10 MPa/mm, p = 0 MPa, g = 10 μm. These figures facilitate the investigation of the influence of pressure on the small scale simulations.

Figs. 5.15 and 5.19 demonstrate for both the conditions investigated that the profiles of pressure over the domain are similar but differ in magnitude by the constraint pressures specified. This leads to the conclusion that the constraint pressure does not have a large influence on the pressure distribution, contrasting the conclusion drawn from the effect of the pressure gradient. Figs. 5.16 and 5.20 support this conclusion because the film thickness distributions are also almost identical but shifted in magnitude by the amount of deformation caused by the constraint pressure, for the conditions investigated the amount by which the film thicknesses differ is approximately 5 μm.

Similar flow features are seen for both conditions investigated, as presented in figs. 5.17, 5.18, 5.21, and 5.22. For each velocity component and domain slice the contour plots presented show small differences at the two conditions.

The x-component of velocity across figs. 5.17, 5.18, 5.21, and 5.22 demonstrates that entrainment from the moving wall dominates the flow. Due to a zero pressure jump being applied over the domain the fluid is increased beyond the moving wall speed or driven to a value less than provided by the no-slip condition at the FSI interface. The y and z components of velocity presented across figs. 5.17, 5.18, 5.21, and 5.22 show that in all the slices taken very similar locations and magnitudes of local maxima and minima are given by the two sets of conditions. The differences in these flow features are not directly scalable by the difference in film thickness between the two conditions, indicating the non-linearity in the velocity field due to the presence of topography.

Despite the difference in pressure and subsequently film thickness for the two conditions it is interesting that there is very little difference in the flow. This indicates that pressure has little influence in determining the flow in the domain. However the difference in film thickness does lead to deviation between the two sets of results and if this was increased further then a larger difference would be observed.

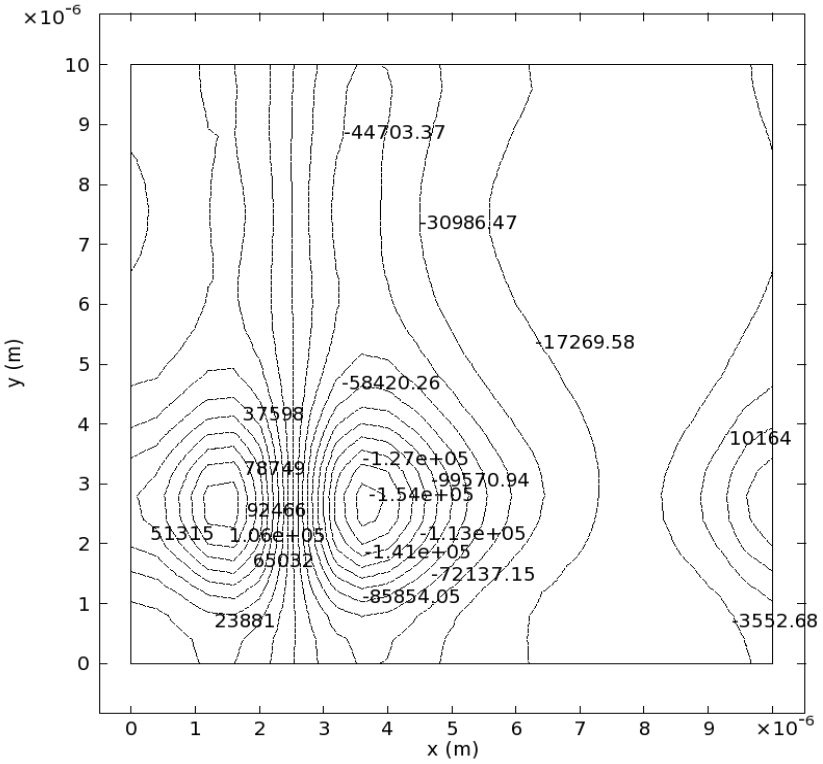

Fig. 5.15 – Contours of pressure at the FSI interface in Pa,

$\frac{dp}{dx}$ = 0 MPa/mm, p = 0 MPa, g = 10 μm

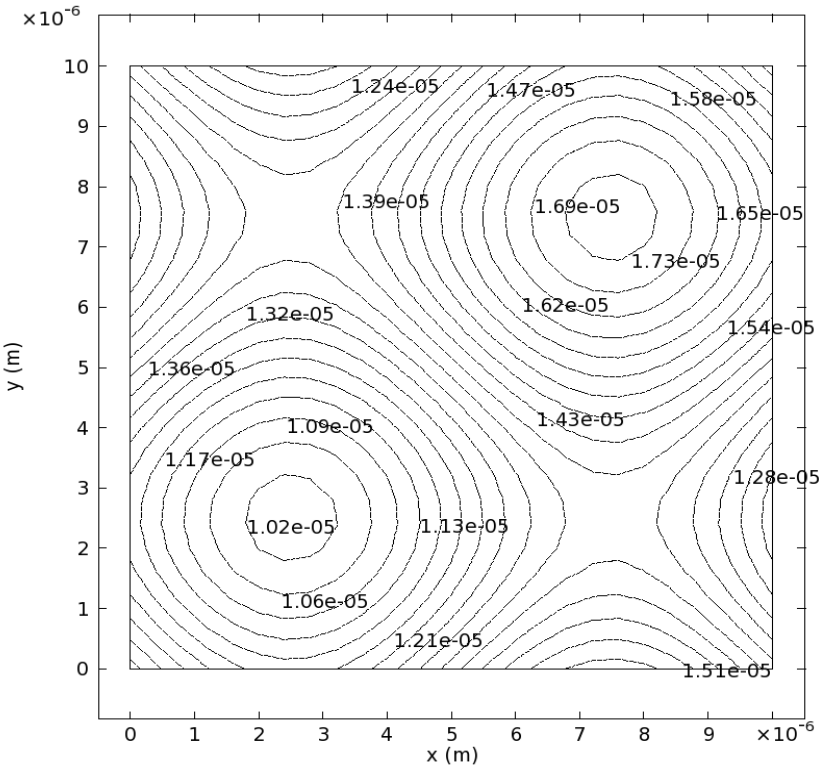

Fig. 5.16 – Contours of film thickness in m,

$\frac{dp}{dx}$ = 0 MPa/mm, p = 0 MPa, g = 10 μm

	x = L/4	x = 3L/4
u	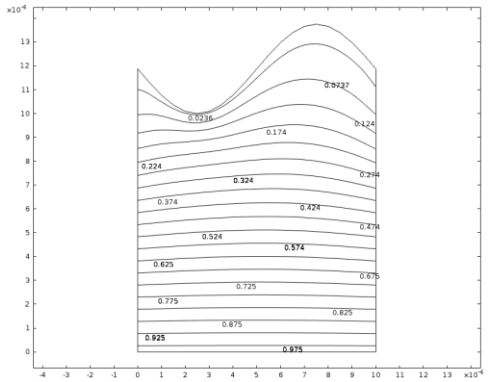	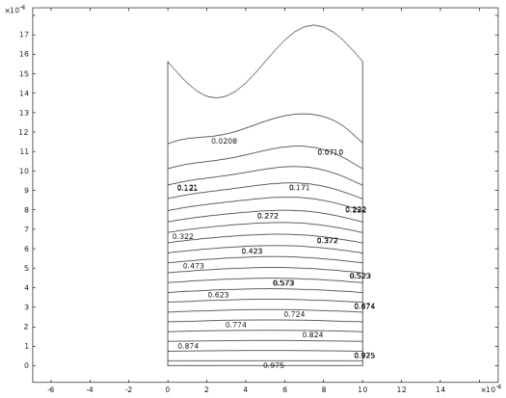
	Fig 5.17.1a – u vs. y and z at x = L/4	Fig 5.17.2a - u vs. y and z at x = 3L/4
v	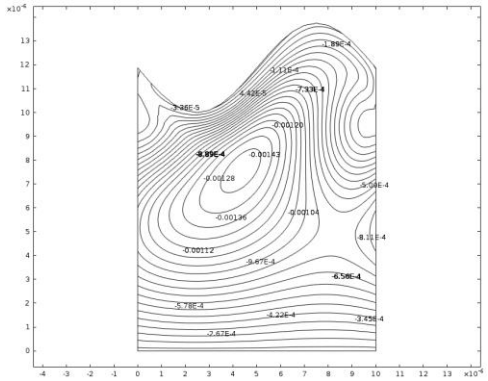	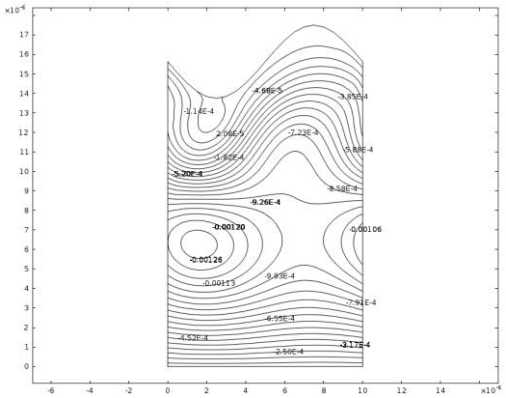
	Fig 5.17.1b - v vs. y and z at x = L/4	Fig 5.17.2b - v vs. y and z at x = 3L/4
w	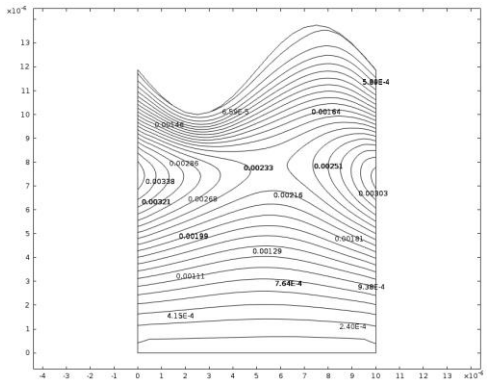	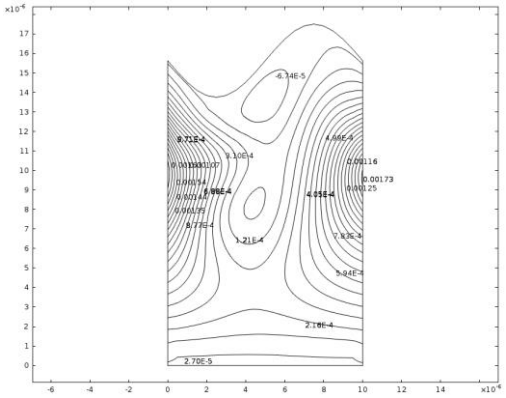
	Fig 5.17.1c - w vs. y and z at x = L/4	Fig 5.17.2c - w vs. y and z at x = 3L/4

Fig. 5.17 – Contours of small scale velocity components in m/s in the y-z plane, $\frac{dp}{dx}$ = 0 MPa/mm, p = 0 MPa, g = 10 μm

	y = L/4	y = 3L/4
u	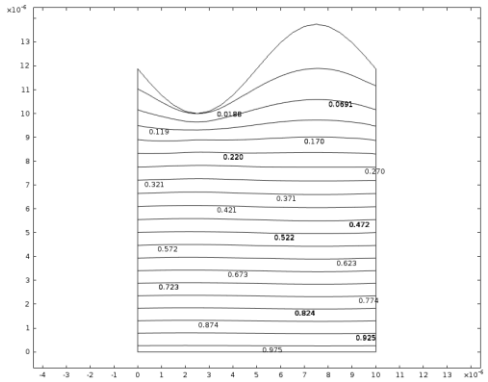	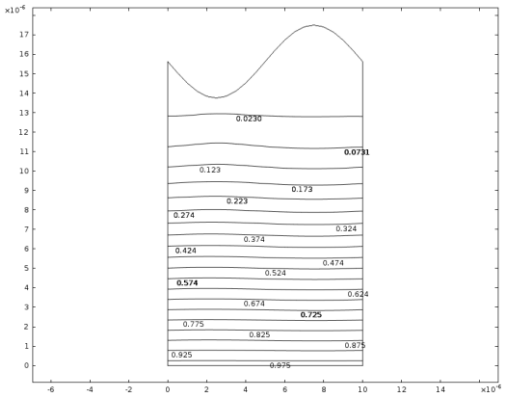
	Fig 5.18.1a – u vs. x and z at y = L/4	Fig 5.18.2a - u vs. x and z at y = 3L/4
v	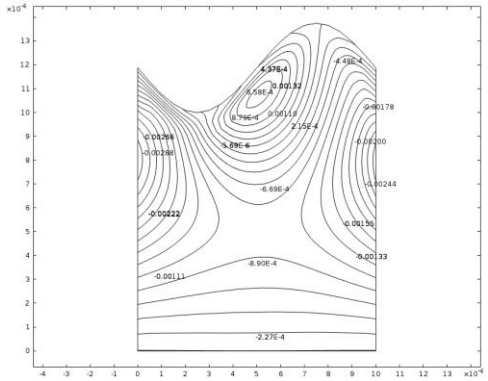	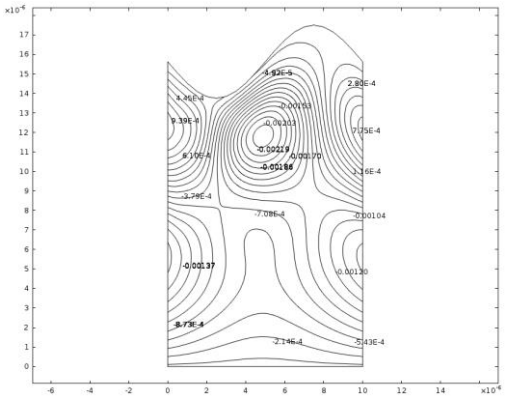
	Fig 5.18.1b - v vs. x and z at y = L/4	Fig 5.18.2b - v vs. x and z at y = 3L/4
w	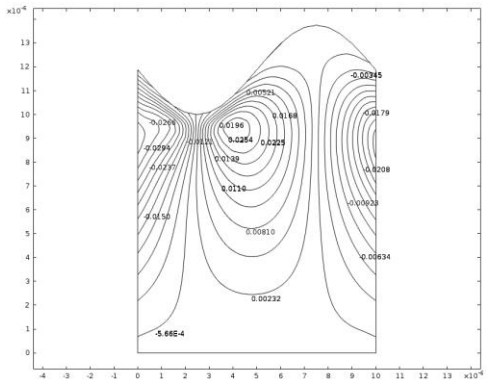	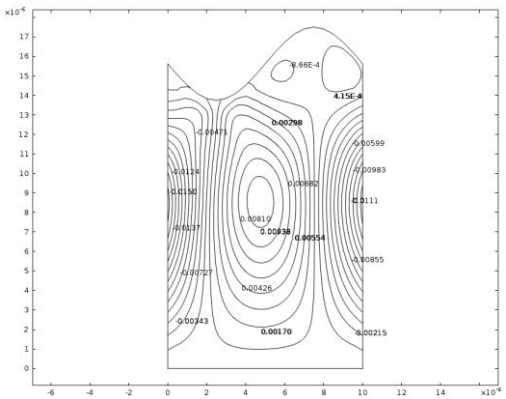
	Fig 5.18.1c - w vs. x and z at y = L/4	Fig 5.18.2c - w vs. x and z at y = 3L/4

Fig. 5.18 – Contours of small scale velocity components in m/s in the x-z plane, $\frac{dp}{dx}$ = 0 MPa/mm, p = 0 MPa, g = 10 μm

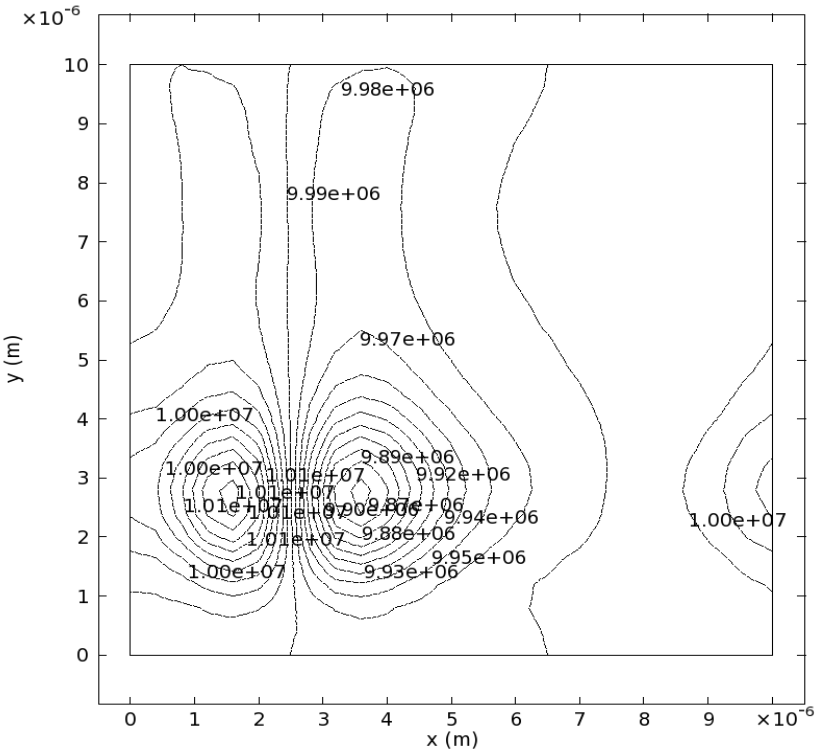

Fig. 5.19 – Contours of pressure at the FSI interface in Pa,

$\frac{dp}{dx}$ = 10 MPa/mm, p = 10 MPa, g = 10 μm

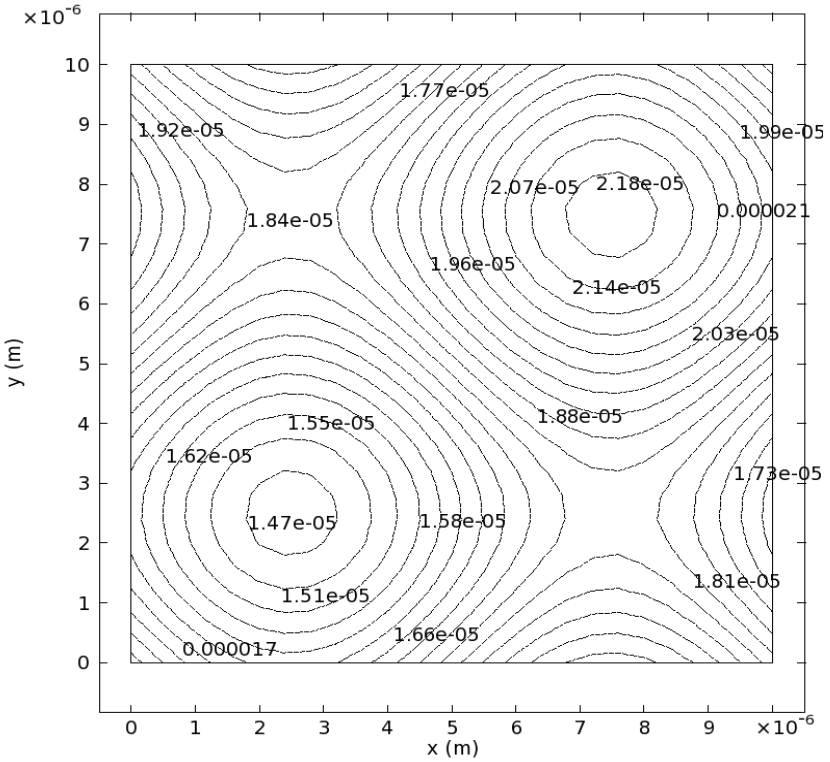

Fig. 5.20 – Contours of film thickness in m,

$\frac{dp}{dx}$ = 10 MPa/mm, p = 10 MPa, g = 10 μm

	x = L/4	x = 3L/4
u	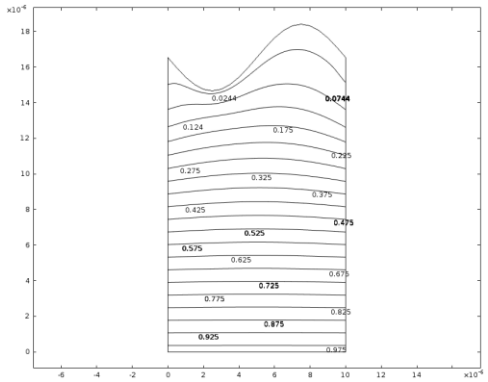	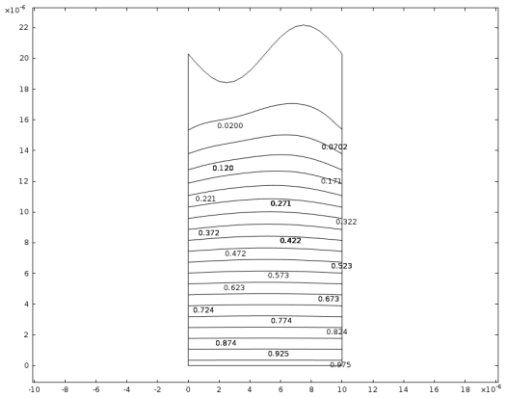
	Fig 5.21.1a – u vs. y and z at x = L/4	Fig 5.21.2a - u vs. y and z at x = 3L/4
v	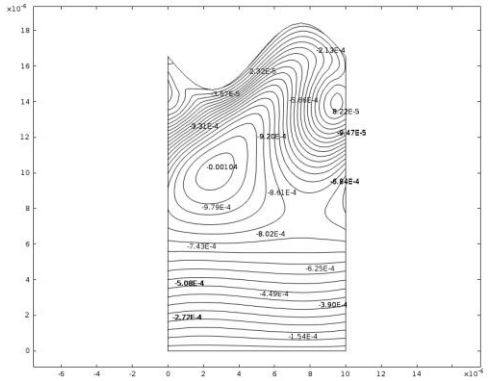	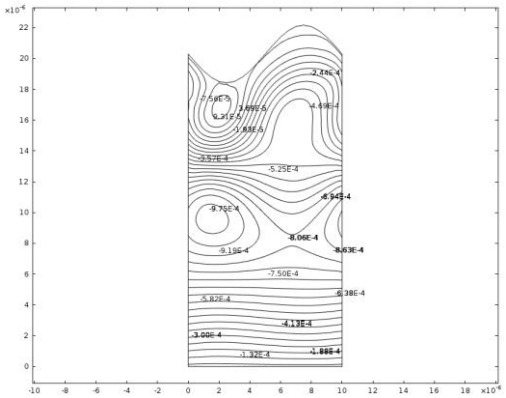
	Fig 5.21.1b - v vs. y and z at x = L/4	Fig 5.21.2b - v vs. y and z at x = 3L/4
w	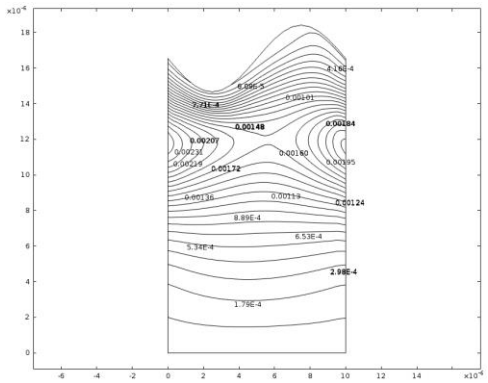	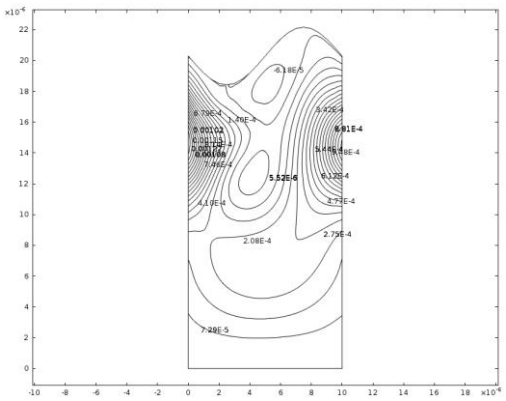
	Fig 5.21.1c - w vs. y and z at x = L/4	Fig 5.21.2c - w vs. y and z at x = 3L/4

Fig. 5.21 – Contours of small scale velocity components in m/s in the y-z plane, $\frac{dp}{dx}$ = 10 MPa/mm, p = 10 MPa, g = 10 μm

	y = L/4	y = 3L/4
u	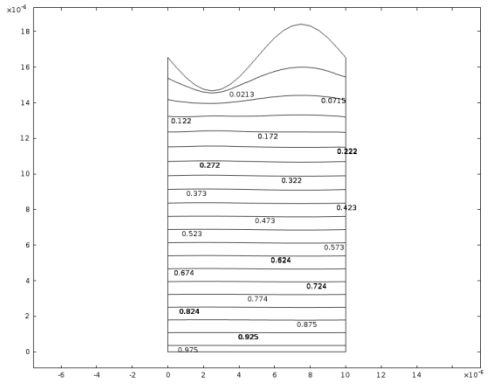	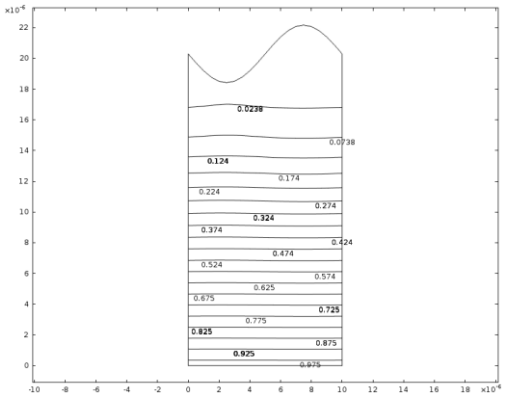
	Fig 5.22.1a – u vs. x and z at y = L/4	Fig 5.22.2a - u vs. x and z at y = 3L/4
v	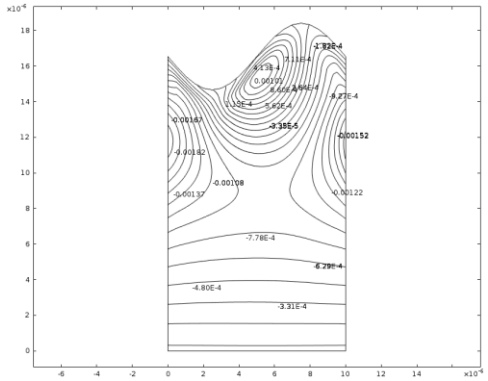	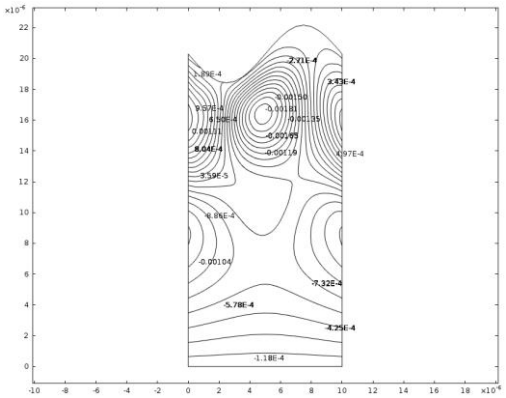
	Fig 5.22.1b - v vs. x and z at y = L/4	Fig 5.22.2b - v vs. x and z at y = 3L/4
w	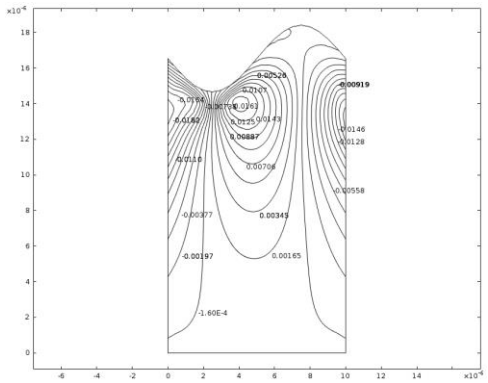	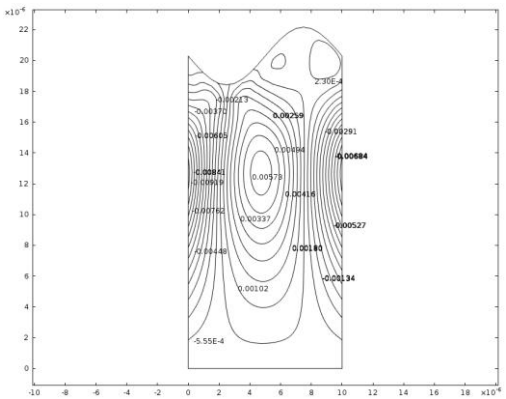
	Fig 5.22.1c - w vs. x and z at y = L/4	Fig 5.22.2c - w vs. x and z at y = 3L/4

Fig. 5.22 – Contours of small scale velocity components in m/s in the x-z plane, $\frac{dp}{dx}$ = 10 MPa/mm, p = 10 MPa, g = 10 μm

Figs. 5.23 – 5.26 show pressure, film thickness and velocity contours of a simulation where $\frac{dp}{dx}$ = 0 MPa/mm, p = 5 MPa, g = 5 μm and figs. 5.27 – 5.30 show the same but for a simulation where $\frac{dp}{dx}$ = 0 MPa/mm, p = 5 MPa, g = 30 μm. These figures facilitate inspection of the influence of film thickness on the small scale simulations.

Pressure contours for the two conditions presented in figs. 5.23 and 5.27 show similar trends whereby the maximum pressure is located near the minimum film thickness and that the minimum pressure is located near to this region. However for the small film thickness simulation in fig. 5.23 the steepness in the pressure distribution and magnitude of the pressure maximum are larger than that shown for the larger film thickness in fig. 5.27. Figs. 5.24 and 5.28 illustrate that the profile of film thickness over the domain are consistent at the two conditions investigated, meaning that the topography is not altered between the two simulations. However the film thickness differs in magnitude by the amount specified for the two conditions and that which deformation dictates.

Velocity contours for the two simulations are presented in figs. 5.25, 5.26, 5.29, and 5.30. Investigating the x-component of velocity indicates that entrainment of the moving wall dominates such that most of the fluid travels parallel to it. Due to the presence of topography and both y and z flow components a slight deviation of the x-component of velocity to that would be predicted from the smooth surface model is observed.

The y and z velocity components observed in the y-z plane from figs. 5.25 and 5.29 show that some similarities exist in the flow features between the two conditions. The z component of velocity has a local maximum which exists at the near-periodic boundaries and can be seen across all figs. 5.25.1c, 5.25.2c, 5.29.1c, and 5.29.2c. The y component is less consistent where the centre of the observed local minimum moves between figs. 5.25.1b and 5.25.2b and in figs. 5.29.1b and 5.29.2b the local maxima and minima seen are smaller in magnitude but more of them exist. Inspection of figs. 5.26 and 5.30 shows that for the y and z velocity components in the x-z plane there exists a consistent set of flow features observed under both conditions. More complexity in the flow field is observed where the film thickness is larger, however the magnitude of these flow features is smaller than for the small film thickness case. Overall the effect of increasing film thickness on the flow field is to reduce the strength of the cross-flow and flow across the film, as well as introducing more local maxima and minima.

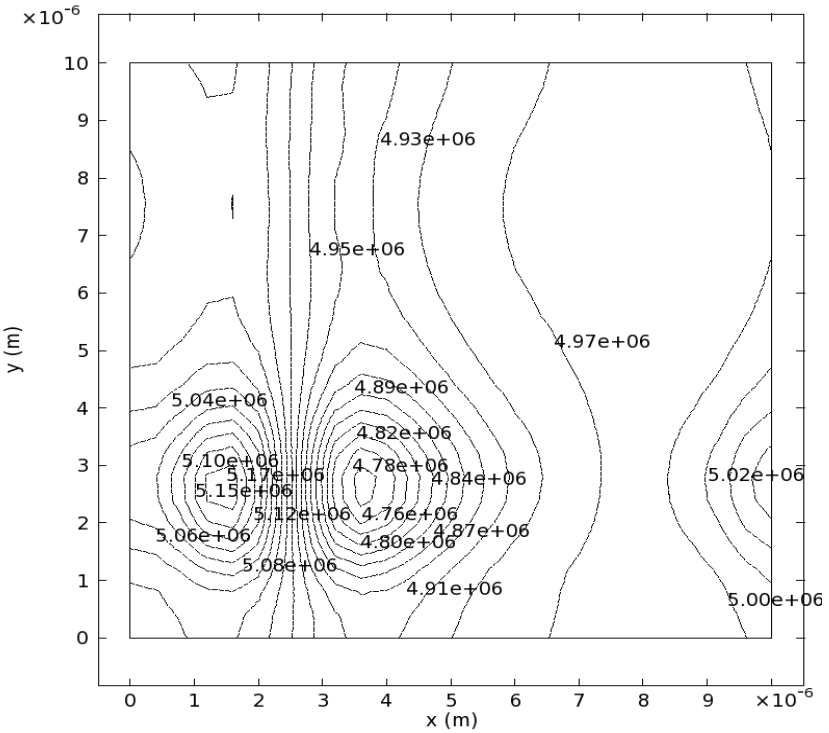

Fig. 5.23 – Contours of pressure at the FSI interface in Pa,

$\frac{dp}{dx}$ = 0 MPa/mm, p = 5 MPa, g = 5 μm

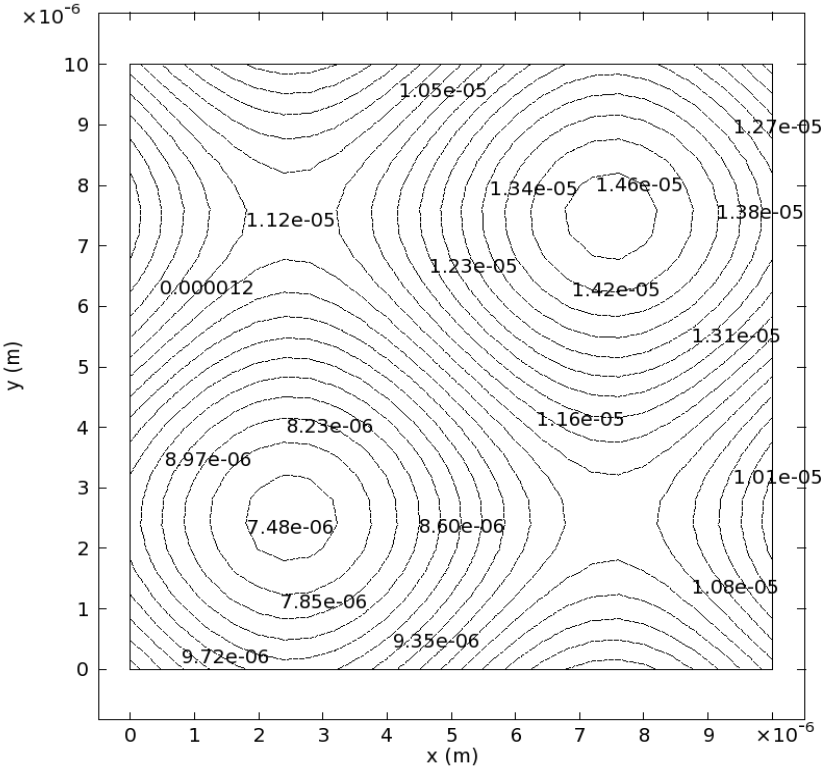

Fig. 5.24 – Contours of film thickness in m,

$\frac{dp}{dx}$ = 0 MPa/mm, p = 5 MPa, g = 5 μm

	x = L/4	x = 3L/4
u	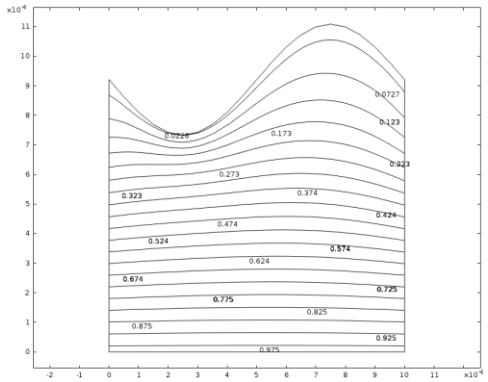	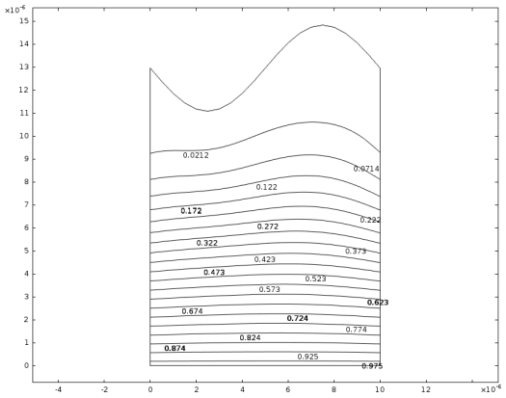
	Fig 5.25.1a – u vs. y and z at x = L/4	Fig 5.25.2a - u vs. y and z at x = 3L/4
v	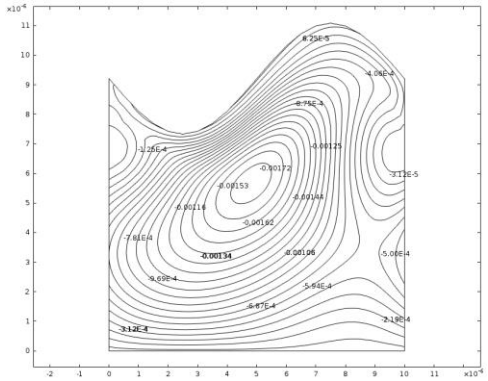	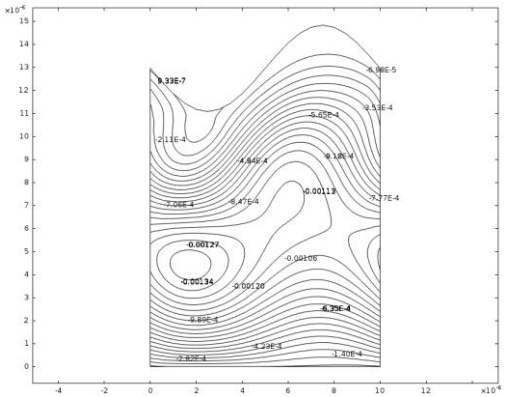
	Fig 5.25.1b - v vs. y and z at x = L/4	Fig 5.25.2b - v vs. y and z at x = 3L/4
w	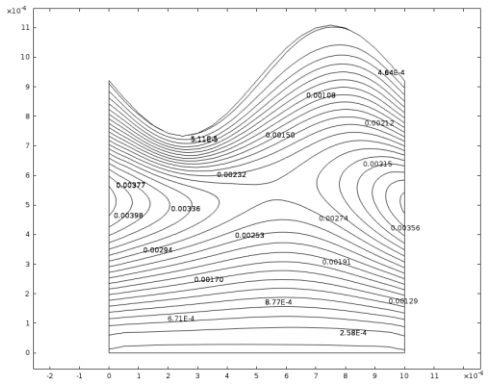	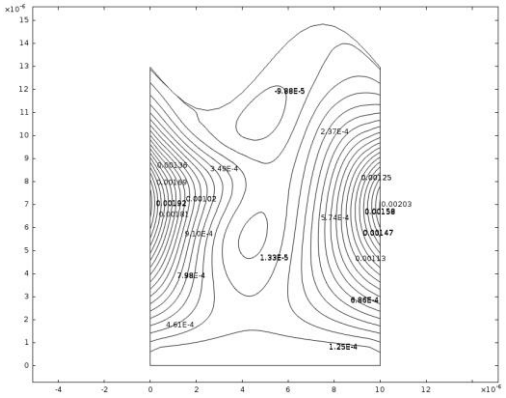
	Fig 5.25.1c - w vs. y and z at x = L/4	Fig 5.25.2c - w vs. y and z at x = 3L/4

Fig. 5.25 – Contours of small scale velocity components in m/s in the y-z plane, $\frac{dp}{dx}$ = 0 MPa/mm, p = 5 MPa, g = 5 μm

	y = L/4	y = 3L/4
u	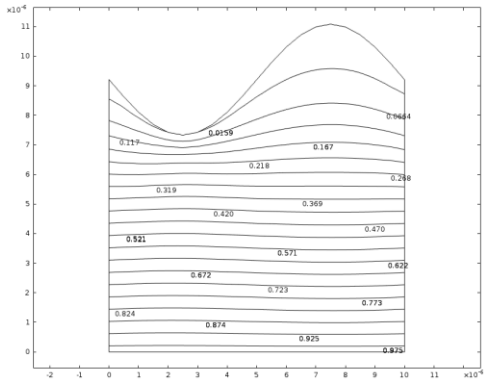	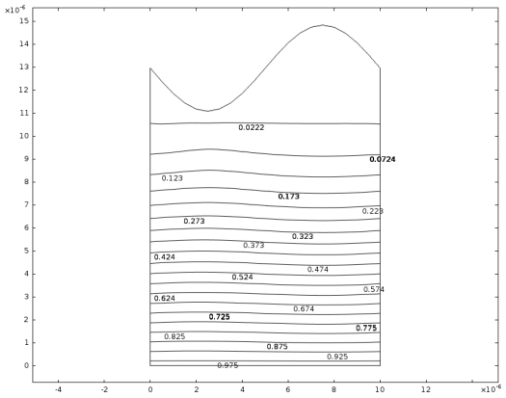
	Fig 5.26.1a – u vs. x and z at y = L/4	Fig 5.26.2a - u vs. x and z at y = 3L/4
v	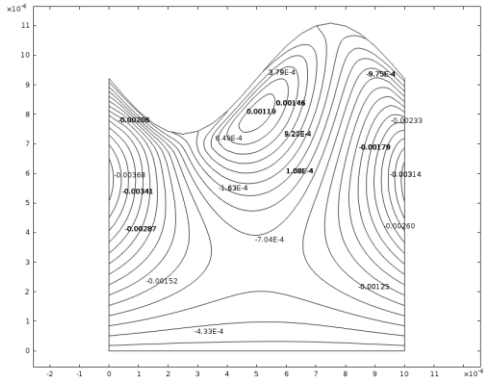	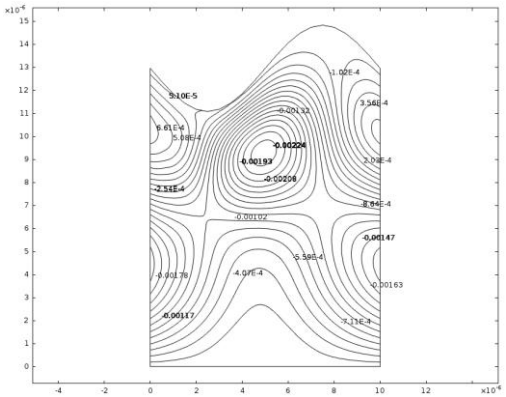
	Fig 5.26.1b - v vs. x and z at y = L/4	Fig 5.26.2b - v vs. x and z at y = 3L/4
w	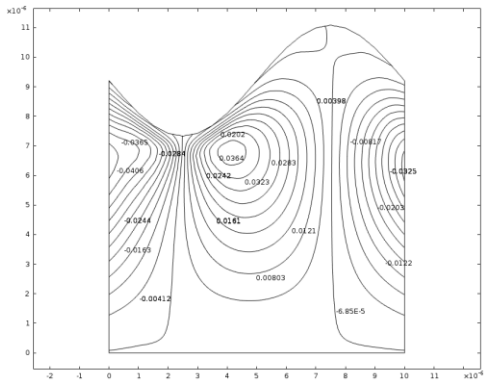	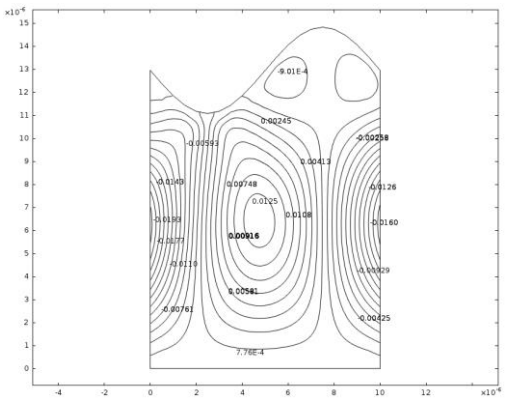
	Fig 5.26.1c - w vs. x and z at y = L/4	Fig 5.26.2c - w vs. x and z at y = 3L/4

Fig. 5.26 – Contours of small scale velocity components in m/s in the x-z plane, $\frac{dp}{dx}$ = 0 MPa/mm, p = 5 MPa, g = 5 μm

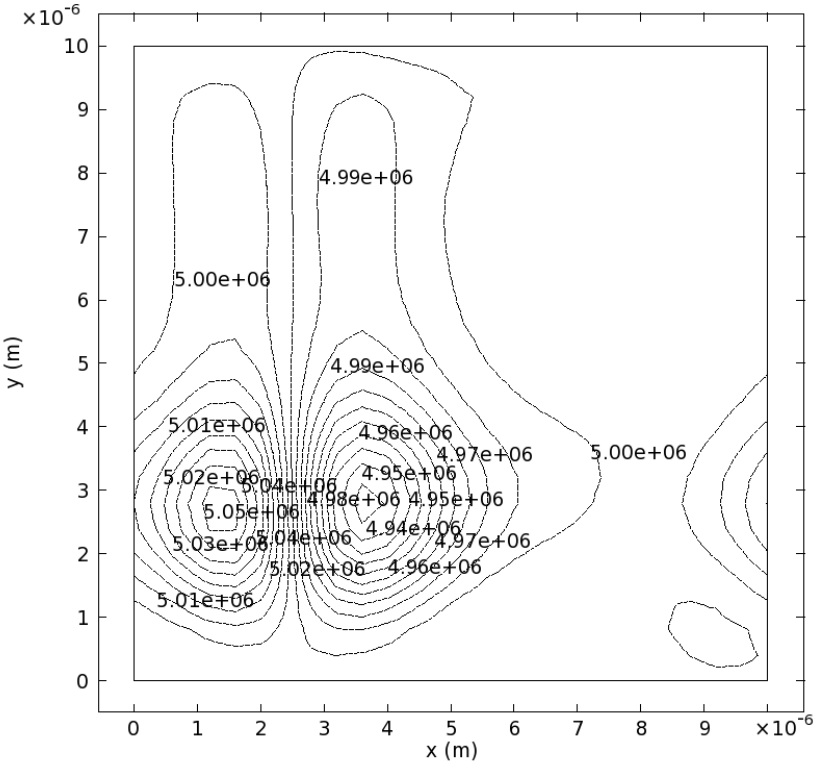

Fig. 5.27 – Contours of pressure at the FSI interface in Pa,

$\frac{dp}{dx}$ = 0 MPa/mm, p = 5 MPa, g = 30 μm

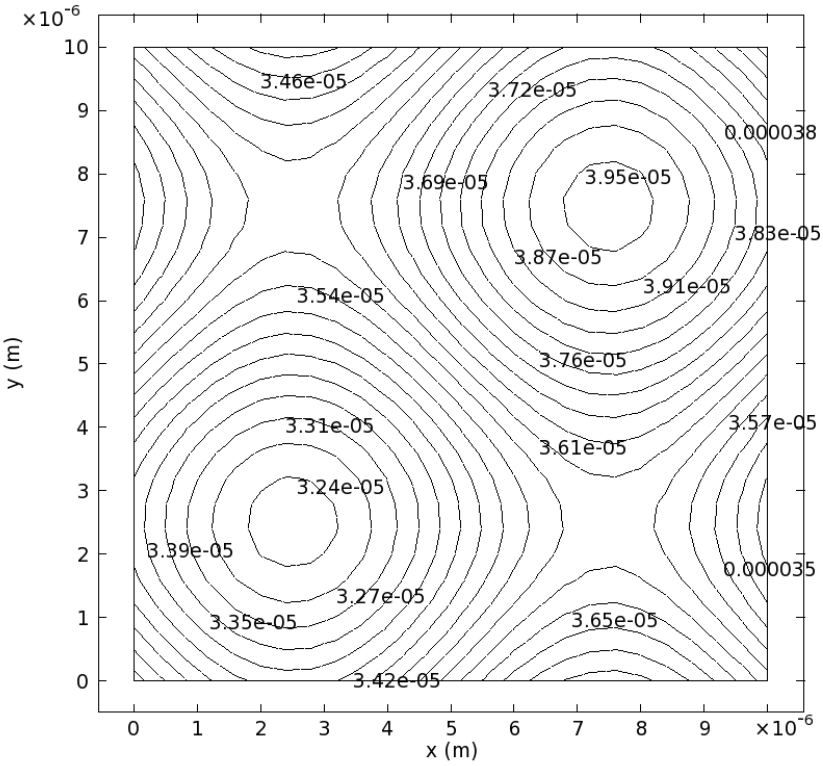

Fig. 5.28 – Contours of film thickness in m,

$\frac{dp}{dx}$ = 0 MPa/mm, p = 5 MPa, g = 30 μm

	x = L/4	x = 3L/4
u	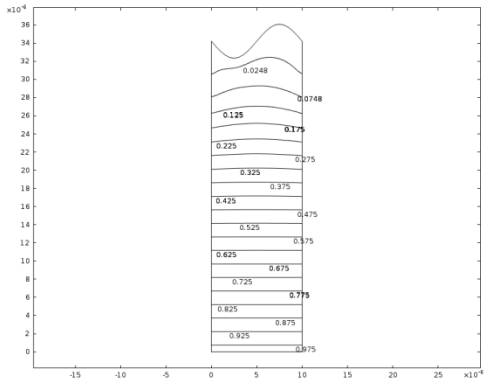	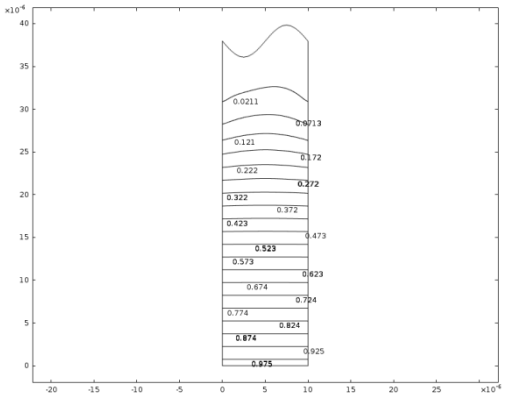
	Fig 5.29.1a – u vs. y and z at x = L/4	Fig 5.29.2a - u vs. y and z at x = 3L/4
v	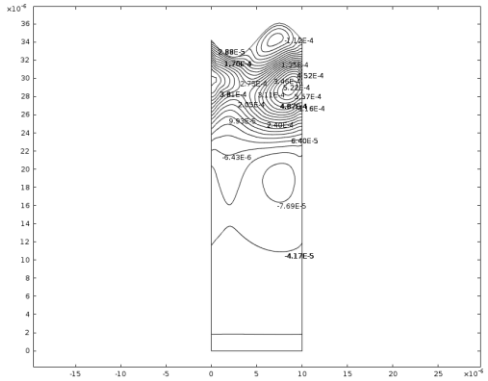	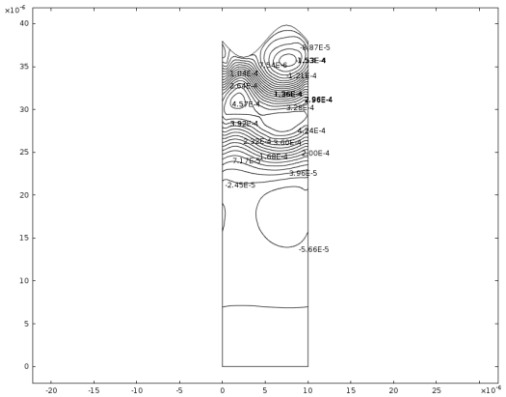
	Fig 5.29.1b - v vs. y and z at x = L/4	Fig 5.29.2b - v vs. y and z at x = 3L/4
w	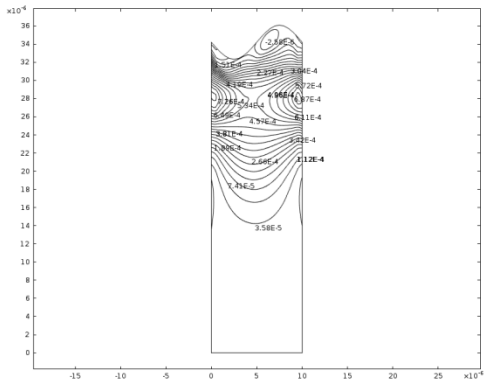	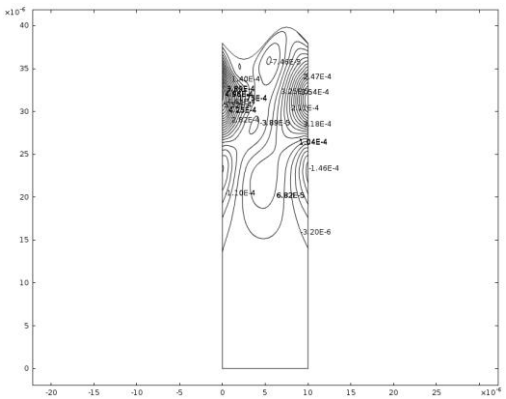
	Fig 5.29.1c - w vs. y and z at x = L/4	Fig 5.29.2c - w vs. y and z at x = 3L/4

Fig. 5.29 – Contours of small scale velocity components in m/s the y-z plane, $\frac{dp}{dx}$ = 0 MPa/mm, p = 5 MPa, g = 30 μm

	y = L/4	y = 3L/4
u	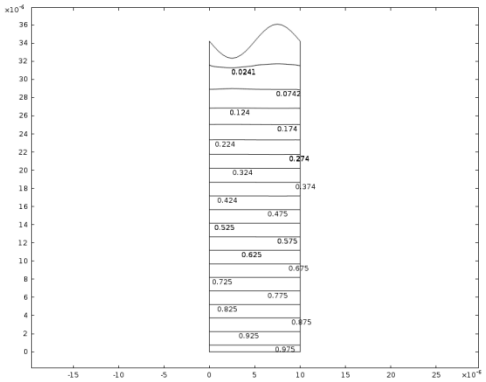	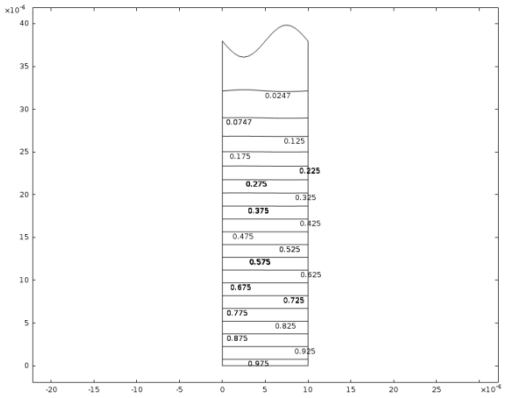
	Fig 5.30.1a – u vs. x and z at y = L/4	Fig 5.30.2a - u vs. x and z at y = 3L/4
v	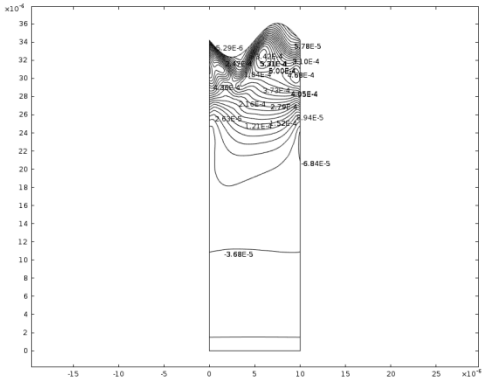	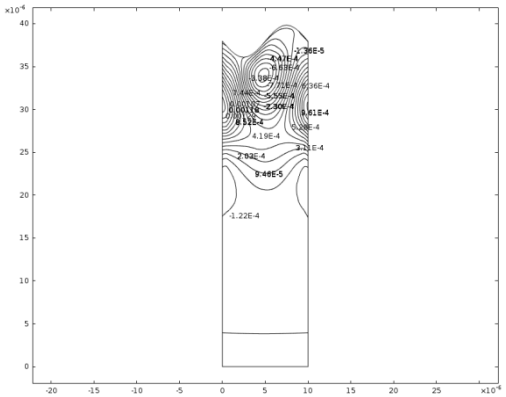
	Fig 5.30.1b - v vs. x and z at y = L/4	Fig 5.30.2b - v vs. x and z at y = 3L/4
w	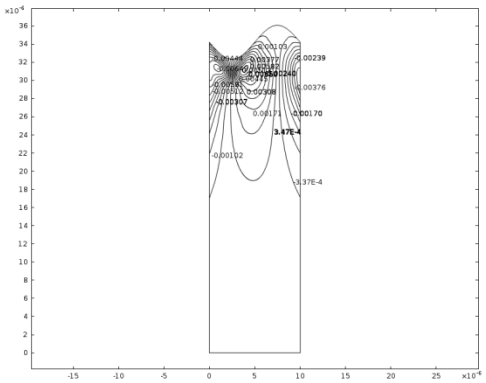	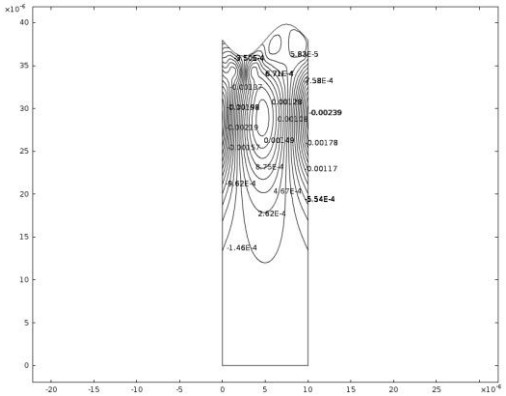
	Fig 5.30.1c - w vs. x and z at y = L/4	Fig 5.30.2c - w vs. x and z at y = 3L/4

Fig. 5.30 – Contours of small scale velocity components in m/s in the x-z plane, $\frac{dp}{dx}$ = 0 MPa/mm, p = 5 MPa, g = 30 μm

5.4 Large Scale Solutions

In order to examine the tribological performance of the bearing, a range of pad lengths and tilt angles were specified and the resulting coefficients of friction and minimum film thicknesses examined under fixed load. With respect to the multiscale method developed and bearing performance two things are of particular interest: (i) the effect of fluid flow phenomena (including compressibility, piezoviscosity, and non-Newtonian behaviour) in conjunction with topography and (ii) the effect of the topography amplitude. Also analysed in this section is the micro-EHL effect of topography on the small scale minimum film thickness.

5.4.1 Effect of Fluid Flow Phenomena

To examine the influence of fluid flow phenomena on the tribological performance of the bearing and to show the range of solutions possible using the two-scale method, three cases are considered: (i) incompressible, isoviscous, and Newtonian flow; (ii) case (i) with the addition of of compressibility and piezoviscosity; (iii) case (ii) with the addition of non-Newtonian (shear-thinning) behaviour. Two loads were specified W = 75 kN and 100 kN, in the low load case the pad length $L_p \in [20, 22.5]$ mm and for the high load case $L_p \in [22.5, 25]$ mm. The tilt angle in both cases $\varphi \in [0.05, 0.06]^\circ$. The 100 kN result is shown in fig. 5.31 and the 75 kN result is presented in fig. 5.32.

For a bearing load capacity of $W = 100$ kN, pad length $L_p = 22.5$ mm, and tilt angle $\varphi = 0.05^\circ$, the percentage difference in mass flow rate (q), coefficient of friction (μ), and minimum film thickness (g_b) produced from the two-scale method compared with that obtained from the smooth surface model are tabulated in Table 5.2.

Case	% difference in q	% difference in μ	% difference in g_b
i	-7.44 %	8.23 %	-12.21 %
ii	-5.79 %	16.43 %	-9.99 %
iii	-5.79 %	16.44 %	-10.01 %

Table 5.2 – Percentage difference in bearing performance from the two-scale method with the smooth surface model: Case (i) – incompressible, isoviscous, $\alpha = 5$ μm, $W =$ 100 kN; Case (ii) – compressible, piezoviscous; Case (iii) – non-Newtonian (shear-thinning) behaviour

Figs. 5.31 and 5.32 demonstrate that, for the range of solutions generated, as the bearing pad length and tilt angle are increased the coefficient of friction and the minimum film thickness monotonically increase for both load cases. Table 5.2 shows that the two-scale method inclusive of topography predicts a lower mass flow rate and minimum film thickness than produced from the smooth surface model, whereas the friction coefficient is increased. Using the information available from table 5.2 and figs. 5.31 and 5.32 it can be seen that as compressibility and piezoviscosity are included in (ii) the magnitude of the mass flow rate, coefficient of friction, and minimum film thickness are, for a given pad length and tilt angle, increased from (i). The inclusion of non-Newtonian (shear-thinning) behaviour in (iii) has a negligible effect on the response when compared to (ii), where the mass flow rate, coefficient of friction, and minimum film thickness remain unchanged.

Closer inspection of the small scale data used to generate Table 5.2 showed that the percentage difference in mass flow rate over all simulations between (i) and (ii) varied from -169.4 to 188.9 %, and between (ii) and (iii) from -0.3 to 3.1 %. Demonstrating that in combination with topography the effects of fluid flow phenomena (compressibility, piezoviscosity, and non-Newtonian (shear-thinning) behaviour) should not be neglected. Much more significant effects due to these fluid flow phenomena would be experienced at higher pressures and shear rates than those modelled in this study. Overall, the non-linear influence of fluid flow phenomena on bearing performance has been successfully captured by the two-scale method and the metamodels representation of the small scale simulations.

Case	μ	g_b (μm)
i	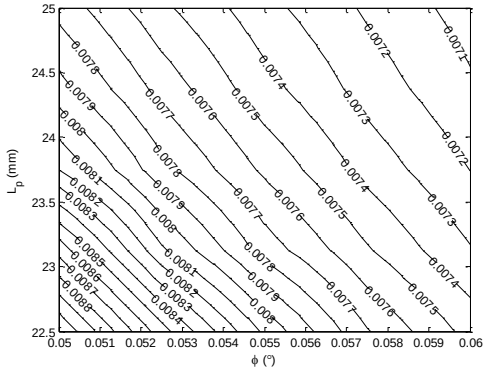	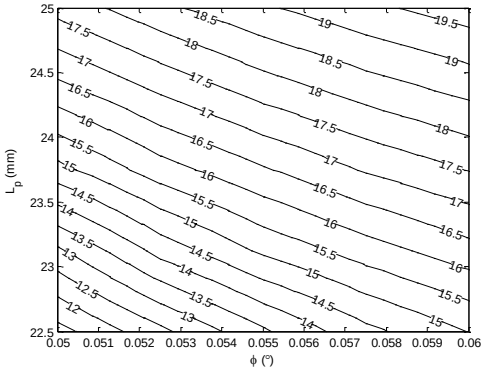
	Fig. 5.31.1a – μ vs. L_p and φ for Case (i)	Fig. 5.31.2a – g_b vs. L_p and φ for Case (i)
ii	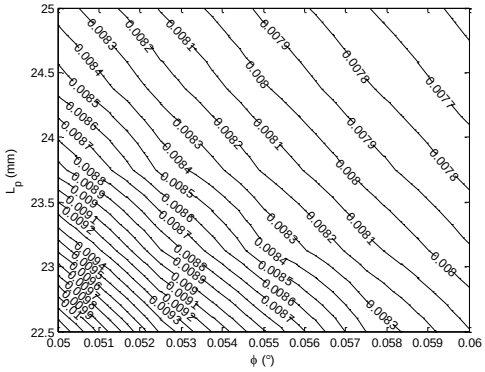	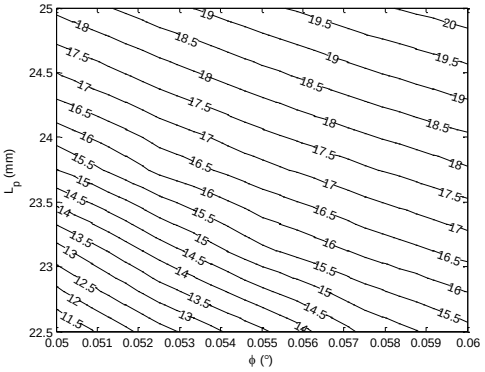
	Fig. 5.31.1b – μ vs. L_p and φ for Case (ii)	Fig. 5.31.2b – g_b vs. L_p and φ for Case (ii)
iii	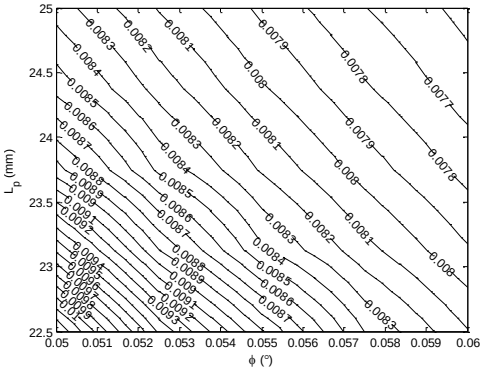	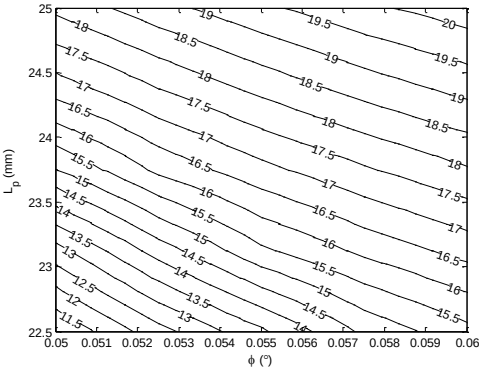
	Fig. 5.31.1c – μ vs. L_p and φ for Case (iii)	Fig. 5.31.2c – g_b vs. L_p and φ for Case (iii)

Fig. 5.31 – Effect of fluid flow phenomena on bearing performance: Case (i) – incompressible, isoviscous, α = 5 μm, W = 100 kN; Case (ii) – compressible, piezoviscous; Case (iii) – non-Newtonian (shear-thinning) behaviour

Case	μ	g_b (μm)
i	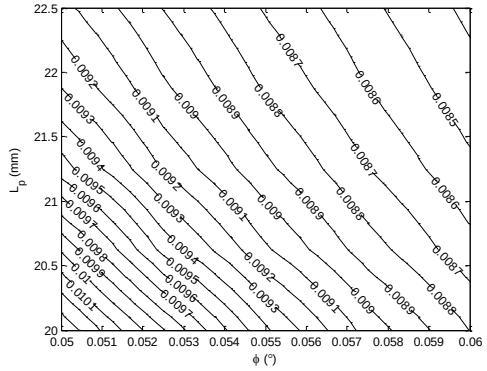	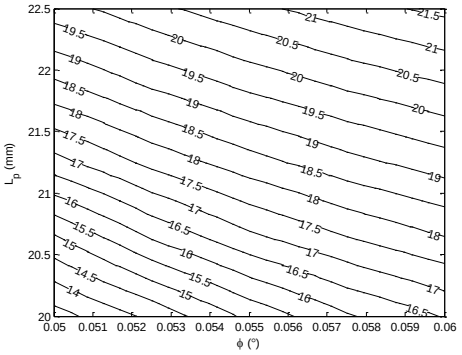
	Fig. 5.32.1a – μ vs. L_p and φ for Case (i)	Fig. 5.32.2a – g_b vs. L_p and φ for Case (i)
ii	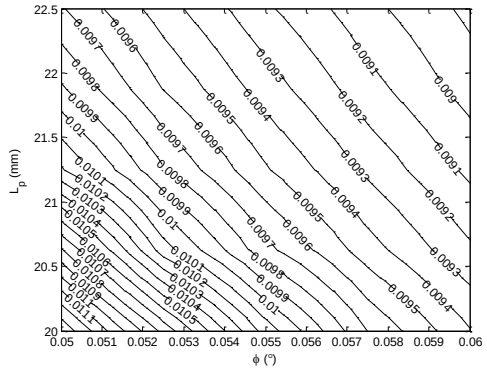	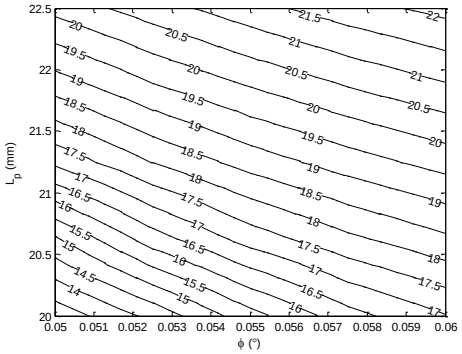
	Fig. 5.32.1b – μ vs. L_p and φ for Case (ii)	Fig. 5.32.2b – g_b vs. L_p and φ for Case (ii)
iii	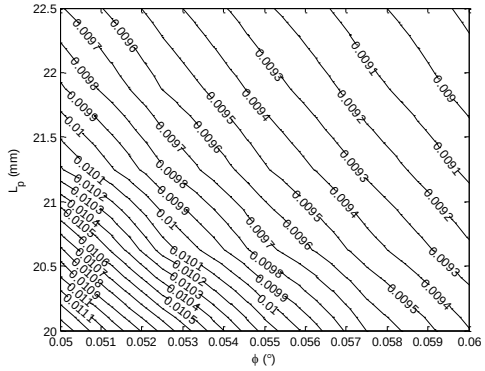	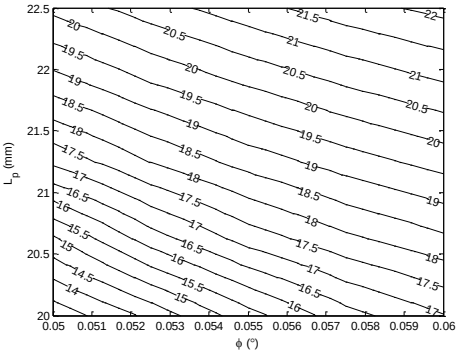
	Fig. 5.32.1c – μ vs. L_p and φ for Case (iii)	Fig. 5.32.2c – g_b vs. L_p and φ for Case (iii)

Fig. 5.32 – Effect of fluid flow phenomena on bearing performance: Case (i) – incompressible, isoviscous, α = 5 μm, W = 75 kN; Case (ii) – compressible, piezoviscous; Case (iii) – non-Newtonian (shear-thinning) behaviour

5.4.2 Effect of Topography Amplitude

By incrementing the topography amplitude in steps of 2.5 μm from α = 0 μm to 7.5 μm the change in performance of the bearing as the size of topography increases was investigated. For each value of the topography amplitude the small scale problem was solved and the metamodels constructed and validated. In order to illustrate the range of solutions that the metamodels can provide, parametric sweeps over pad length and tilt angle were performed for each load and topography amplitude investigated. Two loads were specified W = 75 kN and 100 kN, in the low load case the pad length $L_p \in [20, 22.5]$ mm and for the high load case $L_p \in [22.5, 25]$ mm. The tilt angle in both cases $\varphi \in [0.05, 0.06]^\circ$. The 100 kN result is presented in figs. 5.33 and 5.34, with the 75 kN result shown in figs. 5.35 and 5.36. Figs. 5.33 and 5.35 are contour plots showing the dependency of μ and g_b with L_p and φ over a range of α, whereas figs. 5.34 and 5.36 demonstrate the same information but instead show the influence of α on μ and g_b over a range of L_p and φ.

It is shown in figs. 5.33, 5.34, 5.35, and 5.36 that increasing the topography amplitude tends to increase the magnitude of the coefficient of friction and reduce the magnitude of the minimum film thickness. Although for a topography amplitude of α = 7.5 μm and load capacity of W = 100 kN the minimum film thickness remains almost constant for low values of pad length and tilt angle. For the topography amplitudes investigated, as both pad length and tilt angle are increased the coefficient of friction monotonically increases and the minimum film thickness monotonically decreases. It is also observed that as the topography amplitude is increased that the gradients of the responses with pad length and tilt angle are reduced, particularly in the region of low pad length and tilt angle. These large scale effects can be attributed to the flow features seen in the small scale simulations, where the presence of topography leads to a significant deviation from the smooth surface model in the pressure gradient – mass flow rate relationship derived.

α (μm)	μ	g_b (μm)
0	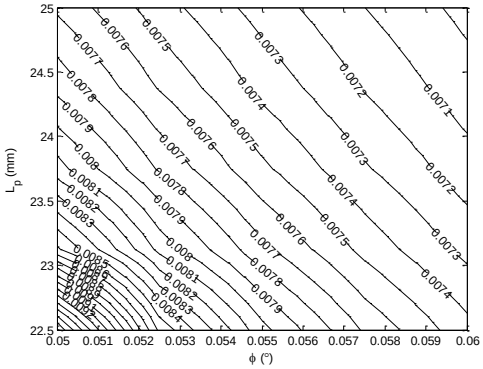 Fig. 5.33.1a – μ vs. L_p and φ for α = 0 μm	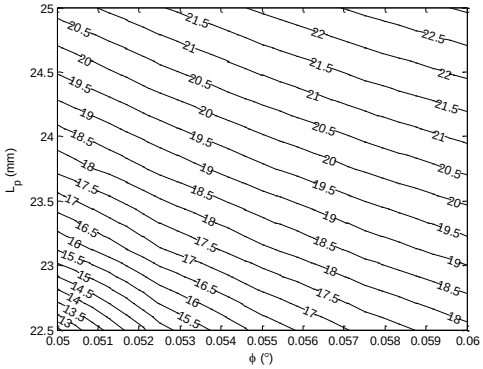 Fig. 5.33.2a – g_b vs. L_p and φ for α = 0 μm
2.5	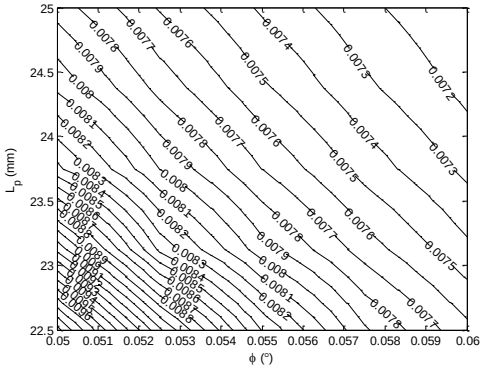 Fig. 5.33.1b – μ vs. L_p and φ for α = 2.5 μm	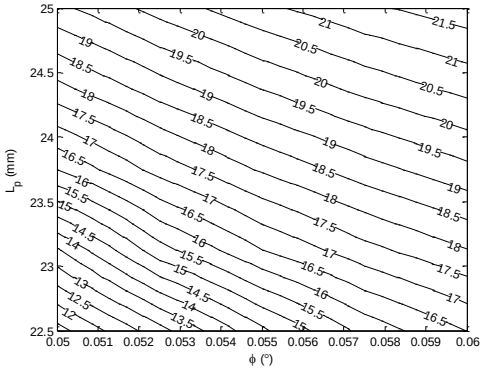 Fig. 5.33.2b – g_b vs. L_p and φ for α = 2.5 μm
5	See fig. 5.31.1c Fig. 5.33.1c – μ vs. L_p and φ for α = 5 μm	See fig. 5.31.2c Fig. 5.33.2c – g_b vs. L_p and φ for α = 5 μm
7.5	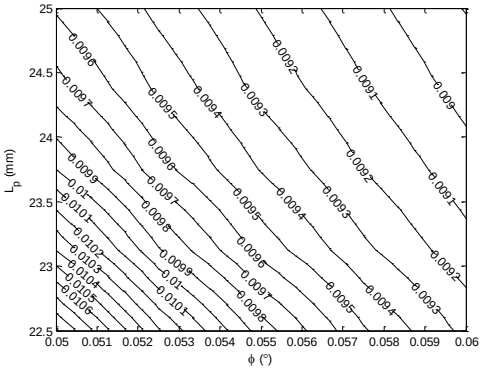 Fig. 5.33.1d – μ vs. L_p and φ for α = 7.5 μm	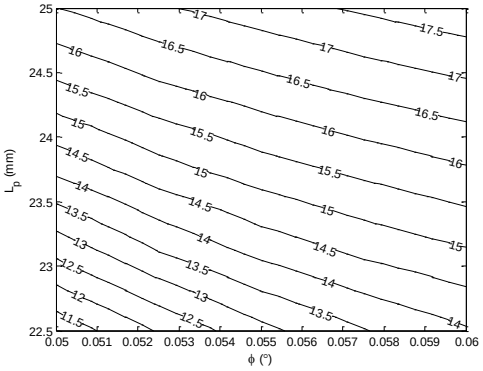 Fig. 5.33.2d – g_b vs. L_p and φ for α = 7.5 μm

Fig. 5.33 – Contour plots showing the effect of topography amplitude on bearing performance, W = 100 kN

φ	μ	g_b (μm)
0.05°	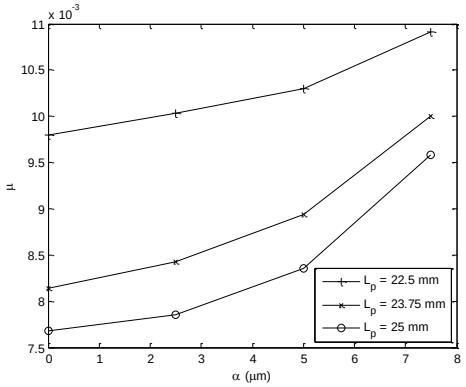 Fig. 5.34.1a – μ vs. α for φ = 0.05°	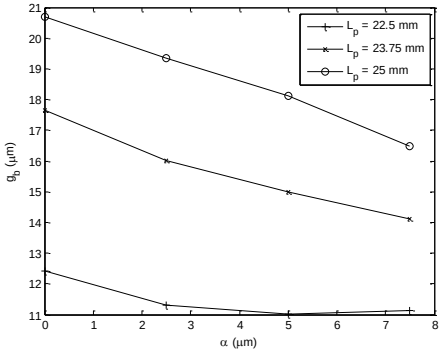 Fig. 5.34.2a – g_b vs. α for φ = 0.05°
0.055°	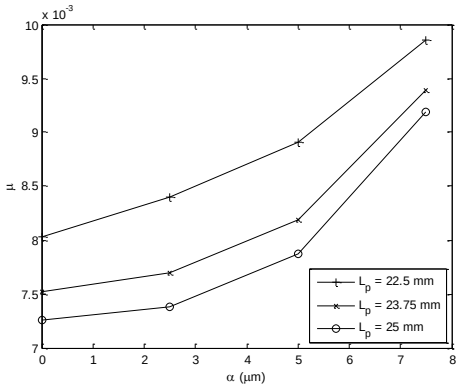 Fig. 5.34.1b – μ vs. α for φ = 0.055°	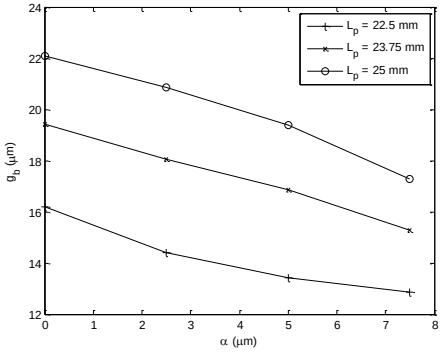 Fig. 5.34.2b – g_b vs. α for φ = 0.055°
0.06°	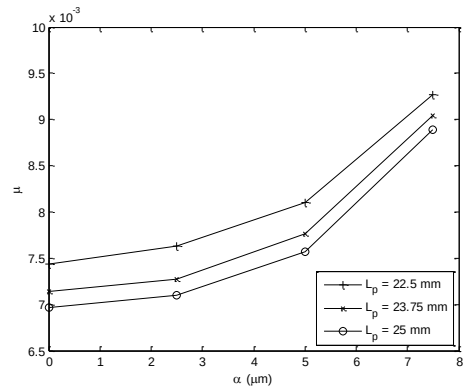 Fig. 5.34.1c – μ vs. α for φ = 0.06°	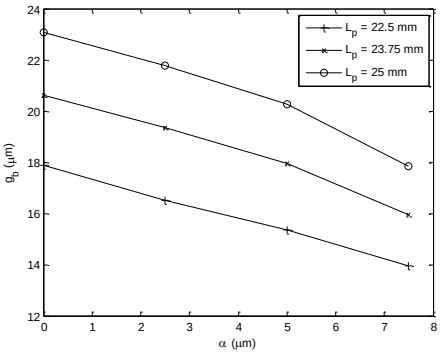 Fig. 5.34.2c – g_b vs. α for φ = 0.06°

Fig. 5.34 – Plot of the effect of topography amplitude on bearing performance, W = 100 kN

α (μm)	μ	g_b (μm)
0	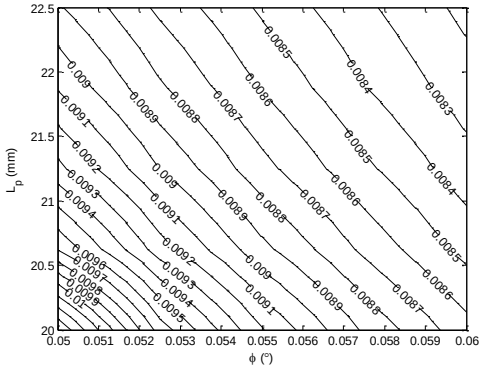 Fig. 5.35.1a – μ vs. L_p and φ for α = 0 μm	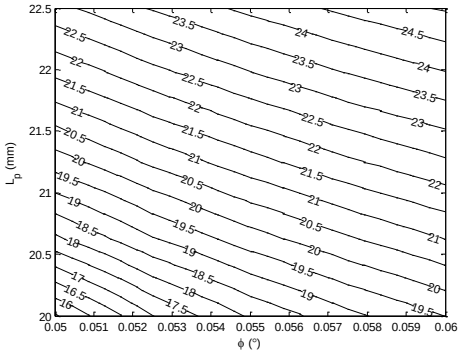 Fig. 5.35.2a – g_b vs. L_p and φ for α = 0 μm
2.5	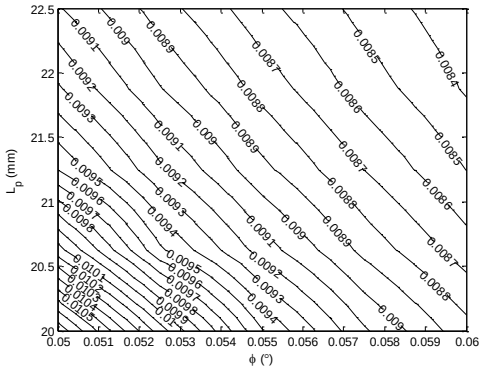 Fig. 5.35.1b – μ vs. L_p and φ for α = 2.5 μm	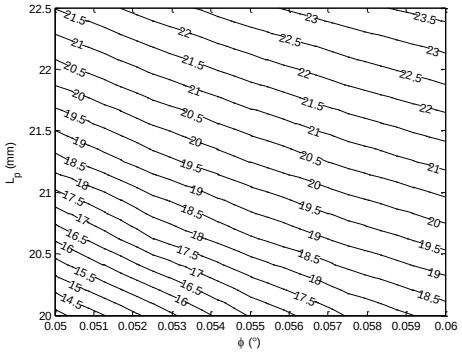 Fig. 5.35.2b – g_b vs. L_p and φ for α = 2.5 μm
5	See fig. 5.32.1c Fig. 5.35.1c – μ vs. L_p and φ for α = 5 μm	See fig. 5.32.2c Fig. 5.35.2c – g_b vs. L_p and φ for α = 5 μm
7.5	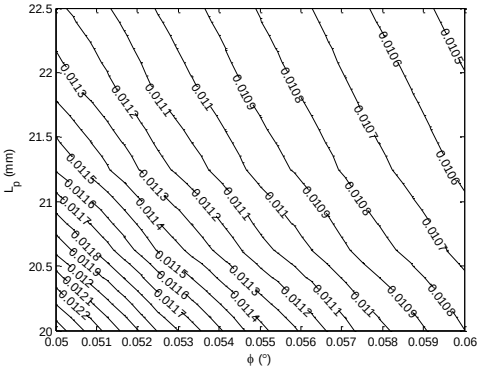 Fig. 5.35.1d – μ vs. L_p and φ for α = 7.5 μm	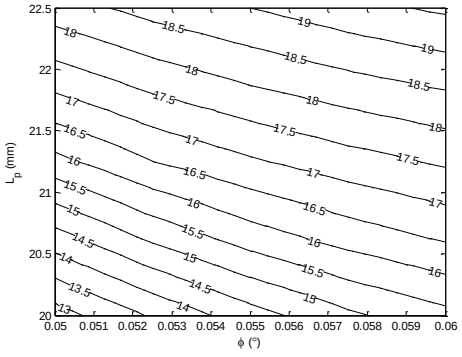 Fig. 5.35.2d – g_b vs. L_p and φ for α = 7.5 μm

Fig. 5.35 – Contour plots showing the effect of topography amplitude on bearing performance, W = 75 kN

φ	μ	g_b (μm)
0.05°	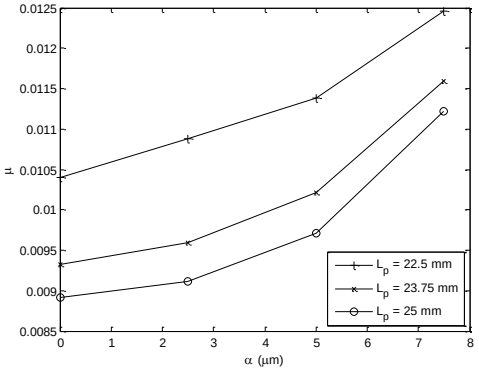	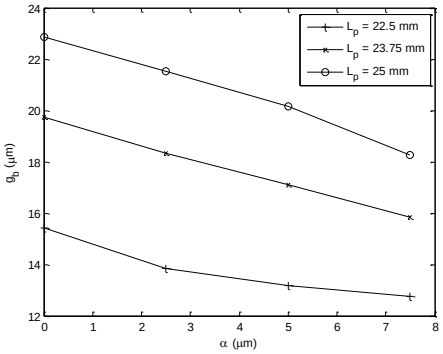
	Fig. 5.36.1a – μ vs. α for φ = 0.05°	Fig. 5.36.2a – g_b vs. α for φ = 0.05°
0.055°	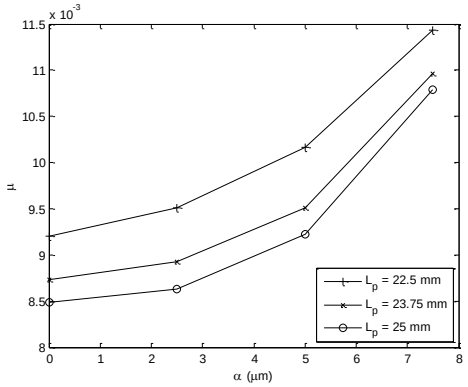	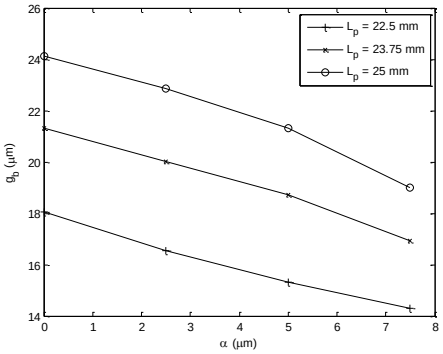
	Fig. 5.36.1b – μ vs. α for φ = 0.055°	Fig. 5.36.2b – g_b vs. α for φ = 0.055°
0.06°	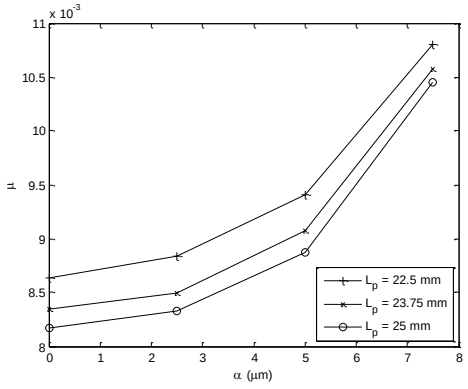	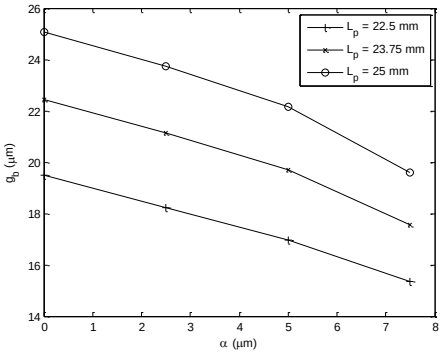
	Fig. 5.36.1c – μ vs. α for φ = 0.06°	Fig. 5.36.2c – g_b vs. α for φ = 0.06°

Fig. 5.36 – Plot of the effect of topography amplitude on bearing performance, W = 75 kN

Figs. 5.37 – 5.42 illustrate over a range of topography amplitudes the pressure, pressure maxima, pressure gradient, load-per-unit-area, film gap, and shear stress respectively for a set of example large scale simulations where the pad length L_p = 23.75 mm, the tilt angle φ = 0.055˚, and the load capacity W = 100 kN. Figs. 5.43 – 5.48 correspond to the same data displayed figs. 5.37 – 5.42 but for a set of example simulations where the pad length L_p = 21.25 mm, the tilt angle φ = 0.055˚, and the load capacity W = 75 kN. Table 5.3 and 5.4 provide the mass flow rates for the 100 kN and 75 kN simulations respectively.

Figs. 5.37 and 5.43 show for both load cases that over a range of topography amplitudes the pressure distributions in the bearing are very similar. Closer inspection of the maximum pressure given by figs. 5.38 and 5.44 indicates that as the topography amplitude is increased there is a reduction in the maximum pressure and that this occurs closer toward the inlet of the bearing, coinciding with the evidence drawn from fig. 5.3. The effect of additional fluid flow phenomena in the parallel plate case (where $\alpha = 0$) leads to an increase in the maximum pressure achieved. The differences in pressure seen over a range of topography amplitudes in figs. 5.37 and 5.43 are obtained through integration of the pressure gradient distributions displayed in figs. 5.39 and 5.45 respectively. These figures show that the pressure gradients generated by the metamodels under constant load are very close together for each of the topography amplitudes investigated. Figs. 5.40 and 5.46 indicate that the load per unit area and pressure in the bearing are almost identical where the difference between these two distributions is orders at least 3 orders of magnitude smaller than that of pressure.

Investigating figs. 5.41 and 5.47 leads to the conclusion that as the topography amplitude is increased the film thickness of the bearing is reduced, this matches the evidence observed in figs. 5.33 – 5.36 for the minimum film thickness. Similar to pressure in the parallel plate case, the effect of additional fluid flow phenomena is to increase the film thickness from that obtained from incompressible, isoviscous smooth surface model.

An increase in the shear stress distribution is observed in figs. 5.42 and 5.48 as the topography amplitude is increased and as additional fluid flow phenomena are included. This increase explains why the coefficient of friction for the bearing increases with topography amplitude and fluid flow phenomena as seen in figs. 5.31 – 5.36.

Tables 5.3 and 5.4 demonstrate that at constant load the mass flow rate through the bearing is reduced with increasing topography amplitude, and that for the parallel plate case additional flow phenomena causes a small increase in the mass flow rate.

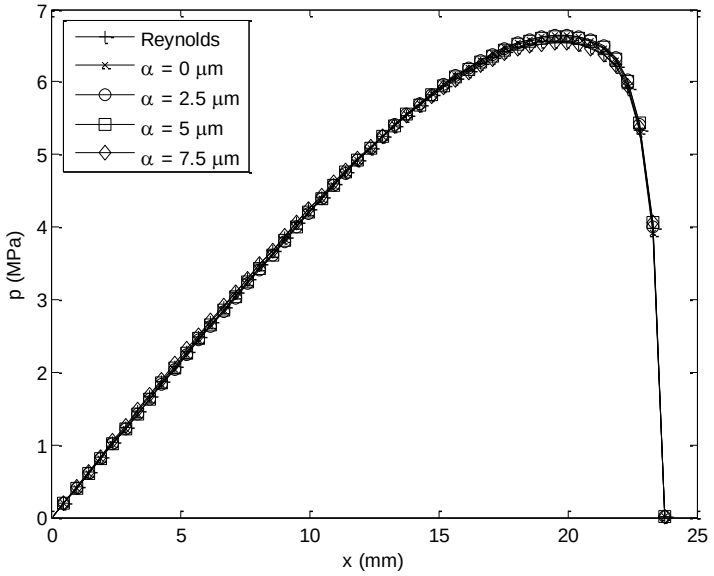

Fig. 5.37 – Pressure distributions from the two-scale method, W = 100 kN

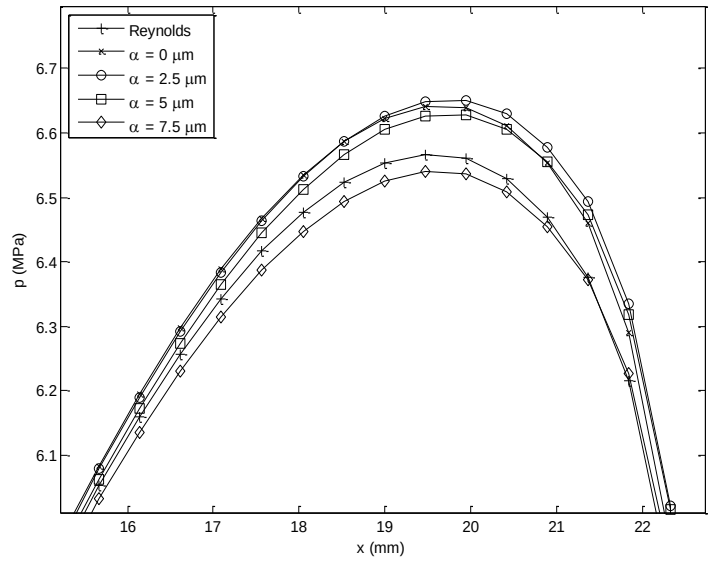

Fig. 5.38 – Close-up of maximum pressures from the two-scale method, W = 100 kN

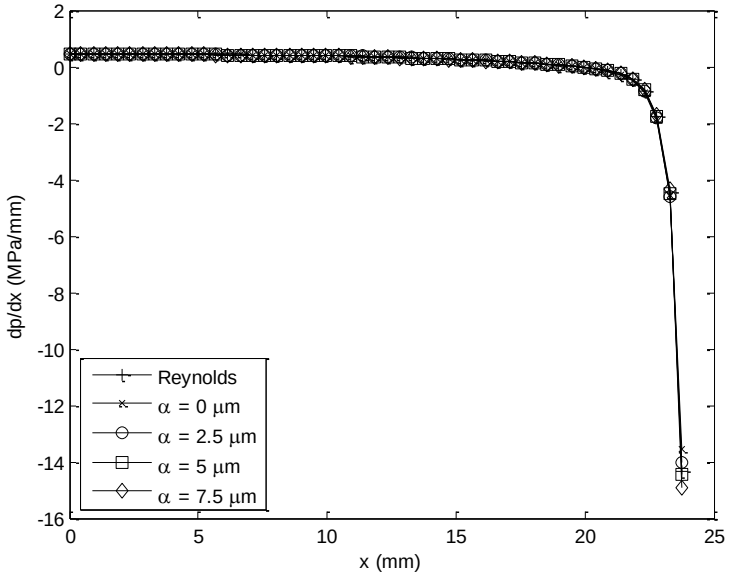

Fig. 5.39 – Pressure gradient distributions from the two-scale method, W = 100 kN

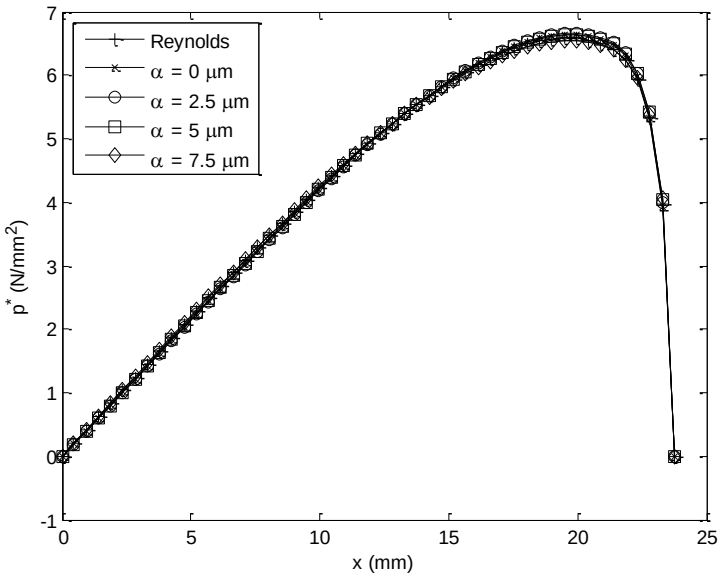

Fig. 5.40 – Load per unit area distributions from the two-scale method, W = 100 kN

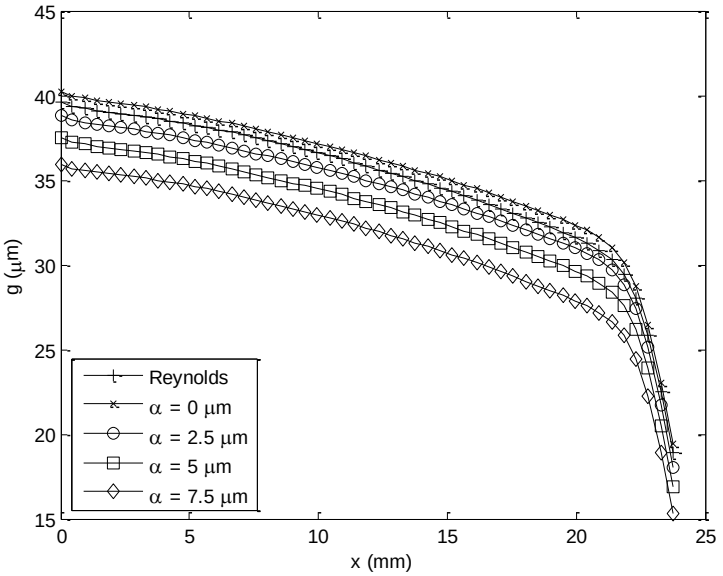

Fig. 5.41 – Film thickness distributions from the two-scale method, W = 100 kN

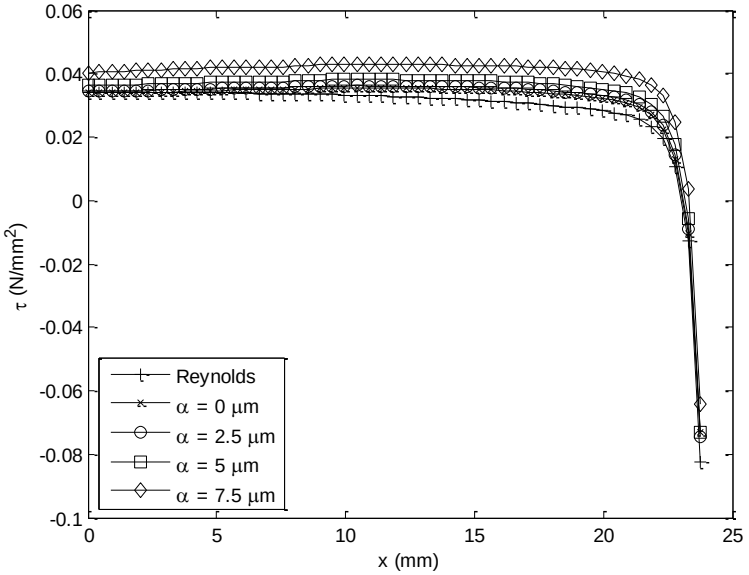

Fig. 5.42 – Shear stress distributions from the two-scale method, W = 100 kN

Case	**Mass flow rate, q**
Reynolds	0.01520 kg/s
$\alpha = 0$ μm	0.01552 kg/s
$\alpha = 2.5$ μm	0.01516 kg/s
$\alpha = 5$ μm	0.01430 kg/s
$\alpha = 7.5$ μm	0.01251 kg/s

Table 5.3 – Mass flow rates from the two-scale method, W = 100 kN

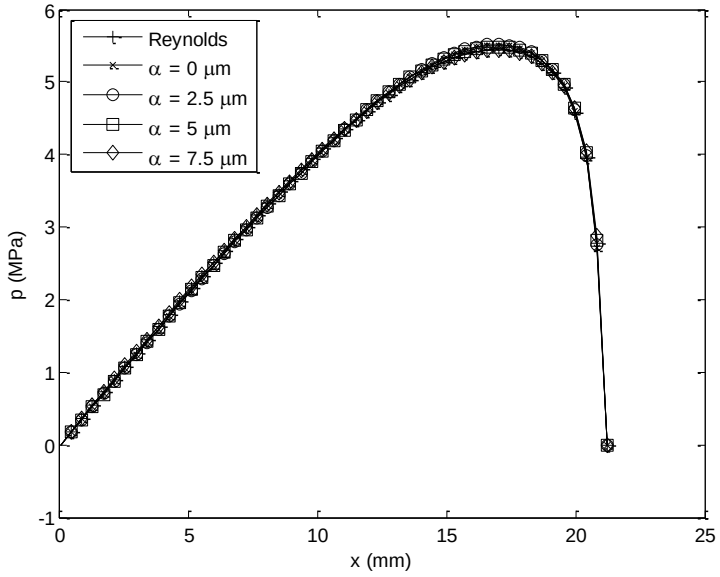

Fig. 5.43 – Pressure distributions from the two-scale method, W = 75 kN

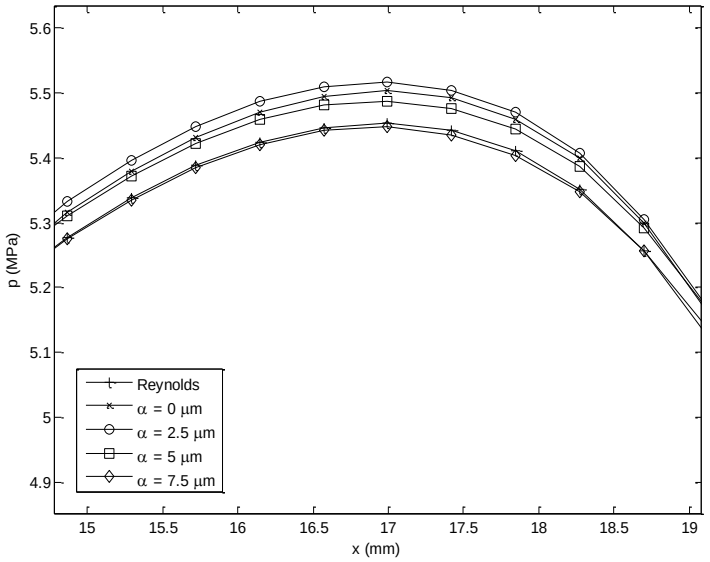

Fig. 5.44 – Close-up of maximum pressures from the two-scale method, W = 75 kN

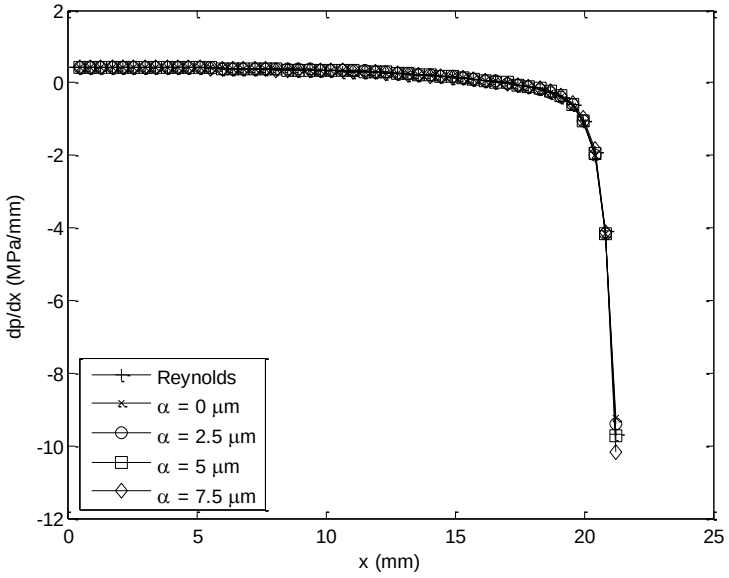

Fig. 5.45 – Pressure gradient distributions from the two-scale method, W = 75 kN

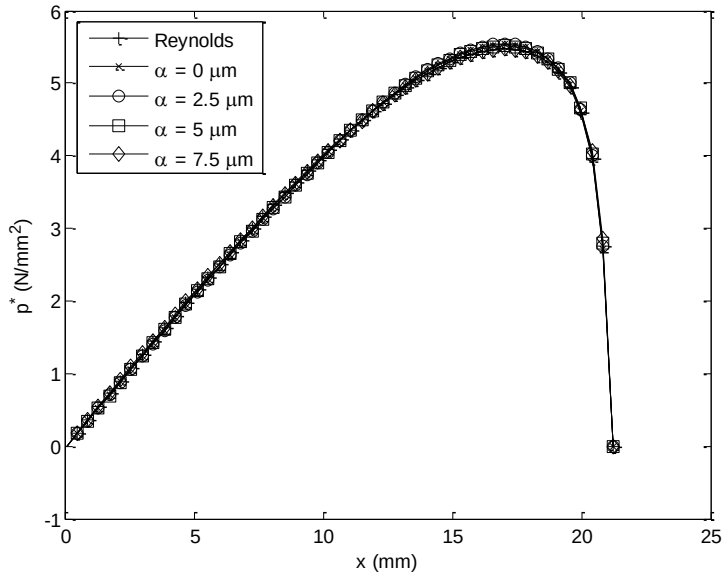

Fig. 5.46 – Load per unit area distributions from the two-scale method, W = 75 kN

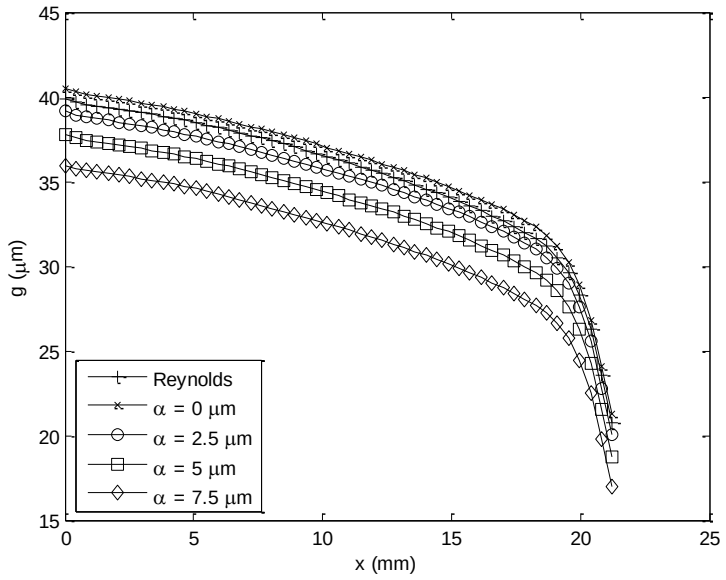

Fig. 5.47 – Film gap distributions from the two-scale method, W = 75 kN

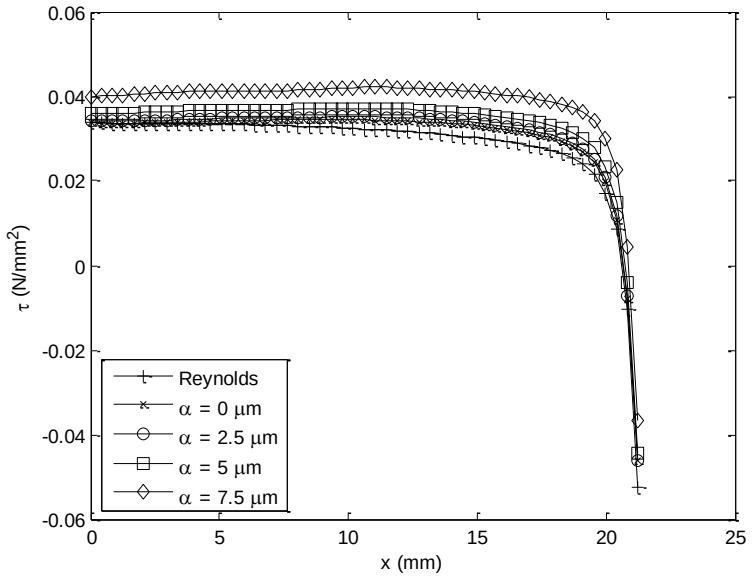

Fig. 5.48 – Shear stress distributions from the two-scale method, W = 75 kN

Case	**Mass flow rate, q**
Reynolds	0.01534 kg/s
$\alpha = 0$ μm	0.01564 kg/s
$\alpha = 2.5$ μm	0.01531 kg/s
$\alpha = 5$ μm	0.01443 kg/s
$\alpha = 7.5$ μm	0.01259 kg/s

Table 5.4 – Mass flow rates from the two-scale method, W = 75 kN

5.4.4 Micro-EHL Effect on Minimum Film Thickness

To investigate the effect of micro-EHL on the predicted minimum film thickness by the two-scale method the parameter r is introduced. This parameter, which was originally defined using the two-scale method for EHL de Boer, et al. [3], allows for the numerical assessment of the influence of micro-EHL.

$$r = \frac{s_{min} - (g + k_1 p)}{g + k_1 p} \times 100\% \tag{5.1}$$

Eq. (5.1) measures the percentage difference between the homogenised small scale minimum film thickness obtained with topography and the deformed film thickness predicted at the small scale without topography. r is therefore representative of the micro-EHL (separate from the large scale EHL) effect on film thickness in comparison to that which would be obtained from the smooth surface model alone. Fig. 5.49 is a plot of r over the x-coordinate direction for a tilted-pad bearing of pad length L_p = 22.5 mm, tilt angle φ = 0.05˚, load capacity W = 100 kN and the topography amplitudes investigated are α = 2.5 μm, 5 μm, and 7.5 μm.

The micro-EHL response on minimum film thickness in fig. 5.49 illustrates a percentage difference in the range of -0.01 to -0.16 % between that predicted by the smooth surface model for a smooth surface and from the two-scale method inclusive of topography. This indicates that topography has deformed by an amount representative of the local stiffness and that the trends seen are due to the effects of flow phenomena and the presence of topography. The magnitude of r suggests that topography deforms locally by an amount at least an order of magnitude or more smaller than that representative of the local stiffness, coinciding with the evidence drawn from fig. 5.8. The minimum film thickness achieved at the small scale is less than that achieved from column deformation of a smooth surface. Increasing the topography amplitude tends to generate a larger magnitude of r. The relationship between r and the pressure, pressure gradient, and film thickness is complex with some dependency of the parameters observed. As the film thickness is decreased and pressure increased along the bearing length r is reduced. A peak in r exists at the location of maximum pressure. Toward the outlet of the bearing where there is a reduction in both pressure and film thickness there is also a corresponding drop in r.

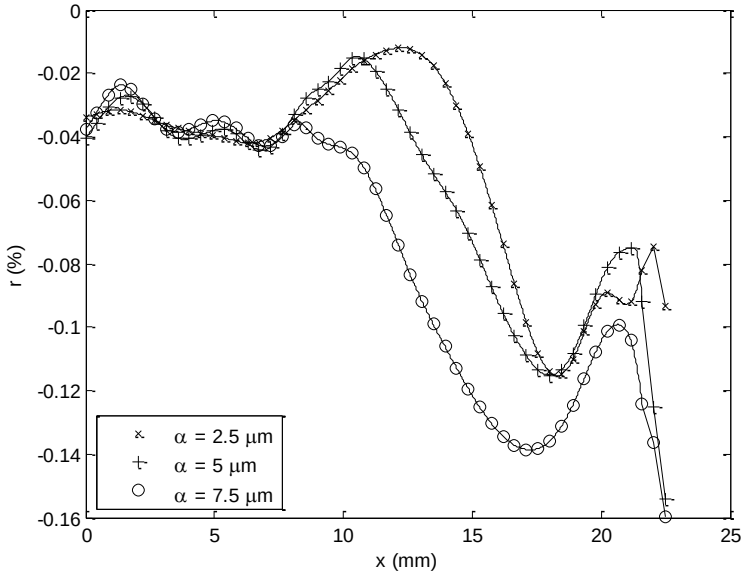

Fig. 5.49 – Micro-EHL effect on minimum film thickness

5.5 Summary

Based on the HMM a new two-scale method for EHL and micro-EHL analyses was developed and applied to tilted-pad bearings with three-dimensional topography. Elastic deformation together with the Navier-Stokes equations inclusive of compressibility, piezoviscosity, and non-Newtonian (shear-thinning) behaviour describe the small scale problem. A pressure gradient – mass flow rate relationship was used to couple the two scales. By decomposing the stiffness matrix into diagonal and non-diagonal terms elastic deformation of the bearing surface was addressed at both the large and small scales. An inverse spring method was introduced in order to model any stiffness at the large scale whilst maintaining consistency with the assumptions of the multiscale theory at the small scale. Small scale solutions were homogenised and through interpolation used at the large scale. A MLS metamodel was used to represent the small scale solutions as a root to interpolation, this process of metamodel building was validated using k-fold CV.

Grid independence and metamodel validation showed that the small scale effects were accurately captured and described at the large scale. Results using this method agreed well with the smooth surface model without topography. Contours of small scale velocity components illustrated that non-symmetrical fluid flow patterns not described by the smooth surface model occur in the presence of topography and that homogenisation of the small scale problem captures micro-EHL effects not described at

the large scale. Analysis at the large scale showed that compressibility and piezoviscosity had a far more significant effect on bearing performance than non-Newtonian behaviour, although more significant effects would be observed at higher pressures than those investigated. For a given pad length and tilt angle it was shown at constant load that the inclusion of topography produced a lower maximum pressure which was located closer towards the inlet and the film thickness was reduced. Increasing topography amplitude at constant load over a range of pad lengths and tilt angles leads to an increase in the friction coefficient and reduction in minimum film thickness. Also the gradients at which both responses increased with pad length and tilt angle were reduced. The micro-EHL effect on minimum film thickness was quantified by introducing the parameter r. It was shown that the micro-EHL effect on film thickness was a non-linear response over the length of the bearing and that it was at least an order of magnitude or more smaller than that representing local stiffness.

Chapter 6 – Two-Scale Elastohydrodynamic Lubrication: Metamodelling and Optimisation of Topography

6.1 Introduction

In this chapter the two-scale method is applied to tilted-pad bearings with a parameterised three-dimensional topography. By using metamodelling techniques, optimisation is conducted and the topography identified which minimises the coefficient of friction. The chapter is divided into three subsections: metamodel building and validation, optimisation of topography, and dissemination of optimal design.

6.2 Metamodel Building and Validation

Building the metamodel required to couple the scales of the two-scale method begins with generating an effective space-filling DoE, this is subsequently populated by small scale simulations and cross validation performed on the resulting approximations, assessment of the accuracy of the metamodels at the large scale can then be obtained.

6.2.1 Metamodel Building

The OLHC DoE was created using the GA code as provided by Bates, et al. [92]. 1000 DoE points were specified and 10^6 iterations of the GA performed. This size of DoE and number of GA iterations were chosen as to ensure that the design space was well populated and the designs well spread, resulting in a metamodel approximation which is accurate in all regions. The DoE building phase took ~13 days of computational time to complete due to the large number of iterations needed by the GA to minimise the distances between all points. Fig. 6.1 shows the frequency histogram of minimum normalised distance of each point to another point in the DoE.

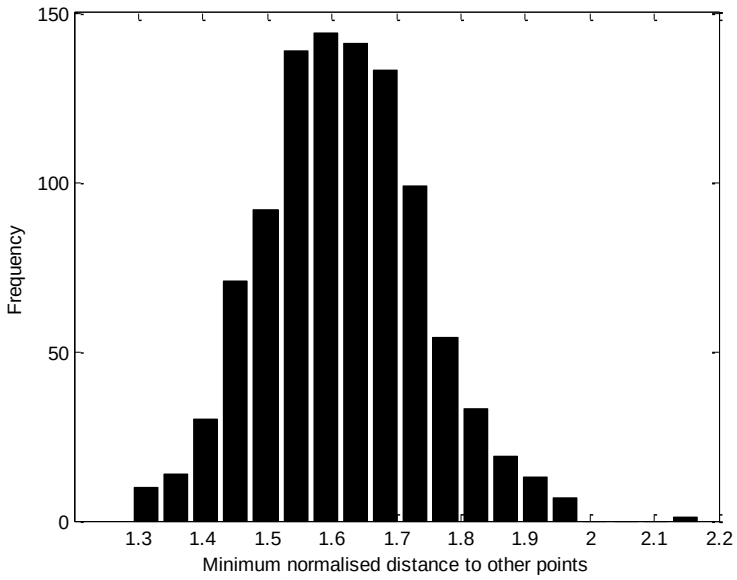

Fig. 6.1 – Frequency histogram of the minimum normalised distance between DoE points

The range of minimum distances shown in fig. 6.1 illustrates that the DoE is relatively well conditioned as the frequency distribution is close to normal, indicating that the OLHC has reduced the spread of the minimum distance to other points across all points in the domain. An outlier does exist and there is a slight skew in the distribution toward larger distances between points. Running the GA for a larger number of iterations would eventually solve these issues, however this was not practical to implement as the process of DoE building already took a long period of time and little change in the distribution was seen after the first 2 days of calculation. The selected DoE shown in fig. 6.1 is a compromise between numerical accuracy and computational expense.

6.2.2 Cross Validation

Using the DoE created in section 6.2.1 the small scale simulations required were set-up and computed. The process of obtaining all 1000 points took ~11 days of calculation. Cross validation for the MLS pressure gradient – mass flow rate, load per unit area – mass flow rate, and shear stress – mass flow rate metamodels were performed using both k-fold CV and LOOCV on the DoE data once all of the small

scale simulations were obtained. The result of the cross validation process is given in fig. 6.2.

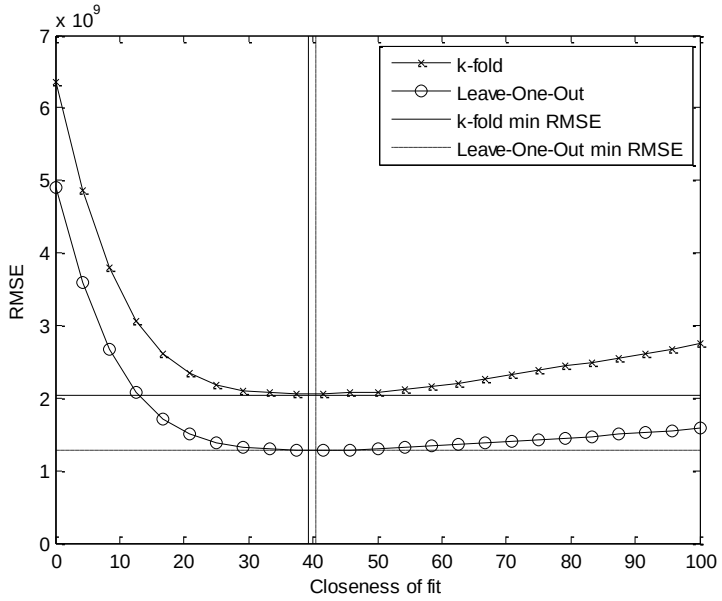

Fig. 6.2 – Cross validation response for the MLS pressure gradient – mass flow rate metamodel building

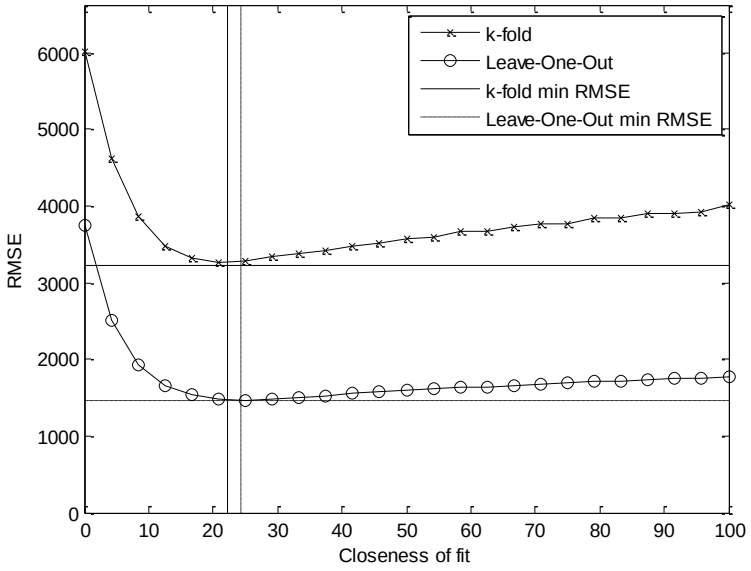

Fig. 6.3 – Cross validation response for the MLS load per unit area – mass flow rate metamodel building

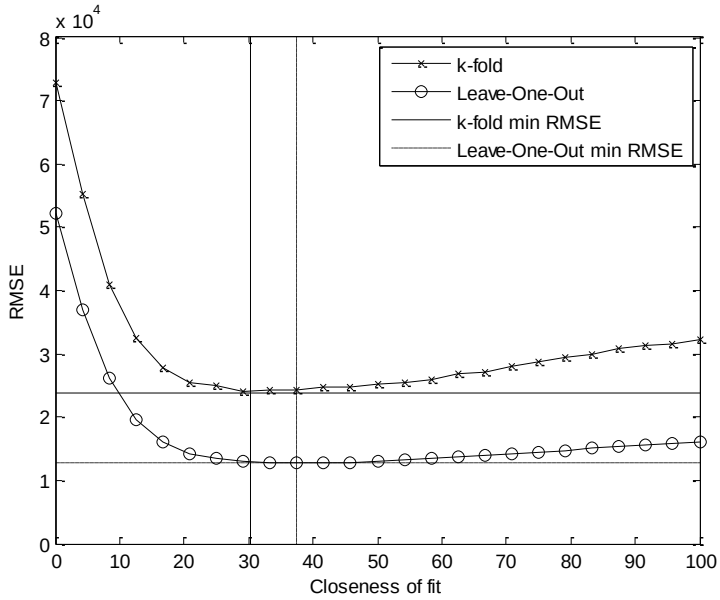

Fig. 6.4 – Cross validation response for the MLS shear stress – mass flow rate metamodel building

Fig. 6.2 indicates that the optimal closeness of fit for the pressure gradient – mass flow rate relationship from both k-fold CV (with $k = 120$) and LOOCV are very close together, k-fold CV gives $\theta = 39.09$ and LOOCV gives $\theta = 40.13$. This shows that both cross validation methods can be used to perform accurate analysis of the closeness of fit response and that the best closeness of fit for this DoE data is approximately 40. Similar conclusions can be drawn from figs. 6.3 and 6.4 for the load per unit area – mass flow rate and shear stress – mass flow rate relationships, in these cases the optimal closeness of fits were found to be approximately 24 and 38 respectively.

Each LOOCV procedure took less than 5 minutes to complete whereas the k-fold CV procedures took more than 2 hours to run, this is because the k-fold CV method requires many more calls to the MLS assessment function than LOOCV and it is therefore recommended that LOOCV should be used for CV procedures of this type in the future. It is also shown in figs. 6.2, 6.3, and 6.4 that the LOOCV error is less than that given by k-fold CV. Because the building DoE used in LOOCV is larger than the building DoE used for k-fold CV it is likely that the approximation generated in regions where the validation points lie will be closer to building points and therefore be more accurately predicted.

6.2.3 RSM Accuracy

Pressure and film thickness distributions for three different values of the longitudinal/transverse ratio ($\psi = 0.25, 0.5, \text{and } 0.75$) are given in figs. 6.5 and 6.6 respectively. These distributions are generated by solving the large scale problem using the MLS metamodel created in sections 6.2.1 and 6.2.2 and the values specified in section 4.9.1.

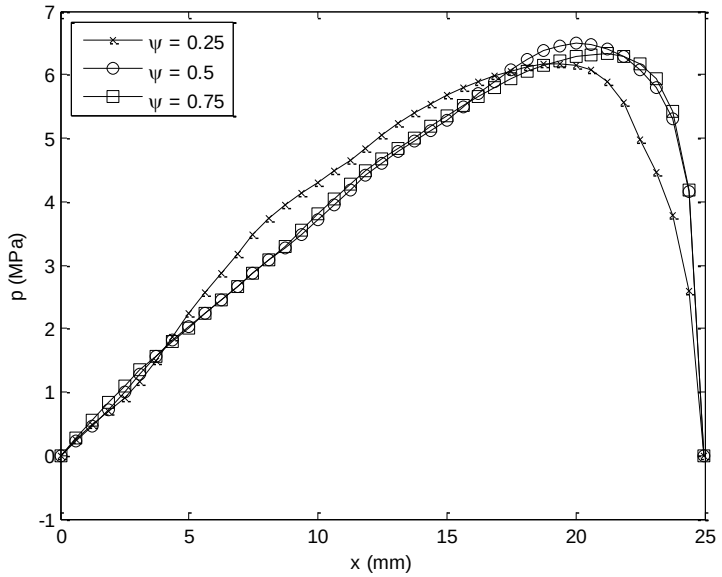

Fig. 6.5 – Pressure distributions for $\psi = 0.25, 0.5, \text{and } 0.75$

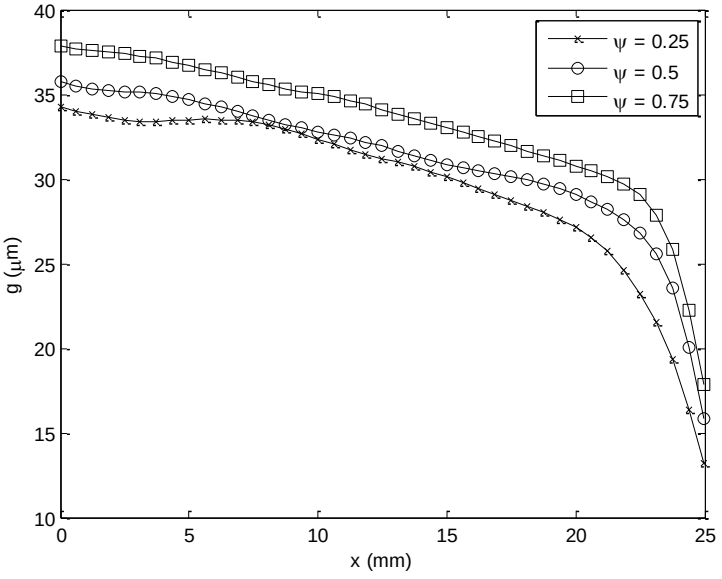

Fig. 6.6 – Film thickness distributions for $\psi = 0.25, 0.5, \text{and } 0.75$

Fig. 6.5 shows that at $\psi = 0.25$ the maximum pressure reached in the bearing is less than that obtained at $\psi = 0.5$ and 0.75 under a constant load, it is also observed that this maximum occurs closer toward the inlet of the bearing. Pressure in the $\psi = 0.25$ case is generally higher over the most of the length of the bearing, the shape of this distribution is significantly different to that given in the $\psi = 0.5$ and 0.75 cases. Fig. 6.6 demonstrates that at $\psi = 0.25$ a larger film thickness is generated than in either of the $\psi = 0.5$ or 0.75 cases, the shape of the $\psi = 0.25$ film thickness differs from the other two cases which coincides with the evidence drawn from fig. 6.5. No clear trend between the longitudinal/transverse ratio and the pressure and film thickness distributions is initially obvious, however the results seen at $\psi = 0.5$ and 0.75 are more similar to each other than at $\psi = 0.25$. This suggests that the effect of a longitudinal roughness on bearing performance is significantly different to that of a transverse or a longitudinal/transverse roughness. This result is of significant interest because similar conclusions about the influence of transverse roughness in EHL have been made by a number of practical and computer experiments (Patir and Cheng [23], Jeng [53], Akamatsu, et al. [54], Greenwood and Johnson [55], Greenwood and Morales-Espejel [56], Venner and ten Napel [57]).

In order to validate the trends presented in figs. 6.5 and 6.6 results generated at the large scale through the metamodel are compared against the exact corresponding small scale simulations, similar to the check performed in section 5.2.2. The mass flow rate as predicted by the large scale solver is compared to the exact corresponding mass flow rate determined at the small scale for three arbitrary locations (0 mm, 10 mm, 20 mm) along the distributions of pressure gradient, pressure and film thickness. This check is performed for each of the longitudinal/transverse ratios shown and the results tabulated in Tables 6.1 – 6.3.

	Large Scale x-Coordinate		
Parameter	0 mm	10 mm	20 mm
Pressure gradient, $\frac{dp}{dx}$	0.4302 MPa/mm	0.2700 MPa/mm	-0.0714 MPa/mm
Pressure, p	0 MPa	4.306 MPa	6.156 MPa
Gap, g	34.27 μm	32.33 μm	27.11 μm
% error in mass flow rate	-0.873 %	3.786 %	2.213 %

Table 6.1 – Percentage error in mass flow rate for $\psi = 0.25$

	Large Scale x-Coordinate		
Parameter	0 mm	10 mm	20 mm
Pressure gradient, $\frac{dp}{dx}$	0.3658 MPa/mm	0.3633 MPa/mm	0.0221 MPa/mm
Pressure, p	0 MPa	3.704 MPa	6.491 MPa
Gap, g	35.71 μm	32.77 μm	29.06 μm
% error in mass flow rate	1.198 %	1.997 %	-0.225 %

Table 6.2 – Percentage error in mass flow rate for $\psi = 0.5$

	Large Scale x-Coordinate		
Parameter	0 mm	10 mm	20 mm
Pressure gradient, $\frac{dp}{dx}$	0.4867 MPa/mm	0.4081 MPa/mm	0.0777 MPa/mm
Pressure, p	0 MPa	3.798 MPa	6.282 MPa
Gap, g	37.83 μm	35.00 μm	30.76 μm
% error in mass flow rate	0.453 %	1.244 %	-0.866 %

Table 6.3 – Percentage error in mass flow rate for $\psi = 0.75$

The absolute percentage error in mass flow rate predicted between the metamodel and exact small scale simulations is < 4% for all cases considered. This indicates that the metamodel is accurately capturing the effects of the parameterised topography on the bearing performance. This also validates the choice in size and spread of the DoE used and implies the subsequent optimisation procedure will lead to an accurate prediction. The largest % error is seen at $\psi = 0.25$, here the result predicted is farther from the smooth surface model than for the remaining two cases (see the

shape of the distributions given figs. 5.37, 5.41, 5.43 and 5.47). This means that the underlying basis function of the metamodel has a poorer fit to the DoE data in this region and is therefore more likely to be less accurate between the DoE locations.

6.3 Optimisation of Topography

Using the metamodels built and validated as described in section 6.2, optimisation of topography was performed by the bracketing procedure outlined in section 4.9. The response and optimisation of the coefficient of friction (μ) with longitudinal/transverse ratio (ψ) is presented in fig. 6.7, with the corresponding minimum film thickness (g_b) and mass flow rate (q) given in figs. 6.8 and 6.9 respectively.

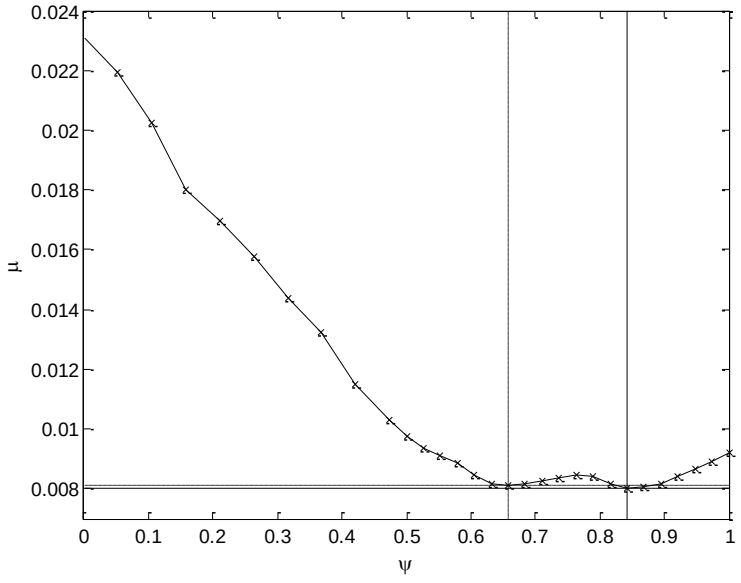

Fig. 6.7 – Response and optimisation of the coefficient of friction with the longitudinal/transverse ratio

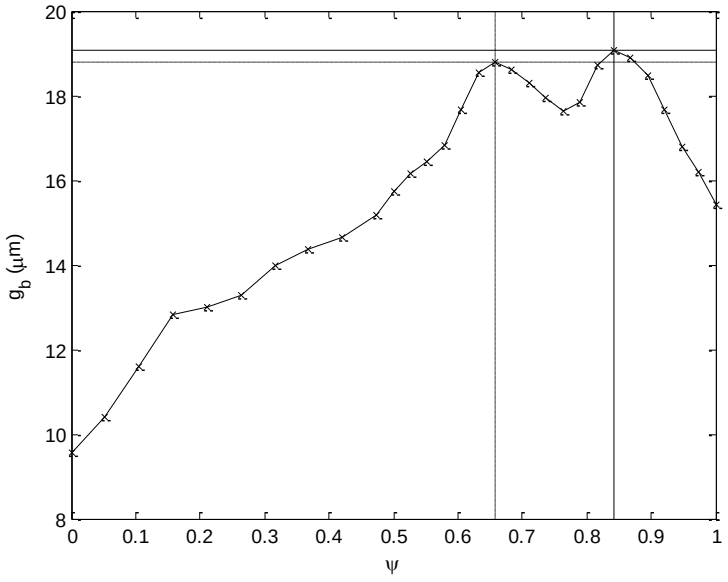

Fig. 6.8 – Response of the minimum film thickness with the longitudinal/transverse ratio

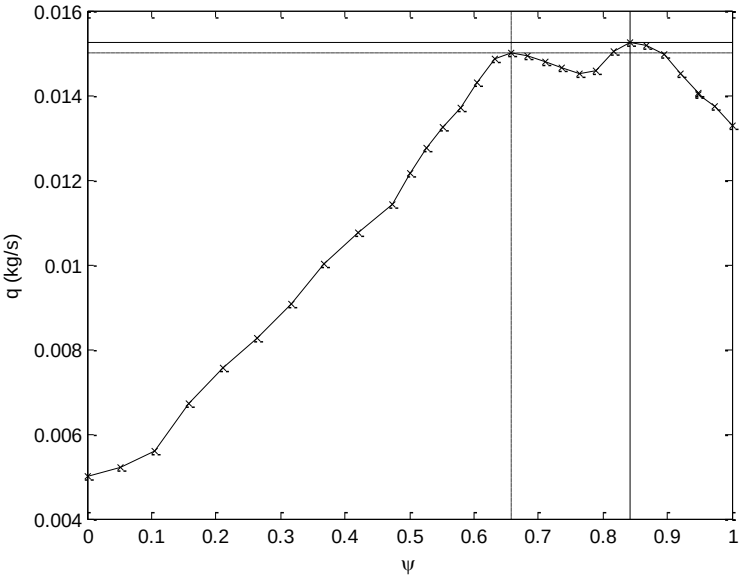

Fig. 6.9 – Response of the mass flow rate with the longitudinal/transverse ratio

The response shown in fig. 6.7 indicates that a purely transverse roughness produces a lower coefficient of friction at constant load than purely longitudinal roughness for the conditions investigated. This observation is similar to that observed by Patir and Cheng [23] when they conducted computer experiments using their flow

factors approach to include the effects of roughness in an EHL simulation. The response of μ with ψ is non-linear, as ψ increases from 0 to 0.65 there is a decrease in μ from 0.023 to 0.08, between $\psi = 0.65$ and $\psi = 0.85$ μ remains between a value of 0.08 and 0.09, and as ψ increases from 0.85 to 1 μ increases from 0.08 to 0.095. The corresponding minimum film thickness (g_b) and mass flow rate (q) given in figs. 6.8 and 6.9 respectively show that across the range of ψ an increase or decrease in μ directly leads to a decrease or increase in g_b and q. The optimisation procedure took a total of ~7.5 hours to converge, this accounted for 30 separate assessments of the coefficient of friction over the determined values of ψ. This implies an average of 15 minutes per large scale simulation using the BVP method which is an improvement of approximately 5 minutes compared to the IVP method used in chapter 5.

Two local minima were identified by the optimisation procedure at $\psi = 0.6579$ and $\psi = 0.8421$ at which $\mu = 8.104 \times 10^{-3}$ and 8.028×10^{-3} respectively. The minimum at $\psi = 0.8421$ is therefore identified as the global minimum of μ for the conditions imposed, this also corresponded to global maxima in the responses of g_b and q. Refinement in the step size of ψ can be seen near the location of these minima, this corresponds to the iterative process undertaken by the bracketing optimisation process. Figs. 6.10 and 6.11 illustrate the topography at the two minima identified.

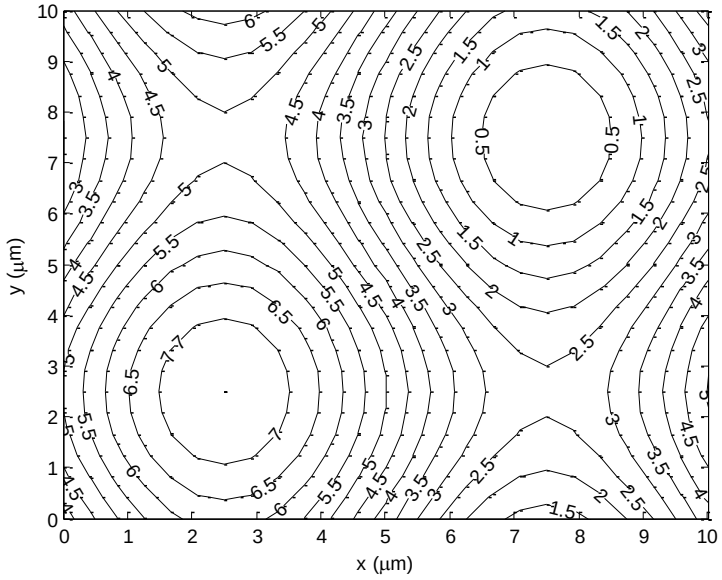

Fig. 6.10 – Contour plot of topography in μm at $\psi = 0.6579$ (local minimum)

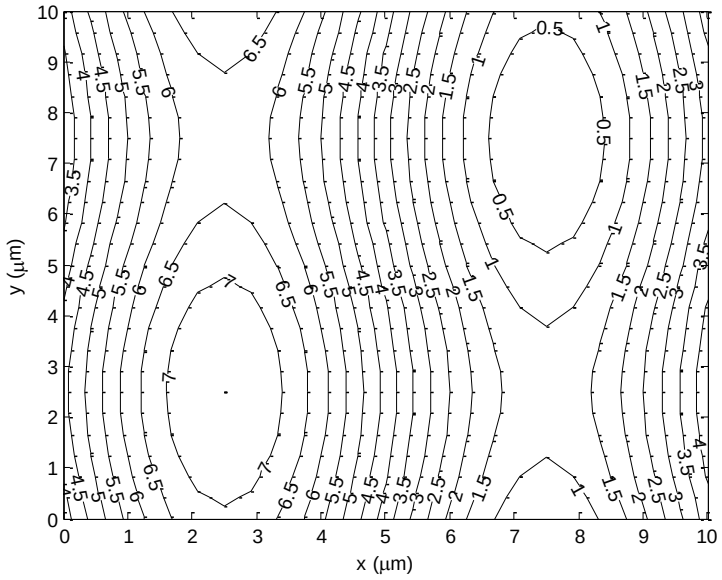

Fig. 6.11 – Contour plot of topography in μm at $\psi = 0.8421$ (global minimum)

Given that the μ produced by both these topographies was almost identical it is interesting to note that they have very different features. In fig. 6.11 the topography is dominated by transverse waviness, whereas in fig. 6.10 the topography is much more of a blend between transverse and longitudinal components. This highlights how the optimisation of topography for bearing performance is not trivial and that to describe the response of μ with ψ the two-scale method and subsequent metamodelling techniques are needed. The coefficient of friction produced by the smooth surface model under the same parameters was found to be $\mu = 7.175 \times 10^{-3}$. Simulations inclusive of topography predicted higher coefficients of friction than their smooth counterparts. However this is not to say that different definitions of the topography function or bearing operating parameters may lead to coefficients of friction less than that given by their corresponding smooth surface counterparts.

6.4 Optimal Design

6.4.1 Bearing Performance

The pressure, pressure gradient, load per unit area, film thickness, and shear stress distributions for the textured bearing under load are shown in figs. 6.12 - 6.16 for the two minima identified in fig. 6.7 and directly from the smooth surface model

(without topography or fluid flow phenomena) respectively. Table 6.4 provides the mass flow rates corresponding to the results presented in figs. 6.12 – 6.16.

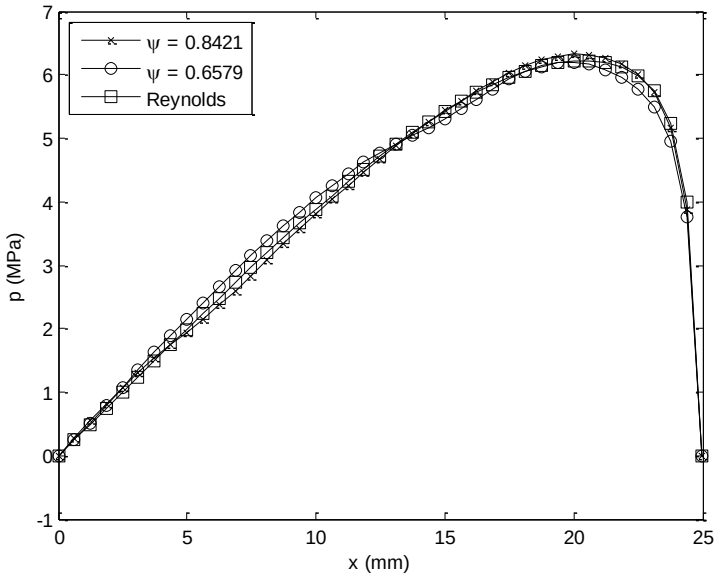

Fig. 6.12 – Pressure distributions for $\psi = 0.6579, 0.8421$ and the smooth surface model

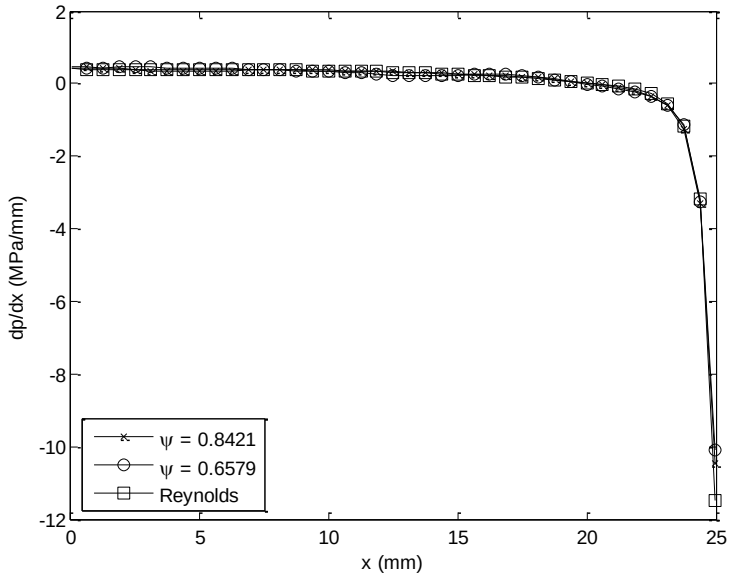

Fig. 6.13 – Pressure gradient distributions for $\psi = 0.6579, 0.8421$ and the smooth surface model

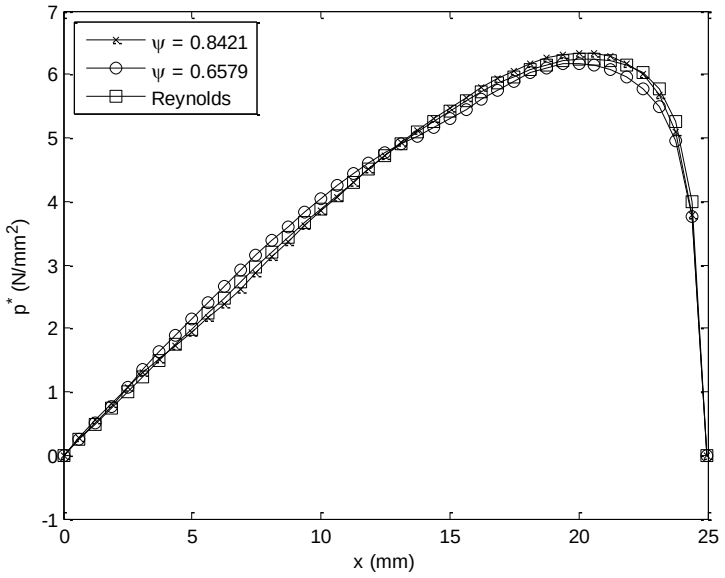

Fig. 6.14 – Load per unit area distributions for $\psi = 0.6579, 0.8421$ and the smooth surface model

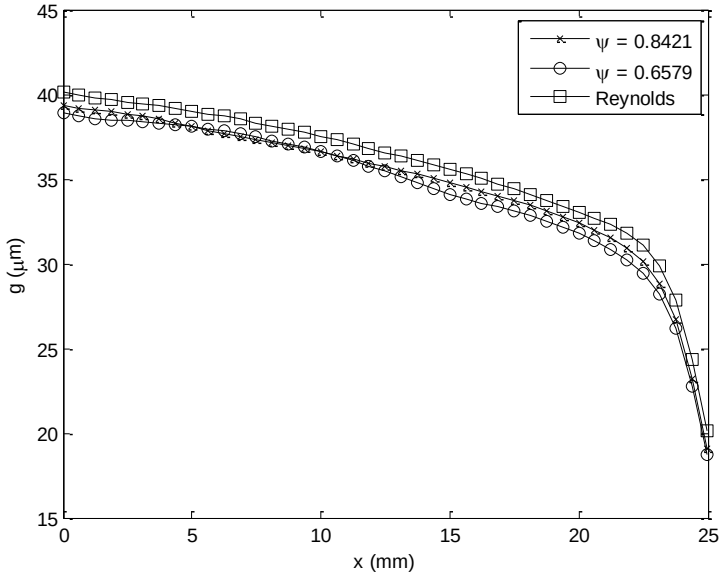

Fig. 6.15 – Film thickness distributions for $\psi = 0.6579, 0.8421$ and the smooth surface model

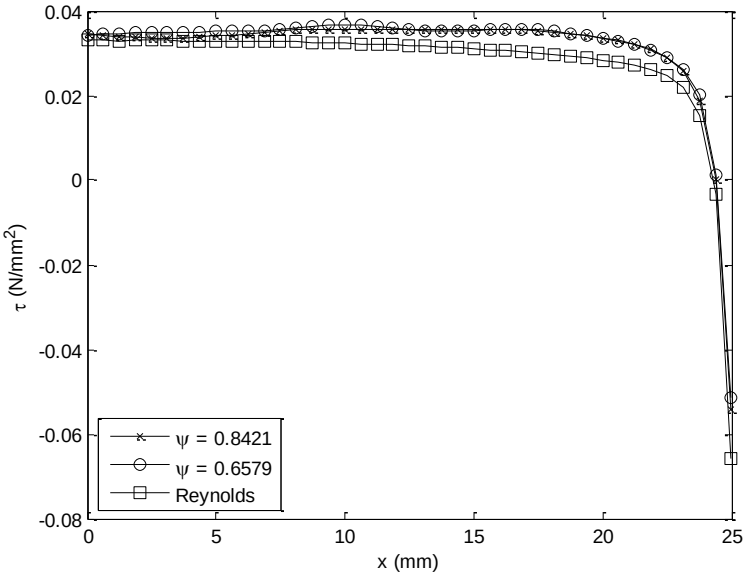

Fig. 6.16 – Shear stress distributions for $\psi = 0.6579, 0.8421$ and the smooth surface model

Case	**Mass flow rate, q**
Reynolds	0.01555 kg/s
$\psi = 0.8421$	0.01524 kg/s
$\psi = 0.6579$	0.01496 kg/s

Table 6.4 – Mass flow rates for $\psi = 0.6579, 0.8421$ and the smooth surface model

The pressure distribution for $\psi = 0.8421$ given in fig. 6.12 shows that at constant load, the peak pressure generated in the textured bearing was higher than given by the smooth surface model. In the region leading up to this peak, the pressure predicted was lower than the smooth surface model. However for the case where $\psi = 0.6579$ the peak pressure was lower than that given by the smooth surface model but over the length of the bearing pressure was generally higher. The pressure distributions shown in fig. 6.12 are obtained from integrating the pressure gradient distributions of fig. 6.13, the pressure gradient distributions seen are very close together which leads to the small differences in pressure observed. Fig. 6.14 displays the load per

unit area for the 3 cases presented, these distributions are almost identical to the pressure distributions shown in fig. 6.12 where the difference between these parameters is orders of magnitude smaller than the magnitude of either the load per unit area or pressure.

The effect of topography on film thickness shown in fig. 6.15 demonstrates that at $\psi = 0.8421$ a lower film thickness was produced than compared with the result obtained from the smooth surface model. This is also true for the $\psi = 0.6579$ result, however the magnitude of this film thickness distribution was even less than at the global minimum ($\psi = 0.8421$). The shape of the $\psi = 0.6579$ film thickness distribution does not directly resemble that produced by the smooth surface model, whereas at the global minimum the shapes of the film thickness distributions are more similar.

The shear stress distributions given in fig. 6.16 indicate that for both the local and global minimum found the magnitudes are greater than that produced by the smooth surface model. The shapes of the distributions for the two minima are similar to each other but both different from the corresponding smooth surface model result. Given that the simulations are conducted at the same load capacity, these observations provide the evidence as to why the optimisation result produces coefficients of friction which are greater than that given by the smooth surface model and that the two minima identified inclusive of topography are close together.

Table 6.4 shows that for both of the minima identified the mass flow rates produced are less than that given by the smooth surface model. It is also shown that the local minimum produced a lower mass flow rate than that provided at the global minimum, this observation indicates that there is no obvious link between the mass flow rate and coefficient of friction produced with and without topography.

6.4.2 MLS Constants

Plots of the MLS constants generated from the metamodels representing the pressure gradient – mass flow rate relationship (Eq. (4.32)), load per unit area – mass flow rate relationship (Eq. (4.33)), and shear stress – mass flow rate relationship (Eq. (4.34)) over the bearing length are given in figs. 6.17 – 6.24 for the distributions at the local and global minima presented in figs. 6.12 – 6.16.

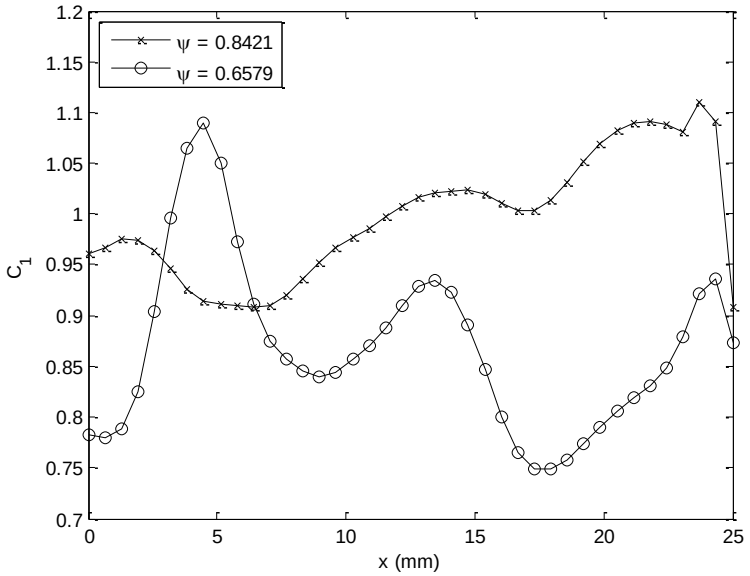

Fig. 6.17 – MLS constant C_1 distributions for $\psi = 0.6579$, and 0.8421

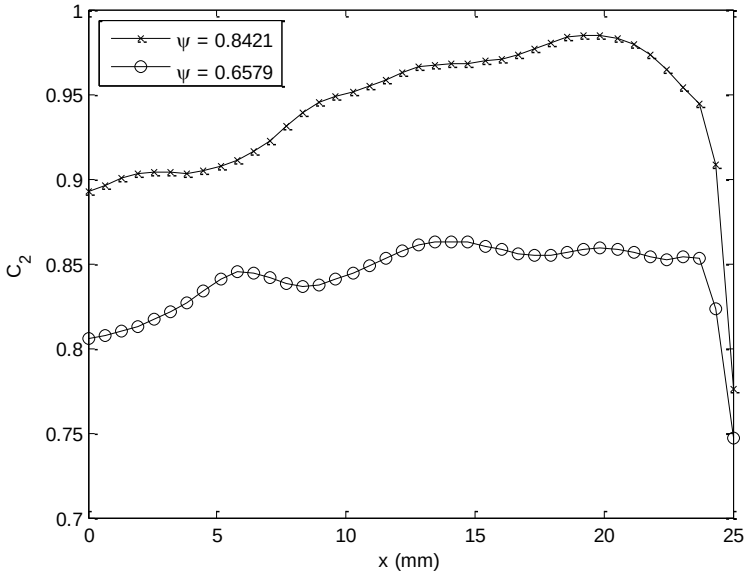

Fig. 6.18 – MLS constant C_2 distributions for $\psi = 0.6579$, and 0.8421

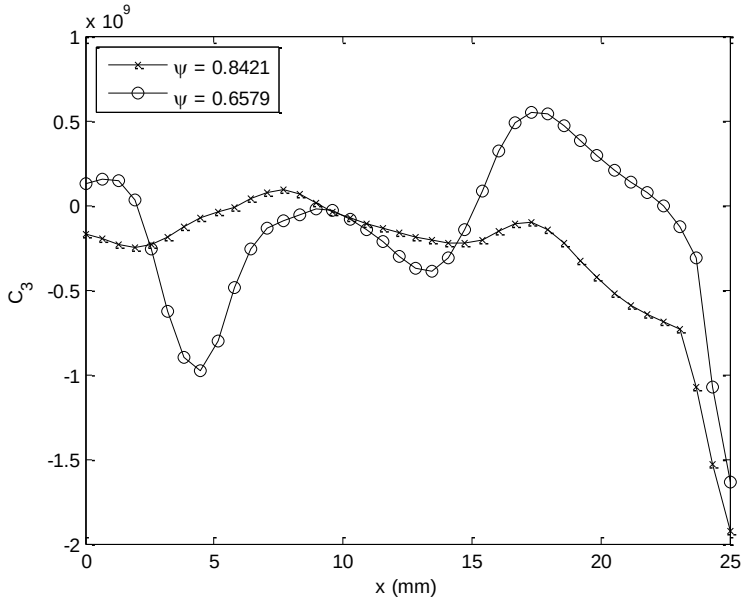

Fig. 6.19 – MLS constant C_3 distributions for $\psi = 0.6579$, and 0.8421

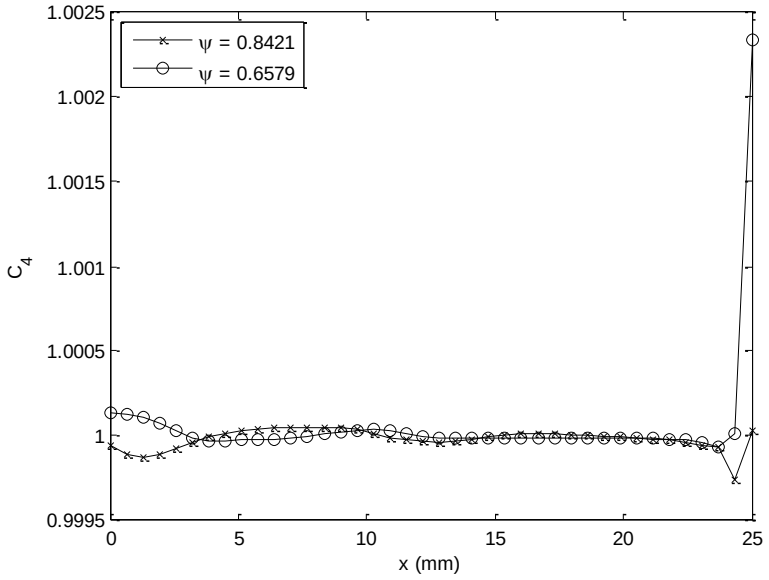

Fig. 6.20 – MLS constant C_4 distributions for $\psi = 0.6579$, and 0.8421

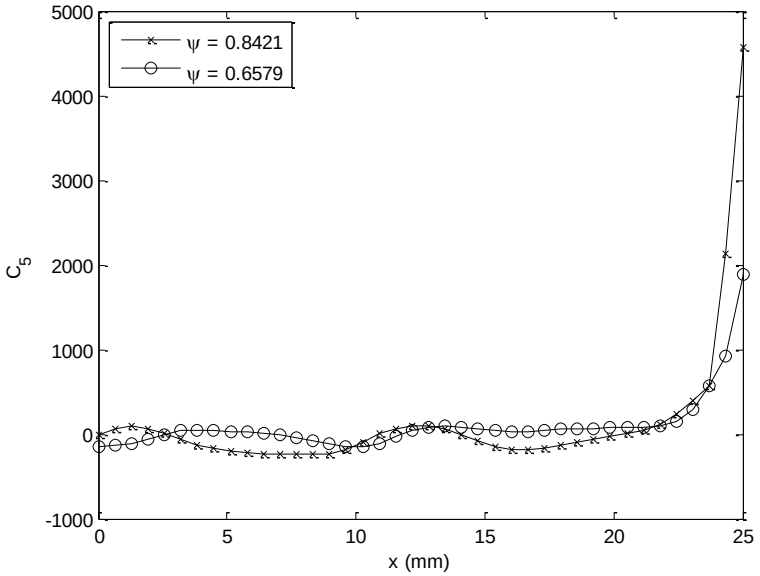

Fig. 6.21 – MLS constant C_5 distributions for $\psi = 0.6579$, and 0.8421

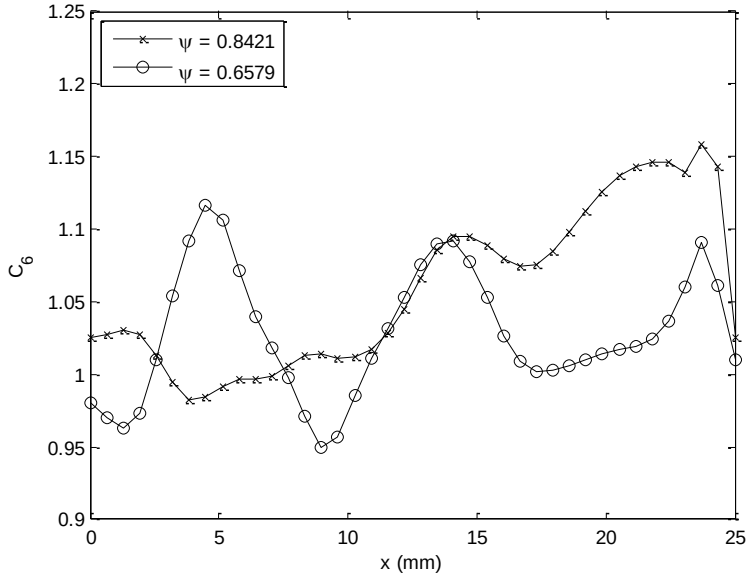

Fig. 6.22 – MLS constant C_6 distributions for $\psi = 0.6579$, and 0.8421

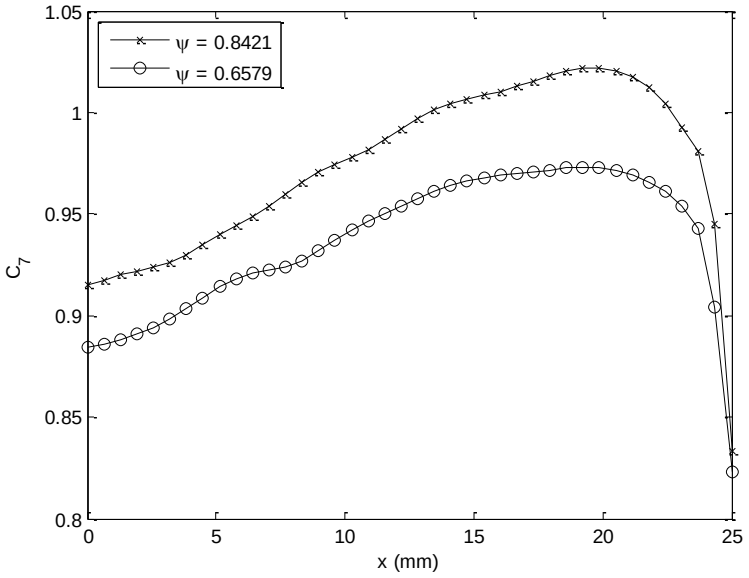

Fig. 6.23 – MLS constant C_7 distributions for $\psi = 0.6579$, and 0.8421

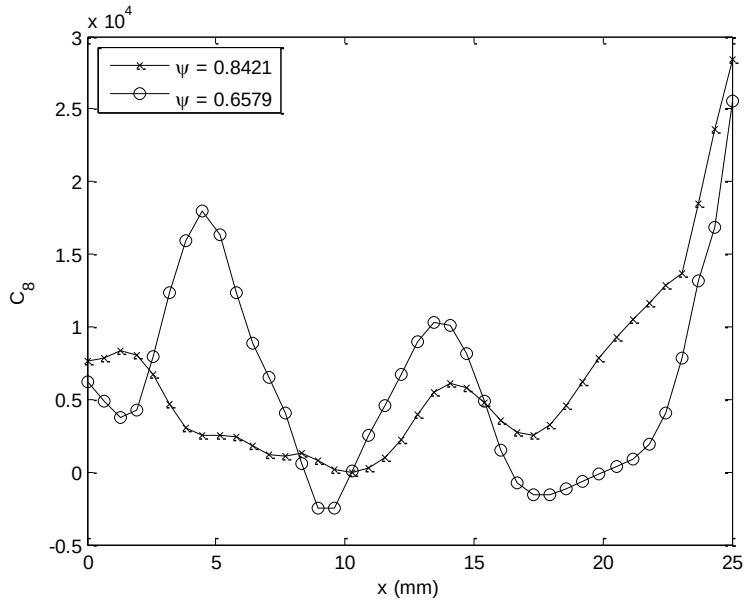

Fig. 6.24 – MLS constant C_8 distributions for $\psi = 0.6579$, and 0.8421

Deviation from the smooth surface model as described by the pressure gradient – mass flow rate, load per unit area – mass flow rate, and shear stress – mass flow rate relationships derived from the small scale simulations are captured through $C_{1\text{-}8}$, thus indicating the influence of topography and fluid flow phenomena on each term in the corresponding smooth surface model models (Eqs. (4.32), (4.33), and (4.34)

respectively with $C_{1\text{-}8}$ equal to unity). From figs. 6.17 – 6.24 it is observed that for each MLS constant plotted the responses are smooth but undulate as functions of x. The magnitudes of the constants are not unity throughout most of the response indicating that the pressure gradient – mass flow rate, load per unit area – mass flow rate, and shear stress – mass flow rate relationships as described by the metamodels are non-linear due to the influence of topography and fluid flow phenomena in the small scale simulations. This causes each of the relationships to be very different to those predicted by the smooth surface model.

Although the coefficients of friction produced by the simulations examined in figs. 6.17 – 6.24 are similar the responses they generate in terms of the pressure gradient – mass flow rate, load per unit area – mass flow rate, and shear stress – mass flow rate relationships are clearly very different. This indicates how the small scale simulations inclusive of topography and fluid flow phenomena introduce non-linearity which causes deviation from the smooth surface model which is captured by the metamodels and leads to the possibility of determining similar bearing performance characteristics with significant variations in the metamodel responses.

The distributions of C_2 and C_7 given in figs. 6.18 and 6.23 respectively indicate similarities to the corresponding pressure distribution shown in fig. 6.12. This implies that the terms each of these constants represents in the smooth surface model (Eqs. (4.32) and (4.34) respectively) are directly linked to pressure in the presence of topography and fluid flow phenomena.

Figs. 6.17, 6.18, 6.19, 6.22, and 6.23 indicate that C_1, C_2, C_3, C_6, and C_7 are subject to a significant decrease in the outlet region of the bearing, figs. 6.20, 6.21, and 6.24 show the inverse such that C_4, C_5, and C_8 significantly increase in the outlet region of the bearing. These observations can be linked to the corresponding pressure gradient distribution presented in fig. 6.13 where a sharp decrease in the pressure gradient is seen in the outlet of the bearing. It can therefore be concluded that in the presence of topography and fluid flow phenomena that each of the terms in the smooth surface model have some dependency on the pressure gradient, especially when a large negative gradient is experienced in the outlet region of the bearing.

6.5 Summary

A two-scale method for the analysis of EHL in tilted-pad bearings with parameterised 3D topography was presented and expanded to optimise longitudinal/transverse topography for bearing performance (coefficient of friction). In this study the global optimal longitudinal/transverse ratio was found to be $\psi = 0.8421$ for the conditions investigated, which produced a coefficient of friction $\mu = 8.028 \times 10^{-3}$. This minima was very close to another local minimum found at $\psi = 0.6579$ for which the coefficient of friction was $\mu = 8.104 \times 10^{-3}$. Both of these values were higher than that found by the smooth surface model (without topography and fluid flow phenomena) $\mu = 7.175 \times 10^{-3}$ but this does not mean that certain topographies or bearing operating parameters can lead to lower coefficients of friction than their corresponding smooth surface counterparts. The topographies produced by the two minima are very different highlighting the non-linearity in the response and the capabilities of metamodelling to couple the scales investigated and perform design optimisation.

Inspecting the pressure distributions generated at the local and global minima indicated that in the presence of topography and under constant load that there was a change in shape of the pressure distribution from the smooth surface model. It was also found that the film thickness and mass flow rate were generally reduced and the shear stress increased from the smooth surface model. Linking the minima found to changes in the response indicated that topography has a non-linear effect and that this is accurately captured by the metamodels created. It was also observed that a longitudinal roughness tended to change the shape and magnitude of the pressure and film thickness distributions when compared to a transverse or longitudinal/transverse roughness. This change in shape and magnitude is directly linked to the increase in the coefficient of friction seen as the transverse/longitudinal ratio tends toward zero. The choice of a BVP solver over the IVP solver used for obtaining the pressure distributions was validated as a computational time saving of approximately 33% was observed over the range of simulations investigated.

Investigating how the MLS constants varied over the length of the bearing quantified the deviation from the smooth surface model in the presence of topography and fluid flow phenomena. It was shown for the two minima identified that the responses generated were non-linear and significantly different to the smooth surface model, inspecting each MLS constant individually allowed the influence of each term in

the smooth surface model equations to be seen. Dependency of some of the MLS constants with pressure was observed due to similarities in the distributions, it was also portrayed that where there is a large negative pressure gradient (toward the outlet region of the bearing) there is a corresponding increase or decrease for all of the MLS constants.

Chapter 7 – Conclusions and Future Developments

7.1 Introduction

This chapter discusses the significance of the research presented in this thesis and the important conclusions which can be drawn from the development of the two-scale method for EHL. Future developments for the method are outlined as an extension to the studies presented in this thesis.

7.2 Conclusions

The aims and objectives of this thesis are to develop a two-scale method for modelling EHL based on the HMM. This method allows the effects of three-dimensional topography in bearings to be investigated and subsequently to conduct optimisation of topography for bearing performance. Conclusions which can be drawn from this work are highlighted in the following subsections.

7.2.1 Numerical Modelling

Numerical modelling of the two-scale method was the focus of much of the work undertaken, developing simulations at two scales and coupling them via the use of metamodelling techniques. The main conclusions which are made from this modelling are:

- Mesh independence of simulations undertaken at both scales proves that the levels of discretisation chosen are of a good accuracy and traded-off well with computational expense.
- Flow fields from the small scale simulations show that velocity is approximately equal from each side of the coupled boundaries. This means that the near-periodic requirements of the multiscale method are met and the effects of including three-dimensional topography and fluid flow phenomena modelled at this scale are, through homogenisation, accurately described at the large scale.
- An effective large scale solver is developed which incorporates the numerical function describing the pressure gradient – mass flow rate relationship derived from homogenised results of small scale simulations.

- Two different approaches are introduced for solving the large scale pressure field using MATLAB (The Math Works Inc., USA). It is determined that the BVP solver is approximately 33% faster than the IVP method but requires a good initial solution for the pressure and mass flow rate to be provided.
- The use of an inverse spring at the large scale allows for any definition of the local stiffness which is used to determine the solid thickness in the small scale simulations. This means any level of discretisation could be used at the large scale, such that the two-scale method presented here is more generic than that of Gao and Hewson [30].
- The error in mass flow rate between large scale simulations inclusive of topography and their exact corresponding small scale simulations are small. This indicates that the MLS metamodels used to couple the scales are an accurate approximation of the non-linear effects introduced at the small scale.
- Both k-fold CV and LOOCV are determined to be capable of predicting the closeness of fit tuning parameter needed by the MLS metamodels. The LOOCV is shown to be a more favourable approach because the same result can be generated with less computational effort. This conclusion is different to that of Loweth, et al. [90], indicating the right choice of CV is problem specific.
- An OLHC DoE is implemented to distribute the necessary small scale simulations effectively over the design space. This reduces the total number needed to describe the effects of topography and fluid flow phenomena at the large scale and allows a range of load capacities to be investigated.
- It is shown that parameterisation of topography can be accurately included through the pressure gradient – mass flow rate relationship. This highlights the adaptability of the MLS approach to include extra dimensions and the potential to conduct optimisation of these features.

7.2.2 Effect of Topography

In chapter 5 the two-scale method is applied to a tilted-pad bearing under load, the effects of topography are studied and the following conclusions made:

- Simulations conducted without topography and fluid flow phenomena show that the two-scale method accurately reproduced the predictions of the smooth

surface model. This provides a benchmark for the two-scale method and solution procedure.

- When compared with incompressible, isoviscous flow simulations inclusive of compressibility and piezoviscosity proved to have a more significant effect than that of non-Newtonian (shear-thinning) behaviour on the minimum film thickness and coefficient of friction.
- Two-scale simulations inclusive of topography show a lower maximum pressure than the smooth surface model which occurs closer toward the inlet of the bearing. Also film thickness is reduced over the length of the bearing.
- It is shown over a range of tilt angles and pad lengths that at constant load increasing the topography amplitude leads to an increase in the coefficient of friction (shear stress) and reduction in the minimum film thickness for the bearing. Increasing the topography amplitude tends to plateau the responses generated over the range of parameters investigated.
- The two-scale method facilitates the measurement of the micro-EHL effect on minimum film thickness. The response is shown to be non-linear over the length of the bearing due to the homogenised effects of small scale simulations and increases with the topography amplitude. This effect is observed to be an order of magnitude or more less than that dictated by column deformation, meaning that topography is not flattened out under the range of loads modelled.

7.2.3 Optimisation of Topography

In chapter 6 it is seen that by parameterisation it is possible to optimise the topography for the minimum coefficient of friction of the bearing. From this study the following conclusions can be made:

- Longitudinal topographies are shown to produce larger coefficients of friction than topographies with either transverse or a mixture of longitudinal and transverse components. This evidence agrees with the observations made by a number of researchers who conducted practical and computational experiments (Patir and Cheng [23], Jeng [53], Akamatsu, et al. [54], Greenwood and Johnson [55], Greenwood and Morales-Espejel [56], Venner and ten Napel [57]).
- Longitudinal topography causes a larger deviation from the smooth surface model than transverse topography as observed through the pressure and film

thickness distributions. The maximum pressure is reduced and the film thickness increased over the length of the bearing.

- For all topographies investigated none produces a coefficient of friction less than that provided by the smooth surface model. Under different configurations of topography or operating conditions, coefficients of friction less than their smooth surface counterparts could be found.
- The bracketing optimisation procedure is a successful means of finding the global minimum. The coefficient of friction versus longitudinal/transverse ratio response generated is non-linear due to the inclusion of topography and fluid flow phenomena in the small scale simulations. The two-scale method accurately captures this, which highlights the necessity of the method for modelling this behaviour.
- Two local minima in the coefficient of friction are identified through the process, with one being determined as the global minimum. Corresponding maxima in the mass flow rate and minimum film thickness are found at the two minima identified.
- The coefficients of friction at the two minima identified are similar but the design variables very different, highlighting the non-linear response and need of the two-scale method to capture this effect.
- Plots of the MLS constants over the length of the bearing quantified deviation from the smooth surface model for the different topographies investigated. It is shown that the MLS constants responses are non-linear over the length of the bearing due to the effects described by small scale simulations, some dependency of the response on the pressure and pressure gradient is observed. This indicates the advantage of the metamodel approach where direct comparison between smooth and rough surfaces can be made.

7.3 Future Developments

The two-scale method for EHL is a very new approach and this study is one of the first to be concerned with it, because of this there are many avenues for future research. The following subsections indicate potential routes which will expand the two-scale method for the effective analysis of any EHL contact.

7.3.1 Cross-Flow and Side-Leakage

Expanding the two-scale method to investigate two-dimensional large scale problems is feasible as discussed in the theoretical formulation presented in chapter 4. By expanding the method to the general large scale case more complex geometries such as point contacts could be investigated. The small scale model would remain unchanged, pressure gradients required to determine cross-flow or side-leakage could easily be imposed with another pressure jump condition normal to the direction of motion of the moving wall. It is recommended that a code be developed specifically for the small scale simulation. Considerable amount of effort was made to develop this stage of the method and subsequently correctly implementing the near-periodic boundary conditions with FSI. Conventional CFD solvers do not have this type of boundary condition available and there are not many architectures which allow generic boundary conditions to be created, for those which do this type of constraint is difficult to implement because it has similarities with periodic type conditions but is fundamentally very different.

The large scale formulation would differ as two separate pressure gradient equations would be required, each with four terms to account for the film thickness, pressure, and mass flow rates in both the x and y directions (q_x and q_y respectively). Conservation of mass would then be needed along with the two partial differential equations described in order to solve the large scale problem. Mathematically this is given by Eqs. (7.1) – (7.3) and can be solved with Dirichlet boundary conditions for zero (ambient) pressure at the surrounding boundaries, cavitation is discussed in section 7.3.3.

$$\frac{\partial p}{\partial x} = f(p, q_x, q_y, g) \tag{7.1}$$

$$\frac{\partial p}{\partial y} = f(p, q_x, q_y, g) \tag{7.2}$$

$$\frac{\partial q_x}{\partial x} + \frac{\partial q_y}{\partial y} = 0 \tag{7.3}$$

Because the two-dimensional large scale problem requires two separate four-dimensional equations a significant increase in metamodelling complexity is inherent. A different solver for the method would also be needed than either the IVP or BVP methods used in the current two-scale architecture. This method would need to account for the divergence of the mass flow rates and couple this into a solution for each of the pressure gradient equations. A significant increase in difficulty and computational expense therefore exists for the two-dimensional large scale problem.

7.3.2 Highly-Loaded Contacts

Investigation of highly-loaded EHL simulations such as those found in converging-diverging geometries such as line or point contacts is entirely feasible using the two-scale method. No changes to the small scale model are needed other than adjusting the parameters representing the change in material properties. In order to maintain the separation in scales between the equivalent thickness and the size (plus deformation of) topography the local stiffness must be carefully chosen to incorporate the difference in Young's modulus described by the highly-loaded simulation.

The choice of large scale solver becomes fundamental to the accuracy and convergence of the resulting simulation. The response of highly-loaded EHL simulations is far more sensitive to the input parameters than in soft-EHL, for example the dependency of viscosity is exponential with pressure. Neither the IVP nor BVP methods introduced here are able to cope with large changes in the output response due to small changes in the input with much accuracy. Suggested solutions would be to reduce the separation in scales by non-dimensionalising the pressure gradient – mass flow rate relationships or concentrate on creating metamodels which are highly accurate in regions of steep gradients.

7.3.3 Cavitation

Cavitation can be modelled at both scales where needed using the two-scale method. Modelling cavitation in the large scale simulation only would require an additional constraint in order to meet the Reynolds exit condition, such that pressure and the pressure gradient are zero at an undefined outlet location. This can be implemented using a moving mesh or shooting type approach to solve for the outlet

location and pressure field. The BVP solver for pressure could also be implemented at the same time reducing the complexity of needing to change solver completely.

Small scale cavitation would require a change of phase in the lubricant properties to be modelled. This can be achieved in a number of ways as various models for cavitation exist. A simple approach would be to model the change of phase from liquid to vapour as pressure reaches the ambient value by a sudden drop in viscosity and density. Small scale simulations inclusive of cavitation would also need the Reynolds exit condition to be met in the large scale solution process. Because the pressure gradient – mass flow rate relationship now incorporates the cavitation effect as pressure tends toward zero, the outlet region will be a more accurate representation of this effect than by only considering the boundary condition on its own.

7.3.4 Representation of Topography

Any description of topography can be modelled at the small scale using the two-scale method so long as the function describing it is smooth and remains periodic over the domain in both the x and y directions. Examples of this kind of function can be generated by spectral methods or Fourier analysis. Further parameterisation of topography is possible and would allow a larger range of designs to be investigated and potentially optimised. The difficulty would come with adding further dimensions to the pressure gradient – mass flow rate relationship and subsequently providing an accurate metamodel without needing thousands of small scale simulations.

Increasing the complexity of topography will increase the computational requirements necessary in order to solve the small scale problem, which is already an issue with the current method. Fourier analysis of real surfaces could provide a representative periodic roughness for two-scale method. This would open up the potential to compare computational results of the two-scale method with experimental results with the same topography. If this was achieved then it would give solid evidence that the observations and inferences made from the two-scale method are an accurate model of the real EHL system.

7.3.5 Design of Experiments

Conventionally, and as implemented in the current two-scale method, the DoE spans a hypercube which is bounded by predetermined limits. In the solution to the two-scale method parts of this design space are populated by small scale simulations but are never used by the large scale solver. For example at high pressure the pressure gradient tends toward zero (at the maximum pressure) and so the large scale solver is not concerned with high pressure and either highly positive or negative pressure gradients.

One solution to this problem would be to populate an orthogonal space about a curve representing the solution to the smooth surface problem. The curve can be generated by solving Reynolds equation, the pressure gradient, pressure and film thickness are then known. Placing a curvilinear coordinate system along the length of this curve and setting arbitrary limits then provides an orthogonal space which can be populated by the DoE and mapped back to the Cartesian system. The DoE now encompasses the Reynolds solution and so long as the two-scale solver does not deviate far from this the metamodel approximation will be accurate and not be populated by small scale simulations that will never be used.

7.3.6 Response Surface Methodology

Other metamodelling techniques than MLS such as Kriging, RBF, SVR, MARS, ANN, etc. may lead to a more efficient means of creating an approximation which can be used to couple the scales of the method. Any of the aforementioned techniques may require fewer small scale simulations to provide the same level of accuracy at the large scale as that observed in the current study. This is because these methods may possibly inherently fit the response data more effectively than the MLS method or may maintain accuracy with more dimensions (as would be very important for tackling the issues of sections 7.3.1 and 7.3.4). An investigation of the number of DoE points would provide useful information for selecting the least number of designs which maintains the required accuracy in the metamodel prediction. MLS is favourable in this sense because it is capable of smoothing numerical noise in the response. Whether the other metamodelling techniques can be used to indicate how far from the smooth surface model simulations inclusive of topography deviate or how well numerical noise maybe be handled, as achieved with MLS, is a another question which would require further investigation.

Bibliography

1. de Boer, G.N., L.M. Gao, R.W. Hewson, and H.M. Thompson, *A two-scale method for incorporating the effects of three-dimensional surface topography in an elastohydrodynamic line contact*, in *5th World Tribology Congress*, 2013: PalaolmpIco, Turin, Italy.

2. Gao, L.M., G.N. de Boer, and R.W. Hewson, *A multiscale framework for lubrication analysis of bearings with textured surface*, in *Advances in Structural Engineering and Mechanics (ASEM)*, 2013: International Convention Centre, Jeju, South Korea.

3. de Boer, G.N., R.W. Hewson, H.M. Thompson, L.M. Gao, and V.V. Toropov, *Two-Scale EHL: Three-Dimensional Topography in Tilted-Pad Bearings.* Tribology International, 2014. **79**: p. 111-125.

4. de Boer, G.N., R.W. Hewson, H.M. Thompson, L.M. Gao, and V.V. Toropov, *Two-scale EHL and optimisation of topography*, in *Lubrication, Maintenance, and Tribotechnology*, 2014: Hilton Deansgate Hotel, Manchester, UK.

5. de Boer, G.N., R.W. Hewson, H.M. Thompson, L.M. Gao, and V.V. Toropov. *Metamodelling and Optimisation in Two-Scale Elastohydrodynamic Lubrication*. in *Proceedings of the 10th ISSMO/ASMO-UK Conference on Engineering Design Optimization Product and Process Improvement*, Delft University of Technology, Delft, the Netherlands, 31st June – 1st July, 2014, University of Leeds, ISBN: 978-0-85316-334-3.

6. Kondo, Y., T. Koyama, and S. Sasaki, *Tribological properties of ionic liquids*, in *Ionic liquids - New aspects for the future*, J. Kadokawa, Editor. 2013.

7. Almqvist, T. and R. Larsson, *The Navier-Stokes approach for thermal EHL line contact solutions.* Tribology International, 2002. **35**(3): p. 163-170.

8. Chu, L.-M., W.-L. Li, Y.-P. Chang, and H.-C. Hsu, *EHL of circular contacts lubricating with mixture of two lubricants.* Industrial Lubrication and Technology, 2010. **62**(2): p. 83-90.

9. Dobrica, M.B. and M. Fillon, *About the validity of Reynolds equation and inertia effects in textured sliders of infinite width.* Proceedings of the Institution of Mechanical Engineers Part J-Journal of Engineering Tribology, 2009. **223**(J1): p. 69-78.

10. Stachowiak, G.W. and A.W. Batchelor, *Engineering tribology*. 3rd ed. 2005: Butterworth-Heinemann.

11. Cavazzuti, M., *Optimization Methods: From Theory to Design Scientific and Technological Aspects in Mechanics*. 2013, Berlin, Germany: Springer.

12. Box, G.E.P. and N.R. Draper, *Emperical Model-Building and Response Surfaces*. 1987, New York: Wiley.

13. Alexa, M., J. Behr, D. Cohen-Or, S. Fleishman, D. Levin, and C.T. Silva, *Computing and rendering point set surfaces.* IEEE Transactions on Visualisation and Computer Graphics, 2003. **9**(1): p. 3-15.

14. Dowson, D., *History of Tribology*. 1999, New York, USA: Wiley and Sons.

15. Jost, H.P. and G.B.M.o. Technology, *Committee on Tribology Report, 1966-67*. 1968: H.M. Stationery Office.

16. Gohar, R., *Elastohydrodynamics*. 2nd ed. 2001: World Scientific.

17. Johnson, K.L., *Contact Mechanics*. 1985, Cambridge, UK: Cambridge University Press.

18. Hamrock, B.J., S.R. Schmid, and B.O. Jacobson, *Fundamentals of Fluid Film Lubrication*. 2004, McGraw-Hill. p. 435.

19. Hartinger, M., M.L. Dumont, S. Ioannides, D. Gosman, and H. Spikes, *CFD modeling of a thermal and shear-thinning elastohydrodynamic line contact*. Journal of Tribology-Transactions of the Asme, 2008. **130**(4).

20. Almqvist, T., *Computational Fluid Dynamics in Theoretical Simulations of Elastohydrodynamic Lubrication*, 2004, Technical University of Lulea, Sweden.

21. Etsion, I., Y. Kligerman, and G. Halperin, *Analytical and experimental investigation of laser-textured mechanical seal faces.* Tribology Transactions, 1999. **42**(3): p. 511-516.

22. Szeri, A.Z., *Fluid Film Lubrication*. 1998, Cambridge, UK: Cambridge University Press.

23. Patir, N. and H.S. Cheng, *Average Flow Model for Determining Effects of 3-Dimensional Roughness on Partial Hydrodynamic Lubrication.* Journal of Lubrication Technology-Transactions of the Asme, 1978. **100**(1): p. 12-17.

24. de Kraker, A., R.A.J. van Ostayen, A. van Beek, and D.J. Rixen, *A multiscale method modeling surface texture effects.* Journal of Tribology-Transactions of the Asme, 2007. **129**(2): p. 221-230.

25. de Kraker, A., R.A.J. van Ostayen, and D.J. Rixen, *Development of a texture averaged Reynolds equation.* Tribology International, 2010. **43**(11): p. 2100-2109.

26. Sahlin, F., R. Larsson, A. Almqvist, P.M. Lugt, and P. Marklund, *A mixed lubrication model incorporating measured surface topography. Part 1: theory of flow factors.* Proceedings of the Institution of Mechanical Engineers Part J-Journal of Engineering Tribology, 2010. **224**(J4): p. 335-351.

27. Sahlin, F., R. Larsson, P. Marklund, A. Almqvist, and P.M. Lugt, *A mixed lubrication model incorporating measured surface topography. Part 2: roughness treatment, model validation, and simulation.* Proceedings of the Institution of Mechanical Engineers Part J-Journal of Engineering Tribology, 2010. **224**(J4): p. 353-365.

28. E, W., B. Engquist, X.T. Li, W.Q. Ren, and E. Vanden-Eijnden, *Heterogeneous multiscale methods: A review*. Communications in Computational Physics, 2007. **2**(3): p. 367-450.

29. Hewson, R.W., N. Kapur, and P.H. Gaskell, *A two-scale model for discrete cell gravure roll coating.* Chemical Engineering Science, 2011. **66**(16): p. 3666-3674.

30. Gao, L.M. and R. Hewson, *A Multiscale Framework for EHL and Micro-EHL.* Tribology Transactions, 2012. **55**(6): p. 713-722.

31. Stribeck, R., *Die wesentlichen Eigenschaften der Gleit- und Rollenlager*. Mitteilungen über Forschungsarbeiten auf dem Gebiete des Ingenieurwesens. Heft 7. 1903: Springer.

32. Hersey, M.D., *Laws of lubrication of horizontal journal bearings.* Journal of the Washington Academy of Science, 1914. **4**: p. 542-552.

33. Cameron, A., *Basic Lubrication Theory*. 1971, London: Longman.

34. Tzeng, S.T. and E. Saibel, *Surface Roughness Effect on Slider Bearing Lubrication.* Asle Transactions, 1967. **10**(3): p. 334-348.

35. Reynolds, O., *On the Theory of Lubrication and Its Application to Mr. Beauchamp Tower's Experiment, Including an Experimental Determination of the Viscosity of Olive Oil.* Philosophical Transactions of the Royal Society of London Series A - Containing Papers of a Mathematical or Physical Character, 1886. **177**: p. 157-234.

36. Martin, H.M., *Lubrication of Gear Teeth.* Engineering, 1916. **102**: p. 119-121.

37. Gümbel, L., *Über Geschmierte Arbeitsräder (On the Lubrication of Gears).* Zeitschrift fur das Gesamte Turbinenwesen, 1916. **13**: p. 357.

38. Meldahl, A., *Contribution to Theory of Lubrication of Gears and of Stressing of Lubricated Flanks of Gear Teeth.* Brown Boveri Review, 1941. **28**(11): p. 374-382.

39. von Mohrenstein-Ertel, A., *Die Berechnung der Hydrodynamischen Schmierung Gekrümmter Oberflächen unter Hoher Belastung und Relativbewegung*. Fortschrittsberichte VDI, ed. O.R. Lang and P. Oster. Vol. 1. 1949, Düsseldorf, Germany: VDI Verlag (First published in 1945 under the name A. M. Ertel).

40. Grubin, A.N. *Invetsigation on the Contact of Machine Components*. in *Central Scientific Reserach Institute for Technology and Mechanical Engineering*. 1949. Moscow.

41. Petrusevich, A.I., *Fundamental Conclusions from the Contact Hydrodynamic Theory of Lubrication.* Izvestiya Akademii Nauk SSSR (OTN), 1951. **3**(2): p. 209-223.

42. Dowson, D. and G.R. Higginson, *A Numerical Solution to the Elasto-Hydrodynamic Problem*. Journal of Mechanical Engineering Science, 1959(1): p. 6.

43. Dowson, D. and G.R. Higginson, *Elastohydrodynamic Lubrication: The Fundamentals of Roller and Gear Lubrication*. 1966, Oxford, UK: Pergamon.

44. Hamrock, B.J. and D. Dowson, *Isothermal Elastohydrodynamic Lubrication of Point Contacts .1. Theoretical Formulation.* Journal of Lubrication Technology-Transactions of the Asme, 1976. **98**(2): p. 223-229.

45. Hamrock, B.J. and D. Dowson, *Isothermal Elastohydrodynamic Lubrication of Point Contacts .2. Ellipticity Parameter Results.* Journal of Lubrication Technology-Transactions of the Asme, 1976. **98**(3): p. 375-383.

46. Hamrock, B.J. and D. Dowson, *Isothermal Elastohydrodynamic Lubrication of Point Contacts .3. Fully Flooded Results.* Mechanical Engineering, 1977. **99**(2): p. 143-143.

47. Lubrecht, A.A., W.E. ten Napel, and R. Bosma, *Multigrid, an Alternative Method for Calculating Film Thickness and Pressure Profiles in Elastohydrodynamically Lubricated Line Contacts.* Journal of Tribology-Transactions of the Asme, 1986. **108**(4): p. 551-556.

48. Lubrecht, A.A., W.E. ten Napel, and R. Bosma, *Multigrid, an Alternative Method of Solution for Two-Dimensional Elastohydrodynamically Lubricated Point Contact Calculations.* Journal of Tribology-Transactions of the Asme, 1987. **109**(3): p. 437-443.

49. Venner, C.H., *Multilevel Solution of the EHL Line and Point Contact Problems*, 1991, University of Twente: Enschede, the Netherlands.

50. Venner, C.H. and A.A. Lubrecht, *Multilevel Methods in Lubrication*. 2000, the Netherlands: Elsevier.

51. Nijenbanning, G., C.H. Venner, and H. Moes, *Film Thickness in Elastohydrodynamically Lubricated Elliptic Contacts.* Wear, 1994. **176**(2): p. 217-229.

52. Tzeng, S.T. and E. Saibel, *On Effects of Surface Roughness in Hydrodynamic Lubrication Theory of a Short Journal Bearing.* Wear, 1967. **10**(3): p. 179-184.

53. Jeng, Y.R., *Experimental-Study of the Effects of Surface-Roughness on Friction.* Tribology Transactions, 1990. **33**(3): p. 402-410.

54. Akamatsu, Y., N. Tsushima, T. Goto, and K. Hibi, *Influence of Surface-Roughness Skewness on Rolling-Contact Fatigue Life.* Tribology Transactions, 1992. **35**(4): p. 745-750.

55. Greenwood, J.A. and K.L. Johnson, *The Behavior of Transverse Roughness in Sliding Elastohydrodynamically Lubricated Contacts.* Wear, 1992. **153**(1): p. 107-117.

56. Greenwood, J.A. and G.E. Morales-Espejel, *The Behavior of Real Transverse Roughness in a Sliding Ehl Contact*. Thin Films in Tribology, 1993. **25**: p. 227-236.

57. Venner, C.H. and W.E. ten Napel, *Surface-Roughness Effects in an Ehl Line Contact*. Journal of Tribology-Transactions of the Asme, 1992. **114**(3): p. 616-622.

58. Zhu, D. and Y.Z. Hu, *Effects of rough surface topography and orientation on the characteristics of EHD and mixed lubrication in both circular and elliptical contacts.* Tribology Transactions, 2001. **44**(3): p. 391-398.

59. Venner, C.H. and A.A. Lubrecht, *Amplitude reduction of non-isotropic harmonic patterns in circular EHL Contacts, under pure rolling*, in *Lubrication of the frontier, Proceedings of the 25th Leeds-Lyon Symposium on Tribology*, D. Dowson, Editor 1999, Elsevier: the Netherlands. p. 151-162.

60. Morales-Espejel, G.E., P.M. Lugt, J. Van Kuilenburg, and J.H. Tripp, *Effects of surface micro-geometry on the pressures and internal stresses of pure rolling EHL contacts.* Tribology Transactions, 2003. **46**(2): p. 260-272.

61. Masen, M.A., C.H. Venner, P.M. Lugt, and J.H. Tripp, *Effects of surface micro-geometry on the lift-off speed of an EHL contact*. Tribology Transactions, 2002. **45**(1): p. 21-30.

62. Dowson, D. and P. Ehret, *Past, present and future studies in elastohydrodynamics.* Proceedings of the Institution of Mechanical Engineers Part J-Journal of Engineering Tribology, 1999. **213**(J5): p. 317-333.

63. Spikes, H.A., *Sixty years of EHL*. Lubrication Science, 2006. **18**: p. 265-291.

64. Lugt, P.M. and G.E. Morales-Espejel, *A Review of Elasto-Hydrodynamic Lubrication Theory*. Tribology Transactions, 2011. **54**(3): p. 470-496.

65. Hooke, C.J., K.Y. Li, and G. Morales-Espejel, *Rapid calculation of the pressures and clearances in rough, rolling-sliding elastohydrodynamically lubricated contacts. Part 2: general, non-sinusoidal roughness.* Proceedings of the Institution of Mechanical Engineers Part C-Journal of Mechanical Engineering Science, 2007. **221**(5): p. 551-564.

66. Krupka, I. and M. Hartl, *The effect of surface texturing on thin EHD lubrication films.* Tribology International, 2007. **40**(7): p. 1100-1110.

67. Almqvist, T., A. Almqvist, and R. Larsson, *A comparison between computational fluid dynamic and Reynolds approaches for simulating transient EHL line contacts.* Tribology International, 2004. **37**(1): p. 61-69.

68. Almqvist, T. and R. Larsson, *Some remarks, on the validity of Reynolds equation in the modeling of lubricant film flows on the surface roughness scale.* Journal of Tribology-Transactions of the Asme, 2004. **126**(4): p. 703-710.

69. van Odyck, D.E.A. and C.H. Venner, *Stokes flow in thin films.* Journal of Tribology-Transactions of the Asme, 2003. **125**(1): p. 121-134.

70. Tichy, J. and B. Bou-Said, *On the Transition from Reynolds to Stokes Roughness.* Transient Processes in Tribology, 2003. **43**(235-242).

71. Arghir, M., N. Roucou, M. Helene, and J. Frene, *Theoretical analysis of the incompressible laminar flow in a macro-roughness cell.* Journal of Tribology-Transactions of the Asme, 2003. **125**(2): p. 309-318.

72. Sahlin, F., S.B. Glavatskih, T. Almqvist, and R. Larsson, *Two-dimensional CFD-analysis of micro-patterned surfaces in hydrodynamic lubrication.* Journal of Tribology-Transactions of the Asme, 2005. **127**(1): p. 96-102.

73. Cupillard, S., S. Glavatskih, and M.J. Cervantes, *Inertia effects in textured hydrodynamic contacts.* Proceedings of the Institution of Mechanical Engineers Part J-Journal of Engineering Tribology, 2010. **224**(J8): p. 751-756.

74. Wilson, S.K. and B.R. Duffy, *On lubrication with comparable viscous and inertia forces.* Quarterly Journal of Mechanics and Applied Mathematics, 1998. **51**: p. 105-124.

75. Aurelian, F., M. Patrick, and H. Mohamed, *Wall slip effects in (elasto) hydrodynamic journal bearings.* Tribology International, 2011. **44**(7-8): p. 868-877.

76. Bruyere, V., N. Fillot, G.E. Morales-Espejel, and P. Vergne, *Computational fluid dynamics and full elasticity model for sliding line thermal elastohydrodynamic contacts.* Tribology International, 2012. **46**(1): p. 3-13.

77. Mourier, L., D. Mazuyer, F.P. Ninove, and A.A. Lubrecht, *Lubrication mechanisms with laser-surface-textured surfaces in elastohydrodynamic regime.* Proceedings of the Institution of Mechanical Engineers Part J-Journal of Engineering Tribology, 2010. **224**(J8): p. 697-711.

78. Zhu, D., T. Nanbu, N. Ren, Y. Yasuda, and Q.J. Wang, *Model-based virtual surface texturing for concentrated conformal-contact lubrication.* Proceedings of the Institution of Mechanical Engineers Part J-Journal of Engineering Tribology, 2010. **224**(J8): p. 685-696.

79. Gao, L.M., P.R. Yang, I. Dymond, J. Fisher, and Z.M. Jin, *Effect of surface texturing on the elastohydrodynamic lubrication analysis of metal-on-metal hip implants.* Tribology International, 2010. **43**(10): p. 1851-1860.

80. Felix-Quinonez, A., P. Ehret, and J.L. Summers, *On three-dimensional flat-top defects passing through an EHL point contact: A comparison of modeling with experiments.* Journal of Tribology-Transactions of the Asme, 2005. **127**(1): p. 51-60.

81. Jai, M. and B. Bou-Said, *A comparison of homogenization and averaging techniques for the treatment of roughness in slip-flow-modified Reynolds equation.* Journal of Tribology-Transactions of the Asme, 2002. **124**(2): p. 327-335.

82. Sahlin, F., A. Almqvist, R. Larsson, and S. Glavatskih, *Rough surface flow factors in full film lubrication based on a homogenization technique.* Tribology International, 2007. **40**(7): p. 1025-1034.

83. Martin, S., *Influence of multiscale roughness patterns in cavitated flows: Applications to journal bearings.* Mathematical Problems in Engineering, 2008.

84. Almqvist, T., S.B. Glavatskikh, and R. Larsson, *THD analysis of tilting pad thrust bearings - Comparison between theory and experiments.* Journal of Tribology-Transactions of the Asme, 2000. **122**(2): p. 412-417.

85. Li, J. and H.S. Chen, *Evaluation on applicability of reynolds equation for squared transverse roughness compared to CFD.* Journal of Tribology-Transactions of the Asme, 2007. **129**(4): p. 963-967.

86. Cheng, H.S. and A. Dyson, *Elastohydrodynamic lubrication of circumferentially-ground round disks.* Asle Transactions, 1978. **21**: p. 25.

87. Hooke, C.J., K.Y. Li, and G. Morales-Espejel, *Rapid calculation of the pressures and clearances in rough, rolling-sliding elastohydrodynamically lubricated contacts. Part 1: low-amplitude, sinusoidal roughness.* Proceedings of the Institution of Mechanical Engineers Part C-Journal of Mechanical Engineering Science, 2007. **221**(5): p. 535-550.

88. E, W. and B. Engquist, *The Heterogenous Multi-Scale Methods.* Communications in Mathematical Sciences, 2003. **1**: p. 87-133.

89. E, W.N., B. Engquist, and Z.Y. Huang, *Heterogeneous multiscale method: A general methodology for multiscale modeling.* Physical Review B, 2003. **67**(9).

90. Loweth, E.L., G.N. de Boer, and V.V. Toropov. *Practical Recommendations on the Use of Moving Least Squares Metamodel Building*. in *Proceedings of the Thirteenth International Conference on Civil, Structural and Environmental Engineering*. 2011. Chania, Crete, Greece: Civil-Comp Press.

91. Narayanan, A., V.V. Toropov, A.S. Wood, and I.F. Campean, *Simultaneous model building and validation with uniform designs of experiments.* Engineering Optimization, 2007. **39**(5): p. 497-512.

92. Bates, S.J., J. Sienz, and V.V. Toropov. *Formulation of the Optimal Latin Hypercube Designs of Experiments*. in *Proceedings of the 45th AIAA/ ASME/ ASCE/ AHS/ ASC Structures, Structural Dynamics & Materials Conference*. 2004. Palm Springs, California, USA.

93. Toropov, V.V., S. Bates, and O.M. Querin. *Generation of Uniform Latin Hypercube Designs of Experiments*. in *Proceedings of the 9th International Conference on the Application of Artificial Intelligence to Civil, Structural and Environmental Engineering*. 2007. St Julians, Malta: Civil-Comp Press.

94. Contry, T.F., Wang, and C. Cusano, *A Reynolds-Eyring equation for elastohydrodynamic lubrication in line contacts.* Journal of Tribology-Transactions of the Asme, 1987. **109**: p. 648-658.

95. Johnson, K.L. and J.L. Tevaarwerk, *Shear Behavior of Elastohydrodynamic Oil Films.* Proceedings of the Royal Society of London Series a-Mathematical Physical and Engineering Sciences, 1977. **356**(1685): p. 215-236.

96. Roelands, C.J.A., *Correlational Aspects of the Viscosity-Temperature-Pressure Relationship of Lubricating Oils*, 1966, Technische Hogeschool Delft: the Netherlands.

97. Dowson, D. and G.R. Higginson, *Elastohydrodynamic Lubrication*. 1977, Oxford: Pergamon Press.

98. Hewson, R.W., N. Kapur, and P.H. Gaskell. *Film Formation Model of Shear Thinning Power Law Fluids Using Lubrication Analysis*. in *European Coating Symposium*. 2005. Bradford, UK.

99. Dowson, D., *A generalised Reynolds equation for fluid-film lubrication.* International Journal of Mechanical Science, 1962. **4**: p. 159-170.

100. Spikes, H.A., *The half-wetted bearing. part 1: Extended Reynolds equation.* Proceedings of the Institution of Mechanical Engineers Part J-Journal of Engineering Tribology, 2003. **217**: p. 1-14.

101. Hertz, H., *Über die Berührung Fester Elasticher Körper.* Journal für die Reine und Angewandte Mathematik, 1881. **92**: p. 156-171.

102. Rodkiewicz, C.M. and P. Yang, *Proposed Tehl Solution System for the Thrust-Bearings Inclusive of Surface Deformations.* Tribology Transactions, 1995. **38**(1): p. 75-85.

103. Jaeger, J.C., *Moving sources of heat and the temperature at sliding contacts.* Proceedings of the Royal Society of NSW, 1942. **76**: p. 203-224.

104. Carslaw, H.S. and J.C. Jaeger, *Conduction of Heat in Solids*. 2nd ed. 1986, Oxford: Clarendon Press.

105. Barus, C., *Isothermals, Isopiestics and Isometrics Relative to Viscosity.* American Journal of Science, 1893. **45**: p. 87-96.

106. Bair, S. and P. Kottke, *Pressure-viscosity relationships for elastohydrodynamics.* Tribology Transactions, 2003. **46**(3): p. 289-295.

107. Houpert, L., *New results of traction force calculations in ehd contacts.* Journal of Lubrication Technology-Transactions of the Asme, 1985. **107**: p. 241-248.

108. Bair, S., *The variation of viscosity with temperature and pressure for various real lubricants.* Journal of Tribology-Transactions of the Asme, 2001. **123**(2): p. 433-436.

109. Yasutomi, S., S. Bair, and W.O. Winer, *An Application of a Free-Volume Model to Lubricant Rheology.* Journal of Tribology-Transactions of the Asme, 1984. **106**(2): p. 304-312.

110. Bair, S., J. Jarzynski, and W.O. Winer, *The temperature, pressure and time dependence of lubricant viscosity.* Tribology International, 2001. **34**(7): p. 461-468.

111. Chittenden, R.J., D. Dowson, J.F. Dunn, and C.M. Taylor, *A Theoretical-Analysis of the Isothermal Elastohydrodynamic Lubrication of Concentrated Contacts .1. Direction of Lubricant Entrainment Coincident with the Major Axis of the Hertzian Contact Ellipse.* Proceedings of the Royal Society of London Series a-Mathematical Physical and Engineering Sciences, 1985. **397**(1813): p. 245-269.

112. Chittenden, R.J., D. Dowson, J.F. Dunn, and C.M. Taylor, *A Theoretical-Analysis of the Isothermal Elastohydrodynamic Lubrication of Concentrated Contacts .2. General-Case, with Lubricant Entrainment Along Either Principal Axis of the Hertzian Contact Ellipse or at Some Intermediate Angle.* Proceedings of the Royal Society of London Series a-Mathematical Physical and Engineering Sciences, 1985. **397**(1813): p. 271-294.

113. Evans, H.P. and R.W. Snidle, *Inverse Solution of Reynolds-Equation of Lubrication under Point-Contact Elastohydrodynamic Conditions.* Journal of Lubrication Technology-Transactions of the Asme, 1981. **103**(4): p. 539-546.

114. Evans, H.P. and R.W. Snidle, *The Elastohydrodynamic Lubrication of Point Contacts at Heavy Loads.* Proceedings of the Royal Society of London Series a-Mathematical Physical and Engineering Sciences, 1982. **382**(1782): p. 183-199.

115. Okamura, H. *A Contribution to the Numerical Analysis of Isothermal Elastohydrodynamic Lubrication*. in *Proceedings of the 9th Leeds-Lyon Symposium on Tribology*. 1982. Elsevier.

116. Lubrecht, A.A., *Numerical Solution of the EHL Line and Point Contact Problem Using Multigrid Techniques*, 1987, University if Twente: Enschede, the Netherlands.

117. Venner, C.H., W.E. ten Napel, and R. Bosma, *Advanced Multilevel Solution of the Ehl Line Contact Problem*. Journal of Tribology-Transactions of the Asme, 1990. **112**(3): p. 426-431.

118. Venner, C.H. and W.E. ten Napel, *Multilevel Solution of the Elastohydrodynamically Lubricated Circular Contact Problem .1. Theory and Numerical Algorithm*. Wear, 1992. **152**(2): p. 351-367.

119. Venner, C.H. and W.E. ten Napel, *Multilevel Solution of the Elastohydrodynamically Lubricated Circular Contact Problem .2. Smooth Surface Results.* Wear, 1992. **152**(2): p. 369-381.

120. Brandt, A. and A.A. Lubrecht, *Multilevel Matrix Multiplication and Fast Solution of Integral-Equations.* Journal of Computational Physics, 1990. **90**(2): p. 348-370.

121. Evans, H.P. and T.G. Hughes, *Evaluation of Deflection in Semi-Infinite Bodies by a Differential Method.* Proceedings of the Institution of Mechanical Engineers Part C-Journal of Mechanical Engineering Science, 2000. **214**: p. 563-584.

122. Holmes, M.J.A., H.P. Evans, T.G. Hughes, and R.W. Snidle, *Transient elastohydrodynamic point contact analysis using a new coupled differential deflection method. Part 1: theory and validation.* Proceedings of the Institution of Mechanical Engineers Part J-Journal of Engineering Tribology, 2003. **217**(J4): p. 289-303.

123. Holmes, M.J.A., H.P. Evans, T.G. Hughes, and R.W. Snidle, *Transient elastohydrodynamic point contact analysis using a new coupled differential deflection method. Part 2: results.* Proceedings of the Institution of Mechanical Engineers Part J-Journal of Engineering Tribology, 2003. **217**(J4): p. 305-321.

124. Holmes, M.J.A., H.P. Evans, and T.G. Hughes, *Analysis of Mixed Lubrication Effects in Simulated Gear Tooth Contacts*. Journal of Lubrication Technology-Transactions of the Asme, 2005. **127**: p. 61-69.

125. Habchi, W., I. Demirci, D. Eyheramendy, G. Morales-Espejel, and P. Vergne, *A finite element approach of thin film lubrication in circular EHD contacts.* Tribology International, 2007. **40**(10-12): p. 1466-1473.

126. Habchi, W., D. Eyheramendy, P. Vergne, and G. Morales-Espejel, *A full-system approach of the elastohydrodynamic line/point contact problem*. Journal of Tribology-Transactions of the Asme, 2008. **130**(2).

127. Habchi, W., D. Eyheramendy, S. Bair, P. Vergne, and G. Morales-Espejel, *Thermal Elastohydrodynamic Lubrication of Point Contacts Using a Newtonian/Generalized Newtonian Lubrication.* Tribology Letters, 2008. **30**: p. 41-52.

128. Habchi, W., P. Vergne, S. Bair, O. Andersson, D. Eyheramendy, and G.E. Morales-Espejel, *Influence of pressure and temperature dependence of thermal properties of a lubricant on the behaviour of circular TEHD contacts.* Tribology International, 2010. **43**(10): p. 1842-1850.

129. Habchi, W., P. Vergne, N. Fillot, S. Bair, and G.E. Morales-Espejel, *A numerical investigation of local effects on the global behavior of TEHD highly loaded circular contacts.* Tribology International, 2011. **44**(12): p. 1987-1996.

130. Box, G.E.P. and N.R. Draper, *Response Surfaces, Mixtures and Ridge Analyses*. 2nd ed. 2007, New York, USA: Wiley and Sons.

131. Keane, A.J. and P.B. Nair, *Computational Approaches for Aerospace Design: The Pursuit of Excellence*. 2005, New York, USA: Wiley and Sons.

132. Box, G.E.P., W.G. Hunter, and S.J. Hunter, *Statistics for experimenters*. 1978, New York, USA: Wiley.

133. Montgomery, D.C., *Design and analysis of experiments*. 5th ed. 2000, New York, USA: Wiley.

134. Koch, P.N., D. Marvis, and F. Mistree. *Multi-level, partitioned response surfaces for modeling complex systems*. in *7th AIAA/USAF/NASA/ISSMO Symposium on Mutlidisciplinary Analysis & Optimisation*. 1998. St Louis, MO, USA: AIAA.

135. Box, G.E.P. and D. Behnken, *Some new three level designs for the study of quantitative variables.* Technometrics, 1960. **2**: p. 455-475.

136. Massart, D.L., *Handbook of Chemometrics and Qualimetrics, Part 1*. Data handling in science and technology. 1997, Amsterdam: Elsevier.

137. Plackett, R.L. and J.P. Burman, *The design of optimum mutlifactorial experiments.* Biometrika, 1946. **33**(4): p. 305-325.

138. Taguchi, G. and Y. Wu, *Introduction to off-line quality control*. 1980, Nagoya: Central Japan Quality Control Association.

139. McKay, M.D., R.J. Beckman, and W.J. Conover, *A comparison of three methods for selecting values of input variables in the analysis of output from a computer code*. Technometrics, 1979. **21**(2): p. 239-245.

140. Sacks, J., W.J. Welch, T.J. Mitchell, and H.P. Wynn, *Design and Analysis of Computer Experiments.* Statistical Science, 1989. **4**(4): p. 409-423.

141. Olsson, A., G. Sandberg, and O. Dahlblom, *On latin hypercube sampling for structural reliability analysis.* Structural Safety, 2003. **25**(1): p. 47-68.

142. Morris, M.D. and T.J. Mitchell, *Exploratory designs for computer experiments.* Journal of Statistical Planning and Inference, 1995. **43**: p. 381-402.

143. Simpson, T.W., D.K.J. Lin, and W. Chen, *Sampling strategies for computer experiments: design and analysis.* International Journal of Reliability and Applications, 2001. **2**(3): p. 209-240.

144. Kalagnanam, J.R. and U.M. Diwekar, *An efficient sampling technique for off-line quality control.* Technometrics, 1997. **39**(3): p. 308-319.

145. van der Corput, J.G., *Verteilungsfunktionen.* Proceedings of the Kroninklijke Nederlandse Akademie van Wetenschappen, 1935. **38**: p. 813-821.

146. Halton, J.H., *On the efficiency of certain quasi-random sequences of points in evaluating multi-dimensional integrals.* Numerische Matematik, 1960. **2**(1): p. 84-90.

147. Faure, H., *Discrepance de suites associees a un systeme de numeration (en dimensions).* Acta Aritmetica, 1982. **41**: p. 337-351.

148. Faure, H., *Good permutations for extreme discrepancy.* Journal of Number Theory, 1992. **42**: p. 47-56.

149. Sobol, I.M., *On the distribution of points in a cube and the approximate evaluation of integrals.* USSR Computational Mathematics and Mathematical Physics, 1967. **7**(4): p. 86-112.

150. Fang, K.T., *Experimental design by uniform distribution.* Acta Mathematice Applicatae Sinica, 1980. **3**: p. 363-372.

151. Fang, K.T. and W. Y., *Number-theoretic methods in statistics*. 1994, New York, USA: Chapman & Hall.

152. Fang, K.T., D.K.J. Lin, P. Winker, and Y. Zhang, *Uniform design: theory and application.* Technometrics, 2000. **42**: p. 237-248.

153. Box, G.E.P. and K.B. Wilson, *Experimental attainment of optimum conditions.* Journal of the Royal Statistical Society, 1951. **13**: p. 1-45.

154. Gauss, J.C.F., *Combinationis observationum erroribus minimis obnoxiae*. 1825, Gottingen: University of Gottingen.

155. McLain, D.H., *Drawing contours from arbitary data points.* Journal of Computation, 1974. **17**: p. 318-324.

156. Gordon, W.J. and J.A. Wixom, *Shepard's method of 'metric interpolation' to bivariate and multivariate data.* Mathematics of Computation, 1978. **32**: p. 253-264.

157. Barnhill, R.E., *Representation and Approximation of Surfaces.* Mathematical Software III, 1977: p. 69-120.

158. Lancaster, P., *Moving Weighted Least Squares Methods,* in *NATO Advanced Study Institute Series C*, S.B. N., Editor 1979: Riedel, Dordecht. p. 91-102.

159. Shepard, D., *A Two-Dimensional Interpolation Function for Irregularly Spaced Points,* in *A.C.M National Conference*1968. p. 517-524.

160. Lancaster, P. and K. Salkauskas, *Surfaces Generated by Moving Least Squares.* Mathematics of Computation, 1981. **37**(155): p. 141-158.

161. Myers, R.H., D.C. Montgomery, and C.M. Anderson-Cook, *Response Surface Methodology: Process and Product Optimization using Designed Experiments*. 3rd ed. 2009, New York, USA: Wiley and Sons.

162. Coelho, R.F., *Metamodels for mixed variables based on moving least squares.* Optimization and Engineering, 2014. **15**(2): p. 311-329.

163. Salehi, R. and M. Dehghan, *A generalized moving least squares kernel method.* Journal of Computation and Applied Mathematics, 2013. **249**: p. 120-132.

164. Salehi, R. and M. Dehghan, *A moving least square reproducing polynomial meshless method.* Applied Numerical Mathematics, 2013. **69**: p. 34-58.

165. Mirzaei, D., R. Schaback, and M. Dehghan, *On generalized moving least squares and diffusive derivatives.* IMA Journal of Numerical Analysis, 2012. **32**(3): p. 983-1000.

166. Song, C.Y. and J. Lee, *Strength design of a knuckle component using moving least-squares response surface-based approximate optimization methods.* Proceedings of the Institution of Mechanical Engineers Part D-Journal of Automobile Engineering, 2009. **223**(D8): p. 1019-1032.

167. Song, C.Y. and J. Lee, *Reliability-based design optimization of knuckle component using conservative method of moving least-sqaures meta-models.* Probabilistic Engineering Mechanics, 2011. **26**(2): p. 364-379.

168. Choi, K.K., B. Youn, and R.-J. Yang. *Moving least squares method for reliability-based design optimization*. in *4th World Congress of Structural and Multidisciplinary Optimization*. 2001. Dalian, China.

169. Hardy, R.L., *Multiquadratic Equations of Topography and Other Irregular Surfaces*. Journal of Geophysical Research, 1971. **76**: p. 1905-1915.

170. Forrester, A., A. Sobester, and A.J. Keane, *Engineering Design via Surrogate Modelling: A Practical Guide*. 2008, New York, USA: Wiley and Sons.

171. Powell, M.J.D., *Radial basis functions for multivariable interpolation: a review*, in *Algorithms for Approximation*, J.C. Mason and M.G. Cox, Editors. 1987, Oxford University Press: London.

172. Vapnik, V., *Statistical Learning Theory*. 1998, New York: John Wiley & Sons.

173. Michelli, A., *Interpolation of scattered data: distance matrices and conditionally positive definite functions*. Constructive Approximation, 1986. **2**: p. 11-22.

174. Krige, D.G., *A statistical approach to some basic mine valuation problems on the Witwatersrand*. Journal of the Chemical, Metallurgical and Mining Engineering Society of South Africa, 1951. **52**(6): p. 119-139.

175. Matheron, G., *Principles of geostatistics*. Economic Geology, 1963. **58**: p. 1246-1266.

176. Jia, G.F. and A.A. Taflanidis, *Kriging metamodeling for approximation of high-dimensional wave and surge responses in real-time storm/hurricane risk assessment*. Computer Methods in Applied Mechanics and Engineering, 2013. **261**: p. 24-38.

177. Vapnik, V. and A. Lerner, *Pattern recognition using generalized portrait method*. Automation and Remote Control, 1963. **24**: p. 774-780.

178. Vapnik, V. and A. Chervonenkis, *A note on one class of perceptrons*. Automation and Remote Control, 1964. **25**.

179. Vapnik, V., *The nature of statistical learning theory*. 1995, New York: Springer.

180. Schölkopf, B. and A.J. Smola, *Learning with kernels*. 2002: MIT Press.

181. Smola, A.J. and B. Schölkopf, *A tutorial on support vector regression*. Statistics and Computing, 2003. **14**(3): p. 199-222.

182. Friedman, J.H., *Multivariate Adaptive Regression Splines*. The Annals of Statistics, 1991. **19**(1): p. 1-67.

183. Chen, V.C.P., *Application of MARS and orthogonal arrays to inventory forecasting stochastic dynamic programs.* Computational Statistics and Data Analysis, 1999. **30**: p. 317-341.

184. Gosavi, A., *Parametric Optimization: Response Surfaces Neural Networks*, in *Simulation-Based Optimization*. 2003, Springer. p. 57-91.

185. Desai, K.M., S.A. Survase, P.S. Saudagar, S.S. Lele, and R.S. Singhai, *Comparison of artificial neural network (ANN) and response surface methodology (RSM) in fermentation media optimization: Case study of fermentative production of scleroglucan.* Biochemical Engineering Journal, 2008. **41**(3): p. 266-273.

186. Jin, R., W. Chen, and T.W. Simpson, *Comparative studies of metamodelling techniques under simple modeling criteria.* Structural and Multidisciplinary Optimization, 2001. **23**(1): p. 1-13.

187. Taflanidis, A.A., G.F. Jia, A.B. Kennedy, and J.M. Smith, *Implementation/optimization of moving least squares response surfaces for approximation of hurricane/storm surge and wave responses.* Natural Hazards, 2013. **66**(2): p. 955-983.

188. Goel, T. and N. Stander, *Comparing three error criteria for selecting radial basis function network topology.* Computer Methods in Applied Mechanics and Engineering, 2009. **198**((27-29)): p. 2137-2150.

189. Qian, P.Z.G., B. Tang, and C.F.J. Wu, *Nested space-filling designs for computer experiments with two levels of accuracy.* Statistica Sinica, 2009. **19**(1): p. 287-300.

190. Sadd, M.H., *Elasticity - Theory, Applications, and Numerics*. 2009, Amsterdam: Elsevier.

191. Ferziger, J.H. and M. Peric, *Computational Methods for Fluid Mechanics*. 2002, London: Springer.

192. Benham, P.P., R.J. Crawford, and C.G. Armstrong, *Mechanics of Engineering Materials*. 2nd ed. 1996, London, UK: Pearson.

193. Donea, J., A. Huerta, J.-P. Ponthot, and A. Rodríguez-Ferran, *Arbitrary Langrangian - Eulerian Methods*, in *Encyclopedia of Computational Mechanics*, E. Stein, R. de Borst, and T.J.R. Hughes, Editors. 2004, John Wiley & Sons.

194. McKeown, J., D. Meegan, and D. Sprevak, *An introduction to unconstrained optimisation (A computer illustrated text)*. 1990, Bristol, UK: A. Hilger.